Multi-Scale Modeling of Mechanical and Electrochemical Properties of 1D and 2D Nanomaterials, Application in Battery Energy Storage Systems

Multi-Skalen-Modellierung Mechanischer und Elektrochemischer Eigenschaften von 1D- und 2D-Nanomaterialien, Anwendung im Batteriespeichersystem

DISSERTATION

Zur Erlangung des akademischen Grades eines
Doktor-Ingenieur
an der Fakultät Bauingenieurwesen
der Bauhaus-Universität Weimar
Germany

vorgelegt von

Mohammad Salavati
(interner Doktorand)

Mentor: Prof. Dr.-Ing. Timon Rabczuk

Gutachter: Prof. Dr. rer. nat. Tom Lahmer
Prof. Dr. Pedro Miguel Almeida Areias

Weimar, 12 June 2020

Dedicated to:

my wonderful daughter Nastaran for her strongest love,

my parents for their eternal love and belief.

Acknowledgements

I would like to express my appreciation and thanks to my advisor Prof. Dr.-Ing. Timon Rabczuk for all of his supports during the Ph.D. study and related research for his patience, motivation, and immense knowledge. I would also like to thank the members of my dissertation committee: Professor Tom Lahmer and Professor Pedro Areias, for generously offering their time, support, and guidance throughout the preparation and review of this document. I would especially like to thanks Dr.-Ing. Bohayra Mortazavi, who has contributed towards shaping this dissertation.
I gratefully acknowledge financial support from European Research Council for COMBAT project (Grant number 615132), international Ph.D. in Germany IPID4all-DAAD funding program, and Bauhaus research school (BRS).
A special thanks to my family. I would like to express my deepest gratitude to my parents and sibling for their support and belief in me. I would also like to thank my whole family, who has been supporting me in difficult moments by their understanding, love, and patience.
Finally, I would also like to thanks Ms. Marlis Terber, Ms. Rosemarie Mayer, and my other colleagues and friends from the Institute of Structural Mechanics at Bauhaus-Universität Weimar for their help and friendly support.

Mohammad Salavati
Weimar, Germany
June 2020

Authorship Declaration

I, Mohammad Salavati, hereby solemnly declare that the following dissertation is my own work and that no impermissible assistance from others or references other than those specially cited were used in its making. Data and/or concepts taken directly or indirectly from other sources have been properly referenced. Parts of the dissertation which have already appeared in examination papers are unambiguously marked as such.
I affirm that no other individuals were involved in producing the content of this dissertation. Furthermore, no placement or consulting services (promotion consultants or other persons) were paid to assist me in any way. I affirm that no one received direct or indirect pecuniary compensation or payment in kind for work conducted in connection with the content of this dissertation.
This dissertation has not been previously submitted in the same or similar form to any other examination authority in Germany or abroad.
I certify that, to the best of my knowledge, the declaration above is absolutely true and nothing has been concealed.

Mohammad Salavati
Weimar, Germany
June 2020

Abstract

Material properties play a critical role in durable products manufacturing. Estimation of the precise characteristics in different scales requires complex and expensive experimental measurements. Potentially, computational methods can provide a platform to determine the fundamental properties before the final experiment. Multi-scale computational modeling leads to the modeling of the various time, and length scales include nano, micro, meso, and macro scales. These scales can be modeled separately or in correlation with coarser scales. Depend on the interested scales modeling, the right selection of multi-scale methods leads to reliable results and affordable computational cost. The present dissertation deals with the problems in various length and time scales using computational methods include density functional theory (DFT), molecular mechanics (MM), molecular dynamics (MD), and finite element (FE) methods.

Physical and chemical interactions in lower scales determine the coarser scale properties. Particles interaction modeling and exploring fundamental properties are significant challenges of computational science. Downscale modelings need more computational effort due to a large number of interacted atoms/particles. To deal with this problem and bring up a fine-scale (nano) as a coarse-scale (macro) problem, we extended an atomic-continuum framework. The discrete atomic models solve as a continuum problem using the computationally efficient FE method. MM or force field method based on a set of assumptions approximates a solution on the atomic scale. In this method, atoms and bonds model as a harmonic oscillator with a system of mass and springs. The negative gradient of the potential energy equal to the forces on each atom. In this way, each bond's total potential energy includes bonded, and non-bonded energies are simulated as equivalent structural strain energies. Finally, the chemical nature of the atomic bond is modeled as a piezoelectric beam element that solves by the FE method.

Exploring novel materials with unique properties is a demand for various industrial applications. During the last decade, many two-dimensional (2D) materials have been synthesized and shown outstanding properties. Investigation of the probable defects during the formation/fabrication process and studying their strength under severe service life are the critical tasks to explore performance prospects. We studied various defects include nano crack, notch, and point vacancy (Stone-Wales defect) defects

employing MD analysis. Classical MD has been used to simulate a considerable amount of molecules at micro-, and meso- scales. Pristine and defective nanosheet structures considered under the uniaxial tensile loading at various temperatures using open-source LAMMPS codes. The results were visualized with the open-source software of OVITO and VMD. Quantum based first principle calculations have been conducting at electronic scales and known as the most accurate Ab initio methods. However, they are computationally expensive to apply for large systems. We used density functional theory (DFT) to estimate the mechanical and electrochemical response of the 2D materials. Many-body Schrödinger's equation describes the motion and interactions of the solid-state particles. Solid describes as a system of positive nuclei and negative electrons, all electromagnetically interacting with each other, where the wave function theory describes the quantum state of the set of particles. However, dealing with the 3N coordinates of the electrons, nuclei, and N coordinates of the electrons spin components makes the governing equation unsolvable for just a few interacted atoms. Some assumptions and theories like Born Oppenheimer and Hartree-Fock mean-field and Hohenberg-Kohn theories are needed to treat with this equation. First, Born Oppenheimer approximation reduces it to the only electronic coordinates. Then Kohn and Sham, based on Hartree-Fock and Hohenberg-Kohn theories, assumed an equivalent fictitious non-interacting electrons system as an electron density functional such that their ground state energies are equal to a set of interacting electrons. Exchange-correlation energy functionals are responsible for satisfying the equivalency between both systems. The exact form of the exchange-correlation functional is not known. However, there are widely used methods to derive functionals like local density approximation (LDA), Generalized gradient approximation (GGA), and hybrid functionals (e.g., B3LYP). In our study, DFT performed using VASP codes within the GGA/PBE approximation, and visualization/post-processing of the results realized via open-source software of VESTA.

The extensive DFT calculations are conducted 2D nanomaterials prospects as anode/cathode electrode materials for batteries. Metal-ion batteries' performance strongly depends on the design of novel electrode material. Two-dimensional (2D) materials have developed a remarkable interest in using as an electrode in battery cells due to their excellent properties. Desirable battery energy storage systems (BESS) must satisfy the high energy density, safe operation, and efficient production costs. Batteries have been using in electronic devices and provide a solution to the environmental issues and store the discontinuous energies generated from renewable wind or solar power plants. Therefore, exploring optimal electrode materials

can improve storage capacity and charging/discharging rates, leading to the design of advanced batteries.

Our results in multiple scales highlight not only the proposed and employed methods' efficiencies but also promising prospect of recently synthesized nanomaterials and their applications as an anode material. In this way, first, a novel approach developed for the modeling of the 1D nanotube as a continuum piezoelectric beam element. The results converged and matched closely with those from experiments and other more complex models. Then mechanical properties of nanosheets estimated and the failure mechanisms results provide a useful guide for further use in prospect applications. Our results indicated a comprehensive and useful vision concerning the mechanical properties of nanosheets with/without defects. Finally, mechanical and electrochemical properties of the several 2D nanomaterials are explored for the first time—their application performance as an anode material illustrates high potentials in manufacturing super-stretchable and ultrahigh-capacity battery energy storage systems (BESS). Our results exhibited better performance in comparison to the available commercial anode materials.

Contents

List of Figures

List of Tables

Nomenclature

Symbol	Description
$PDEs$	Partial differential equations
FDM	Finite difference method
BEM	Boundary element method
FEM	Finite element method
RVE	Representive volume element
$\sigma_{i,j}$	Symmetric Cauchy stress tensor
D_i	Electric displacement vector
C_D	Equivalent damping coefficient of FVDs
f_i	Mechanical body force
F_i	Surface force components
ρ	Mass density
s	Cauchy strain tensor
E	Electric field vector
q	Electric body charge
ϕ	Electric potential
Q	Surface charge
G_E	Gibbs free energy
δu	Variation of displacement
$\delta\Phi$	Variation of electric potential
W_{me}, W_{el}	Virtual work of surface displacement and electrical field per unit area
L	Lagrangian
T	Kinetic energy
U_{total}	Total bond potential energy
e_{33}	Piezoelectric coefficient
κ	Dielectric constant
Y	Elastic modulus
$BNNT$	Boron nitride nanotube
CNT	Carbon nanotube
QM	Quantum mechanics
CM	Continiuum mechanics
MD	Molecular dynamics

MM	Molecular mechanics
$MEMS\&NEMS$	Micro/nanoelectromechanical devices
MC	Monte Carlo method
DFT	Density functional theory
TB	Tight-binding
$BOPs-TB$	bond-order potentials tight binding
$BOPs-TBP$	bond-order potentials Tersoff–Brenner potential
$QMs-MNDO$	quantum-chemical semiempirical modified neglect of differential overlap
S	Least action function
$q, \dot{q}, \ddot{q}$	Position, Velocity, Acceleration
$\ddot{q}_p, \ddot{q}_c$	Predicted, estimated accelerations
LJ	Lennard-Jones potential
q_{ij}	Distance between i^{th} and j^{th} atoms
Q_i, Q_j	Charges of i^{th} and j^{th} atoms
SW	Stillinger-Weber potential
q_{list}	Neighboring list sphere radius
q_{cutoff}	Neighboring list cutoff radius
NVT	Canonical ensemble
NPT	Isothermal-isobaric ensemble
NVE	Microcanonical ensemble
μVT	Grand canonical ensemble
HPC	High performance computers
H	Hamiltonian
$\hat{H}$	Hamiltonian operator
T	Absolute temperature
k	Boltzman constant
Z	Partition function
$h-BN$	Hexagonal boron-nitride
$\mathcal{H}$	Hilbert space
$\|\psi\rangle$	State vector of a physical system
$\hbar$	Plank constant
ψ	State vector of the quantum system
Ψ	Many-body wave function
E	Total energy of the quantized system

U_{ne}	Potential energy (nucleus–electron interactions)
U_{ee}	Potential energy (electron–electron interactions)
U_{nn}	Potential energy (nucleus–nucleus interactions)
U_H	Hartree potential
U_{ext}	External potential energy (attractive interaction between electrons and nuclei)
T_e	Electrons kinetic energy
T_n	Nucleus kinetic energy
$\bigtriangledown^2$	Laplacian operator
HF	Hartree-Fock
SCF	Self-consistent field
ρ	Electrons densities

Chapter 1

Introduction

1.1 Motivation

Scale-dependent computational methods are promising tools to understand the fundamental mechanisms in different engineering fields. Physical systems in nature and artificially manufactured devices are intrinsically multi-scale phenomena. In a wide range of scientific/engineering disciplines, problems arise in different scales and need to be treated in multiple time and length scales. The complexity of underlying physics from the atomic to the bulk scale (bottom-up) necessitates using valid theoretical models in separate scales. Multi-scale modeling plays a critical role in an accurate simulation of physical systems. It has become prevalent for scrutinizing complex systems in essential applications in biology, medicine, energy, and aerospace. In these methods, modeling a different time and length scales is the critical issue and is generally divided into hierarchical, semi-concurrent, and concurrent modelings. The main difference between these classifications is the modeling of the scales as a bridged (fine-scale linking to coarse-scale) or separate scales. In the hierarchical modeling approach, adaptive computational methods independently calculate physical properties in a fine-scale to evaluate constitutive relations for coarser scale models. The semi-concurrent and concurrent processes not only model hierarchical levels but also linking parameters between scales. Multi-scale modeling uses theories in classical Newtonian, quantum, and statistical mechanics to estimate precise results. These methods are used to explore the fundamental properties of complex systems and identify efficient parameters that influence bulk-scale characteristics. Therefore, multi-scale problems are the major challenge of computational science.
Theoretical models in various scales explicitly depend on the applied length and time ranges that generally divide into four scales include nano-, micro-, meso-, and macro-scales. Advanced computational methods in multiple scales that contribute to the precise modeling, contains the finite-element method (FEM), molecular mechanics/force

field (MM), molecular dynamics (MD), and density functional theory (DFT) techniques.
The FEM is a powerful discretization tool to analyze the continuum domains. This method can even solve higher-order differential equations with proper boundary and initial conditions for complex structures. In the molecular scale (mesoscale), MD, based on time averaging, simulates molecular interactions using Newton's equations of motion (classical model) and predefined interatomic potentials. Likewise, the MM models the interatomic bonding and non-bonding potential energies as a function of atomic coordinates. In this method, forces acting on each atom are equal to the negative derivative of potential energy respect to the positions. This method neglects electrons' interactions and applicable for a system with a considerable amount of atoms. Indeed, all the mentioned methods have advantages and limitations depending on applied domains and scales. In the lowest possible scale (electronic-scale), first principal or ab initio methods are the most reliable approaches. The DFT deals with systems of identical particles (solid) where the Schrödinger equation is valid. According to the Kohn-Sham theorem, the DFT based on the wave function theory solves the many-body Schrödinger equation (interacting system) as an independent-body equation (non-interacting system). The equivalency between interacting and non-interacting systems are satisfying using exchange-correlation functionals, which are the heart of DFT analysis.
Computational modeling is the most efficient approach to exploring the nature of complex systems like human bodies, living organisms, and human-made structures besides the advanced experimental methods. Computational multi-scale modeling not only provides a useful platform for interpretation of experimental results but also unraveling the comprehensive prediction of the properties. Robustness of computational methods cannot be neglected since their advantages have explored in unlocking of the many commercial applications.
The present dissertation is devoted to the multi-scale modeling of 1D and 2D materials to investigate the mechanical and electrochemical properties, which are gain primary importance in practical applications like battery energy storage systems. Nowadays, advanced batteries with ultra-high energy storage capacity and reliable performance are of importance for engineering devices. Increasing adverse environmental effects of using fossil fuels and, on the other hand, developing renewable power plants that necessitate storing discontinuous energies, and also increasing demand for electrified transport and mobile devices attract scientists to search for the efficient improvement of batteries. Therefore, one of the main challenges in the performance improvement of batteries is exploring alternative novel electrode materials with fast ion diffusion, high capacity, long-lasting battery life, and affordable prices.

1.2 Literature review

Over recent decades, the importance of computational modelings in various scales has demonstrated in a wide range of scientific disciplines [1, 2, 3, 4] like mechanics, materials science, biology, chemistry, physics, and mathematics [5, 6, 7, 8]. Computational multi-scale methodologies have considered in a broad range of developing applications in material design, energy production/storage, health and disease healing, climate variations, and economic fluctuation predictions [9, 10, 11, 12, 13, 14, 15, 16]. Practical application developments depend on the combination and correlation of scale-dependent valid theories. For instance, the computational prospect of biology and biomedicine is extending theoretical modeling in different scales to find a reliable clinical therapeutic plan for a critical human disease like cancer, vascular, and organ dysfunction syndrome [8, 17, 18, 19]. Likewise, the multi-scale approach has gained crucial importance in most engineering applications, [20, 21]. The most common challenges in energy engineering include the search for novel energy production technologies and overcome to storage problem of discontinuous energy production from available renewable power-plants. The multi-scale methods can play an essential role in the development of the energy systems, especially in the modeling of nuclear energy power-plants [22, 23] and the invention of new energy resources and advanced storage systems like batteries [24, 25].
Novel energy production and storage systems have received remarkable research interest. Increasing energy demand and developing renewable power plants attract scientists to searching for more reliable and robust storage systems. Ultrahigh-energy storage systems have been demanded in most industrial devices. Desirable energy-storage devices must satisfy the high energy density, safety, and lower cost criteria [26]. Indeed, rechargeable Lithium-ion batteries (LIB) are among the best available storage devices due to high energy density and long-life performance [27, 28]. The electrochemical reactions inside ordinary LIB make lithium ions insertion/extraction into/from electrodes during the charging and discharging process. Batteries based on intercalation electrode materials have played a crucial role in a wide range of portable electronic devices [29, 30, 31]. Generally, conventional metal-ion-storage batteries' performance depends on the energy/power density and transmission/diffusion rate of the ions on the electrode materials. Graphite is the commercial anode electrode that is stable, but it has a low ion diffusion rate and charge capacity due to irreversible capacity loss due to the formation of clustered ions between the electrode-electrolyte interface [32, 33]. Consequently, one of the critical issues to improve the performance of the metal-ion batteries is to find efficient alternative electrodes at the material level and in the upper scale configuring novel battery cells to satiate the growing market.

1.3 Objectives of the dissertation

The main objectives of the present dissertation generally are divided into three categories: first, modeling atomic bonds as piezoelectric continuum element and estimating mechanical and piezoelectric properties of a nanotube as a 1D nanomaterial. The second aim involved the investigation of the mechanical properties and failure mechanisms of 2D nanomaterials. The final objective includes exploring electrochemical properties to evaluate the performance of novel 2D nanomaterials as electrodes for the batteries. The first goals include method development of the computationally efficient multi-scale modeling from discrete-atomic to the continuum-bulk scales and performance assessment of the existed computational methods in various problems. The second aim covers exploring different defect impacts on the mechanical properties of the nanosheet. The third aim involves the application development of battery energy storage systems. The first-principal method, as the most reliable approach, is needed to gain deep insight into the enhancement of rechargeable batteries.
Novelties of the thesis originate from the ongoing research trends in the computational science community. They include successful modeling and simulation methods in various scales to solve different problems in critical industrial applications like energy storage in the energy industry. The novelties can outline within four categories: a) Development of a multi-scale atomistic-continuum framework for a 1D nanotube. b) Investigation of the failure mechanisms of the nanosheets in the presence of the various defects. c) Estimation of the mechanical and electrochemical properties of the novel 2D materials. d) Assessment of the novel electrode materials for metal-ion batteries.

1.4 Overview of the dissertation

The dissertation's topic, methodology, objectives, and innovations are introduced in the previous sections. The rest of the thesis is organized as follows:
Chapter 2 contains the fundamental formulations of the finite element method (FEM), which are used in this dissertation.
Chapter 3 is devoted to the multi-scale modeling and expansion of the atomic fine-scale to the continuum coarser-scale. In this chapter, a novel modeling approach is proposed.
Chapter 4 deals with molecular-level simulations using molecular dynamics(MD) methods. The mechanical properties and failure mechanism of the defected nanosheet were estimated employing classical molecular dynamics.
Chapter 5 focuses on the first principal method, where the ab-initio analysis conducted using density functional theory (DFT). Where the Ab-initio mechanical and electrochemical responses of the 2D nanomaterials are investigated.
Chapters 6, 7, contain the development of battery energy storage systems. The performance of novel electrode materials is investigated, employing first-principle analysis.

Chapter 8 summarized results and outlined the main contributions. Finally, some recommendations for future work are suggested.

Chapter 2

Fundamentals of Finite Element Method

2.1 A brief introduction to finite element methods

A wide range of engineering disciplines deals with different types of problems in their respective fields. All these physical phenomena can mathematically model as partial differential equations (PDEs). Solving the PDEs derived from a system with complex geometries and finding an exact solution is not possible with classical methods. The numerical approach is needed to approximate a solution for engineering problems where the final solution plan depending on domain boundaries and interior field variables that are space and time-dependent.
The macro-scale physics defines by the continuum field theories such as the theory of elasticity or plasticity, where the governing equations in continuum mechanics are solving through numerical methods like the finite difference method (FDM), the boundary element method (BEM), the finite volume method (FVM), finite element methods (FEM), and meshfree FEM methods. FEM is a numerical approach to find out the spatial and temporal variations of the field variables. Mathematically, FEM formulation of a field problem (entire domain problems like elastic and thermal problems) is defined by differential equations or by integral expressions. FEM yields approximate solution at discrete numbers of nodes in the continuum element. The basic idea is approximating the field variables in each element connecting by the simple interpolation functions; shape functions in the entire domain. The element quantities calculate in nodes where the elements linked together and loads and boundary conditions applying there. Discretization of continuum domain to piecewise finite elements and nodal quantities interpolation results in the final approximate solution. The discretizing technique has been using for predicting the behavior of the structural, mechanical, electrical, thermal, and chemical systems, since many engineering problems like strain-stress analy-

sis, heat transfer, convection-diffusion, fluid flow, mass transport, and electromagnetic can be solved using this approach.

2.2 Overview of strong- and weak-forms

The engineering problems with simple or complex geometries are treating by the numerical methods that include the higher-order operators. Classical numerical methods such as finite differences and spectral approximations can solve simple problems, while most of the applications involve complex geometries that arise the need for compatible methods. FEM is a geometry compatible method that widely used in engineering analysis. In this method, constitutive PDEs with boundary condition build a problem in strong-form. Generally, finding a solution to the strong-formulation of a problem is not easy. So, we need to convert the PDEs representation of a problem to the integral expressions, such as a functional, which implicitly contains the differential equations and is known as the weak-form formulation. The strong- and weak-forms are mathematically equivalent to the same problem. The weak-forms representation of the PDEs facilitates the finite element approximation procedure[34].
The weak-form of the PDEs is derived using weighted residual or variational methods. To define the weak-form from strong-representation, first, the trial solutions and weighting functions characterize using Dirichlet and Neumann boundary conditions, respectively. A weighted residual method expresses the PDEs of a problem as an integral form. The most common weighted residual method is called the Galerkin method that generally used for the finite element formulations. An alternative approach for developing the finite element equations is the variational method. The variational principle defines an integral form, which is called a functional that result in the governing differential equations and boundary conditions. The results of these methods are equivalent to the weak-form for symmetric systems. For example, the variational principle corresponding to the weak-form for elasticity is called the minimum potential energy theory. The principle of stationary potential energy is one of the most popular variational principles. Despite the critical role of FEM in solving various engineering problems, its validity domain is limited by the order of PDEs derived from the physical problem. For instance, the Cahn–Hilliard equation involves fourth-order spatial partial differential operators, and the FEM solution for this equation is computationally expensive. FEM has an affordable computational cost in treating second-order spatial operators.

2.3 Finite-element implementation of the piezoelectric beam

2.3.1 Governing equations

In this section, the governing equations of the piezoelectric continuum element and discretizing process are represented using FEM. The electrostatic response of the piezoelectric element with volume of Ω , and boundary surface of Γ are derived by the momentum conservation equations and divergence theorem. The stress equation of motion in Cartesian component and electrostatic equilibrium is defined as:

$$\sigma_{ij,j} + f_i = \rho \ddot{u}_i \tag{2.1}$$

$$D_{i,i} - q = 0 \tag{2.2}$$

Where, f_i, ρ , q are mechanical body force, mass density, and electric body charge, respectively. σ_{ij} and D_i are the components of the symmetric Cauchy stress tensor and electric displacement vector. They are related to the Cauchy strain tensor (s) and the electric field vector (E) components which lead to the formation of the constitutive equations of the piezoelectric continua. The constitutive equations of the piezoelectric materials can be derived from different thermodynamic potentials like the internal energy; U= U (s_{ij}, Di), the Helmholtz free energy; F = F (σ_{ij}, Di), the elastic Gibbs energy; $G_{E=}$ G_E (σ_{ij}, P_i), the Gibbs free energy; G= G (σ_{ij}, E_i), and the electric enthalpy or the electric Gibbs energy; H= H (s_{ij}, E_i). The different set of piezoelectric constitutive formulations will derive using whichever thermodynamic potentials. We used the electric Gibbs energy density or electric enthalpy to derive the constitutive equation of the piezoelectric element.
The first law of thermodynamics (conservation of energy) for the piezoelectric continuum is represented as:

$$\dot{U} = \sigma_{ij}\dot{s}_{ij} + E_i\dot{D}_i \tag{2.3}$$

where, U, σ_{ij}, s_{ij}, E_i, and D_i represent the stored energy density, stress tensor, strain tensor, electric field tensor, and electric displacement tensor, respectively, and overdot represents the differentiation respect to time. The electric enthalpy is defined as following equation;

$$H = U - E_iD_i \tag{2.4}$$

Time derivitive of Eq. (2.4) is as follows:

$$\dot{H} = \dot{U} - E_i\dot{D}_i - \dot{E}_iD_i \tag{2.5}$$

By substituting Eq.(2.3) into Eq.(2.5), time derivitive of the electric enthaly function becomes as following equation:

$$\dot{H} = \sigma_{ij}\dot{s}_{ij} - D_i\dot{E}_i \tag{2.6}$$

It should be noted that electrostatic relations can be represented in four transformed formulations depend on considering independent variables to describe the coupled interactions between mechanical and electrical variables. They take different electric enthalpy function correspondingly. The most common representation used in linear piezoelectricity is as current presented form. Equation (2.6) implies that the electric enthalpy function; H, has two independent variables; strain (s_{ij}) and electric field vector (E_i), and two dependent variables; stress (σ_{ij}) and electric displacement (D_i) that implies $H = H(s_{ij}, E_i)$, therefore dependent variables ;stress and electric displacement; and further constitutive equations could be derived as follows:

$$\sigma_{ij} = \frac{\partial H\left(s_{ij}, E_i\right)}{\partial s_{ij}} = C_{ijkl} s_{kl} - e_{kij} E_k \tag{2.7}$$

$$D_i = -\frac{\partial H\left(s_{ij}, E_i\right)}{\partial E_i} = e_{ikl} s_{kl} + \kappa_{ik} E_k \tag{2.8}$$

The electric enthalpy function that included elastic, electric, and coupling terms is give as:

$$H\left(s_{ij}, E_i\right) = \frac{1}{2}\left(C_{ijkl} s_{ij} s_{kl} - \kappa_{ij} E_i E_j\right) - e_{kij} s_{ij} E_k \tag{2.9}$$

where C_{ijkl}, e_{kij}, and κ_{ij} are the fourth-order elastic tensor measured at a constant electric field, piezoelectric tensor, and dielectric tensor measured at a constant strain, respectively. The strain tensor and electric field vector components related to the displacement vector u and the electric potential Φ, described by the following equations:

$$s_{ij} = \frac{1}{2}\left(u_{i,j} + u_{j,i}\right) \tag{2.10}$$

$$E_i = -\Phi_{,i} \tag{2.11}$$

in which a comma denotes partial differentiation. The electro-mechanic problem includes finding the mechanical displacement components; u_{i}, and electric potential; Φ, satisfying the mechanical and electrical boundary conditions like:

- Mechanical B.C.:

$$u_i = u_i^s \qquad or \qquad \sigma_{ij} n_j = F_i \tag{2.12}$$

- Electrical B.C.:

$$\Phi_i = v \qquad or \qquad D_i n_i = -Q \tag{2.13}$$

Where ${u_i}^s$, F_i, v, Q and n_i are specified mechanical displacement, surface force components, electric potential, surface charge, and outward unit normal vector components.

2.3.2 Variational method

The Hamilton principle derives the dynamic equations of a piezoelectric continuum. The Lagrangian and virtual work should be adapted to hold the electrical and mechanical contributions in Hamiltonian. Suppose that the surface tractions; f_i, and surface charge per unit area; q, assigned to a linear piezoelectric continuum. The virtual work done by predefined forces in a small variation of the displacement (δu) and electric potential ($\delta\Phi$) in the surface[35] are as follow:

$$\delta W_{me} = \overline{f}_i \delta u_i \tag{2.14}$$

$$\delta W_{el} = -\overline{q}\delta\Phi_i \tag{2.15}$$

where $\overline{()}$ denotes the changed functions and W_{me} and W_{el} are the virtual work of surface displacement and electrical field per unit area, respectively. In the variational principle for the electromechanical medium the electric enthalpy/Gibbs energy equal to the electromechanical internal energy function in the Lagrangian (L). The variational principle for the arbitrary space and time dependent variable vanishing at t_0 and t_1, takes the following equation forms;

$$\delta \int_{t_0}^{t_1} (L+W)\, dt = 0 \tag{2.16}$$

Sum of the Eqs. (2.14) and (2.15), and using the divergence theorem the virtual work variation is derived as;

$$\delta W = \int_\Gamma \left[\overline{f}_i \delta u_i - \overline{q}\delta\Phi_i\right] d\Gamma \tag{2.17}$$

$$= \int_\Gamma \overline{f}_i \delta u_i d\Gamma - \int_\Gamma \overline{q}\delta\Phi_i d\Gamma = \int_\Omega f_i \delta u_i d\Omega - \int_\Omega q\delta\Phi_i d\Omega \tag{2.18}$$

The Lagrangian is defined by integration of the kinetic (T) and electric enthalpy (H) energies over domain as follows:

$$L = \int_\Omega \left[\frac{1}{2}\rho \dot{u}_i \dot{u}_i - H\left(s_{ij}, E_i\right)\right] d\Omega \tag{2.19}$$

$$\delta L = \delta \int_{t_0}^{t_1} \int_\Omega \left[\frac{1}{2}\rho \dot{u}_i \dot{u}_i - H\left(s_{ij}, E_i\right)\right] d\Omega dt \tag{2.20}$$

The integrations of Eq. (2.20) express as term by term and time-dependent variables (δu_i and $\delta\Phi$) vanishing at t_0 and t_1 [36, 37]:

- First term:

$$\delta \int_{t_0}^{t_1} \int_\Omega \left(\frac{1}{2}\rho \dot{u}_i \dot{u}_i\right) d\Omega dt = \int_{t_0}^{t_1} \int_\Omega \left(\rho \dot{u}_i \delta \dot{u}_i\right) d\Omega dt$$

$$= \int_{t_0}^{t_1} \int_{\Omega} \left[\frac{\partial}{\partial t} \left(\rho \dot{u}_i \delta u_i d\Omega \right) - \rho \ddot{u}_i \delta u_i d\Omega \right] dt \tag{2.21}$$

$$= \int_{\Omega} \left[\rho \dot{u}_i \delta u_i \right]_{t_0}^{t_1} d\Omega - \int_{t_0}^{t_1} \int_{\Omega} \left[\rho \ddot{u}_i \delta u_i d\Omega \right] dt = - \int_{t_0}^{t_1} \int_{\Omega} \rho \ddot{u}_i \delta u_i d\Omega dt \tag{2.22}$$

- Second term:

$$\delta \int_{t_0}^{t_1} \int_{\Omega} \left[H \left(s_{kl}, E_k \right) \right] d\Omega dt = \int_{t_0}^{t_1} \int_{\Omega} \left[\frac{\partial H}{\partial s_{kl}} \delta s_{ij} + \frac{\partial H}{\partial E_k} \delta E_i \right] d\Omega dt \tag{2.23}$$

By using following variations of Eqs. (2.10) and (2.11):

$$\delta s_{ij} = \frac{1}{2} \delta \left(u_{i,j} + u_{j,i} \right) = \frac{1}{2} \left[\left(\delta u_i \right)_{,j} + \left(\delta u_j \right)_{,i} \right] \tag{2.24}$$

$$\delta E_i = -\delta \Phi_{,i} = - \left(\delta \Phi_i \right)_{,i} \tag{2.25}$$

Considering constitutive equations and substituting Eqs. (2.24) and (2.25) into Eq. (2.23), and using divergence theorem with considering to the symmetry of σ_{ij}, we have:

$$\int_{t_0}^{t_1} \int_{\Omega} \left[\sigma_{ij} \left(\delta u_i \right)_{,j} + D_i \left(\delta \Phi_i \right)_{,i} \right] d\Omega dt \tag{2.26}$$

$$= \int_{t_0}^{t_1} \int_{\Gamma} \left[n_i \sigma_{ij} \delta u_i + n_i D_i \delta \Phi_i \right] d\Gamma dt - \int_{t_0}^{t_1} \int_{\Omega} \left[\sigma_{ij} \delta s_{ij} - D_i \delta E_i \right] d\Omega dt \tag{2.27}$$

$$= \int_{t_0}^{t_1} \left[\int_{\Gamma} F_i \delta u_i d\Gamma - \int_{\Gamma} Q \delta \Phi_i d\Gamma - \int_{\Omega} \sigma_{ij} \delta s_{ij} d\Omega + \int_{\Omega} D_i \delta E_i d\Omega \right] dt \tag{2.28}$$

Substituting Eq. (2.22) and Eq. (2.28) into Eq. (2.20), we have the Lagrangian variation:

$$\delta L = \int_{t_0}^{t_1} \left[- \int_{\Omega} \rho \ddot{u}_i \delta u_i d\Omega + \int_{\Gamma} F_i \delta u_i d\Gamma - \int_{\Gamma} Q \delta \Phi_i d\Gamma - \int_{\Omega} \sigma_{ij} \delta s_{ij} d\Omega + \int_{\Omega} D_i \delta E_i d\Omega \right] dt \tag{2.29}$$

Therefore, after substituting Eqs. (2.18) and (2.29) into the Eq. (2.16), the variational principle takes the final weak form as follow:

$$\int_{t_0}^{t_1} \left(\delta L + \delta W \right) dt = \int_{t_0}^{t_1} \begin{bmatrix} - \int_{\Omega} \sigma_{ij} \delta s_{ij} d\Omega + \int_{\Omega} f_i \delta u_i d\Omega + \int_{\Gamma} F_i \delta u_i d\Gamma \\ - \int_{\Omega} \rho \ddot{u}_i \delta u_i d\Omega + \int_{\Omega} D_i \delta E_i d\Omega - \int_{\Gamma} Q \delta \Phi_i d\Gamma \\ - \int_{\Omega} q \delta \Phi_i d\Omega \end{bmatrix} dt = 0 \tag{2.30}$$

Substituting constitutive into Eqs. (2.7) and (2.8) concludes to the variational principle which is the beginning point for the discretization using independent variables u_i and Φ_i . The first line of Eq. (2.30) denotes as the virtual displacement principle and the second line refers as the virtual electric potential.

$$\int_\Omega \rho \ddot{u}_i \delta u_i d\Omega + \int_\Omega \left(C_{ijkl} s_{kl} - e_{kij} E_k\right) \delta s_{ij} d\Omega - \int_\Omega \left(e_{ikl} s_{kl} + \kappa_{ik} E_k\right) \delta E_i d\Omega$$

$$= \int_\Omega f_i \delta u_i d\Omega + \int_\Gamma F_i \delta u_i d\Gamma - \int_\Gamma Q \delta \Phi_i d\Gamma - \int_\Omega q \delta \Phi_i d\Omega \tag{2.31}$$

2.3.3 Finite-element discretization

In the finite element discretization process, a continuum element divided into several numbers of simple geometrical shapes, which are known as finite elements. These meshing elements connected by the nodes where the unknown variables defined as the nodal values. The overall field variables calculated throughout the computation of the contribution of each nodal value. In the piezoelectric continuum element, the displacement field $\{u\}$ and the electrical potential Φ variables define as the corresponding nodal representations using corresponding shape functions; $[N_u]$ and $[N_\Phi]$, which as the following equations:

$$\{u\} = [N_u] \{u_i\} \tag{2.32}$$

$$\Phi = [N_\Phi] \{\phi_i\} \tag{2.33}$$

The independent variables; strain and the electric fields vectors,$\{s\}$ and $\{E\}$, are related to the displacement field and the electric potential and subsequently to the nodal correspondence values as following equations:

$$\{s\} = [D] \{u\} = [D] [N_u] \{u_i\} \tag{2.34}$$

$$\{E\} = -\nabla \Phi = -\nabla [N_\Phi] \phi_i \tag{2.35}$$

where ∇ is the gradient operator and $[D]$ is the derivation operator. The shape functions derivatives $[B_u]$ and $[B_\Phi]$, and derivation operator defined as:

$$[B_u] = [D] [N_u] \tag{2.36}$$

$$[B_\Phi] = -\nabla [N_\Phi] \tag{2.37}$$

$$[D] = \begin{bmatrix} \frac{\partial}{\partial x} & 0 & 0 \\ 0 & \frac{\partial}{\partial y} & 0 \\ 0 & 0 & \frac{\partial}{\partial z} \\ 0 & \frac{\partial}{\partial z} & \frac{\partial}{\partial y} \\ \frac{\partial}{\partial z} & 0 & \frac{\partial}{\partial x} \\ \frac{\partial}{\partial y} & \frac{\partial}{\partial x} & 0 \end{bmatrix} \tag{2.38}$$

Substituting Eqs.(2.32) to (2.38) into matrix form of the variational principle in Eq.(2.31), the matrix representation of the discretized parameters satisfy the essential boundary conditions for any arbitrary variation of displacements and electric potentials; $\{\delta u_i\}$ and $\{\delta\phi_i\}$, and for an element can be derived as:

$$\begin{bmatrix} [M] & 0 \\ 0 & 0 \end{bmatrix} \begin{bmatrix} \ddot{u}_i \\ \ddot{\phi}_i \end{bmatrix} + \begin{bmatrix} [K_{uu}] & [K_{u\Phi}] \\ [K_{\Phi u}] & [K_{\Phi\Phi}] \end{bmatrix} \begin{bmatrix} u_i \\ \phi_i \end{bmatrix} = \begin{bmatrix} f_i \\ g_i \end{bmatrix} \tag{2.39}$$

where M, K_{uu}, $K_{u\Phi}$ /$K_{\Phi u}$, $K_{\Phi\Phi}$ represent the element mass, stiffness, piezoelectric coupling and capacitance matrix and f_i and g_i denote the external mechanical force and electric charge, respectively as follow:

$$[M] = \int_\Omega \rho \, [N_u]^T \, [N_u] \, d\Omega \tag{2.40}$$

$$[K_{uu}] = \int_\Omega [B_u]^T \, [C] \, [B_u] \, d\Omega \tag{2.41}$$

$$[K_{u\Phi}] = \int_\Omega [B_u]^T \, [e]^T \, [B_\Phi] \, d\Omega \tag{2.42}$$

$$[K_{\Phi u}] = [K_{u\Phi}]^T \tag{2.43}$$

$$[K_{\Phi\Phi}] = \int_\Omega [B_\Phi]^T \, [\kappa]^T \, [B_\Phi] \, d\Omega \tag{2.44}$$

$$\{f_i\} = \int_\Omega [N_u]^T \, \{f\} \, d\Omega + \int_\Gamma [N_u]^T \, \{F\} \, d\Gamma \tag{2.45}$$

$$\{g_i\} = \int_\Omega [N_\Phi]^T \, \{q\} \, d\Omega + \int_\Gamma [N_\Phi]^T \, \{Q\} \, d\Gamma \tag{2.46}$$

Each part of the discretized finite elements or meshing elements is connected to the adjacent elements throughout the global nodes, where the field variables are continuous

from one to another element. Localization matrices; $[L_u]$ and $[L_\Phi]$, can transform the local degree of freedoms (DOFs) to the global DOFs as follows:

$$\{u_i\} = [L_u]\{U\} \tag{2.47}$$

$$\{\phi_i\} = [L_\Phi]\{\Phi\} \tag{2.48}$$

$$\begin{bmatrix}[M] & 0\\ 0 & 0\end{bmatrix}\begin{bmatrix}\ddot{U}\\ \ddot{\Phi}\end{bmatrix} + \begin{bmatrix}[K_{UU}] & [K_{U\Phi}]\\ [K_{\Phi U}] & [K_{\Phi\Phi}]\end{bmatrix}\begin{bmatrix}U\\ \Phi\end{bmatrix} = \begin{bmatrix}F\\ G\end{bmatrix} \tag{2.49}$$

$$[M] = \sum_n [L_{un}]^T [M^n] [L_{un}] \tag{2.50}$$

$$[K_{UU}] = \sum_n [L_{un}]^T [K^n_{uu}] [L_{un}] \tag{2.51}$$

$$[K_{U\Phi}] = \sum_n [L_{un}]^T [K^n_{u\Phi}] [L_{\Phi n}] \tag{2.52}$$

$$[K_{\Phi U}] = \sum_n [L_{\Phi n}]^T [K^n_{\Phi u}] [L_{un}] \tag{2.53}$$

$$[K_{\Phi\Phi}] = \sum_n [L_{\Phi n}]^T [K^n_{\Phi\Phi}] [L_{\Phi n}] \tag{2.54}$$

$$\{F\} = \sum_n [L_{un}]^T [f_i] \tag{2.55}$$

$$\{G\} = \sum_n [L_{\Phi n}]^T [g_i] \tag{2.56}$$

where U, Φ, F, G are mechanical variables, electric potentials of the continuum structure, external forces applied to the structure, and electric charges, respectively.

Chapter 3

Development of a Multi-Scale Atomistic-Continuum Framework

3.1 Introduction

Most of large molecular systems problems cannot be treated using quantum mechanics methods. Quantum mechanics deals with the electronic structure of molecular systems; even one neglects some electrons, like in the semi-empirical methods, there are still many particles that should be taken into account. Molecular mechanics (MM) or force-field methods rely on classical mechanics and are an essential part of computational material science. MM methods have been used to obtain quantitative information about the chemical reaction of the large molecules. MM emanated from Hill [38], Westheimer [39], and Mayer's works in 1946 and developed by the Engler et al. [40] in 1973, and later in 1976 by the Allinger [41]. MM methods neglect the electronic interactions of a system and expresses system energy as a function of the nucleus positions. So, MM can predict the molecular energy and corresponding physical properties of the large molecular systems with an affordable computational cost. In fact, during the formation process of a molecule in nature, the molecular structure has received the lowest energy or stable form of a molecule. The main principle behind the MMs method is to calculate the energy as a function of the bond stretching, bending, inversion, and in-plane/out of plane torsion. Using this model of a molecule should find the minimum energy structure. MM is an empirical method that depending on parameters derived from experimental data and known as the force field parameters.

3.2 Molecular mechanics/force field method

MM's method is defined based on several assumptions. Born-Oppenheim approximation [42] is the most crucial postulation and indicates the nuclei movements are negli-

gible in comparison to the quick motion of electrons. In fact, without this assumption, it is not possible to express the system energy as a function of the nuclei coordinates. MM modeling is a relatively simple model of system-interactions that define as simple mass-spring models. The electronic interactions are not considered in these models, and molecular energy express as a function of bonds' stretch, torsion, and angles variations.
In MM or force field method, the negative derivative of the potential energy with respect to the displacement of the particles is equal to the forces on each particle. Generally, a sum of bonded and non-bonded potential energies represents each bond's total potential energy. Bonded energies include the bond stretching, bond angles (bending contributions), and torsion angles, while the non-bonded energies contain van der Waals and Columbic electrostatic interactions.

$$U_{total} = U_{bonded} + U_{non-bonded} \tag{3.1}$$

The most crucial advantage of the MM method is that it requires less computing time compared to the more complex quantum mechanics methods and can be applied for large molecular systems. However, using this method has some disadvantages like it is not applicable for investigation of the electronic properties and limited by the force-field parameters, which change for different force-fields and atoms.

3.3 Extension of chemical bond-energy as an equivalent mechanical strain-energy

In this part, we developed an atomic-continuum multi-scale framework where a structural beam element is accounting for coupled multi-physics problems representing a chemical bond. To capturing bonded and non-bonded interatomic interactions, the chemical bond is modeled as a piezoelectric beam element, including the coupled electrical and mechanical properties, for the first time. The formulation is based on the piezoelectric element enthalpy energy density and chemical bond potential energy to set up an equivalency between chemical bond and structural beam nature.
The DREIDING force field is employed since ideally suited for predicting structures, relative energies, rotational barriers, and dynamics of organic/biological and inorganic molecules. The total potential energy in this force field can be additively decomposed as [43]:

$$U = U_a + U_\theta + U\varphi + U_\omega + U_{vdW} + U_{el} \tag{3.2}$$

where U_a, U_θ, U_φ and U_ω denote the potential energy due to axial stretching, bending, torsion and inversion (one of three bonds in the same plane is inverted), U_{vdW} and U_{el} are the non-bonded potential energies that determine the van der Waals and electrostatic terms, respectively. The subscripts a , θ , φ , ω , vdW and el indicate bond

length, bond angle, dihedral angle, inversion angle, van der Waals and electrostatic, respectively. Some of these parameters are shown in Fig. (3.1). We assume small strain theory accounting for the electrostatic non-bonded energy to model the piezoelectric behavior. Only the van der Waals non-bonded energy is neglected in the calculation. The DREIDING force field describes the total energy terms for one single bond [44]. They need to be related to the energy terms expressed as:

$$U_a = \frac{1}{2} K_a \left(a - a_0\right)^2 \tag{3.3}$$

$$U_\theta = \frac{1}{2} K_\theta \left(\theta - \theta_0\right)^2 \tag{3.4}$$

$$U_\varphi = \frac{1}{2} K_\varphi \left\{1 - cos\left[2\left(\varphi - \varphi_0\right)\right]\right\} \tag{3.5}$$

$$U_\omega = \frac{1}{2} K_\omega \left(\omega - \omega_0\right)^2 \tag{3.6}$$

where K_a , K_θ , K_φ , and K_ω are the force field coefficient for the bond axial stretching, bending, dihedral torsion, and inversion, respectively. The subscript "0" refers to the equilibrium positions.
According to [45], the harmonic expression appropriately describes the potential energies. In order to simplify the calculation, the total bond potential energy in the DREIDING force field is modified by combining the dihedral angle, torsion and inversion. This compound energy is considered as an equivalent torsion energy in the harmonic form. Eq. (3.5) and Eq. (3.6) then becomes:

$$U_\varnothing = U_\varphi + U_\omega = \frac{1}{2} K_\varnothing \left(\varphi - \varphi_0\right)^2 \tag{3.7}$$

in which, bond axial stretching and bending energy coefficients (K_a , K_θ and $K_\varnothing$) are given in the DREIDING force field [44].
One can write the last term of Eq. (3.2) as [46]:

$$U_{el} = \frac{q^2}{4\pi\varepsilon_0 a} \tag{3.8}$$

where q , ε_0 and a are the electric charge, vacuum permittivity, and the length of the bond, respectively. The most significant advantage of the molecular mechanics approach is the separation of the potential energy components into physically meaningful terms. It makes the modeling process easier, and facilitates establishing an equivalency between the discrete atomistic lattice structure and continuum elements.
On the other hand, the constitutive equation of the piezoelectric materials can be derived from different thermodynamic potentials. In this study, the electric Gibbs energy

density or electric enthalpy is used to derive the constitutive equation of the piezoelectric element. The electric enthalpy function; $H\left(s_{ij},E_i\right)$; has two independent-variables (strain (s_{ij}), electric field vector (E_i)), and two dependent-variables (stress (σ_{ij}), electric displacement (D_i)) and can be written as [47].

$$H\left(s_{ij},E_i\right) = U_{pe} - U_{cf} \tag{3.9}$$

where U_{pe} , and U_{cf} are the piezoelectric potential energy density and the coupling field energy densities, respectively given by:

$$U_{pe} = \frac{1}{2}\left(C^E_{ijkl}s_{ij}s_{kl} - k^s_{ij}E_iE_j\right) \tag{3.10}$$

$$U_{cf} = e_{kij}s_{ij}E_k \tag{3.11}$$

in which C^E_{ijkl}, e_{kij}, and k^ε_{ij} are the fourth order elasticity tensor, the third order piezoelectric tensor, and the second order dielectric tensor, respectively. The superscripts E and s refer to 'electric' and 'strain', respectively. By substituting Eq.(3.10) and Eq.(3.11) into Eq.(3.9), the electric enthalpy function becomes:

$$H\left(s_{ij},E_i\right) = \frac{1}{2}\left(C^E_{ijkl}s_{ij}s_{kl} - k^s_{ij}E_iE_j\right) - e_{kij}s_{ij}E_k \tag{3.12}$$

where s, and E being the linear strain tensor and the electric field vector related to the displacement vector u and the electric potential Φ:

$$s_{ij} = \frac{1}{2}\left(u_{i,j} + u_{j,i}\right),\ E_i = -\Phi_{,i} \tag{3.13}$$

where a comma denotes spatial derivatives. In order to make further equivalency between bonded/non-bonded energies and mechanical/ electrostatic counterpart energies, according to Eq. (3.12), the complex electric enthalpy energy term which contains the electrostatic, mechanical and piezoelectric field energies, should be divided into two parts which are expressed as:

$$H\left(s_{ij},E_i\right) = H_m\left(s_{ij},E_i\right) + H_{el}\left(s_{ij},E_i\right) \tag{3.14}$$

$$H_m\left(s_{ij},E_i\right) = \left(\frac{1}{2}C^E_{ijkl}s_{ij}s_{kl}\right) - W_n\left(e_{kij}s_{ij}E_k\right) \tag{3.15}$$

$$H_{el}\left(s_{ij},E_i\right) = \left(\frac{1}{2}k^s_{ij}E_iE_j\right) - \left(1-W_n\right)\left(e_{kij}s_{ij}E_k\right) \tag{3.16}$$

where H_m, H_{el}, and W_n are the pure mechanical energy, electrostatic energy, and contribution of coupled field energy percentage to each part, respectively. We assume

$W_n = 0.99$ [48] which means that 1% of the coupled field energy is attributed to the electrical part of the energy density function.
The bond potential and piezoelectric continuum energies can be separated into elastic and electrostatic terms. Equivalence energies between molecular and continuum models is satisfied as follows:

$$U \equiv \int_{\Omega} H d\Omega \tag{3.17}$$

$$U_a + U_\theta + U_\varnothing = \int_{\Omega} H_m d\Omega \tag{3.18}$$

$$U_{el} = \int_{\Omega} H_{el} d\Omega \tag{3.19}$$

Eq. (3.18) states the equivalence mechanical energies, while Eq. (3.19) guarantees the equivalence electrostatic energies.
By assuming one-dimensional piezoelectric properties in axial direction, the mechanical and electrostatic equivalence energies yield following equations:

- Bending:

$$\frac{1}{2}K_\theta\left(\Delta\theta^2\right) = \frac{YI}{2a}\left(\Delta\theta^2\right) \tag{3.20}$$

- Torsion:

$$\frac{1}{2}K_\varnothing\left(\Delta\varphi^2\right) = \frac{GJ}{2a}\left(\Delta\varphi^2\right) \tag{3.21}$$

- Axial:

$$\frac{1}{2}K_a\left(\Delta a^2\right) = \frac{YA}{2a}\left(\Delta a^2\right) - W_n\left(e_{33}\frac{\Delta a}{a}E\Omega\right) \tag{3.22}$$

- Electrostatic:

$$\frac{q^2}{4\pi\varepsilon_0 a} = \frac{1}{2}\kappa E^2 - (1 - W_n)\left(e_{33}\frac{\Delta a}{a}E\Omega\right) \tag{3.23}$$

where Y , G, E , e_{33} , κ , A , Ω, q are the elastic modulus, shear modulus, electric field, piezoelectric coefficient, dielectric constant, cross-sectional area, volume of element and charge, respectively.

3.4 Electromechanical properties of 1D Boron Nitride Nanotube

3.4.1 Introduction

Boron Nitride Nanotubes (BNNTs) are one-dimensional nanostructures with unique mechanical, electrical, and thermal characteristics. They have been synthesized in the

1990s and have been the interest of research in various research communities [49, 50]. The importance of BNNTs emanates from their outstanding strength, lightweight, high heat resistance, radiation shield, and piezoelectric properties, making them excellent candidates in industries like energy, health, aerospace, defense, and security. BNNTs are also smart materials being frequently used in micro/nanoelectromechanical devices (MEMS/NEMS) [51]. They show potential in fire-retardant products, drug delivery, water desalination, hydrogen storage, energy harvesters, and power generation [50, 52]. The structure of BNNT is similar to hexagonal Carbon Nanotube (CNT). However, BNNTs do not only possess 95% of the CNT's elastic modulus but also they show superior characteristics like high thermal stability and piezoelectricity [53, 54].
Research of BNNT materials has focused on the prediction of effective properties such as elastic and shear modulus, piezoelectric and dielectric coefficients. Since it is sometimes difficult to extract those parameters experimentally, computational modeling has become a complementary and excellent alternative. A wide range of approaches from quantum mechanics (QM) and molecular dynamics (MD) to continuum mechanics (CM), including multi-scale modeling, have been developed and employed for this purpose. For instance, QM simulations based density functional theory (DFT) [55] solve the Schrödinger equation, while MD [56] and Monte Carlo (MC) methods are based on the numerical solution of the equation of motion.
QM-based models are usually very accurate, but they are computationally expensive and cannot be used for large systems. Force field methods such as molecular mechanics (MMs) are based on energy minimization. These methods reduce the computational cost. However, they also require more input parameters such as the aspect ratio, length, chirality, volume fraction, aligned direction, number of nanotube layer, and composite contents [57]. The total potential energy in the harmonic force field, for example, is the sum of the bonded and non-bonded potential energies. The bonded potential energy is based on two, three, and four atoms body interactions, which are referred to as the axial, bending, and torsion energies. The non-bonded potential energy includes the electrostatic and Van-der-Waals energies related to each bond. These energies can also be formulated in so-called equivalent elements, in which the spring, rod, and beam elements have been used to model the atomistic structure in multi-scale analysis [9, 58, 59, 60].
Xiang et al. [61] predicted the piezoelectric properties of zigzag BNNTs with a hybrid density functional (B3LYP) method. They found that the piezoelectric properties of BNNTs are higher compared to those of most polymers. Nakhmanson et al. [62] studied the spontaneous polarization and predicted piezoelectric properties of a zigzag BNNT by ab-initio simulations and the polarization theory of Berry phases or Wannier functions. The results revealed the spontaneous polarization coupling with lattice symmetry breaking, leading to the piezoelectric behavior of BNNT. The results also implied that the zigzag BNNT piezoelectric properties are lower than the inorganic piezo-ceramic contents such as PZT, BTO, and STO materials, but higher than those

in the piezo-polymer categories like PVDF. Sai and Mele [63] used ab-initio and a tight-binding (TB) approach to predict the piezoelectric properties of a BNNT. The zigzag and armchair tubes are induced by uniaxial and torsional strains yielding different piezoelectric behavior. While the zigzag tubes only respond to the uniaxial strain, the armchair nanotubes have a linear electric dipole moment related to torsion. Zhang and Meguid [64] investigated the effect of the number of tube layers on the piezoelectric properties of a multi-wall BNNT employing MD simulations and a CM model. The MD simulation for the zigzag single-walled BNNT resulted in $e_{11} = 0.24\frac{C}{m^2}$ while CM modeling gave a similar value of $e_{11} = 0.25\frac{C}{m^2}$. Also, both approaches for the armchair counterpart led to an equal torsional piezoelectric coefficient of $e_{14} = 0.25\frac{C}{m^2}$. The piezoelectric coefficient is positive/negative for the odd/even layers' number and decreased by increasing the number of layers. The MD results were replicated well by the CM model. Yamakov et al. [65] presented a strain-dependent dipole energy term in their MD model to investigate the piezoelectric properties of a BNNT for all chiral angles under axial and torsional loading showing the dependency of the piezoelectric properties on both chiral angle and nanotube radius.
Jaffari et al. [66] studied the effective elastic, and piezoelectric characteristics of a thin film made of BNNT reinforced polymers exploiting the finite element method (FEM) and representative volume elements (RVEs). They considered several volume fractions, aspect ratios, and compared their predictions to three analytic approaches (Voigt, Reuss, and Mori–Tanaka). They showed that the effective elastic and piezoelectric properties improved with increasing the BNNT volume fraction, while the dielectric properties decreased slightly. Jaffari et al. [48] predicted the Young's and shear modulus as well as the axial and torsional piezoelectric constants of zigzag BNNTs. Therefore, they employed a structural element accounting for chemical bonds and interactions. The results showed that the axial piezoelectric coefficients fluctuated depending on the diameters of the nanotubes and then approached a value of $0.2\frac{C}{m^2}$ while Young's modulus increased with increasing tube diameter and converged to a maximum value of 1 TPa. Several studies have revealed that the average elastic module range is from 0.5 TPa up to $1.22\pm$ 0.24 TP [67, 68, 69]. Also, the torsional piezoelectric coefficients are varying around a value of $5 \times 10^{-6}\frac{C}{m^2}$.
In this study, we present a structural beam element accounting for modeling the atomistic bond scale as a piezoelectric continuum scale. The bonded and non-bonded interatomic interactions are captured by satisfying the equivalency of chemical bond and structural beam element formulation. The formulation is based on our extended method that could set up equivalency between chemical and structural nature.

3.4.2 Chemical bond modeling as a piezoelectric beam

The BNNT bond length is between 0.137 to 0.148 nanometers. In this study, we adopted a value of 0.145 nanometers [70, 71, 72, 73]. Fig. (3.1). shows the atomic structure of the zigzag nanotube. In order to design the chemical bonds as equiv-

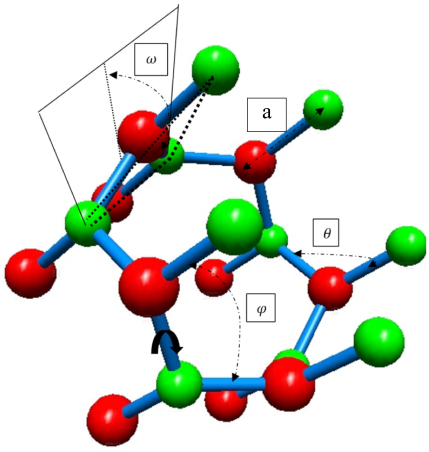

Figure 3.1: Atomic structure of zigzag nanotube (BNNT)

alent structural beam elements; represent the discrete atomistic-scale in continuous continuum-scale, we used the Eqs.(3.20)-(3.23). Where the B-N bond axial stretching and bending energy coefficients are given in the DREIDING force field [44], such that; $K_a = 700\ \left[\frac{kcal/mol}{\text{Å}^2}\right]$, $K_\theta = 100\ \left[\frac{kcal/mol}{rad^2}\right]$ and $K_\emptyset$ is the modified torsion energy coefficient [45] that is predicted as $K_\emptyset = 90\ \left[\frac{kcal/mol}{rad^2}\right]$, and Y, G, E, e_{33}, κ, A, q are the elastic modulus, shear modulus, electric field, piezoelectric coefficient, dielectric constant, cross-sectional area and charge, respectively.
In this case, the length-to-height ratio of the beam is assumed to be about 10 with circular cross section [48]; I and J are the second and polar moment of the circular cross section with radius r.

$$I = \frac{\pi}{4} r^4 \quad , \quad J = \frac{\pi}{2} r^4 \tag{3.24}$$

The charge value for the BNNTs ranges from 2.605 to 2.739 units of electron [63], so $q = 2.6e$ $\left(1e = -1.6022 \times 10^{-19}\ C\right)$ is used in the calculations here. The electric force between two charges (F) is described by Coulomb's law. The Coulomb field; electric field surrounding a point charge, is given by [74];

$$E = \frac{F}{q} = \frac{q}{4\pi\varepsilon_0 a^2} \tag{3.25}$$

The required parameters for the piezoelectric beam element are accourding Eq. (3.20) to Eq. (3.25), and calculated as following values;

$Y = 0.0468\frac{N}{nm^2}$, $G = 0.0211\frac{N}{nm^2}$, poison ratio $\nu = 0.1115, e_{33} = 9.0542e-10\frac{C}{nm^2}$ and $\kappa = 7.0866e-13$.

3.4.3 Finite-element solution

The finite element simulations are done with the commercial FE-software ANSYS and Nanotube Modeler software to extract the atomic coordinates of the BNNT. In ANSYS, we use the piezoelectric solid-beam element – SOLID227 – with ten nodes and up to five degrees of freedoms (DOFs) per node, i.e. translational (UX, UY *and* UZ), electrical ($VOLT$) and thermal ($TEMP$). In this study four DOFs – UX, UY, UZ and $VOLT$ – are assigned to each node. Fig.(3.2) a) and b) shows the piezoelectric element local orientations and polarization vectors. Each element has a piezoelectric property along the local z-axis. The piezoelectric constitutive equations are given by:

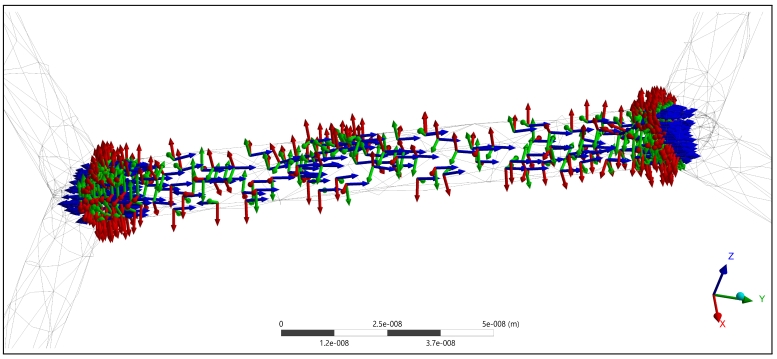

a)

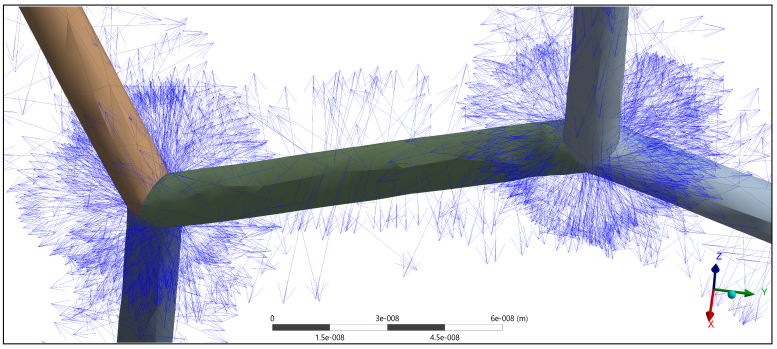

b)

Figure 3.2: a) Piezoelectric element orientation. b) Element's polarization vectors.

$$\sigma_{ij} = \frac{\partial H(s,E)}{\partial s_{ij}} = C_{ijkl}s_{kl} - e_{kij}E_k \tag{3.26}$$

$$D_i = -\frac{\partial H(s,E)}{\partial E_i} = e_{ikl}s_{kl} + \kappa_{ik}E_k \tag{3.27}$$

where σ , C , s , e , κ, D and E are the stress tensor, fourth-order elasticity tensor, linear strain tensor, piezoelectric tensor, dielectric tensor, electric displacement vector and the electric field vector, respectively. In order to extract the Young's modulus, the nanotube is fixed at the left-hand side. The electric field is assumed to be zero and a small displacement is applied to the free end of the nanotube. In order to estimate the effective axial piezoelectric coefficient of the nanotube, zero axial displacements are assumed and a potential V is applied at one end of the nanotube. The materials constants are obtained by the following equations:

$$Y = \frac{F_{re}}{A_{eq}}\frac{L}{\Delta L} \tag{3.28}$$

$$e_{33} = \frac{F_{re}}{A_{eq}}\frac{L}{V} \tag{3.29}$$

where F_{re}, L, A_{eq} denote the reaction force for each boundary condition. The length of the nanotube and the equivalent cross section of the continuum nanotube is given by:

$$A_{eq} = \pi\left[(R+r)^2 - (R-r)^2\right] \tag{3.30}$$

where R being the average radius of the nanotube. The finite element discretization of the isolated zigzag BNNT including the polarization vectors due to axially stretching is shown in Fig.(3.3).

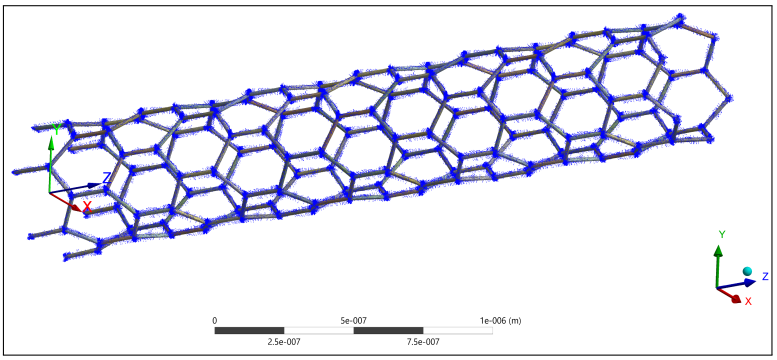

Figure 3.3: Finite element discretization of a BNNT

3.4.4 Result and discussion

We now predict the electromechanical properties of the isolated zigzag BNNT. The elastic modulus versus the aspect ratio for two diameters can be found in Fig. (3.4).

It increases with increasing aspect ratio and approaches a stationary value. Nanotubes with larger diameters tend to this stationary value quicker. In other words: They are less sensitive with respect to the aspect ratio. The length variations do not affect the elastic modulus of the nanotubes with higher aspect ratios for small diameters. The opposite tendency is observed for nanotubes with larger diameters. Table(3.1) lists

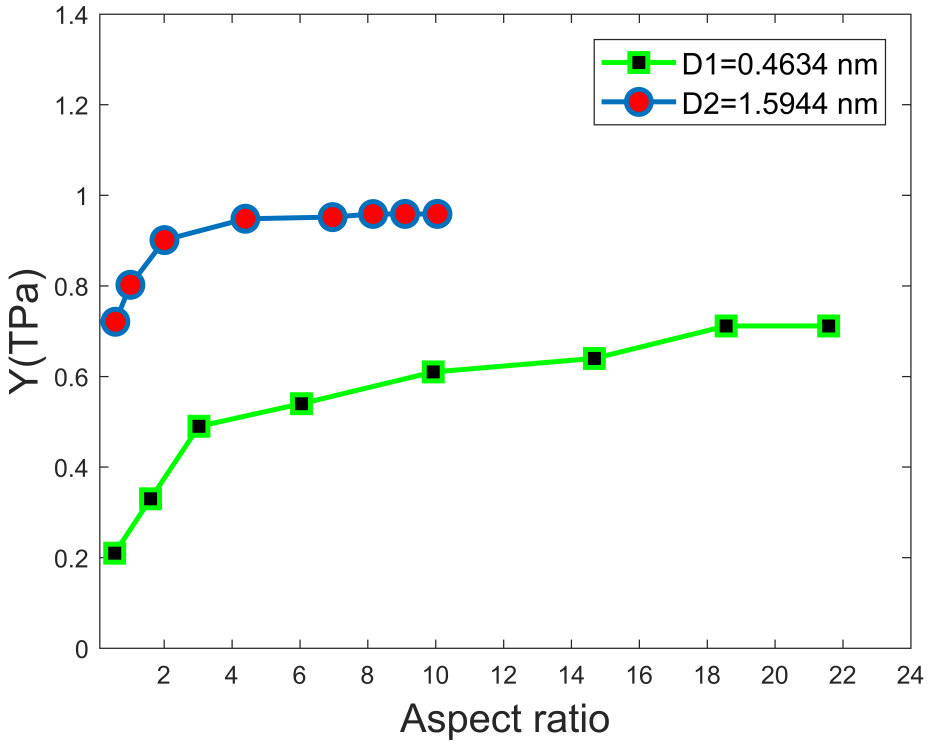

Figure 3.4: Elastic modulus of the zigzag BNNT over different length / diameter aspect ratio

the elastic moduli and axial piezoelectric coefficients for various aspect ratios. The variation of these parameters depends on the nanotube chirality and the diameter. An increased elastic modulus and decreased value of the piezoelectric coefficients are observed for increasing chirality and diameter, indicating the bonded and non-bonded interatomic interaction are well captured and coupled. Moreover, the identified elastic moduli are consistent with other predictions which are in the range of 0.5 to $1.22TPa$ [48, 67, 68, 69]. Although the piezoelectric coefficients fluctuate, they remain in already predicted intervals about 0.1 to $0.4\frac{C}{m^2}$ [61, 62]. Due to the interconnected nature of the potential energy in the atomic structure and the coupled energies (mechanical and electrostatic), defining energy equivalence is challenging. However, the good results – which agree well with experimental data and analytical theories [63, 75] – suggest the validity of our approach. Furthermore, due to the electronic and structural arrangement of the zigzag nanotubes, they exhibit a coupled piezoelectric coefficient

in the axial strain. This point is not the case for torsional loading, unlike in the armchair BNNTs [63]. In this investigation, the effective torsional piezoelectric coefficient is not considered for the zigzag nanotube. As previously stated, this study deals with

Table 3.1: Elastic moduli and axial piezoelectric coefficients of the BNNT

BNNT (*n,0*)	D(*nm*)	Y(*TPa*)	$e_{33}\frac{C}{m^2}$
(6,0)	0.4634	0.7117	0.2359
(8,0)	0.6378	0.7969	0.2281
(10,0)	0.7972	0.8414	0.2041
(12,0)	0.9567	0.8616	0.1762
(14,0)	1.1161	0.89224	0.1684
(16,0)	1.2756	0.9154	0.1725
(18,0)	1.4350	0.9469	0.1521
(20,0)	1.5944	0.9589	0.1009

the prediction of mechanical and piezoelectric properties. Earlier studies neglected the non-bonded electrostatic interaction in the structural element. However, as indicated in Fig. (3.5) and Fig. (3.6), in small strain theory, the compatible trend of the piezoelectric and elastic module curvature is noticeable. This deficiency is removed when accounting for the non-bonded electrostatic interaction within the piezoelectric element yielding physical meaning results, i.e., the intrinsic dependency between the elastic and electrostatic properties leads to an increase/decrease when the other quantity is decreased/increased.
The predicted values in Fig. (3.5)[45, 69, 76, 77] and Fig. (3.6)[61, 62, 78] also agree well with other more complicated models in the literature(bond-order potentials tight-binding(BOPs-TB) and bond-order potentials Tersoff–Brenner potential(BOPs-TBP) or quantum-chemical semiempirical modified neglect of differential overlap (QMs-MNDO). Although the influence of the non-bonded electrostatic interaction in the elastic modulus prediction is small, it plays a significant role in the prediction of the piezoelectric coefficient. Hence, by neglecting the non-bonded electrostatic interaction, it is not possible to predict the piezoelectric coefficient using the force field method.

3.4.5 Conclusion

We have presented a new approach to model the intrinsic discrete nature of the atomistic structure by using a beam element. To capture the physical phenomena at the atomistic scale, bonded and non-bonded interactions are accounted for in the piezoelectric beam element. Accuracy of the proposed method is evaluated by performing several simulations and extracting the elastic and piezoelectric coefficients respect to the nanotube chirality, diameter, and aspect ratio of the isolated zigzag BNNT. We

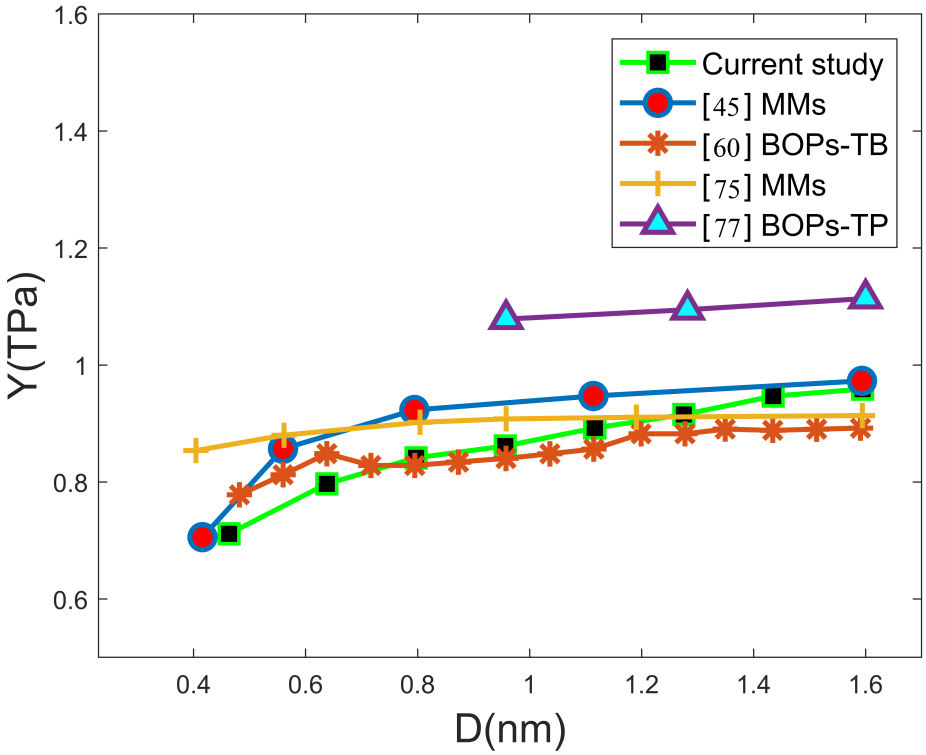

Figure 3.5: Elastic modulus of the zigzag BNNT for different diameters

were able to match the predicted values of other, more sophisticated models or experiments. The model seems to be particularly useful in extensive scale simulations, which will be studied in the future.

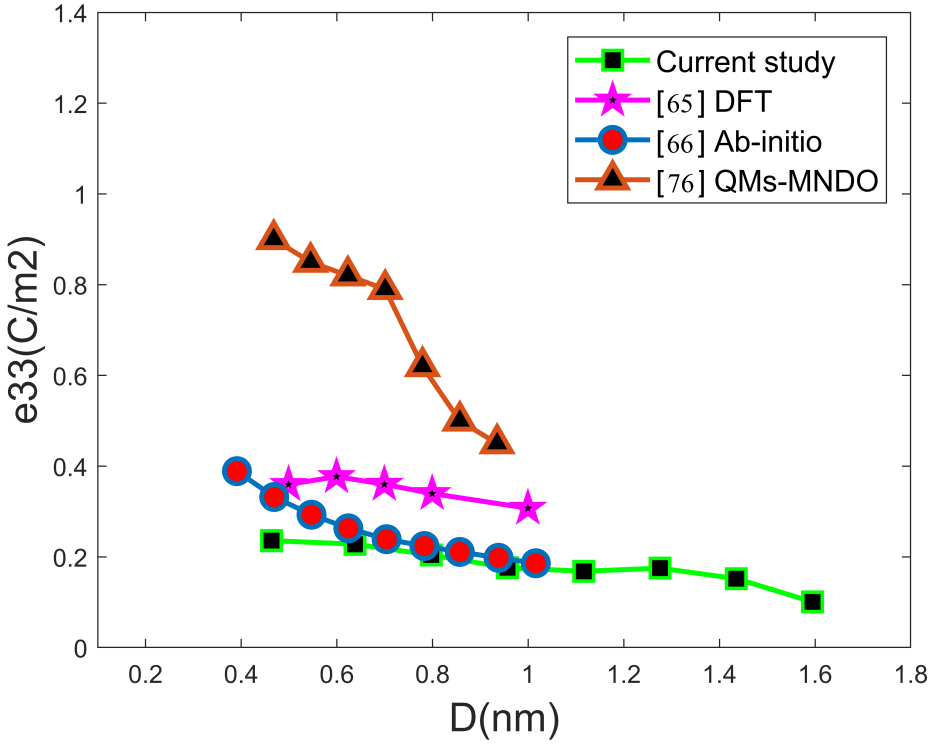

Figure 3.6: Piezoelectric coefficients of the zigzag BNNT for different diameters

Chapter 4

Molecular Dynamics Simulation

4.1 Introduction

Energy quantization of a system of particles like molecular or atomic systems is described by the quantum mechanics using the Schrödinger equation. The result of this equation is not continuous and varies in quantities. There are discrete states for allowed values of specific physical quantities, and the results for given systems have a distinct set of allowed energies. Several distinct states have the same amount of degenerate energies for each energies level of a system.
To explore any physical properties of all system states, we need to know the average energy of all states. Statistical mechanics, based on the Ergodic hypothesis and conservation energy laws, describes the probability of a system to be in each distinct state. Ergodic hypothesis indicates that all distinct energy states with the same energy (degenerate states) have the same probability that the system be in those states.
In dealing with many-particles or large molecular systems, to find the most stable structure of a system, first, the energy minimization or geometry optimization is conducting using steepest descent or conjugate gradient methods. A set of lowest energy configurations considers further analysis to explore any physical quantities of the system. However, to estimate the precise properties of a system, instead of just considering a set of low-energy structures, we need to explore average or ensemble properties over the contribution of all states of a system or all structures.
The ensemble or average property of a system can be calculated using statistical mechanics. Any physical property of a system like A, where it can be energy, bond length, pressure, temperature or other properties, is given by:

$$\text{Probability of ensemble properties} \rightarrow \overline{A} = \int_{i-states} P_i(\vec{q}^N) A_i(\vec{q}^N) d\vec{q}^N \qquad (4.1)$$

4.1 Introduction

The probability that the system is going to be in a given state is proportional to the Boltzmann factor of the state:

$$\text{Probability of each state} \rightarrow \; P_i \propto e^{-\frac{E_i}{k_b T}} \quad \leftarrow \textbf{Boltzmann factor} \tag{4.2}$$

Where E_i, k_b, and T are the energy of the states, Boltzmann constant, and temperature, respectively. The partition function of a system is the most important function of statistical mechanics. By knowing this function, all (average) properties of a thermodynamic system can be explored. Any physical properties that can learn about a system are carrying inside a partition function:

$$\textbf{Partition function} \rightarrow \; Z = \int_{\mathbb{R}^N} e^{-\frac{E(\vec{q}^N)}{k_b T}} d\vec{q}^N \tag{4.3}$$

The probability of all states properties, normalized by partition function, and add up to one:

$$P_i = \frac{1}{Z} e^{-\frac{E_i}{k_b T}} = 1 \tag{4.4}$$

Finally, the Boltzmann-weighted average of property A is given by:

$$\overline{A} = \frac{\int_{\mathbb{R}^N} e^{-\frac{E_i(\vec{q}^N)}{k_b T}} A(\vec{q}^N) d\vec{q}^N}{\int_{\mathbb{R}^N} e^{-\frac{E_i(\vec{q}^N)}{k_b T}} d\vec{q}^N} \tag{4.5}$$

Finding an analytic or exact solution for this high dimensional integral which has 3N coordinate (N is the number of atoms) is challenging issue, and computational cost is exponentially increasing by increasing constituent atoms. So, numerical approximations are the most common approach to solve this integration. Numerical approximation methods include integrate on grids, molecular dynamics (MD) (time averaging), and Monte Carlo method (random averaging).
MD, based on classical mechanics, simulates the time evolution of the large particle or molecular systems and can cover the system's possible states within an affordable computational framework. The theory of molecular dynamics and applications originated from a theoretical physicist's studies in the 1950s [79, 80]. The time evolution of an interacting atomic system calculates by integrating the Newtonian equation of motion for the constituent particles. The atoms/molecules in the system are spherically symmetric and interactions define by implemented potentials. The potential depends on the instantaneous atomic positions and interatomic spacing known as a soft-sphere model. Numerical methods like finite difference, Verlet algorithm, predictor-corrector (Gear), and multiple timestep methods solve the dynamics of a set of N particles system over

time. Solving the equations for each timestep leads to the estimation of a dynamical trajectory that describes the variations of the positions and velocities of particles; their instantaneous position and velocity define a trajectory of the particles. An isolated volume of particles includes identical energy, temperature, and pressure, which are conserved along time. The average of any dynamic property over trajectory is an approximation of the observable value of that property for the thermodynamic state of a specific number of atoms, volume, and energy. This average is equivalent to an average over a microcanonical ensemble if the identified trajectory passes through all states of phase space that has the specified energy [81]. The time correlation functions like stationary correlation, cross-correlation, and autocorrelation functions, which are a measure of the time-dependent quantities, can be derived directly through MD data. One can calculate the thermal conductivity and diffusion coefficients by using these functions. MD simulations are usually applying in a nano/picosecond time scale for 1000 to 1,000,000 atoms such that for 100 picosecond MD simulation with one femtosecond timestep, we need10^5 steps. Hence, the macroscopic properties of the system can be obtained by taking the average of the observable properties approximated by MD simulation.
The graphical representation of the classical MD simulation procedure is shown in Fig. (4.1). Initial positions of particles derived using Maxwell-Boltzmann distribution or from previous MD run. The particles should define slightly away from their known equilibrium positions so that the atoms will eventually reach their global equilibrium position during the relaxation period. Initial velocities of atoms are generally assigned randomly. However, those velocities are rescaled by the thermostat during the simulation to achieve the desired temperature. The simulation loop runs until satisfying the termination condition, which is usually the number of iterations.

4.2 Equations of motion

MD simulates the dynamic of a particle system using statistical and classical mechanics laws. Early MD simulations were based on molecular mechanics or force-field method, where the atoms and bonds modeled as small mass and spring, respectively. This approach was able to calculate systems with a few atoms. Advanced high-performance computers with high processing rates are facilitated computing of the complex models for large molecular systems. MD simulation takes atoms as the primary particles, neglects nuclei and electron interactions, and simplifies calculation by just considering atoms interactions, and finally, classical Newton's equations describe the dynamics of an atomic system.
Different formalisms are available to represent or derive the classical equations of motion. Some of these formalisms are more adaptive to theoretical interpretations and

4.2 Equations of motion

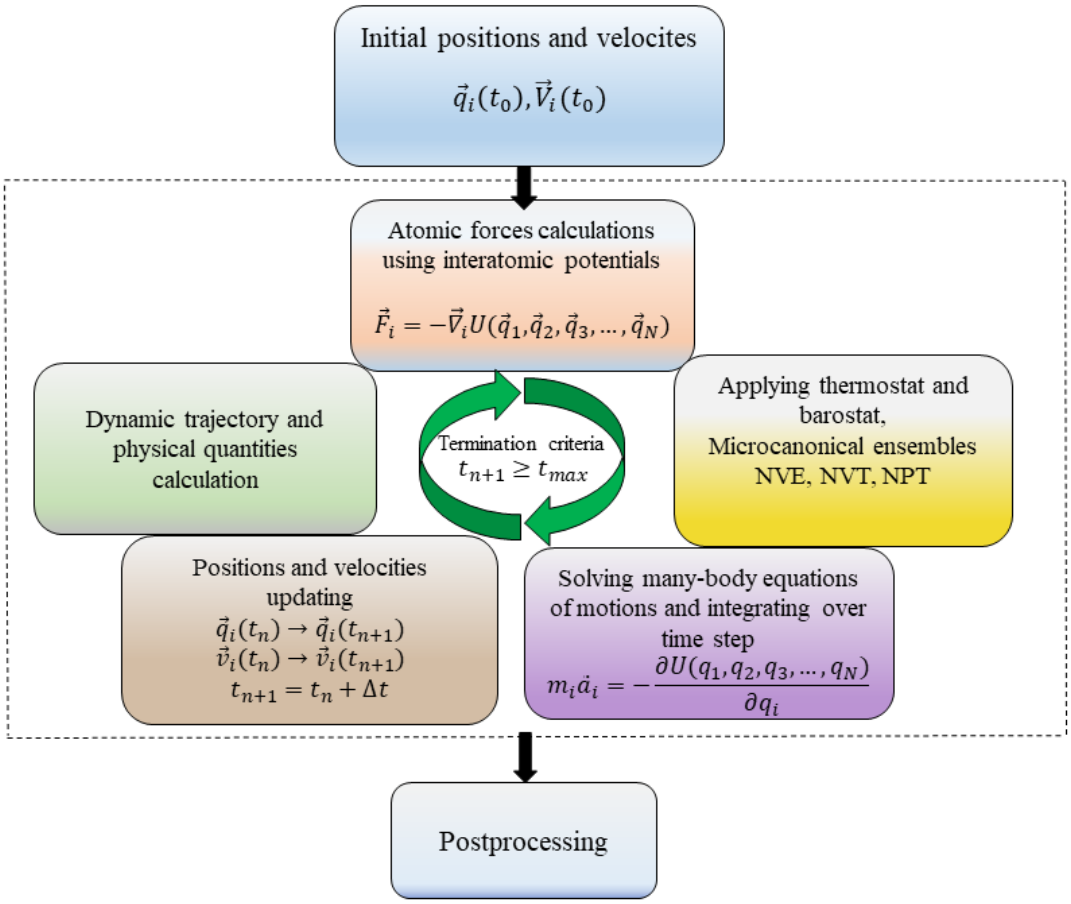

Figure 4.1: Graphical representation of the basic MD simulation procedure.

analysis of complex systems as follows:

- Newtonian mechanic's framework: force and acceleration vectors should analyze precisely, and the governing equations in any coordinate system have the same form.
- Lagrangian formalism: there are no force and accelerations vectors and no need for analyzing them. Euler-Lagrange equations of motion independent from the coordinate systems, which make them mathematically pleasant formulation.
- Hamiltonian formalism: appropriates for extension of the classical mechanics within the quantum mechanics framework.

4.2.1 Classical/Newtonian mechanics

The translational motions of a particle due to external forces are described by Newton's second law, which established a direct relationship between acting forces and particle motions:

$$F_i = m\ddot{q}_i \quad i = 1,2,3,.....,N \tag{4.6}$$

where F, m, $\ddot{q}$, and N are the force, particle mass, acceleration, and number of particles respectively. The particle mass is assumed to be independent of the position, velocity, and time. For the N particles system, the second law of motion in three directions is described as 3N second-order differential equations. If any forces act on a mobile particle, it continues moving with constant velocity already had, which is the first law of Newton. By using the second law, the third law of Newton can be derived. In an isolated system of two particles, there are no external forces, and the total force should be zero. Consequently, the interaction force between two particles should be contracted by each other, which refers to Newton's third law.

$$F_{tot} = F_1 + F_2 = 0 \quad \rightarrow F_1 = -F_2 \tag{4.7}$$

By using Newton's law of motion, the kinetic energy (T) is calculated as in the following equation. The kinetic energy is defined as the needed energy for a particle to start motion from rest state to velocity of $\dot{q}$

$$T = \frac{1}{2}m\dot{q}^2 \tag{4.8}$$

4.2.2 Lagrangian mechanics

Consider a system that describes by position set of $(q_1, q_2, q_3, \ldots, q_N)$. The coordinate system can be Cartesian, polar coordinate or length, angle or any other coordinate sets that needed for describing the state of the system. The extended velocities are defined

as $(\dot{q_1}, \dot{q_2}, \dot{q_3}, \ldots, \dot{q_N})$. We consider a set of parameters $q_i, \dot{q}_i$ for configuration space of a system with 2N degree of freedom. The obvious law of the nature is by using the position and velocity parameters the acceleration of a system can be calculated in a moment. This means for the next small period of time, the positions and velocities can be calculated as follows:

$$q_i(t+\varepsilon) = q_i(t) + \varepsilon \dot{q}_i \tag{4.9}$$

$$\dot{q}_i(t+\varepsilon) = \dot{q}_i(t) + \varepsilon \ddot{q}_i(t) \tag{4.10}$$

Therefore, if a physical system configuration is known in a specific time, then the time evolution of all configurations of this system can be uniquely estimated. So, with knowing $(q(0), \dot{q}(0))$ one can estimate the other configurations $(q(t), \dot{q}(t))$ or the motion's trajectory uniquely. It is worthy to remind that the coordinates and velocities of a configuration space are independent quantities. It means that by knowing just one of them in a specific moment, it is impossible to estimate the other quantity at the same time.

The system's trajectory in a configuration space can be estimated using the least action principle. The least action principle is a significant mechanic's law that conceptually means that a system tends to pass through the pathway with a minimum force acting on its components. In all possible trajectory space of a system, it mathematically means the first derivative with respect to the small variation is equal to zero, which is the description of an extremum point and shown as:

$$S(q_i, \dot{q}_i) = \int_{t_1}^{t_2} L(q_i, \dot{q}_i)\, dt \tag{4.11}$$

where $L(q, \dot{q})$ is Lagrangian function. This equation describes the least action function (S) for a system that in t_1 time is on configuration of $(q_a, \dot{q_a})$ and dynamic evolution of system move it to the configuration of $(q_b, \dot{q_b})$ in time t_2. Hence, the trajectory of the system can be estimated between configurations as follows:

$$\frac{\delta S}{\delta q} = 0 \quad or \rightarrow \lim_{\Delta q \to 0} (S(q+\Delta q) - S(q)) = 0 \tag{4.12}$$

$$S(q_i + \Delta q_i, \dot{q}_i + \Delta \dot{q}_i) = \int_{t_1}^{t_2} L(q_i + \Delta q_i, \dot{q}_i + \Delta \dot{q}_i)\, dt \tag{4.13}$$

Using the increment theorem for two-variables functions the following equations can be derived:

$$\begin{aligned} \Delta S(q_i, \dot{q}_i) &= S(q_i + \Delta q_i, \dot{q}_i + \Delta \dot{q}_i) - S(q_i, \dot{q}_i) \\ &= \frac{\partial S(q_i, \dot{q}_i)}{\partial q} \Delta q_i + \frac{\partial S(q_i, \dot{q}_i)}{\partial \dot{q}} \Delta \dot{q}_i + \varepsilon_1 \Delta q_i + \varepsilon_2 \Delta \dot{q}_i \end{aligned} \tag{4.14}$$

where;

$$\begin{aligned}\varepsilon_1 &= \varepsilon_1(\Delta q_i, \Delta \dot{q}_i) \to 0 \\ \varepsilon_2 &= \varepsilon_2(\Delta q_i, \Delta \dot{q}_i) \to 0\end{aligned} \tag{4.15}$$

using Eqs.(4-12), (4-14) and (4-15) we have:

$$\int_{t_1}^{t_2} \left[L(q_i, \dot{q}_i) + \frac{\partial L(q_i, \dot{q}_i)}{\partial q_i} \Delta q_i + \frac{\partial L(q_i, \dot{q}_i)}{\partial \dot{q}_i} \Delta \dot{q}_i \right] dt \tag{4.16}$$

where the first term equal to the least action function and by the expansion of the last function using integral by parts the following equations derived as:

$$\begin{aligned}&= S(q_i, \dot{q}_i) + \int_{t_1}^{t_2} \left[\frac{\partial L(q_i, \dot{q}_i)}{\partial q_i} \Delta q_i + \frac{d}{dt} \left(\frac{\partial L(q_i, \dot{q}_i)}{\partial \dot{q}_i} \Delta q_i \right) - \frac{d}{dt} \left(\frac{\partial L(q_i, \dot{q}_i)}{\partial \dot{q}_i} \right) \Delta q_i \right] dt \\ &= S(q_i, \dot{q}_i) + \frac{\partial L(q_i, \dot{q}_i)}{\partial \dot{q}_i} \Delta q_i \Big|_{t_2}^{t_1} + \int_{t_1}^{t_2} \left[\frac{\partial L(q_i, \dot{q}_i)}{\partial q_i} \Delta q_i - \frac{d}{dt} \left(\frac{\partial L(q_i, \dot{q}_i)}{\partial \dot{q}_i} \right) \Delta q_i \right] dt \\ &= S(q_i, \dot{q}_i) + 0 + \int_{t_1}^{t_2} \Delta q_i \left[\frac{\partial L(q_i, \dot{q}_i)}{\partial q_i} - \frac{d}{dt} \left(\frac{\partial L(q_i, \dot{q}_i)}{\partial \dot{q}_i} \right) \right] dt\end{aligned} \tag{4.17}$$

According to the fact that for a little variation on the system's trajectory, changes of S function should be zero. We can conclude the following equation:

$$\frac{\partial L(q_i, \dot{q}_i)}{\partial q_i} - \frac{d}{dt} \left(\frac{\partial L(q_i, \dot{q}_i)}{\partial \dot{q}_i} \right) = 0 \tag{4.18}$$

This equation is known as the Euler-Lagrange equation. The Lagrangian function, L, for a system is defined as the difference between the potential, and kinetic energies (U and T) expressed as a function of positions and velocities respectively, as follows:

$$L(q_i, \dot{q}_i) = T(q_i, \dot{q}_i) - U(q_i) \tag{4.19}$$

For a particle in the potential, U, in a Cartesian coordinate system, the Lagrangian is described as:

$$L = \frac{1}{2} m \left(\dot{x}^2 + \dot{y}^2 + \dot{z}^2 \right) - U(x, y, z) \tag{4.20}$$

By solving the Euler-Lagrange equation for this system, we have:

$$m\ddot{x} = -\frac{\partial U}{\partial x}, m\ddot{y} = -\frac{\partial U}{\partial y}, m\ddot{z} = -\frac{\partial U}{\partial z} \tag{4.21}$$

Eq.(4.21) are the classical equations of motion. For a system with N degree of freedom, there is N number of second-order differential equations. Finally, the unique trajectory of a system can be derived in configuration space by using initial coordinates and velocities.

4.3 Numerical integration methods

Realistic modeling of the inter-molecular interactions depend on the continuous potential description where all particles' motion is interdependent. Finding an analytical solution for the many-body interacting systems is not applicable. So, the time evolution of many-particle systems in the MD simulations calculates by numerical integration of the equations of motion.

4.3.1 Finite difference method

Molecular dynamics trajectories can be estimated using finite difference methods. In this method, the integration time is divided into several small timesteps—the forces and subsequently accelerations of each particle derived from vector summation of the interactions with other particles. The dynamic trajectory in each time step depends on the previous time step values, considering that the force is constant in time intervals. So, in high temperatures for light molecules and potential functions with sharp variations, a very small timestep should be selected. A wide range of finite difference algorithms developed based on Taylor series expansion to estimate the dynamic properties of a molecular system. The consecutive positions, velocities, and accelerations can be estimated using the following equations:

- Position:

$$q(t+\delta t) = q(t) + \delta t \dot{q}(t) + \frac{1}{2}\delta t^2 \ddot{q}(t) + \frac{1}{6}\delta t^3 \dddot{q}(t) + \ldots \tag{4.22}$$

- Velocity:

$$\dot{q}(t+\delta t) = \dot{q}(t) + \delta t \ddot{q}(t) + \frac{1}{2}\delta t^2 \dddot{q}(t) + \ldots \tag{4.23}$$

- Acceleration:

$$\ddot{q}(t+\delta t) = \ddot{q}(t) + \delta t \ddddot{q}(t) + \ldots \tag{4.24}$$

where q, $\dot{q}$, and $\ddot{q}$ are the position, velocity and acceleration. For a dynamic trajectory like S(q, $\dot{q}$, $\ddot{q}$), the forward, backward and central differences in each time intervals can be calculated as:

- Forward:

$$\left(\frac{\partial S}{\partial t}\right)_i \cong \frac{S_{i+1} - S_i}{\delta t} \tag{4.25}$$

- Backward:

$$\left(\frac{\partial S}{\partial t}\right)_i \cong \frac{S_i - S_{i-1}}{\delta t} \tag{4.26}$$

- Central:

$$\left(\frac{\partial S}{\partial t}\right)_i \cong \frac{S_{i+1} - S_{i-1}}{2\delta t} \tag{4.27}$$

4.3.2 Verlet algorithm

The Verlet algorithm [82] is one of the most common numerical integration in MD simulations. The main idea behind this algorithm is by using the summation of the forward and backward Taylor series for positions, the new positions can be estimated based on the previous positions and acceleration at time t and positions at a previous time (t-δt), as following equations:

$$q(t+\delta t) = q(t) + \delta t \dot{q}(t) + \frac{1}{2!}\delta t^2 \ddot{q}(t) \tag{4.28}$$

$$q(t-\delta t) = q(t) - \delta t \dot{q}(t) + \frac{1}{2!}\delta t^2 \ddot{q}(t) \tag{4.29}$$

by adding two equations the forward step at $t + \Delta t$ is derived as follows:

$$q(t+\delta t) = 2q(t) - q(t-\delta t) + \delta t^2 \ddot{q}(t) \tag{4.30}$$

Velocities disappear in the Verlet integration algorithm, Eq.(4.30). To find the velocities, one can take the position difference divided by time difference as follows:

$$\dot{q}(t) = \frac{q(t+\delta t) - q(t-\delta t)}{2\delta t} \tag{4.31}$$

or by using Verlet leap-frog algorithm [83]; half-time step method as:

$$\dot{q}\left(t + \frac{1}{2}\delta t\right) = \frac{q(t+\delta t) - q(t)}{\delta t} \tag{4.32}$$

$$\dot{q}\left(t + \frac{1}{2}\delta t\right) = \dot{q}\left(t - \frac{1}{2}\delta t\right) + \delta t \ddot{q}(t) \tag{4.33}$$

The velocity Verlet algorithm [84] is another equivalent method that can compute the positions, velocities, and accelerations simultaneously;

$$q(t+\delta t) = q(t) + \delta t \dot{q}(t) + \frac{1}{2}\delta t^2 \ddot{q}(t) \tag{4.34}$$

$$\dot{q}(t+\delta t) = \dot{q}(t) + \frac{1}{2}\delta t \left[\ddot{q}(t) + \ddot{q}(t+\delta t)\right] \tag{4.35}$$

This algorithm is a three-step procedure because of Eq. (4.35), the accelerations at two-time steps (t and $t+\delta t$) are needed for calculating the new velocities. Thus,

in the first step, by using velocities and acceleration at the time (t), the positions at time ($t+\delta t$) are computed according to Eq. (4.34), then the velocities at half-timestep ($t+\frac{1}{2}\delta t$) can be calculated using the following equation:

$$\dot{q}\left(t+\frac{1}{2}\delta t\right)=\dot{q}\left(t\right)+\frac{1}{2}\delta t\ddot{q}\left(t\right) \tag{4.36}$$

From the current positions at the time ($t+\delta t$), the new forces and accelerations are calculated. Finally, the velocities at ($t+\delta t$) are calculated using:

$$\dot{q}\left(t+\delta t\right)=\dot{q}\left(t+\frac{1}{2}\delta t\right)+\frac{1}{2}\delta t\ddot{q}\left(t+\delta t\right) \tag{4.37}$$

4.3.3 Predictor-corrector methods

The predictor-corrector [85] method include three main stages. In a first step, the positions, velocities, and accelerations are calculated using Taylor series expansion. Then the forces compute in the new positions and accelerations are obtained at time $t+\delta t$. Eventually, in the correction stage, the difference between predicted acceleration ($\ddot{q}_p$) by Taylor series and estimated acceleration ($\ddot{q}_c$) are used to find the corrected positions, velocities, and accelerations as in the following equations:

$$\Delta\ddot{q}\left(t+\delta t\right)=\ddot{q}_c\left(t+\delta t\right)-\ddot{q}_p\left(t+\delta t\right) \tag{4.38}$$

$$q_c\left(t+\delta t\right)=q_p\left(t+\delta t\right)+c_0\Delta\ddot{q}\left(t+\delta t\right) \tag{4.39}$$

$$\dot{q}_c\left(t+\delta t\right)=\dot{q}_p\left(t+\delta t\right)+c_1\Delta\ddot{q}\left(t+\delta t\right) \tag{4.40}$$

$$\frac{\ddot{q}_c\left(t+\delta t\right)}{2}=\frac{\ddot{q}_p\left(t+\delta t\right)}{2}+c_2\Delta\ddot{q}\left(t+\delta t\right) \tag{4.41}$$

$$\frac{\dddot{q}_c\left(t+\delta t\right)}{6}=\frac{\dddot{q}_p\left(t+\delta t\right)}{6}+c_3\Delta\ddot{q}\left(t+\delta t\right) \tag{4.42}$$

where c_0, c_1, c_2, and c_3 are the proposed coefficient by Gear [85] and take the values of $\frac{1}{6}, \frac{5}{6}, 1$, and $\frac{1}{3}$, respectively.

4.4 Potential energy

The position of atoms and molecules are playing an essential role in the modeling of molecular interactions. The positions can express globally as a coordinate system like

Cartesian coordinate or as a local coordinate such as the bond length, bond angles, and dihedral angles. In molecular modeling, the Born-Oppenheimer approximation [42] is always assumed to distinguish the nucleus and electrons motions. Due to the tiny mass of electrons in comparison to the nucleus and very quick motion of the electrons, they can be compatible with any changes in the nucleus positions. Thus, the molecular energy in the electronic ground state considers as a function of the nucleus coordinates. Force field methods derive the total energy of a molecular system. The energy in molecular mechanics is defined as the sum of contributions of the bonded and non-bonded energies. Bonded energies include the bond stretching, bending, and torsions, while the non-bonded energies contain Van der Waals and Columbic electrostatic interactions.

The interaction energy of the two atoms in an infinite distance is equal to zero. By decreasing the interatomic distance, the potential energy decreases to a minimum amount. However, after a specific interatomic distance, which is known as a stable bond length, distance decrement results in a quick increment in the potential energy. Interatomic energy fluctuation is interpreted by the balancing of the attractive and repulsive forces that arise from non-bonded interactions. These forces are effective in long and short-range distances, respectively. The attractive forces are due to the dispersive forces described by London [86] in the quantum mechanics framework. A sudden increase of the potential energy in very close interatomic distance is described by the Pauli exclusion principle. According to this principle, two electrons with similar quantum numbers or the same spin electrons cannot be in the same quantum state with a quantum system simultaneously. Due to this reason, the repulsion forces known as exchange forces.

The dispersion and exchange force interactions can be described using quantum mechanical principles that account for interactions at both atomic and subatomic levels, where the electronic correlations should be taken into account. However, such simulations are computationally expensive and can simulate only a small number of atoms. Thus, non-bond interatomic potentials are developed based on an empirical approach. MD simulation adopts a classical approach to simulate a more significant number of atoms by using interatomic potentials.

The potential energy due to non-bonded interactions between the system's particles is the sum of energies due to external forces, pairwise, and triplets' interactions, of the form:

$$U\left(q_1,q_2,q_3,\ldots,q_n\right)=\sum_i U_1\left(q_i\right)+\sum_{i,\ j>i} U_2\left(q_i,q_j\right)+\sum_{i,\ j>i,\ k>j} U_3\left(q_i,q_j,q_k\right)+\ldots \tag{4.43}$$

where q_n is the radius of the n^{th} atom, U_i is an i-body potential. In order to reduce computational costs, the energy due to external forces are usually ignored, and multi-body interactions are usually restricted to three.

4.4.1 Pairwise interactions

Pairwise interactions potential provides the attractive and repulsive forces between atoms nuclei surrounded by negatively charged electrons cloud. One of the most used potentials which describe pairwise interactions is the Lennard-Jones (LJ) potential [87], as follow:

$$U\left(q_{ij}\right) = 4\varepsilon\left[\left(\frac{\sigma}{q_{ij}}\right)^{12} - \left(\frac{\sigma}{q_{ij}}\right)^{6}\right] \quad , \quad q_{ij} = q_i - q_j \tag{4.44}$$

where q_{ij} is the distance between the atoms i and j, σ represents equilibrium distance, the distance at which the energy $U(q)$ is zero meaning that the attractive and repulsive forces are in equilibrium, and ε is the well depth that indicates the energy needed for pulling a pair of atoms in the strongest van der Waals binding state apart or how strongly the atoms attract each other. The $1/q^{12}$ term in the potential represents short range repulsive forces and is based on Pauli exclusion principle, while long range attractive forces represented by the $1/q^6$ term is based on Van der Waals forces. Fig. (4.2) shown the potential energy parameters respect to the interatomic distance. has unit is electron volt (eV). The force between atoms can be computed as the derivative of the potential function with respect to interatomic distance as:

$$F_{ij} = -\frac{\partial U\left(q\right)}{\partial q} = \left(\frac{48\varepsilon}{\sigma^2}\right)\left[\left(\frac{\sigma}{q_{ij}}\right)^{14} - \frac{1}{2}\left(\frac{\sigma}{q_{ij}}\right)^{8}\right] q_{ij} \tag{4.45}$$

A precise interatomic potential function should model a large number of the Van der Waals interactions for many pairwise atoms. To reduce the computational cost and optimize the modeling implementation, a cutoff radius q_c is defined, to separate a set of interacted atoms within the cutoff radius. A cutoff radius of 2.5σ and 3.2σ are commonly used in simulations that use LJ potential. The LJ potential function in Eq. (4.44) can be written as the following function using cutoff radius:

$$U\left(q\right) = \begin{cases} U\left(q_{ij}\right) & q \leq q_c \\ 0 & q > q_c \end{cases} \tag{4.46}$$

A harmonic or Morse potential [88] describes the pairwise interactions where the Coulomb force is often subtracted for covalently bonded atoms, and the attractive interaction comes from the chemical bond formation. These potentials are described as:

- Harmonic:

$$U\left(q_{ij}\right) = \frac{1}{2}k_{ij}\left(q_{ij} - q_0\right)^2 \tag{4.47}$$

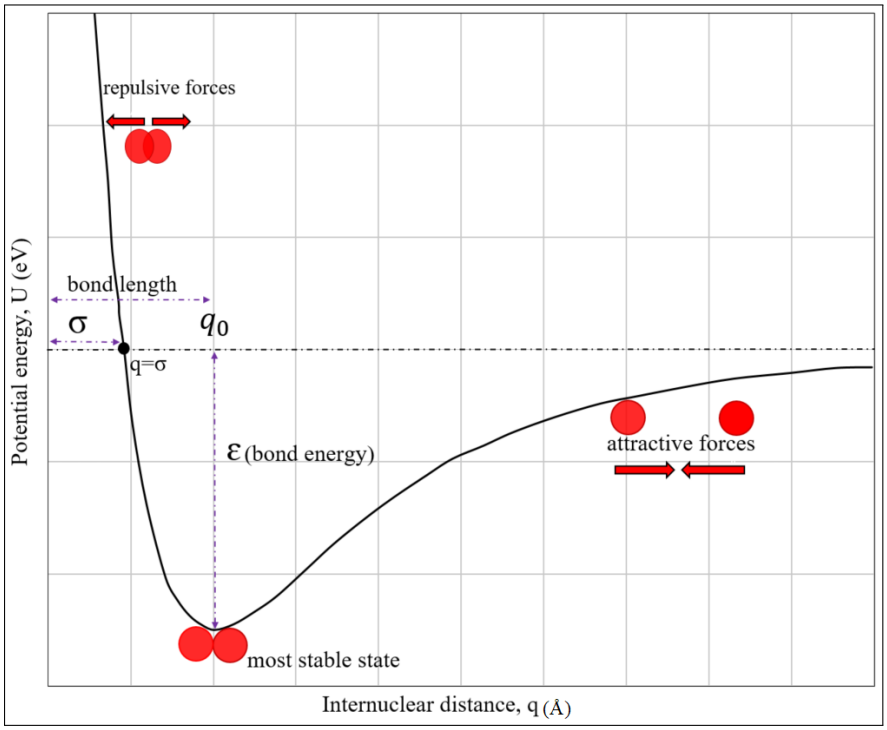

Figure 4.2: Interatomic potential energy respect to the distance.

- Morse:

$$U\left(q_{ij}\right) = A + \varepsilon\left(e^{-2a\left(q_{ij}-q_0\right)} - 2e^{-a\left(q_{ij}-q_0\right)}\right) \tag{4.48}$$

where a, k, and A are the related potentials coefficients. The following is a list of other pairwise potential functions which is comprehensively investigated in [89].

- Buckingham potential [90]:

$$U\left(q_{ij}\right) = \frac{Q_i Q_j}{q_{ij}} + A_{ij} exp\left(-\frac{q_{ij}}{\rho_{ij}}\right) - \frac{C_{ij}}{q_{ij}^6} \tag{4.49}$$

  Q_i and Q_j are the charges of i^{th} and j^{th} atoms. C, A, and ρ are the potential parameter.

- Lennard-Jones Buffered potential:

$$U\left(q_{ij}\right) = \frac{A_{ij}}{\left(q_{ij}+q_0\right)^m} - \frac{B_{ij}}{\left(q_{ij}+q_0\right)^n} \tag{4.50}$$

- Rydberg potential:

$$U\left(q_{ij}\right) = -A_{ij}\left(1 + B_{ij}\left(\frac{q_{ij}}{q_0} - 1\right)\right) exp\left(-B_{ij}\left(\frac{q_{ij}}{q_0} - 1\right)\right) \tag{4.51}$$

- Covalent exponential potential:

$$U\left(q_{ij}\right) = -D_{ij}exp\left(-\frac{a_{ij}\left(q_{ij}-q_0\right)^2}{2q_{ij}}\right) \tag{4.52}$$

where *B, A, C, m, n* are the related potentials known coefficients.

4.4.2 Triplet interaction

Simple force fields cannot describe the n-body interactions for systems containing more than a few atoms. On the other hand, the n-body interactions are not easy to define and put into account. Thus, the many-body potential implementation is generally restricted to the three-body interactions by taking some assumptions that takes other possible interactions. These potentials have been commonly used for metallic systems and many large molecules. Commonly used multi-body potentials include Tersoff potential, embedded atom method, and Stillinger-Weber.
The Tersoff potential [91, 92] is a triplet interaction function which includes an angular contribution of force to calculate the complex covalently bonded systems. The interatomic potential is taken to have the form:

$$U\left(q_{ij}\right) = \frac{1}{2}\sum_{i\neq j} f_c\left(q_{ij}\right)\cdot\left[f_R\left(q_{ij}\right) + b_{ij}f_A\left(q_{ij}\right)\right] \tag{4.53}$$

where, b_{ij} represents a measure of the bond order. f_c, f_R, and f_A are smooth cutoff function, repulsive pair, and attractive pair bonding related respectively, and given by:

$$f_R\left(q_{ij}\right) = A_{ij}exp\left(-\lambda_{ij}q_{ij}\right) \tag{4.54}$$

$$f_A\left(q_{ij}\right) = -B_{ij}exp\left(-\mu_{ij}q_{ij}\right) \tag{4.55}$$

$$f_c\left(q_{ij}\right) = \begin{cases} 1 & q_{ij} < R_{ij} \\ \frac{1}{2} + \frac{1}{2}cos\left(\frac{\pi\left(q_{ij}-R_{ij}\right)}{S_{ij}-R_{ij}}\right) & R_{ij} < q_{ij} < S_{ij} \\ 0 & q_{ij} > S_{ij} \end{cases} \tag{4.56}$$

where,

$$b_{ij} = x_{ij}\left(1+\beta_i^n\xi_{ij}^{n_i}\right)^{-\frac{1}{2n_i}} \tag{4.57}$$

$$\xi_{ij} = \sum_{k\neq i,j} f_c\left(q_{ij}\right)\omega_{ij}g\left(\theta_{ijk}\right) \tag{4.58}$$

$$g\left(\theta_{ijk}\right) = 1 + \left(\frac{c_i}{d_i}\right)^2 - \frac{c_i^2}{\left(h_i - cos\theta_{ijk}\right)^2} \tag{4.59}$$

$$\omega_{ij} = 1 \quad ; \; x_{ij} = 1 \tag{4.60}$$

$$\begin{gathered} A_{ij} = \left(A_i A_j\right)^{\frac{1}{2}} \quad ; B_{ij} = \left(B_i B_j\right)^{\frac{1}{2}} \quad ; \quad \lambda_{ij} = \frac{\left(\lambda_i + \lambda_j\right)}{2} \quad ; \mu_{ij} = \frac{\left(\mu_i + \mu_j\right)}{2} \\ R_{ij} = \left(R_i R_j\right)^{\frac{1}{2}} \quad ; S_{ij} = \left(S_i S_j\right)^{\frac{1}{2}} \end{gathered} \tag{4.61}$$

i , j and k subscripts indicate the atoms of the system, θ_{ijk} is the bond angle between ij and ik bonds. The parameter x_{ij} has a value of unity if between two atoms of the same type. A_i , B_i, S_i, R_i, λ_i, n_i and μ_i , are material constants depending on the atoms type. β , n, c, d, and h parameters depend on atom type. The energy is modeled as a sum of interactions, however, the coefficient of attractive term in the pair-like potential or bond strength depends on the local environment.

Embedded atom method (EAM) [93] is a first principle-based approach for the description of metallic systems properties. EAM deals with the atoms in electronic clouds overlapping, which is defined as well-using quantum mechanics approach like density functional theory (DFT). Atom energy nonlinearly depends on the number and distance of the surrounding atoms, which measured using electron density. EAM embeds an atom into a linear superposition of spherically averaged atomic electron densities with its neighbors.

The embedded atom method energy potential is provided energy as all-atom-summation function of the electron density ($F(\rho_i)$) at i^{th} nucleus and the usual pairwise interaction accounting for the cores repulsion effect ($U(q_{ij})$), as shown below:

$$U_{EAM} = \sum_{i=1}^{N-1} \sum_{j=i+1}^{N} U\left(q_{ij}\right) + \sum_{i=1}^{N} F\left(\rho_i\right) \tag{4.62}$$

where, i and j are the atoms pairs and N is number of all atoms. $F(\rho_i)$ is an embedding function defining the energy required to embed atom i into an environment with electron density ρ_i [94, 95]. The contribution to the electron density function from all neighboring atoms; j^{th}, at the i^{th} coordinate is represented by a linear summation of partial electron density ($f_j(q_{ij})$) which describes the contribution of an atom to the electron density field [96].

$$\rho_i = \sum_{j=1}^{N} f_j\left(q_{ij}\right) \tag{4.63}$$

Stillinger-Weber (SW) potential [97] is for semiconductor modeling contains two-body and three-body interactions terms as follows:

$$U_{SW} = \sum_i \sum_{j>i} U_2\left(q_{ij}\right) + \sum_i \sum_{j\neq i} \sum_{k>j} U_3\left(q_{ij}, q_{ik}, \theta_{ijk}\right) \tag{4.64}$$

$$U_2\left(q_{ij}\right) = A_{ij}\varepsilon_{ij}\left[B_{ij}\left(\frac{\sigma_{ij}}{q_{ij}}\right)^{p_{ij}} - \left(\frac{\sigma_{ij}}{q_{ij}}\right)^{z_{ij}}\right] exp\left(\frac{\sigma_{ij}}{q_{ij} - a_{ij}\sigma_{ij}}\right) \tag{4.65}$$

$$U_3\left(q_{ij}, q_{ik}, \theta_{ijk}\right) = \lambda_{ijk}\varepsilon_{ijk}\left(cos\theta_{ijk} - cos\theta_{0ijk}\right)^2 exp\left(\frac{\gamma_{ij}\sigma_{ij}}{q_{ij} - a_{ij}\sigma_{ij}}\right) exp\left(\frac{\gamma_{ik}\sigma_{ik}}{q_{ik} - a_{ik}\sigma_{ik}}\right) \tag{4.66}$$

where θ_{ijk} is an angle between *ij* and *ik* bonds. *A, B, p* and *z* are constant parameters of the SW potential for pairwise interactions. ε , σ and *a* are constant parameters of the SW potential which is used for both pairwise and triplet interactions. γ and λ are constant parameter of the SW potential which are used only for triplet interactions.
This potential gives a reasonably realistic description of crystalline silicon. The potential parameters for carbon and germanium are also available in the literature. SW potential is widely used in research, due to merely modeling the structural and dynamical properties with very high precision.

4.5 Initializing simulation procedure

In the MD simulation process, some restrictions should be taken into account to reduce the computation time. Several initial inputs should be prepared to minimize meaningless data to have reliable results. These constraints include the cutoff potential, periodic boundary conditions, neighbor list, number of atoms and system size, initial positions and velocities, timestep and total simulation time, and ensemble types.

4.5.1 Potential cutoff distance

The process that increases the computation time in the MD run is accounting the forces generated by the potentials acting on atoms. Generally, for a long-distance from an atom, the potential is cutting through describing a cutoff distance value. Fig. (4.3) shown the cutoff distance under periodic boundary condition in two dimensions. A cutoff distance must be smaller than half of the original simulation box size to correlate the atomic interactions. As shown in Fig. (4.3), the atom *i* has a neighboring atom *k* in the primary box and many $k^{'}$ in the surrounding image boxes. The minimum image criterion indicates that only the closest atoms ($k^{'}$) will be considered for force calculation. Thus, two atoms in the image box at the left are included for force calculation

instead of their first box counterparts (k). The eliminated part of the potential (attractive portion) is usually negligible or may re-contributing as a constant value. Normal cutoff distances for usual potentials include LJ potentials, EAM potentials, and Tersoff potentials are the values of 2.5–3.2 σ, $\sim$ 5 Å, and 3–5 Å, respectively.

4.5.2 Periodic boundary conditions

Modeling of a large number of atoms such as modeling one-mole bulk containing $\sim 10^{23}$ atoms is not possible in any computational framework. Generally, periodic boundary conditions proposed by Born and Karman [98] are used to solve this problem. Fig. (4.3) has shown the periodic boundary condition by the infinite number of image boxes around a primary box. The simulation only was done for the primary box, and other boxes are its copy. By imposing periodic boundary conditions, for example, if one atom in primary box moves out into an image box, then the same counterparts in an image box will follow the same trajectory to maintain the number of atoms constant in the primary box. The forces between an atom and its periodic image remove each other and coordinate transformation update the neighboring image boxes positions.

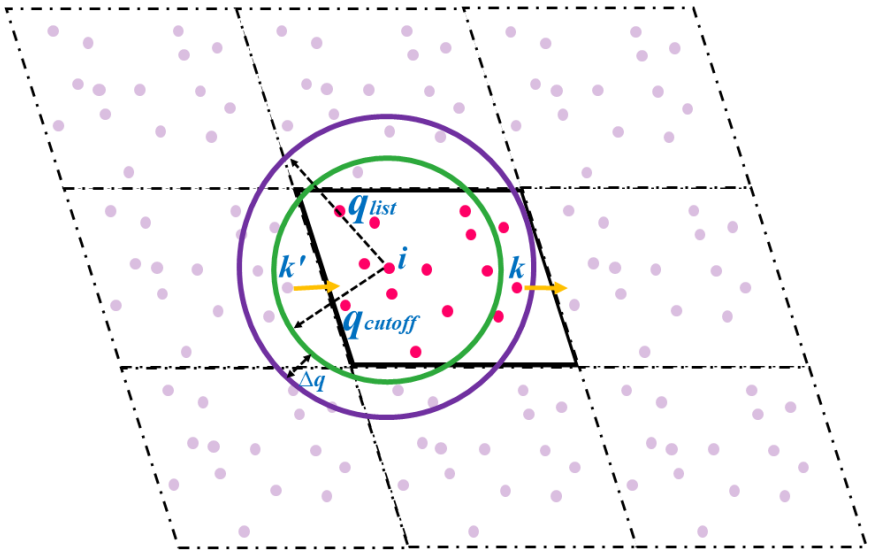

Figure 4.3: representation of potential cutoff distance and neighbor-list radius under periodic boundary conditions in two dimensions.

4.5.3 Neighbor lists

In order to optimize the atomic force calculations and naturally the calculation time, neighboring list criteria select a set of atoms that passed enough distance from the pri-

mary positions. The force calculation of atoms that has negligible movement is not meaningful. Verlet [82] proposed a neighboring list approach to reduce the calculations by listing adjacent pairs of atoms and checking their movement distances. The neighboring list sphere radius; q_{list}, is shown in Fig.(4.3), which is generally fix to the default value of the 1.1 q_{cutoff}. A list covers all the neighbors of each atom within the circle. Finally, the list updates every defined timestep and force calculation only done for the atoms in the list which usually moved more than $\Delta q/2$.

$$q_{list} - q_{cutoff} > N_{update} v \Delta t \tag{4.67}$$

where $N_{update,}$ v, and Δ t are the number of timesteps for updates, velocity, and the timestep for a considered atom.

4.5.4 Initial configuration

The system size or the number of considered atoms in the primary simulation box plays a vital role in MD simulation. The size of the considered system should be small enough to satisfy a reasonable computation process and should also be sufficiently large as long as it represents the real system. Generally, more than a hundred atoms needed to incorporate in simulation for acceptable results.
The initial positions and velocities as input simulation data define the primary configuration to solving Newton's equations of motion for the system. The initial positions can be randomly selected or defined by the already-known lattice coordinates that are available in many sources. The initial velocities can be zero or statistically chosen from the Maxwell-Boltzmann or Gaussian distribution in a given temperature:

$$P(v) = \left(\frac{m}{2\pi k_B T}\right)^{\frac{1}{2}} exp\left(-\frac{mv^2}{2k_B T}\right) \tag{4.68}$$

where $P(v)$, k_B, and m are the probability that an atom has a velocity v at an absolute temperature T, Boltzmann's constant and particle's mass, respectively.
The time evolution of a many-particle MD simulation calculates by numerical integration of the equations of motion. The velocity, acceleration, and force are assumed to be constant in each timestep. Generally, the timestep is chosen according to the lattice vibration period, which in the solid lattice is the range of 10^{-14} second (100 femtoseconds). In this way, the time step of 10^{-15} second (1 femtosecond) should be reasonable for an MD calculation. The large timestep will speed up the computation process; however, it may cause the system to exchange energy instability.
On the other hand, the small timestep may lead to a precise result; however, it increases the computational cost. Thus, proper timestep could satisfy the accurate and cost-efficient computations. Furthermore, the total simulation time should be large enough to capture the system's static and dynamic properties. The MD simulation time usually should be longer than the full relaxation time of the system.

4.5.5 Thermodynamic ensembles

In each timestep in MD simulation, various movements and behavior of atoms build a new microstate of the system. A set of possible microstate configurations are form an ensemble which has the same macroscopic and thermodynamic properties. Different ensembles are using in the MD simulation process to represent the experimental conditions of a real system. The ensembles, namely microcanonical, canonical, isobaric-isothermal, and grand canonical, are shown in Fig. (4.4). All have own fixed variables and virtually surrounded by constraining systems like an isolated experiment in the laboratory. The different types of ensembles are using to estimate the interested-property of a particular system. These properties include entropy (*S)*, Helmholtz free energy (*F)*, Gibbs free energy (*G)*, and the chemical potential (μ). The microcanonical ensemble (NVE) fixes the number of atoms (N), the simulation box volume (V), and total energy (E) and is an isolated system without any exchange with its surroundings. This ensemble is most often used in MD since it represents actual systems properly. The canonical ensemble (NVT) fixes the number of atoms (N), the simulation box volume (V), and temperature (T). The isothermal–isobaric ensemble (NPT) fixes the number of atoms (N), pressure (P), and temperature (T), whereas the grand canonical ensemble (μ VT) fixes chemical potential (μ), volume (V), and temperature (T), with a various number of atoms. Where, Ω is the accessible phase-space volume or partition function

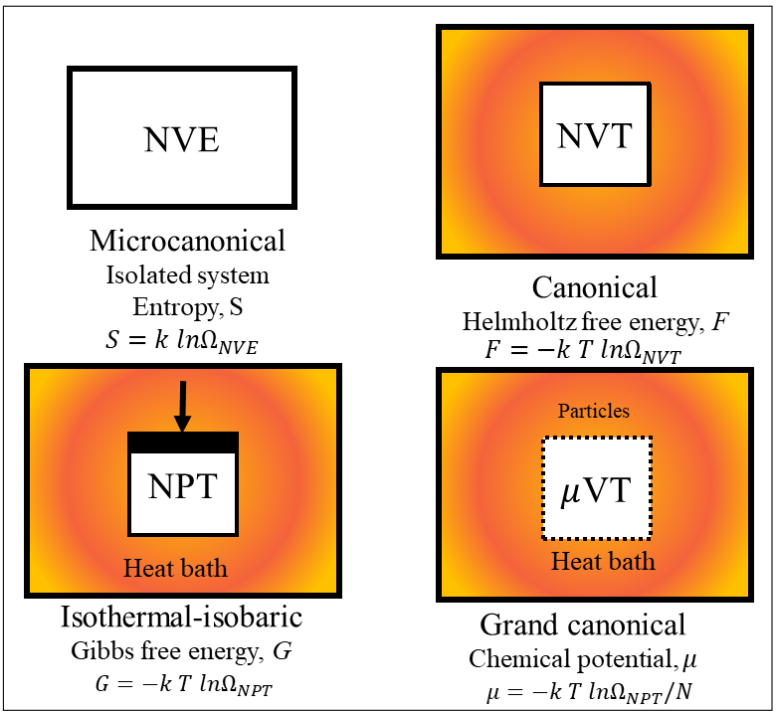

Figure 4.4: MD thermodynamics ensembles.

(Z) for the corresponding ensembles.

4.5.6 Equilibration - temperature and pressure control

In the MD simulation process, the configured initial system should bring to the equilibrium as a start point for further analysis. The isolated system has any exchange energy with surroundings, and the energy remains constant. The equations of motion are solved until the system properties have any further changes over time. Thus, after initial fluctuation, the atoms will eventually reach their global equilibrium position where no force is acting on atoms.
When a system is in equilibrium at the T temperature with its surrounding, the statistical physics described the system distribution function on any possible configurations. The Boltzmann-Gibbs theorem is the fundamental principle of the statistical mechanics and expresses the following probability density function:

$$P(q_i, p_i) = \frac{1}{Z} e^{-\beta H(q_i,p_i)} \tag{4.69}$$

$$Z = \int dqdp e^{-\beta H(q_i,p_i)} \tag{4.70}$$

$$\beta = \frac{1}{kT} \tag{4.71}$$

where (q_i,p_i), $H(q_i,p_i)$, T, k, and Z are the generalized coordinates of a system (positions, momentums), sum of kinetic and potential energy of a system or Hamiltonian, absolute temperature, Boltzman constant, and partition function of a system respectively. According to this principle, a system takes any configuration with E energy by the probability of Eq. (4-69). Where the probability density of that a system takes the configurations of the neighboring volume of $dqdp$ near the point (q,p) in the phase space. Indeed, the sum of all probability functions should be equal to one. The partition function of a system, Z, could define all macroscopic thermodynamic properties like average energy or the system's behavior.
On the other hand, the equipartition theorem states that energy is shared equally amongst all energetically accessible degrees of freedom of a system with the value of kT. For the generalized coordinate (q_i,p_i), each will have the equal values from the average energy of a system; $\frac{1}{2}kT$. In other word, each degrees of freedoms of a system in equilibrium at T temperature takes the $\frac{kT}{2}$ energy value.
In the MD simulation, for the NVE/microcanonical ensemble, the constant temperature mostly needed to be controlled instead of the energy fixing. The temperature control could be done by rescaling of the velocities. In this sense, temperature corresponds to the instantaneous kinetic energy of a system. Thus, the temperature is directly related

with average velocity, for particles in the three-dimensional degree of freedoms ($3N$) is as the following equation:

$$\langle kinetic\ energy \rangle = \langle \frac{1}{2} \sum_i m_i v_i^2 \rangle = 3N \frac{kT}{2} \tag{4.72}$$

$$\langle v \rangle = \left(\frac{3kT}{m} \right)^{\frac{1}{2}} \propto T^{\frac{1}{2}} \tag{4.73}$$

Therefore, temperature control could be done by multiplying each velocity component with a factor as follows:

$$\langle v_{new} \rangle = \langle v_{old} \rangle \left(\frac{T'}{T} \right)^{\frac{1}{2}} \tag{4.74}$$

Using this equation, the velocities of all atoms are gradually increased to the desired value in predetermined iteration steps. However, in this way, the system is not exactly equal to an NVT/canonical ensemble in a strict thermodynamic viewpoint. Several methods have been introduced to maintain a constant temperature on average using the microcanonical ensemble. Temperature controlling techniques include this velocity rescaling, the Andersen thermostat [81], the Nosé–Hoover thermostat [99], Nosé–Hoover chains [100], the Berendsen thermostat [101] and Langevin dynamics [102].
In order to use the NVT/canonical ensemble, a thermostat should add to the MD simulation. A thermostat is interacting with the system by coupling system to a heat bath or by extending the system with artificial coordinates and velocities.
In the NPT/isothermal–isobaric ensemble, to keep constant pressure, there is an extended ensemble; barostat is used while the system volume is allowed to change. Generally, the simulation box length is coupled to the pressure piston that has its degree of freedom, as shown in Fig. (4.4).

4.5.7 Energy minimization

The energy minimization of a system is an iterative process that finally derives the most stable system configuration. Generally, the minimized structure acquired by changing the individual bond potential energy parameters as described in the molecular mechanics/force field methods. Interatomic bond length and angels determine the size and shape of the molecular structures. The final atomic lattice coordinates depend on the globally minimized-energy structure, which is also known as optimized geometry. The energy minimization is gradually developing in each iteration by tracking the local minimum energies to reach the ever-possible global minimum point. Usually, numerical methods like steepest-descent and conjugate gradient are used in the minimization process to follow the energy decrement/increment slope and correlating steps.

4.6 MD-estimated properties

MD simulation can product various properties of the considered system like microscopic characteristics include positions and momenta of atoms, energies, forces, stresses. Likewise, macroscopic properties contain bulk modulus, and the thermal expansion coefficient can be calculated from the individual atom trajectory employing statistical processing. The static and dynamic properties of a system can be generated from atomic-scale data via a time-averaging method.

4.7 Mechanical responses of pristine and defective hexagonal boron-nitride nanosheets

In this part, we conducted classical molecular dynamics (MD) simulation to investigate the mechanical characteristics and failure mechanism of hexagonal boron-nitride (h-BN) nanosheets. Pristine and defective structure of h-BN nanosheets were considered under the uniaxial tensile loadings at various temperatures. Three types of initial defects, which are the most common types of defects in engineering materials are considered, which includes cracks and notches with various size and point vacancy defects with a wide range of concentration. MD simulation results demonstrate a high load-bearing capacity of extremely defective (amorphized) h-BN nanosheets. Our results also reveal that the tensile strength decline by increasing the defect content and temperature as well. Our MD results provide a comprehensive and useful vision concerning the mechanical properties of h-BN nanosheets with/without defects, which is very critical for the designing of nanodevices exploiting the exceptional physics of h-BN.

4.7.1 Introduction

Successful realization of graphene with outstanding properties [103] has attracted scientists to focus more on novel two dimensional (2D) materials in various research communities. A wide range of experimental and theoretical studies confirmed the remarkable properties of 2D materials in comparison to their bulk counterparts [104, 105, 106]. Hexagonal boron-nitride (h-BN) bulk materials were investigated experimentally by Lynch and Drickamer back to the 1960s [107]. In recent years, h-BN nanosheets [108] have been fabricated with outstanding semiconducting, mechanical strength, and heat conduction properties [109, 110, 111]. h-BN nanostructures have been discussed in a wide range of research studies due to their extraordinary mechanical, electrical, and chemical characteristics. They have proven to show high thermal stability up to $\sim$ 1000° C [112] and thermal conductivity of $\sim$ 500 $Wm^{-1}K^{-1}$ [113, 114]. Their prospect

applications are in aerospace, energy storage/conversion, medical, and many other industries [115, 116]. The crystal structure of h-BN is strongly stable due to its covalent bonding nature and is very close to that of the graphene. However, h-BN presents a wide bandgap of $\sim$ 5 - 6 eV and acts as an insulator, in sharp contrast with the zero bandgaps and highly electrical conductivity of graphene [49, 117].
The material's durability during the service strongly depends on their tensile strengths under extreme loading conditions. However, materials may have primary defects, which can reduce the prospect's performance. Specially in lower scales, deficiency of precise control during growth or processing, some possible defects may form spontaneously, which can deteriorate the application performance of materials and suppress the mechanical and thermal conduction properties and affect the electronic properties [118]. Defect assessment thus plays a critical role in material's commercial applications as micro/nanoelectromechanical (MEMS/NEMS) devices. Generally, material properties have to be investigated in the presence of various kinds of defects like; impurity atoms, point vacancy, Stone-Wales, bivacancy, cracks, grain boundaries, and notches as they may substantially affect the properties [119, 120, 121, 122, 123, 124, 125, 126]. Experimental advances [127, 128] demonstrated the importance of ongoing studies to explore the defect-related deterioration of material properties for novel structures. Since the complexities and high cost of experimental methods in lower scales, computational approaches have become a complementary and versatile alternative. A wide range of approaches from quantum mechanics (QM) and molecular dynamics (MD) to continuum mechanics (CM), including multiscale modeling, have been developed and employed for this purpose [129, 130, 131]. Katzir et al. [132] were the first to carry out the study of point defects, impurities, and vacancies in h-BN by electron paramagnetic resonance (EPR). Jimenez et al. [133] identified the formation of point defects in boron nitride by x-ray absorption near-edge spectroscopy (XANES). Hirano et al. [134] synthesized the amorphous BN by pressure pyrolysis of borazine with a high yield below 700° C at 100 MPa. Amorphous boron nitride (BN) powder was prepared by mechanically milling hexagonal BN and used as a starting material for studying BN phase transformation behavior. Fabricated amorphous BN (aBN) powder was significantly reactive with humidity in the air [135]. Mortazavi and Ahzi [136] conducted classical MD simulations to investigate the effects of point vacancy, Stone–Wales, and bivacancy defects on the thermal conductivity and tensile responses of single-layer graphene sheets. They found out decrement in the mechanical properties of graphene by increase of defects concentrations. They confirmed that defects can substantially suppress the thermal conduction, considerably larger than the mechanical properties. Ding et al. [137] investigated vacancy defects between interface of graphene and h-BN using density functional theory (DFT). They found out vacancies have significant effect on the mechanical and electronic properties of the hybrid graphene/h-BN. Güryel et al. [138] studied structural defects and chemical functionalization influence on mechanical properties of graphene employing finite element method. They demonstrated

reduction of the elastic limit in the presence of structural defects. Han et al. [139] and Abadi et al. [140] performed MD simulations to evaluate the effects of temperature, strain rate, and grain size on the mechanical properties of pristine h-BN nanosheets. Their results reveal decreasing trends in the ultimate tensile strength and failure strain by increasing the defect content and temperature. In this study, we conducted extensive MD simulations to explore the mechanical deterioration and failure mechanism of the h-BN with/without defects. Various initial and well-known defects like cracks, notches, and Stone-Wales point defects were considered in the h-BN nanosheets. The mechanical properties of the pristine and defective h-BN in various temperatures were estimated by applying uniaxial tension loading.

4.7.2 MD simulation

MD simulations were conducted employing the large-scale atomic/molecular massively parallel simulator (LAMMPS) [141]. The interactions between boron and nitrogen atoms were represented by modified Tersoff potential proposed by Matsunaga et al. [142], which have been successfully employed in the previous studies for the mechanical properties of h-BN nanosheets [111, 140]. Once the system was fully relaxed by the Nosé-Hoover barostat and thermostat method (NPT) [99, 100, 143, 144], the mechanical properties of the pristine and defected h-BN in various temperatures were estimated by applying the uniaxial tension loading [145, 146, 147]. Periodic boundary conditions were applied in the plane directions, so the simulated systems are representative of nanosheets and not the nanoribbons. During the uniaxial loading, the size of the simulation box along the loading direction was increased by a constant engineering strain rate of $2 \times 10^8 s^{-1}$, in which we used a time step of 0.25 fs, which is small enough to simulate the thermal and mechanical properties by the MD simulations [59, 148, 149]. In order to guarantee the uniaxial stress condition, the size of the box in the perpendicular direction of loading was controlled by the NPT method to reach the negligible stress values in the transverse direction of loading [145, 146, 147, 150, 151]. The stress tensors were computed based on the Virial theorem [152]. The atomistic models were visualized using the OVITO [153] package. Worthy to note that the methods which do not require any discretization have been presented in very recent works based on deep machine learning [154, 155, 156]. In Fig.(4.5) atomic lattice of the h-BN monolayer is illustrated, which shows the honeycomb structure as that of the graphene. In this work, we studied the h-BN monolayers with different degrees of defects, from a little density to fully amorphized structures. In Fig.(4.6) , fully amorphized h-BN monolayers after the relaxation at the room temperatures are illustrated. In this work, we considered Stone–Wales defects on the h-BN nanosheet mechanical properties. Stone–Wales defect does not contain removed or added atoms. In this defect, by rotating one of the B-N bonds by 90° with respect to the midpoint of the B-N bond, four hexagons transform into two pentagons and two heptagons. We found

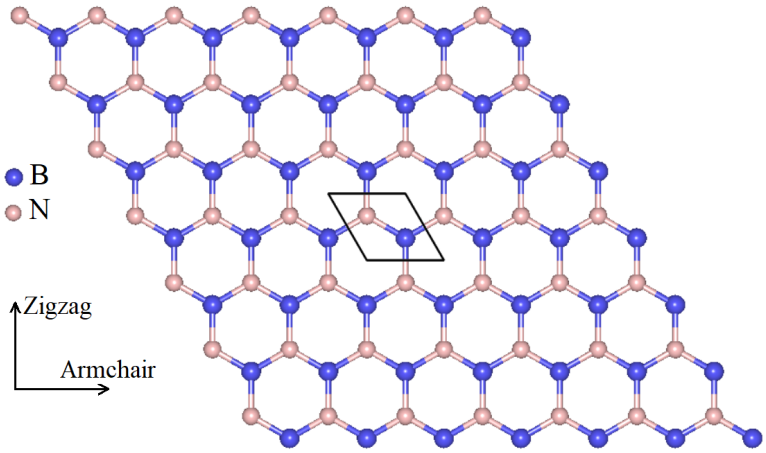

Figure 4.5: lattice structure of monolayer h-BN. The unit cell is shown as a parallelogram contains one nitrogen and one boron atoms.

that in order to have stabilized defective h-BN structures, the system should initially be energy-minimized using the conjugate gradients method. The number of formed non-hexagon lattices introduces the Stone–Wales defects concentrations concerning the total number of hexagons in the pristine structure.

4.7.3 Results and discussion

First of all, in order to have reference structural parameters for comparison with defected lattice properties, we investigate the mechanical properties of pristine nanosheet with dimensions of 300$\times$ 300 and the thickness of 3.4 Å within a temperature range of 200, 300, 400, 500, 700, and 900 K. Fig.(4.7) revealed stress-strain curves of all considered configurations. The ultimate tensile stress/strain decreased by increasing temperature and subsequently resulted in elastic module decrement, as we demonstrated in Table (4.1). High-temperature values increase phonon frequencies, which cause an easier stretch of the atomic bonds [157, 158, 159]. According to our results, pristine h-BN nanosheets at 300 K can keep its load-bearing ability within a considerable strain value of ~ 0.38, which is higher in comparison to the pristine graphene with the value of ~ 0.27 and ~ 0.20 [160]. They also exhibited more strong tensile capacity than 2D phagraphene and graphene-like C_3N with maximum strain values of ~ 0.13 [161] and ~ 0.18 [162, 163] in the same direction and temperature, respectively. Influence of

Table 4.1: Young's Modulus (E) of the pristine nanosheet at the 200, 300, 400, 500,700, and 900 K

Temperature(K)	200	300	400	600	900
E (GPa)	635.56	627.52	619.61	605.40	586.50

4.7 Mechanical responses of pristine and defective hexagonal boron-nitride nanosheets

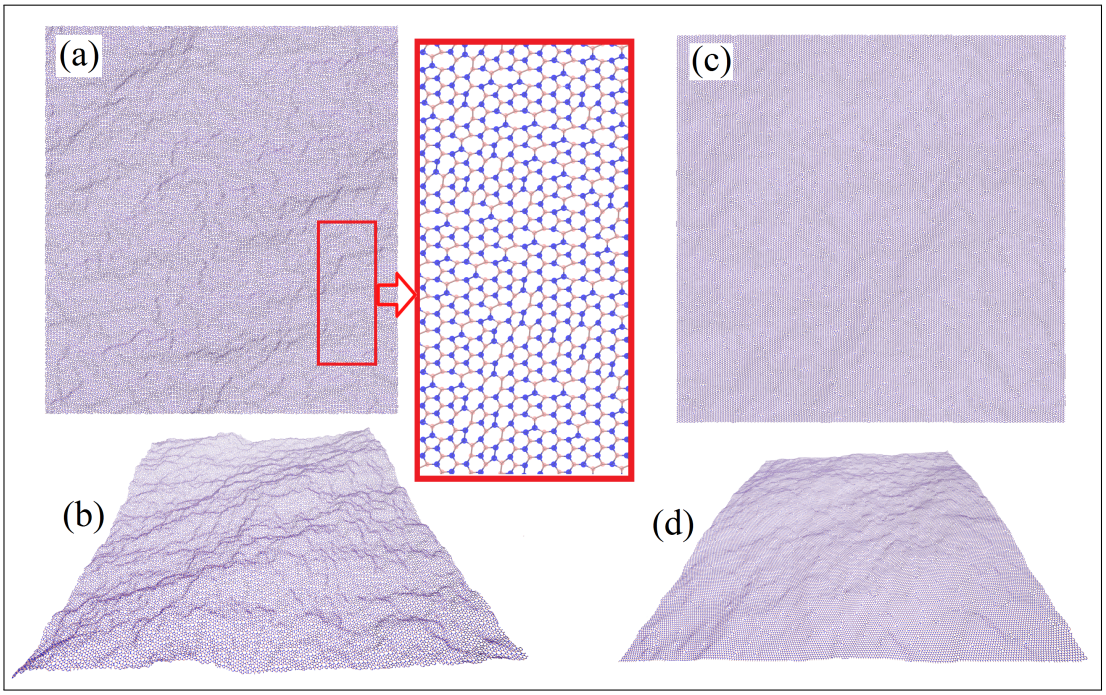

Figure 4.6: Top and side views of the atomistic model of amorphized h-BN with (a and b) 70% and (c and d) 10% defect concentrations made from 92,800 atoms. The inset shows a detailed view focusing on a highly defective zone.

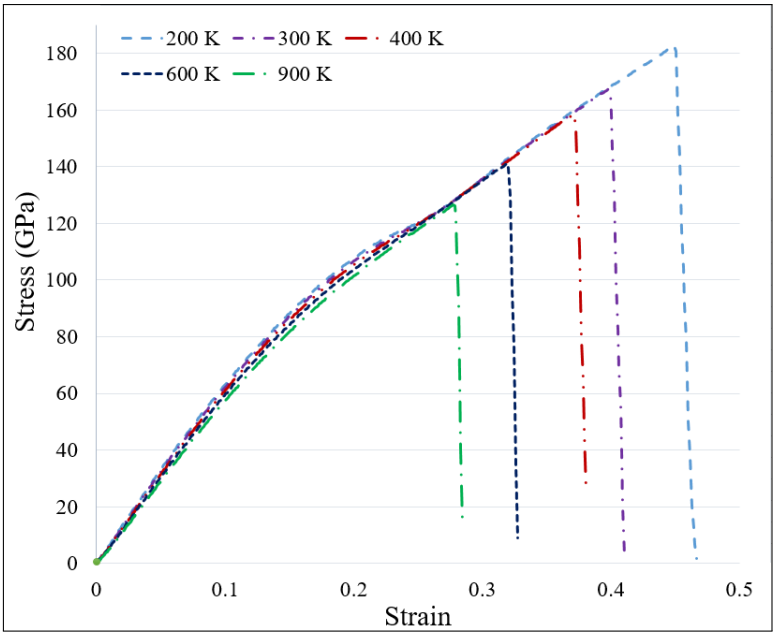

Figure 4.7: Stress-strain response of the pristine h-BN nanosheet under the uniaxial tension at temperatures of 200, 300, 400, 500, 700, and 900 K.

crack and notch defects on the ultimate tensile strength and failure mechanisms of the h-BN lattice were investigated by considering four different sizes. First, cracks with the length of L/3, L/6, L/9, and L/12 lengths were modeled, L is the size of sheets width. To investigate crack propagation, cracks were considered to be in-plane tension loading along the perpendicular to the loading direction. Several MD simulations in various temperatures range of 200, 300, 600, and 900 K were performed. Fig.(4.8) represent failure mechanisms and crack propagation of the h-BN nanosheet with an initial crack length of L/9 at 300 K. Maximum stress concentration of 95 GPa occurs at the strain value of 0.18 which indicates propagation crack leading to complete rupture of the nanosheet. The maximum bearing stress of h-BN nanosheet in the presence of

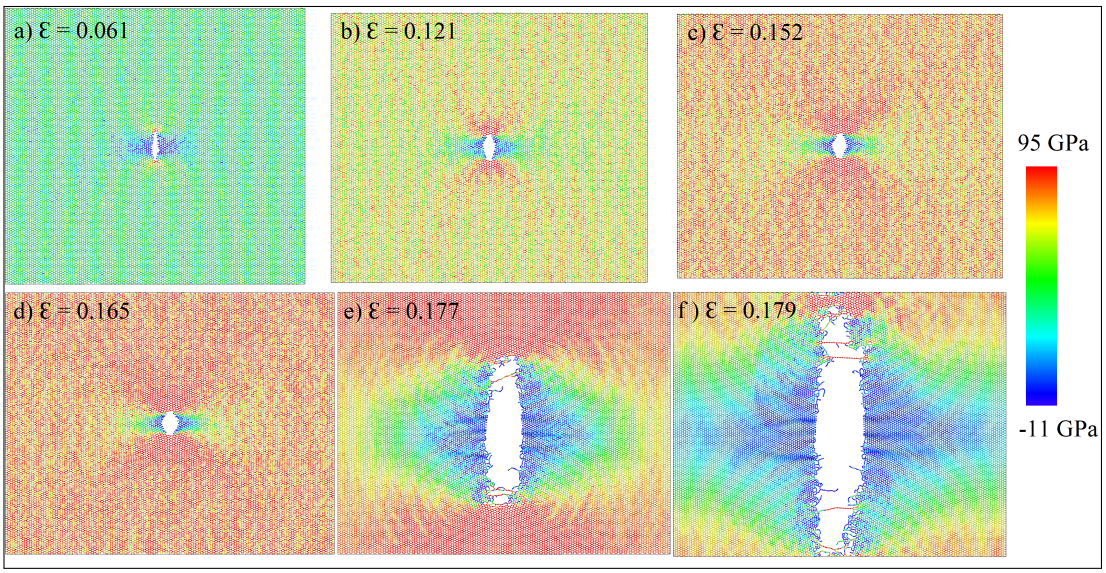

Figure 4.8: Failure mechanisms and crack propagation of h-BN nanosheet with a length of L/9 at 300 K under tensile loading in various strain values.

cracks with various lengths and temperatures are summarized in Fig.(4.9a). Crack free pristine lattice is considered as 0L to compare the results. As expected, ultimate tensile strength decreases by increasing the crack length and takes $\sim$ 30% of the pristine lattice strength for the crack length of L/3. Accordingly, the ultimate tensile strength of the nanosheet reduces by increasing temperature. Strain values at the maximum tensile stress were exhibited in Fig.(4.9b). As it is clear from these results, maximum bearing strains of h-BN nanosheet decrease by increasing the crack length and temperature as well. Initial notch defect was investigated to demonstrate failure mechanisms and defect propagation under the various diameter of L/3, L/6, L/9, L/12 and temperature range of 200, 300, 600, 900 K. Fig.(4.10) depicts the failure mechanisms and crack propagation of the sample h-BN nanosheet with initial notch diameter of L/9 at room temperature. In Fig.(4.10) d), defect starts to propagate in the transverse direc-

4.7 Mechanical responses of pristine and defective hexagonal boron-nitride nanosheets

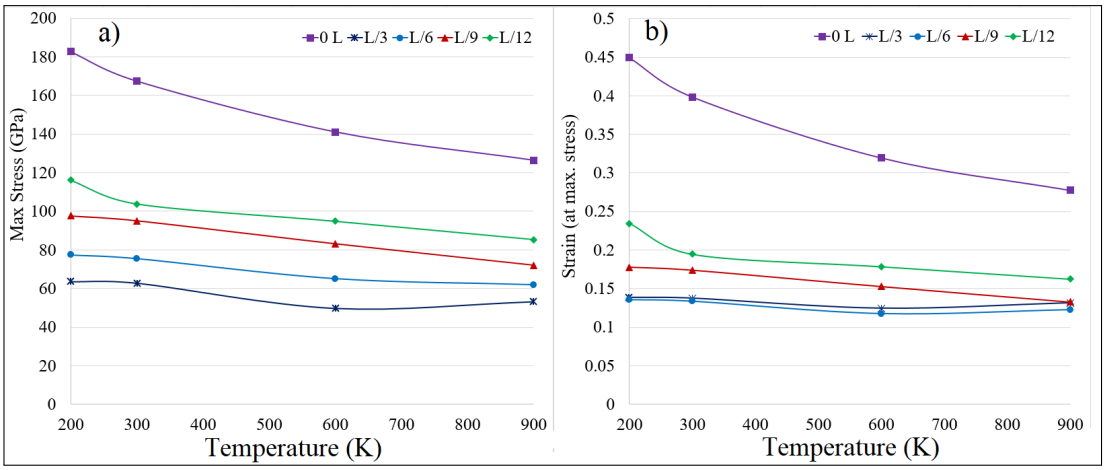

Figure 4.9: a) The tensile strength of the nanosheet in the presence of crack with different lengths, which are studied at a range of temperatures from 200 K to 900 K, b) Engineering strain at a maximum tensile strength of the C3N nanosheet with various cracks at different temperatures.

tion of loading at the strain value of ~ 0.16 and experience the complete failure strain value at Fig.(4.10) f) with a value of ~ 0.17. The maximum stress concentration of ~ 89 GPa occurs at the failure strain value of ~ 0.17. To elaborate on the ultimate tensile strength of pristine and notch-defected h-BN nanosheet, we reported maximum stresses and equivalent strains, in Fig. 7a and b, respectively. These results illustrate the decrement of the maximum stress/strain due to an increase of notch diameter and temperature as well. Strain at maximum stress of the defected lattice with smaller notch diameters of L/6 and L/9 at room temperature is less than the strain of the lattice that the system with a larger notch diameter of L/3. This observation is because of the folding of the lattice in the perpendicular direction and exhibiting higher tensile strain under stretch. The elastic modulus and tensile strength of the h-BN nanosheet as a function of crack or notch sizes at different temperatures are compared in Fig.(4.12). In all calculated cases, elastic modulus and tensile strength decreased by increasing the size of crack/ notch or temperature. Our results show that h-BN nanosheet, even with the largest defect size, could exhibit a remarkably high elastic modulus of ~ 480 and ~ 475GPa and tensile strengths of ~ 62 and ~ 71GPa at 300 K for crack and notch, respectively. In comparison to the amorphized graphene with the ~ 500 GPa elastic modulus and 60 GPa tensile strength [164], we predict h-BN structures bearing considerable loading even in the presence of high defects. Besides, we found that h-BN nanosheets maintain their excellent mechanical properties even at high defects and temperature levels. In Fig.(4.13), stress-strain responses of defect-free and highly defective h-BN monolayers are compared. Initial defects were imposed in the various concentration range of 10% , 40% , and 70% . As can be observed, a linear relation

4.7 Mechanical responses of pristine and defective hexagonal boron-nitride nanosheets

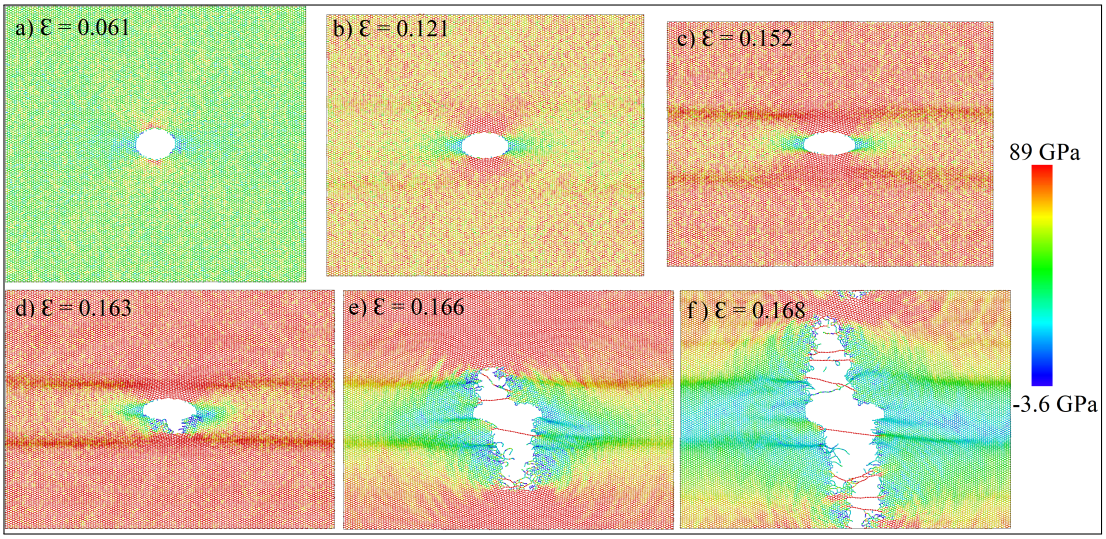

Figure 4.10: Failure mechanisms and notch propagation of h-BN nanosheet with a length of L/9 at 300 K in various strain values under the uniaxial tensile loading.

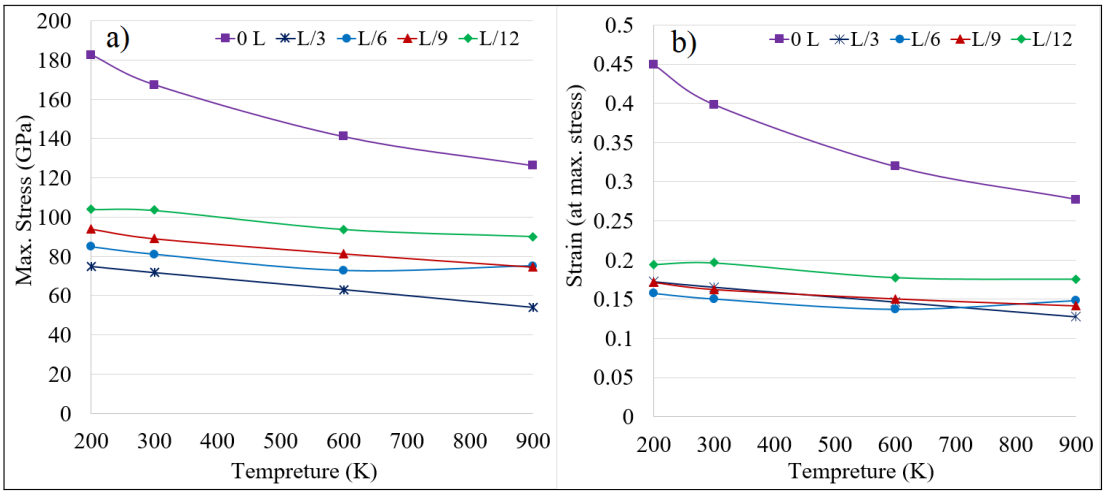

Figure 4.11: a) The ultimate tensile strength of the nanosheet in the presence of the notch defect with different diameters, b) Engineering strain at maximum tensile strength in the presence of notch defect with different diameters, at various temperatures of 200, 300, 500, 700, and 900 K

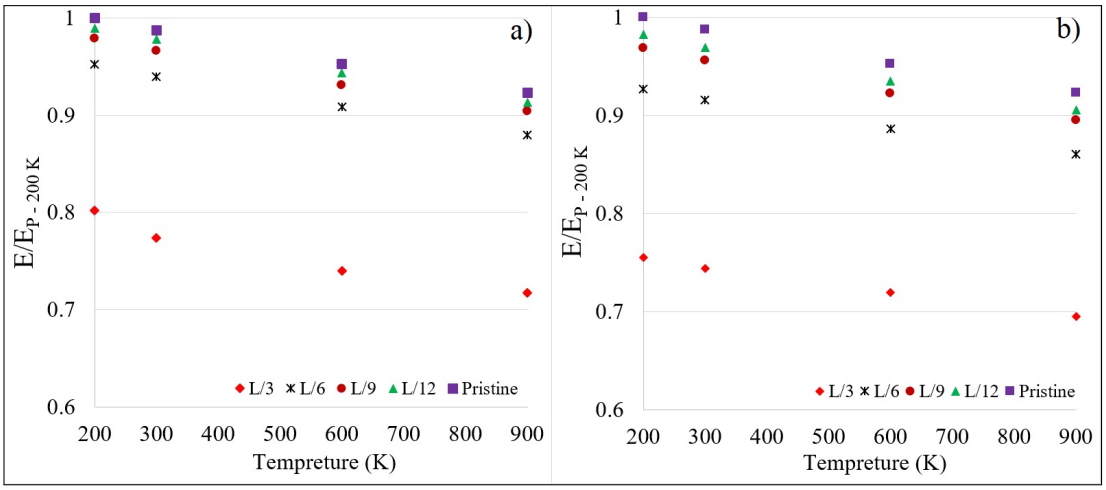

Figure 4.12: h-BN nanosheet elastic modulus (E) in the presence of a) crack b) notch defects. Elastic modulus values normalized by the pristine elastic modulus at 200 K ($E_{P\text{-}200\ K}$= 635.56 GPa

exists at a low strain level, which is followed by a non-linear response up to the tensile strength point and leading to a sudden decline, which corresponds to the nanosheet failure. Stone-Wales defects reduced the ultimate tensile strength by increasing defect concentrations. As it clears from results, imposing 70% defect concentration reduced ultimate tensile strength to the value of $\sim$ 20% less than the defect-free nanosheet. Since the number of atoms in Stone–Wales defects is as same as the defect-free h-BN nanosheet, the minimum effect on ultimate tensile strength could be observed in comparison to the crack and notch defects. Ultimate tensile stress/strain and associate elastic modulus were shown in Fig. (4.14) . In order to better understand the defect dependent variations, we normalized the values by related pristine amounts at room temperature (P-300K). The elastic modulus and tensile strength decreased by increasing defects concentration. Our results show that h-BN nanosheet with high defect concentration shows the elastic modulus of $\sim$ 200 GPa and tensile strengths of $\sim$ 135 GPa at 300 K. Obviously, imposing 70% defect concentration reduced elastic modulus to the $\sim$ 30% of the defect-free nanosheet value. It could be concluded that more than 10% concentration of Stone-Wales defects has the most severe reduction effect on the elastic modulus of h-BN nanosheets in comparison to the crack and notch defective nanosheets.

4.7.4 Conclusions

We conducted extensive MD simulations to investigate and explore the mechanical properties and failure mechanism of h-BN nanosheets under critical conditions. The pristine h-BN at room temperature exhibits remarkable strain at failure of $\sim$ 0.38 and

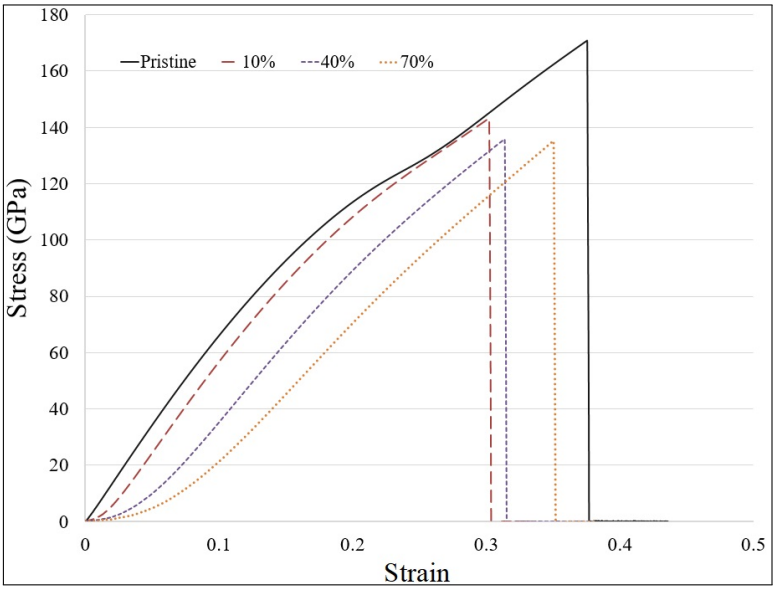

Figure 4.13: Stress-strain response of the pristine h-BN nanosheet under the uniaxial tension at different Stone-Wales defects concentrations (10% , 40% , and 70%) in room temperature

the ultimate tensile stress of $\sim$ 170 GPa. To provide a comprehensive vision concerning mechanical aspects of h-BN nanosheets, we modeled most critical types of defects in engineering materials, cracks, notches, and point vacancies with various sizes and concentrations under the different loading temperatures. At 300 K, ultimate tensile stresses of $\sim$ 95, $\sim$ 89 GPa, and $\sim$ 130 GP at corresponding strain levels of $\sim$ 0.18, $\sim$ 0.17, and $\sim$ 0.35 were estimated for the systems with the largest crack, notch, and Sone-Wales defects, respectively. MD simulations showed that the decrement of the maximum tensile stress/strain due to the increase of defect size and temperature.
Consequently, our results demonstrate that h-BN nanosheet, even with large crack and notch, could exhibit a remarkably high elastic modulus of $\sim$ 480 and $\sim$ 475 GPa at 300 K, respectively. However, Stone-Wales defects yield the most serious elastic modulus reduction in comparison to crack or notch. Our MD results reveal outstanding mechanical properties of h-BN nanosheets with and without defects, which are attractive for the designing of nanodevices with h-BN as a building block.

4.7 Mechanical responses of pristine and defective hexagonal boron-nitride nanosheets

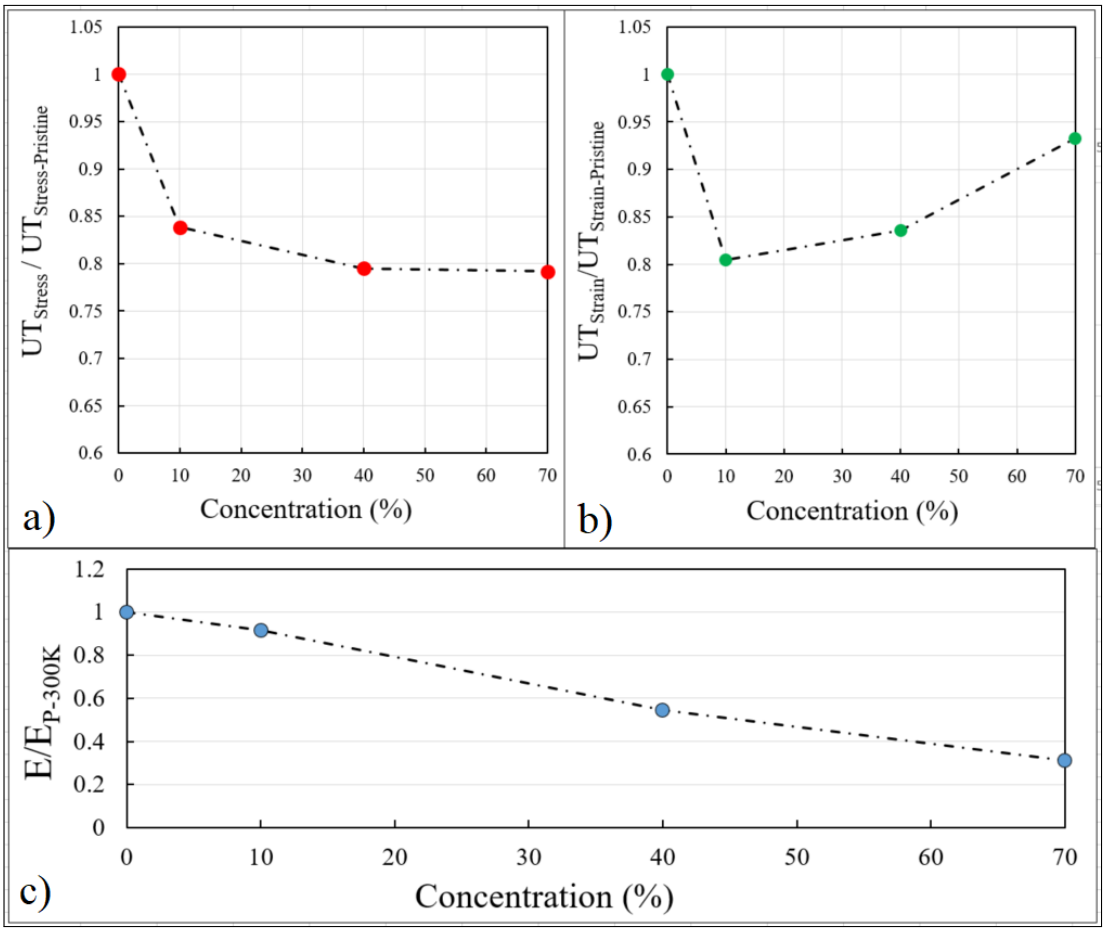

Figure 4.14: Normalized a) Ultimate tensile stress (UT_{Stress}) b) Ultimate tensile strain (UT_{Strain}) c) Elastic modulus (E) by corresponding pristine values versus to the Stone-Wales defects concentration content (%)

Chapter 5

First-Principle Density Functional Theory

5.1 Introduction

Quantum mechanics is one of the most important fundamental concepts discovered at the end of 19^{th} century. The microscopic world has been discovering by quantum mechanics principals. In quantum mechanics, a solid described as a system of the positively/negatively charged nuclei/electrons that interact electromagnetically and obeying the Schrödinger equation. Solving a many-body interacting as in a solid-system is impossible and necessitates a robust computational platform. Computational science advancement is vital to develop quantum computing from the viewpoint of either hardware or software. The high-performance computers (HPC) and advanced quantum methods include the first principle, or ab-initio methods enable fast, efficient, reliable, and affordable calculations.

The quantum behavior of an atomic or molecular system could be estimated using the first-principle (ab-initio) methods. These methods are the most robust and reliable approaches that ever developed without requiring input data from the experiment. The advance of remarkable first-principle methods started from the modeling of hydrogen-like atoms in the 1930s. This progress builds a platform for calculating systems that have a large number of atoms by extending density functional theory (DFT) [165, 166]. Solid-state systems typically have a large number of interacting particles, and their solution needs to be treated and optimized computationally. The DFT methods are based on Hohenberg-Kohn-Sham theorems provide a computationally applicable and precise approach to deal with the many-body systems. In this approach, instead of the wave function in the direct solution of the Schrödinger equation, the equivalent density functional theory describes the whole characteristics of solid-state systems.

5.2 Hamiltonian mechanics

Hamilton provides a mechanism for deriving equations of motion and presents different formalism for extension of the classical mechanics within the quantum mechanics framework. Hamiltonian mechanics aims to replace the generalized velocity variables with generalized momentum variables, also known as conjugate momenta. Momentum and the coordinates of a system are independent variables in Hamilton's formalism. Conjugate momenta; p_i, and first derivatives; $\dot{p}_i$, describe as following equations:

$$p_i = \frac{\partial L}{\partial q_i} \qquad , \qquad \dot{p}_i = \frac{\partial L}{\partial q_i} \tag{5.1}$$

Hamiltonian is defined as follows:

$$H = \sum_{i=1}^{N} \dot{q}_i p_i - L \tag{5.2}$$

In order to derive the equation of motion in Hamilton formalism, we have:

$$dH = \sum_{i=1}^{N} d\dot{q}_i p_i + \dot{q}_i dp_i - dL = \sum_{i=1}^{N} d\dot{q}_i p_i + \dot{q}_i dp_i - \frac{\partial L}{\partial q_i} dq_i - \frac{\partial L}{\partial \dot{q}_i} d\dot{q}_i \tag{5.3}$$

By substituting Eq.(5.1) into Eq.(5.3);

$$dH = \sum_{i=1}^{N} \dot{q}_i dp_i - \frac{\partial L}{\partial q_i} dq_i = \dot{q}_i dp_i - \dot{p}_i dq_i \tag{5.4}$$

The Hamiltonian equations of motion can be as follows:

$$\dot{q}_i = \frac{\partial H}{\partial p_i} \tag{5.5}$$

$$\dot{p}_i = -\frac{\partial H}{\partial q_i} \tag{5.6}$$

The system's unique trajectory will be estimated by imposing the initial conditions for the two independent variables. Hamiltonian can convert N number of second-order differential equations, which are derived by Lagrangian in Eq. (4.22), to the N number of first-order differential equations for a system with an N degree of freedom.
Hamiltonian is also known as the energy function for a system. The Hamiltonian relation with kinetic and potential energies (T and U) defines as the following equations by considering the Lagrangian function (L) description in Eq.(4.15):

$$H = \sum_{i=1}^{N} \dot{q}_i \frac{\partial L}{\partial \dot{q}_i} - L = \sum_{i=1}^{N} \dot{q}_i \frac{\partial T}{\partial \dot{q}_i} - (T - U) \tag{5.7}$$

Generally, the kinetic energy function (T) is a second-order homogeneous function of velocities. According to a mathematical theorem that indicates for an n-order homogenous function like, *f*, we have:

$$\sum_{i=1}^{n} x_i \frac{\partial f}{\partial x_i} = nf \tag{5.8}$$

Using this theorem in Eq. (5-7) the Hamiltonian derives as;

$$H = 2T - T + U = T + U \tag{5.9}$$

5.3 Quantum mechanics

The principles of quantum mechanics were derived based on the phenomenon include Planck's black body radiation, photoelectric effect, Compton effect, particle-wave duality, and the Bohr atomic model. The intrinsic properties are derived from the postulates of quantum mechanics.. The first postulation indicates that a Hilbert space attributes to any physical system. System conditions could be defined as a vector of Hilbert space. Generally, $\mathcal{H}$ refer to a Hilbert space and state vector of a physical system shown as $|\psi\rangle$. The second postulation is the observable, dynamic-observable for a classical system like *A(p,q)* is defined as a function on the phase space. A linear self-adjoint operator (Hermitian operator) devoted to each observable in a system. Measurement is expressed mathematically by acting the operator corresponding to the physical observable on the state vector. Possible values of a measurement (outcomes) are the set of eigenvalues for that operator. They are the direct physical result of the spectral theorem. The third postulate of quantum mechanics is the measurement and known as the canonical quantization postulation. If an observable like A to be measured from a physical system on the $|\psi\rangle$ state, the eigenvalues of the operator $\hat{A}$ like a will be acquired stochastically, and state of the system will be reduced to the corresponding eigenvalue of a. The probability domain of acquiring value is $\langle a|\psi\rangle$, and the probability is as follow:

$$P(a) = |\langle a|\psi\rangle|^2 \tag{5.10}$$

If the eigenvalues of operator $\hat{A}$ are continuous, this equation expresses the probability density function. The fourth postulation is the dynamics of a physical system. The time evolution of a physical system in quantum mechanics estimates by the Schrödinger equation as follows:

$$i\hbar \frac{d}{dt}|\psi(t)\rangle = \hat{H}(t)\,|\psi(t)\rangle \tag{5.11}$$

$$\hbar = \frac{h}{2\pi} \tag{5.12}$$

where $\hat{H}$, $\hbar$, ψ are the Hamiltonian operator, Plank constant, and the state vector of the quantum system respectively. The state-space *(q,t)* Schrödinger equation written as:

$$i\hbar\frac{\partial}{\partial t}\left|\psi(q,t)\right\rangle = \hat{H}\left(q,t\right)\left|\psi(q,t)\right\rangle \tag{5.13}$$

5.4 Fundamentals of first-principles method

First-principle/ab-initio method is based on quantum mechanics governing equations and calculates the electromagnetically interacting particle system. Only the atomic number of the constituent atoms are required as input information. The electromagnetic properties and bonds forming/breaking can be calculated using first-principles methods. In this principle, particular microstate energy determines by solving the many-body Schrödinger equation;

$$\hat{H}\Psi\left(q_i,t\right) = E\Psi\left(q_i,t\right) \tag{5.14}$$

$$\hat{H} = T_n + T_e + U_{ne} + U_{ee} + U_{nn} \tag{5.15}$$

which is an eigenvalue problem where E represents the total energy of the quantized physical system (eigenvalues), and Ψ is a many-body wavefunction (eigenstates) for a configuration. The Hamiltonian operator, $\hat{H}$, is a sum of all system's energies included kinetic; T, and potential energies; U. The subscripts 'n', 'e' indicate the nucleus and electrons contributions. The kinetic energies are sum of the nucleus and electrons kinetic energies. The potential energy involves the Coulomb interactions by nucleus–electron; U_{ne}, electron–electron, U_{ee}, and nucleus–nucleus; U_{nn}.
This equation could be solved and obtain the eigenstates and energies of a many-body system. However, such an approach is extremely computationally expensive and does not apply to a real solid-system. Thus, some assumptions and approximation approaches are needed to treat real solid systems. In order to simplify equations, Born-Oppenheimer approximation [43] usually allows us to assume that the nuclei and electron wave functions are independent due to the significant difference between their masses. Thus the nuclei positions are assumed to be fixed with respect to the electron wavefunction. Therefore, the terms connected with nuclei could be ignored as:

$$\hat{H} = T_e + U_{ne} + U_{ee} \tag{5.16}$$

The kinetic energies of N electrons defined as following equation:

$$T_e = -\frac{\hbar^2}{2m}\sum_i^N \nabla_i^2 \tag{5.17}$$

where ∇^2 is the Laplacian operator described as:

$$\nabla^2 = \frac{\partial^2}{\partial x^2} + \frac{\partial^2}{\partial y^2} + \frac{\partial^2}{\partial z^2} \tag{5.18}$$

The attractive potential energies of N electrons due to the M number of nuclei given by:

$$U_{ne} = -\sum_{i}^{M}\sum_{j}^{N} \frac{Q_i}{|q_{ij}|} \tag{5.19}$$

where Q_i is charges of the nuclei. The interaction from all electrons to all nuclei indicated by adding a double sum. The electrons move around fixed nuclei, so from the electron's view, this potential is called the static external potential. The positions of nuclei; q vectors, are involved potential and can be expressed in Cartesian coordinates as:

$$|q| = \left(x^2 + y^2 + z^2\right)^{\frac{1}{2}} \tag{5.20}$$

The third part of Hamiltonian operator, is repulsive potential energies of N electrons interactions with each other, is given with the usual correction factor of $\frac{1}{2}$ for double counting correction between i^{th} and j^{th} electrons, as follow:

$$U_{ee} = \frac{1}{2}\sum_{i\neq j}^{N} \frac{1}{|q_{ij}|} \tag{5.21}$$

Since the many-body problems, where the m electrons interact with all other electrons at the same time, are not easy to be solved directly. Multiple approximation approaches like Hartree-Fock (HF) approach, density functional theory (DFT), and various hybrid methods yield somewhat decent results [167]. HF ignores the correlation effect of electrostatic repulsion between electrons; two electrons are not allowed to occupy the same position in the space. However, HF is more computationally expensive than DFT. DFT is a widely used method due to its versatility, the low computational cost in comparison, and satisfactory results. The major challenge of the DFT approach is finding an exact exchange-correlation functional. However, hybrid functionals somehow resolve this problem by allowing the exchange energy to get involved as in the Hartree-Fock theory.

5.4.1 Hartree method

Hartree's method (1928) described a simple model of one electron. In order to solve the wave equations, each particle assumes to be an independent body that interacted with others in an averaged feeling. Where for several electrons, each electron recognizes others as a mean-field of electrons. Thus, a set of electrons becomes a set of non-interacting one-electron, and each electron moves in the average density of the other

electrons. Hartree treated one electron at a time and introduced a procedure he called the self-consistent field (SCF) method to solve the wave equation:

$$\left(-\frac{1}{2}\nabla^2 + U_{ext}(q) + U_H(q)\right)\Psi(q) = E\Psi(q) \tag{5.22}$$

where U_{ext} and U_H represented the attractive interaction between electrons and nuclei, and the Hartree potential coming from the classical Coulomb repulsive interaction between each electron and the mean-field respectively. Thus, only for the two electron-electron interaction, the Hartree energy is approximate by considering the mean-field as electrons densities (ρ) interaction function as follow;

$$E_H = \frac{1}{2}\iint \frac{\rho(q)\,\rho\left(q^{'}\right)}{|q-q^{'}|}dqdq^{'} \tag{5.23}$$

Since electrons are independent, the total energy and wavefunction are the sum and product of one-electron energies and wavefunctions, respectively, as follow:

$$E = E_1 + E_2 + E_3 + \ldots + E_m \tag{5.24}$$

$$\Psi = \psi_1 \times \psi_2 \times \psi_3 \times \ldots \times \psi_m \tag{5.25}$$

The Hartree model was tested for the hydrogen atom, and the ground-state energy is acquired as precise as the experimental value. However, for complex models will estimate an approximate value due to simplifying assumptions. Thus, Hartree proposed a starting point for the other first-principle methods.

5.4.2 Hartree-Fock method

In Hartree-Fock (1930) method is based on the one-electron and mean-field. The wavefunction of interacting system is assumed to be a single Slater determinant of spin orbitals. The ground-state wavefunction (Ψ_0) is estimated as an anti-symmetrized product of N orthonormal spin orbitals ($\psi_i(\Phi_i)$), where each one is a product of a spatial orbital ($\Phi_i(q_i)$) and a spin function (up or down). The Slater determinant represent as follow:

$$\Psi_0(\Phi_i) \approx \Psi_{HF}(\varnothing_i, \uparrow or \downarrow) = \frac{1}{\sqrt{N!}}\begin{vmatrix} \psi_1(\varnothing_1,\uparrow) & \psi_2(\varnothing_1,\downarrow) & \ldots & \psi_N(\varnothing_1,\uparrow or \downarrow) \\ \psi_1(\varnothing_2,\uparrow) & \psi_2(\varnothing_2,\downarrow) & \ldots & \psi_N(\varnothing_2,\uparrow or \downarrow) \\ \vdots & \vdots & & \vdots \\ \psi_1(\varnothing_N,\uparrow) & \psi_2(\varnothing_N,\downarrow) & \ldots & \psi_N(\varnothing_N,\uparrow or \downarrow) \end{vmatrix} \tag{5.26}$$

Spin is the intrinsic angular momentum of a particle, and according to Pauli's principle, two electrons cannot occupy the same-spin wavefunctions or spin-orbitals. Where it is satisfied with the determinant of two identical rows or columns is equal to zero. So, by neglecting the spin variable, the general expression of the Slater determinant takes the form:

$$\Psi(q_i) = \frac{1}{\sqrt{N!}} \begin{vmatrix} \psi_1(q_1) & \psi_2(q_1) & \dots & \psi_N(q_1) \\ \psi_1(q_2) & \psi_2(q_2) & \dots & \psi_N(q_2) \\ \vdots & \vdots & & \vdots \\ \psi_1(q_N) & \psi_2(q_N) & \dots & \psi_N(q_N) \end{vmatrix} \tag{5.27}$$

where $1/\sqrt{N!}$ is the normalization factor for an N-electrons system. For even numbers of electrons, a one slater determinant is enough to describe wavefunction fully, while for the odd number of electrons, a linear combination of more than two Slater determinants could estimate the wavefunction.
The variational principle for the ground-state energy estimation, derives a minimum energy value (E) by using a trial wavefunction. This energy is a close value in upper bound to the real ground-state energy (E_0), and by integrating over the whole space the energy equation becomes as;

$$\begin{aligned} E[\Psi] &= \frac{\langle\Psi|\hat{H}|\Psi\rangle}{\langle\Psi|\Psi\rangle} \geq E_0[\Psi_0] \\ E[\Psi] &= \frac{\int \Psi^* \hat{H} \Psi dq}{\int \Psi^* \Psi dq} \end{aligned} \tag{5.28}$$

$$\langle\Psi|\hat{H}|\Psi\rangle = \int \Psi^* \hat{H} \Psi dq \tag{5.29}$$

where Ψ^* is the complex conjugate of the wavefunction and gives the physical meaning of probability to the wave function. The actual ground-state energy could be estimated by minimizing the energy functional ; $E[\Psi]$, with respect to the all electrons wavefunctions. It should remind here, for any quantum system wavefunction, the orthogonality and normality conditions should be satisfied.

$$\int \psi_i \psi_j dq = 0 \;\; orthogonality\,(i \neq j) \tag{5.30}$$

$$\int \psi_i \psi_j dq = 1 \;\; normality\,(i = j) \tag{5.31}$$

These conditions indicate that the probability of finding an electron as a product of wavefunction and integrate it over the whole space should be equal to one.
The total energy in the Hartree-Fock method is described as the following equation:

$$E_{HF} = E_{kin} + E_{ext} + (E_H + E_{xch}) \tag{5.32}$$

where E_{kin}, E_{ext}, and (E_H, E_{xch}) are the kinetic and external (electron-nucleus attraction) energies for one electron and last term is the Coulomb energy for the interactions between two electrons which is the Hartree energy and the exchange energy coming from the antisymmetric nature of wavefunction in the Slater determinant form. The Hartree-Fock energy equal to the Eq.(5.29) that can be express as:

$$E_{HF} = \langle \Psi | \hat{H} | \Psi \rangle = \sum_{i=1}^{N} H_i + \frac{1}{2} \sum_{i,j=1}^{N} \left(J_{ij} - K_{ij} \right) \tag{5.33}$$

where;

$$H_i = \int \Psi_i^* \left[-\frac{1}{2} \nabla^2 - U_{ext} \right] \Psi_i dq \tag{5.34}$$

$$J_{ij} = \iint \Psi_i(q_1) \Psi_i^*(q_1) \frac{1}{q_{12}} \Psi_j^*(q_2) \Psi_j(q_2) dq_1 dq_2 \tag{5.35}$$

$$K_{ij} = \iint \Psi_i^*(q_1) \Psi_j(q_1) \frac{1}{q_{12}} \Psi_i(q_2) \Psi_j^*(q_2) dq_1 dq_2 \tag{5.36}$$

where J_{ij}, K_{ij} are Coulomb integrals and exchange integrals respectively. J_{ij} defines as the average repulsive potential experience by the i$^{\text{th}}$ electron due to the rest of other electrons, and known as Coulomb operator:

$$\hat{J}_j(q_1) = \int |\Psi_j(q_2)|^2 \frac{1}{q_{12}} dq_2 \tag{5.37}$$

The Coulomb operator, $\hat{J}$, represents the potential that an electron at position q_1 experiences due to the average charge distribution of another electron in spin-orbital Ψ_j. The exchange operator describes through its effect when operating on a spin-orbital as follow:

$$\hat{K}_j(q_1) \Psi_i(q_1) = \int \Psi_j^*(q_2) \frac{1}{q_{12}} \Psi_i(q_2) dq_2 \Psi_j(q_1) \tag{5.38}$$

If we minimize the system energy with respect to wavefunction (as much as possible), the energy at the end will be the ground-state energy.

$$E_{HF} = min\left(E\left(\Psi_{HF}\right)\right) \tag{5.39}$$

According to the variation principle in the ground-state energy, the following equation should be zero:

$$\delta \left(\int \Psi^* \hat{H} \Psi dq \right) = 0 \tag{5.40}$$

Eventually, the initially estimated wavefunction in the Slater determinant will approach to the actual ground-state energy.

5.4.3 Density functional theory

First-principles density functional theory (DFT) deals with the constituents' atoms and their electronic structure. The electron density, ρ *(q),* is the number of electrons per unit volume at point q, where the q is the spin coordinates and the spatial variables (KS-orbitals). It is written as integration over a set of squares or occupied non-interacting KS-orbitals as following:

$$\rho(q) = \int \cdots \int |\psi(q_1, q_2, q_3, \ldots, q_N)|^2 dq_1 dq_2 dq_3 \ldots dq_N \tag{5.41}$$

The electron density is observable and could be measured in practice by an X-ray diffraction experiment. Subsequently, it means in quantum physics, there should be an operator for that property. All electron densities over whole space naturally identify the total number of electrons, N, as:

$$\int \rho(q)\, dq = N \tag{5.42}$$

The density of electrons in atoms and molecules is the most crucial concept in DFT calculations. The density function represents particle wavefunctions, number of electrons, and directly related to all the properties of the system, such as energies and potentials. The electron density operator is describing as delta function as follow:

$$\hat{\rho}(q) = \delta\left(q' - q\right) \qquad \begin{cases} 0 & q' \neq q \\ \infty & q' = q \end{cases} \tag{5.43}$$

where for one electron it becomes as:

$$\rho(q) = \langle \psi | \hat{\rho}(q) | \psi \rangle = \int \psi^*\left(q'\right) \psi(q)\, \delta\left(q' - q\right) dq' = \psi^*(q)\, \psi(q) = |\psi(q)|^2 \tag{5.44}$$

It is interpreted as the probability of finding an electron at q. The wavefunctions contain all information about the system; however, it depends on 4N variables (three coordinates and spin (spin up and spin down)) where N is the number of electrons and is very complicated to be identified using experimental methods.
The first theorem of Hohenberg-Kohn [166] expresses that the ground-state energy from Schrödinger's equation is a unique functional of the electron density, and demonstrates that the electron density could uniquely find the Hamiltonian operator and subsequently all the properties of the system. This theorem derives the external potential as a unique functional of the electron density. In other words, since the external potential fixes the Hamiltonian of a system, it could be concluded that the many-body ground-state is a unique functional of electron density. Therefore, the electron density determines the number of electrons and the external potential that can subsequently

identify the ground-state properties like kinetic energy, potential energy, and eventually, the total energy of the system. The total energy can be written as a function of electron density;

$$\hat{E}[\rho] = \hat{T}[\rho] + \hat{E}_{ee}[\rho] + \hat{E}_{ne}[\rho] \tag{5.45}$$

$$\hat{E}_{ne}[\rho] = \int \rho(q) U_{ne} dq \tag{5.46}$$

$$\hat{F}_{HK}[\rho] = \hat{T}[\rho] + \hat{E}_{ee}[\rho] \tag{5.47}$$

$$\hat{E}_{ee}[\rho] = \frac{1}{2} \iint \frac{\rho(q_1)\rho(q_2)}{q_{12}} dq_1 dq_2 + \hat{E}_{ncl}[\rho] = \hat{J}[\rho] + \hat{E}_{ncl}[\rho] \tag{5.48}$$

where $\hat{F}_{HK}[\rho]$ is the Hohenberg-Kohn functional; which is the main part of DFT calculation and the Schrödinger equation can be solved by using this functional. It is a universal functional and independent from the considered system. The kinetic energy functional, $\hat{T}[\rho]$, and the electron-electron interaction functional, $\hat{E}_{ee}[\rho]$, which are included to this functional are not easy to identify explicitly. However, the $\hat{E}_{ee}[\rho]$ can be divided into two terms: the classical part as $\hat{J}[\rho]$ and the non-classical contribution as $\hat{E}_{ncl}[\rho]$, like self-interaction correction, exchange and Coulomb correlation.
The second theorem of the Hohenberg-Kohn [166] states that a universal functional for the energy in terms of the electron density, $\hat{E}[\rho]$ (Eq.(5.45)), can be defined for any external potential ($\hat{E}_{ne}[\rho]$). The exact ground-state energy of the system is the global minimum, and the density that minimizes this functional is the exact ground-state energy density. In other words, the functionals that determine the ground-state energy of the system derives the lowest energy if and only if the input density is the actual ground-state density. For any trial density associated with some external potential, the energy obtained from the functional, $\hat{E}[\rho]$, represents an upper bound to the actual ground-state energy.
The Hohenberg-Kohn theorems imply that the importance of the density function such that density function contains all information of N interacted electronic system in ground-state and as import as a ground-state wavefunction. Furthermore, since the Hamiltonian operator gives the energy, the system's ground-state energy can be written as functional of density function using the variational principle.
To solve the particle equations of motion or many-body Schrödinger equation, Kohn and Sham decomposed the energies of n electrons and mapping the n-electron system (interacting) to the n single-electron system (non-interacting) using the exchange-correlation energy functionals. The most critical challenge of the DFT is dealing with functional, $\hat{F}_{HK}[\rho]$, to find the precise expressions for the kinetic and non-classical functionals ($\hat{T}[\rho], \hat{E}_{ncl}[\rho]$). To solve this problem, Kohn-Sham [165] proposed the approach that calculates the exact kinetic energy of a fictitious system of non-interacting

electronics where the ground-state density is equal to the real system, which includes the interacting electrons. The real and artificial systems with interacting and non-interacting electrons have the same positions and atomic number of the nuclei which emphasize that they have the same density;

$$\rho(q) = \rho_S(q) \tag{5.49}$$

where the subscript 'S' reminds that it belongs to the artificial system. Kohn and Sham defined the functional $\hat{F}[\rho]$ as follows:

$$\hat{F}[\rho] = \hat{T}_S[\rho] + \hat{J}[\rho] + \hat{E}_{XC}[\rho] \tag{5.50}$$

where $\hat{E}_{XC}[\rho]$ represents the exchange-correlation functional that contains whatever is unknown and affects the precision of the calculated energy, and describe as the sum of the distinct exchange and correlation terms, as follow:

$$\hat{E}_{XC}[\rho] \equiv \left(\hat{T}[\rho] - \hat{T}_S[\rho]\right) + \left(\hat{E}_{ee}[\rho] - \hat{J}[\rho]\right) \tag{5.51}$$

The next step is finding the orbitals or external potential uniquely for a non-interacting system derived from Slater determinant with the contribution to the same density as the real system. The total energy of the interacting system can be written as:

$$\begin{aligned}
\hat{E}[\rho] &= \hat{T}_S[\rho] + \hat{J}[\rho] + \hat{E}_{XC}[\rho] + \hat{E}_{ne}[\rho] \\
&= \hat{T}_S[\rho] + \frac{1}{2}\iint \frac{\rho(q_1)\rho(q_2)}{q_{12}} dq_1 dq_2 + \hat{E}_{XC}[\rho] + \int \rho(q) U_{ne} dq \\
&= -\frac{1}{2}\sum_i^N \langle\psi_i|\nabla^2|\psi_i\rangle + \frac{1}{2}\sum_i^N\sum_j^N \iint |\psi_i(q_1)|^2 \frac{1}{q_{12}} |\psi_j(q_2)|^2 dq_1 dq_2 \\
&\quad + \hat{E}_{XC}[\rho] - \sum_i^N \int \sum_A^M \frac{Z_A}{q_{1A}} |\psi_i(q_i)|^2 dq_1
\end{aligned} \tag{5.52}$$

By applying the variational principle and minimizing the energy functional, the Kohn-Sham equations result as follows:

$$\begin{aligned}
\left(-\frac{1}{2}\nabla^2 + \left[\int \frac{\rho(q_2)}{q_{12}} + U_{XC}(q_1) - \sum_A^M \frac{Z_A}{q_{1A}}\right]\right)\psi_i &= \varepsilon_i \psi_i \\
\left(-\frac{1}{2}\nabla^2 + U_S\right)\psi_i &= \varepsilon_i \psi_i
\end{aligned} \tag{5.53}$$

$$U_S = U_H + U_{ext} + U_{XC} \tag{5.54}$$

where U_S, U_H, U_{ext}, and U_{XC} denote the effective, Hartree, external, and exchange-correlation potentials respectively.

5.4.4 Exchange-Correlation functional

Exchange-Correlation energy is estimated in terms of electron density and contains of all quantum effects;

$$\hat{E}_{XC} = \hat{E}_X + \hat{E}_C \tag{5.55}$$

where $\hat{E}_X$ and $\hat{E}_C$ are the exchange energy functional between electrons with the same spin, and the correlation energy functional between electrons with a different spin, respectively, the exact form of the exchange-correlation functional is not known. However, there are widely used methods to derive functionals like local density approximation (LDA) and Generalized gradient approximation (GGA). GGA includes more physical information than the LDA because it includes information about the local electron density and the local gradient in the electron density. In our study, the GGA/Perdew-Burke-Ernzerhof functional (PBE) approximation was used to estimate the exchange-correlation energy functional. Various types of GGA functionals have been widely used and demonstrated excellent results for different physical problems.

5.5 First-principles mechanical properties of 2D nanomaterials

5.5.1 Introduction

Graphene [103, 168, 169] is among the most popular 2D materials. The materials dimension affects the features of the same chemical compounds and may exhibit unique properties. For instance, 2D transition metal dichalcogenides (TMDs) have a direct energy bandgap, whereas its 3D counterpart has an indirect energy bandgap [104]. Two dimensional (2D) materials such as graphene, TMDs (MX_i, M= transition metals, X= chalcogen elements such as S, Se, and i=2) and transitional metal halides (TMHs) attracted attention due to their outstanding mechanical, optical, electrical, energy storage, magnetic, and heat conduction properties [105, 136, 149, 170, 171, 172, 173]. In order to evaluate the mechanical properties, advanced computational approaches can be used as effective and inexpensive alternatives to experimental testing.
Transition metal halides (TMHs) in 3D form were synthesized in the past decade [174, 175]. Recently, TMHs were synthesized in the 2D form with ABC stacking arrangement of the layers up to each other, interacting with weak van-der-Waals forces. Their general formula is known as M_nY_m in which M= Zr, Hf, Ti, V, Cr, Fe, Mo, Ru, Rh, Ir, and Y= Cl, Br, I [176, 177, 178]. These 2D materials have gained attention in recent studies due to their catalytic nature and photochemical, thermodynamic, electrical, and magnetic properties [179, 180, 181, 182, 183, 184]. These attractive 2D nanostructures can be fabricated from bulk TMHs structures by a chemical exfoliation approach or restacking of individual 2D nanosheets [185] and chemical vapor transport (CVT)

method [186]. Multi-layered α -$RuCl_3$ ($RuCl_3$), β -$RuCl_3$ and Oxide chlorides with different properties have been obtained by Kolbin and Raybov [187]. They examined the residues remaining when ruthenium was attacked by chlorine alone at temperatures from 280 to 840° C. They result indicated $RuCl_3$ as lustrous black plates, insoluble, and volatile above 6oo° C; and β -$RuCl_3$ as a dark brown, matt, fluffy, hygroscopic, and soluble in aqueous alcohol; and oxide chlorides with hygroscopic, soluble, volatile above 300° C. In recent experimental studies [188, 189] based on neutron diffraction, scanning transmission electron and scanning tunneling microscopy, a novel layered $RuCl_3$ crystals nanosheets were realized. The 2D layered $RuCl_3$ have displayed Kitaev physics on a 2D honeycomb lattice, and attracted interest to elaborate as a Kitaev material, with strong interests for their high interactions between spin-orbit coupling (SOC) [179, 181, 189, 190, 191, 192], and electronic correlations and unusual magnetism [185, 193, 194]. Iyikanat et al. [195] conducted DFT calculation to investigate the structural, vibrational, electronic, and magnetic properties of monolayer $RuCl_3$. They found strong magnetic anisotropy and interaction between Ru atoms with a magnetic moment of 0.9 μ B per Ru atoms. Their most interesting results were changing of magnetic ground state by external strains and the considerable variation of the valence and conduction band-edges under in-plane strains. Sarikurt et al. [196] studied electronic and magnetic properties of single-layer $RuCl_3$ using DFT and Monte Carlo (MC) simulation methods. They found that the cleavage energy (CE) values are smaller than that of graphite, indicating that single layer $RuCl_3$ can be obtained from its bulk phase. The magnetic momentum of 1 μ B per Ru atoms and 4μ B total magnetic moment per square cell were measured. The energy band gap around high symmetry points, $\Gamma - M$, has been identified around 3 meV using the Perdew-Burke-Ernzerhof [197] functional, while by considering SOC-effect, a value of 57 meV was predicted. Ersan et al. [198] studied the magnetic and electric properties of $RuBr_3$ and RuI_3 in their bulk and single-layer phases using DFT and MC methods. They found that these materials can also form 2D layered structures like other TMHs. Moreover, they observed that the monolayers of RuX_3 prefer ferromagnetic spin orientation in the plane for Ru atoms. They also find intense magnetic properties different from those of the bulk counterpart to a single-layer of the $RuBr_3$ and RuI_3.

Super-stretchable material refers to a material that can highly stretch without any bond breaking and defects on the lattice structure and return to its original length. Super-stretchable materials with excellent mechanical stretchability and electrical properties have critical potential applications in various nanoelectronics devices. Stretchable conductors and semiconductors are crucial components of nanoelectronics, energy harvesters, and biomedical devices. Generally, stretchable materials are based on metallic nanowires, liquid metals, carbon nanomaterials, polymers, and composites [199].

2D materials can exhibit extraordinary properties when subjected to an external strain [200, 201]. Indeed, studying the mechanical properties is vital to gain more in-depth insight into their applicability [131, 151, 202, 203, 204, 205, 206]. In this study, we

perform spin-polarized DFT calculations to investigate the dynamic behavior and mechanical properties of single-layer $RuCl_3$ and $RuBr_3$.

5.5.2 DFT computational modeling

This work was carried out by performing the spin-polarized DFT [207, 208] calculations. The *Vienna Ab-initio Simulation Package* (VASP) [209, 210, 211] was employed using the generalized gradient approximation (GGA) functional proposed by Perdew-Burke-Ernzerhof (PBE) [197] for the exchange-correlation potential. The projector augmented wave (PAW) method [212] as a pseudo-potential approach with plane-wave cutoff energy of 500 eV was set for the DFT calculations. The PAW is classified as frozen-core all-electron (AE) potential, which exploits the efficiency of the pseudopotential (PP) and the accuracy of the AE potential. The graphical representation of the atomic structures was done with the VESTA package [213]. The energy minimized structures were acquired using the robust mixture of the Davidson and RMM-DIIS algorithms and then employing the conjugate gradient method for the ionic relaxation with energy convergence criteria of 10^{-5} eV, and a $13\times$ $13\times$ 1 Monkhorst-Pack [214] k-points mesh size. Subsequently, the mechanical properties were calculated by performing uniaxial tensile simulations [145, 147, 163].
In this study, we investigated the mechanical properties and phonon dispersions of single layer $RuCl_3$ and $RuBr_3$ structures. We obtained the phonon dispersion to investigate the dynamic stability and conducted density functional perturbation theory (DFPT) simulations for $2\times$ 2 super-cells within the finite displacement method using the Phonopy code [215, 216]. The phonon frequencies were calculated along with the high symmetry directions $(\Gamma - M - K - \Gamma)$ in the Brillouin zone. The uniaxial tensile loading was applied in both zigzag and armchair directions, assuming periodic boundary conditions (PBC). Since PBCs are applied along the planar directions and dynamical effects like temperature are not considered, only unit-cell modeling is accurate enough for the evaluation of mechanical response [160]. We used a unit-cell with a vacuum layer of 17 Å to avoid image-image interactions along the normal planar direction to analyze the mechanical properties of $RuCl_3$ and $RuBr_3$. Once we obtained the minimized energy structures, the (external) strain was applied along armchair and zigzag direction, while the negligible stress condition was satisfied along the transverse direction of loading (uniaxial loading condition $\sigma_l \neq 0$, $\sigma_t \cong 0$) by changing the corresponding simulation box size.

5.5.3 Results and discussions

The atomic configurations of the energy minimized $RuCl_3$ and $RuBr_3$ monolayers with corresponding lattice constants of 5.92 and 5.99 Å are shown in Fig. (5.1). Unit-cell of considered nanosheets present as a parallelogram with two Ru and six Cl/Br atoms.

Phonons govern the dynamic behavior and thermal properties of materials. We there-

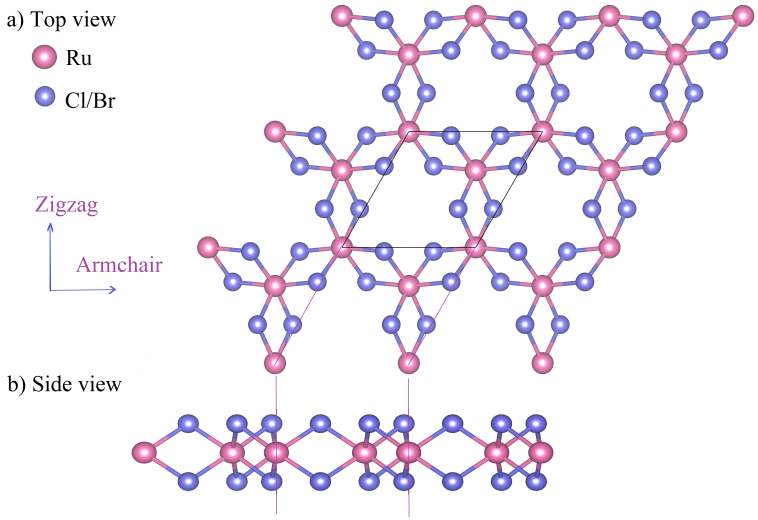

Figure 5.1: (a) Top and (b) side views of atomic configuration in $RuCl_3$ and $RuBr_3$lattice.

fore first calculated the phonon dispersions using the DFPT. As illustrated in Fig. (5.2), the dynamic stability of $RuCl_3$ and $RuBr_3$ monolayers were examined by calculating the phonon frequencies along with the high symmetry directions $(\Gamma - M - K - \Gamma)$ in the 2D Brillouin zone. The results confirmed the inexistence of negative frequencies in the Brillouin zone, demonstrating the dynamic stability of these structures. For both structures, a gap in the phonon dispersion frequencies is observable. By increasing the weight of the halogen atoms, the gap in the phonon dispersions is narrowed. Also, lattices with lighter halogen atoms were found to exhibit slightly higher frequencies than those with heavier halogen atoms.

To evaluate the nanosheets' elastic properties, we employed Hooke's law by applying the unidirectional straining. Hence, the strain stays zero perpendicular to the loading direction, i.e. $\varepsilon_t = 0$ (uniaxial strain condition). Hooke's Law for a plate with orthotropic elastic properties can be written as:

$$\begin{bmatrix} \varepsilon_{xx} \\ \varepsilon_{yy} \end{bmatrix} = \begin{bmatrix} \frac{\sigma_{xx}}{E_x} - \nu_{yx}\frac{\sigma_{yy}}{E_y} \\ -\nu_{xy}\frac{\sigma_{xx}}{E_x} + \frac{\sigma_{yy}}{E_y} \end{bmatrix} \tag{5.56}$$

here ε_{ii} , σ_{ii} , ν_{ij} and E_i are the strain, stress, Poisson's ratio and elastic modulus along the "i" direction, respectively. With ε_{yy}=0, we obtain:

$$\nu_{xy} = \frac{\sigma_{yy} E_x}{\sigma_{xx} E_y} \tag{5.57}$$

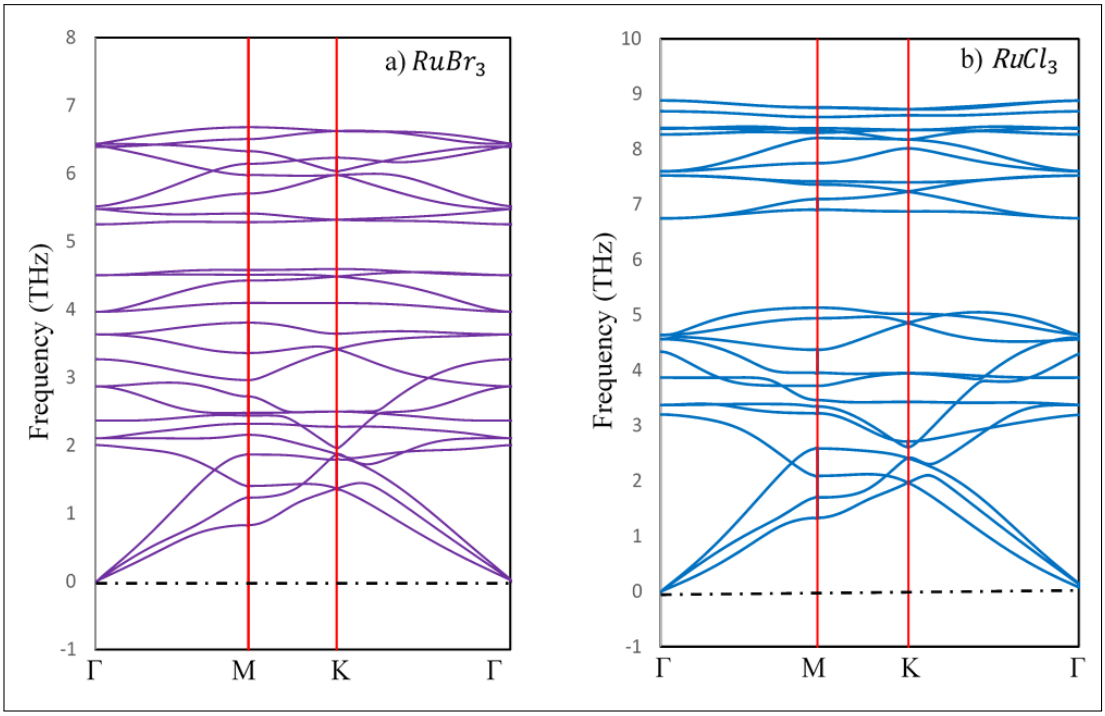

Figure 5.2: Phonon dispersions of free-standing and single-layer a) $RuBr_3$ and b) $RuCl_3$.

However, based on the symmetry of the stress and strain tensors [217], the following relation exist:

$$\frac{\nu_{yx}}{\nu_{xy}} = \frac{E_y}{E_x} \tag{5.58}$$

By substituting the Eq.(5.58) in Eq.(5.57), the Poisson 's ratio can compute as;

$$\nu_{yx} = \frac{\sigma_{yy}}{\sigma_{xx}} \tag{5.59}$$

By computing E_x and E_y from Eq. (5.58) and substituting in Eqs. (5.56),

$$E_y = \frac{E_x \nu_{yx}}{\nu_{xy}} \qquad \rightarrow \qquad \varepsilon_{xx} = \frac{\sigma_{xx}}{E_x} - \nu_{yx}\frac{\sigma_{yy}}{E_y} \tag{5.60}$$

$$E_x = \frac{E_y \nu_{xy}}{\nu_{yx}} \qquad \rightarrow \qquad \varepsilon_{yy} = -\nu_{xy}\frac{\sigma_{xx}}{E_x} + \frac{\sigma_{yy}}{E_y} \tag{5.61}$$

Finally, the elastic moduli can be calculated in both directions using Eqs. (5.60) and (5.61):

$$E_x = \frac{\sigma_{xx}}{\varepsilon_{xx}} - \nu_{xy}\frac{\sigma_{yy}}{\varepsilon_{xx}} \tag{5.62}$$

$$E_y = -\nu_{yx}\frac{\sigma_{xx}}{\varepsilon_{yy}} + \frac{\sigma_{yy}}{\varepsilon_{yy}} \tag{5.63}$$

where σ_{xx} and σ_{yy} are the stresses in longitudinal and transverse directions, respectively. In Fig.(5.3), the stress-strain relations for the uniaxial tensile straining along the armchair directions for both nanosheets are illustrated, which reveal completely linear relations corresponding to the linear elasticity. We, therefore, fitted lines to the stress-strain values for the strain values below 0.02 to report the elastic properties based on the mentioned relations. Our results for the uniaxial tensile straining along the zigzag direction (not shown in Fig.(5.3)) reveal that the initial linear responses of the considered 2D structures in both directions match closely, which means isotropic elasticity in the studied nanosheets. It is also evident that the elastic properties of $RuCl_3$ structure are higher compared to $RuBr_3$, and the bromide compound of the considered structures is softer than the chloride counterparts. The DFT estimations of the mechanical properties are summarized in Table (5.1). The elastic modulus along the zigzag and armchair directions are nearly identical. Interestingly, the calculated Poisson's ratios were found to be almost independent of the lattice structure, and slightly higher Poisson ratios were acquired along the zigzag direction. Note that the reported elastic moduli and the Poisson ratios are size-independent since we applied PBC boundary conditions in all directions. The strain values at the ultimate tensile strength are highest along the armchair direction.

Structure	$E_{armchair}$	E_{zigzag}	ν armchair	ν zigzag	$\varepsilon_{u\text{-armchair}}$	$\varepsilon_{u\text{-zigzag}}$	$UTS_{armchair}$	UTS_{zigzag}
$RuBr_3$	17.07	17.16	0.24	0.27	0.70	0.67	4.76	5.08
$RuCl_3$	24.55	24.83	0.41	0.42	0.45	0.42	6.07	6.70

Table 5.1: Mechanical properties of $RuCl_3$ and $RuBr_3$sheets, E, ν, ε_u and UTS indicate the elastic modulus, Poisson's ratio, strain and stress at ultimate tensile strength points, respectively. The stress units are in GPa.nm.

We subsequently study the mechanical responses of these 2D structures by performing uniaxial tensile simulations. Fig.(5.4) depicts the uniaxial stress-strain responses of $RuCl_3$, and $RuBr_3$monolayers extended along with the armchair and zigzag directions. In both cases, the stress-strain response exhibits an initial linear relation followed by a nonlinear trend up to the ultimate tensile strength. It is obvious from stress-strain curves that the tensile response is not perfectly isotropic and, in both cases, slightly stronger along the zigzag direction compared to the armchair direction. Our results also reveal a 30% higher strain level along with the armchair and zigzag directions of $RuBr_3$ compared with $RuCl_3$. The most striking result is that the stretchability of both $RuCl_3$ and $RuBr_3$ monolayers are considerably higher than other 2D porous networks [218] and graphyne [219] structures. Nevertheless, they show lower stretchability in comparison with boron-graphdiyne [150]. To further highlight the considerable

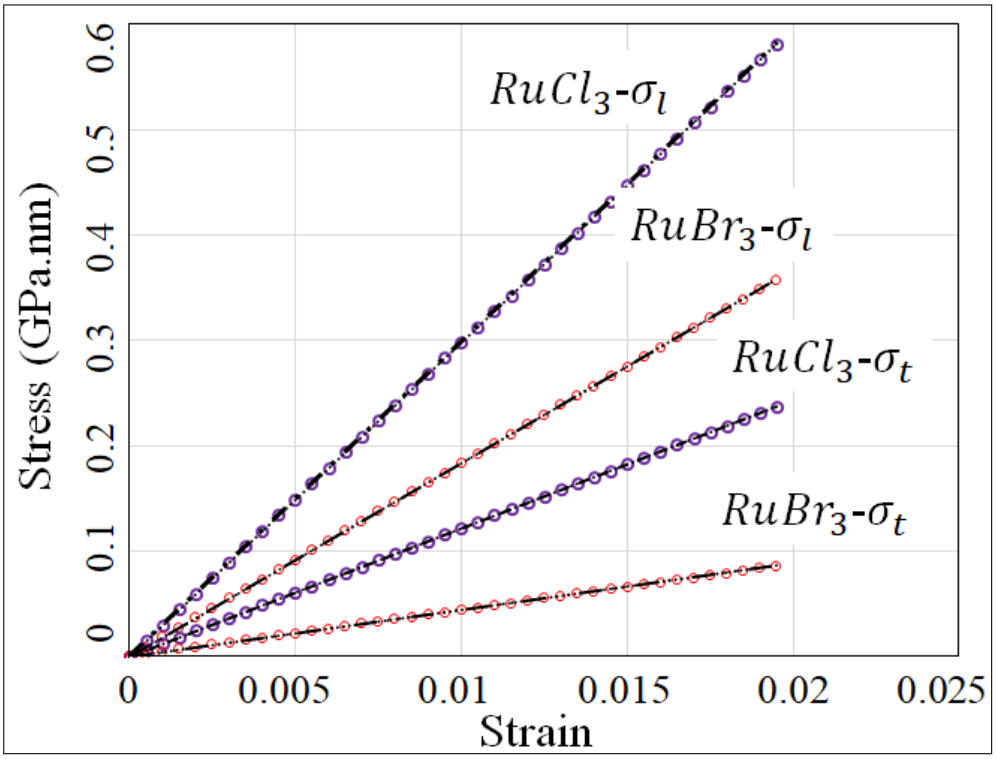

Figure 5.3: DFT predictions for the stress-strain responses of single-layer $RuCl_3$ and $RuBr_3$uniaxially strained along the armchair direction. Here, σ_l and σ_t denote the stress values along the loading and transverse directions, respectively. Using Hooke's Law, the elastic modulus and Poisson's ratio were then calculated. We remind that for the uniaxial tensile straining, the stress tensor includes two main components, longitudinal and transverse, whereas for the uniaxial tensile loading, only the longitudinal component is important, and other terms are negligible.

stretchability of the studied nanosheets, we should remind that the strain at the ultimate tensile strength for the pristine graphene and hexagonal boron-nitride were found to be ~ 0.27 and ~ 0.20 [160], ~ 0.31 and ~ 0.29 [220, 221] along armchair and zigzag directions, respectively. Besides, for the graphene kirigami and h-BN kirigami structures were get the value of ~ 0.65 [222] and ~ 0.67 [223], respectively. Overall, these results indicate ultrahigh stretchability and considerable mechanical properties of $RuCl_3$ and $RuBr_3$ nanosheets.

In order to demonstrate the deformation process (according to the lattice structure similarities of these 2D materials), we exemplary plot the bromide compound structure along the armchair loading direction in Fig.(5.5) at three different strain levels (ε): first energy minimized structure ($\varepsilon = 0$), second under half of the strain at ultimate tensile strength ($\varepsilon = 0.5\varepsilon_u$) and finally at the ultimate tensile strength point ($\varepsilon = \varepsilon_u$). The extension along the loading direction not only causes a shrinkage along the transverse

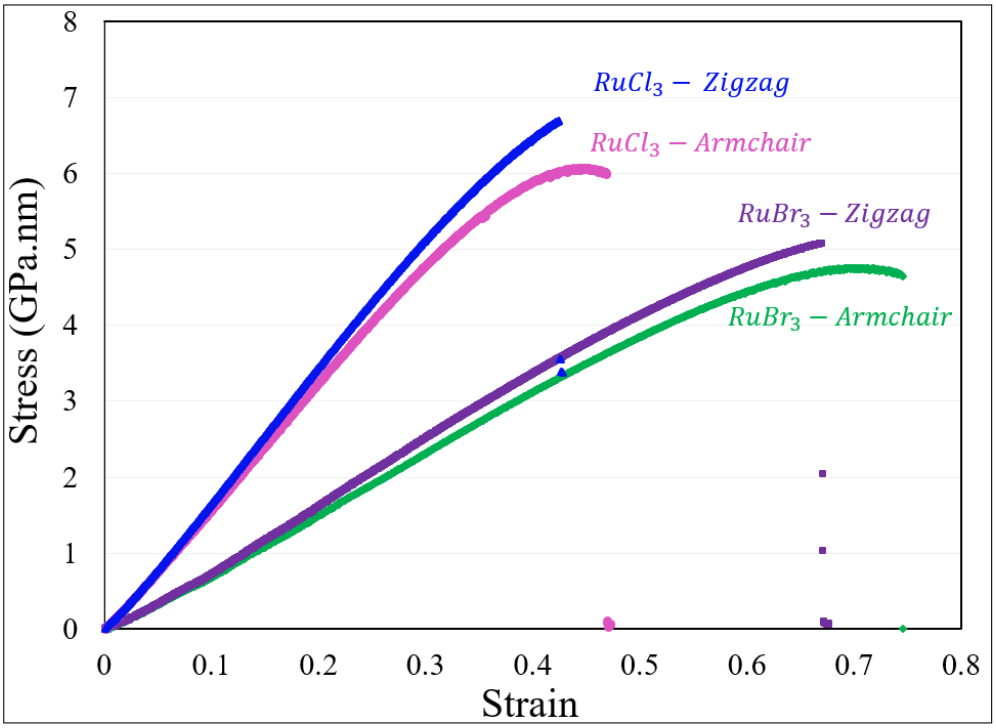

Figure 5.4: Uniaxial stress-strain responses of single-layer $RuCl_3$ and $RuBr_3$ stretched along the armchair and zigzag directions.

direction, implying a positive Poisson ratio of these TMHs but also results in a gradual decrease in thickness by increasing the strain level. In both structures, we observed higher ratios in zigzag directions when the structure is stretched along the armchair direction, which is obvious from Fig.(5.5) for $RuBr_3$.

To better understand the failure mechanism of the studied nanosheets, we consider the structures at different strain levels concerning the strain at the tensile strength point. The important bond lengths and thickness of the hexagonal unit-cell structure are shown in Fig.(5.5). During uniaxial tensile loading, twelve bonds named as "*Ri*" i=1,2, 3 ... ,12 and two unit-cell diagonals are indicated by "*d1*" and "*d2*"; the thickness of unit-cell is represented as "*h*". The armchair direction is the "*x*" direction, and the variations of the $RuBr_3$ structure were obtained in this direction.

The unit-cell structure was imposed to the five strain levels (ε) as a function of the ultimate strain value (ε_u), i.e. $\varepsilon = 0$, $\varepsilon = 0.25\ \varepsilon_u$, $\varepsilon = 0.5\ \varepsilon_u$, $\varepsilon = 0.75\ \varepsilon_u$, and $\varepsilon = \varepsilon_u$. Fig. (5.6) illustrates the coding that we used for distinguishing the various bonds in these monolayers. The unstrained form length normalized these variations. For the deformation during the uniaxial loading, expected symmetry bonds can be distinguished in bond groups with similar bond length variations. According to our results, which is shown in Fig. (5.7), the first group includes R1, R3, R6, and R12, which are elongated

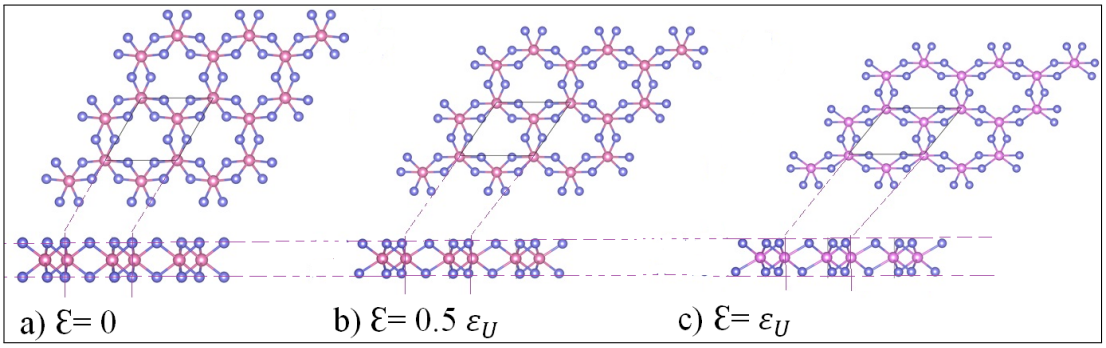

Figure 5.5: Top and side view of uniaxial tensile deformation processes of single-layer $RuBr_3$ elongated along the armchair at different strain levels (ε) with respect to the strain at ultimate tensile strength (ε_u).

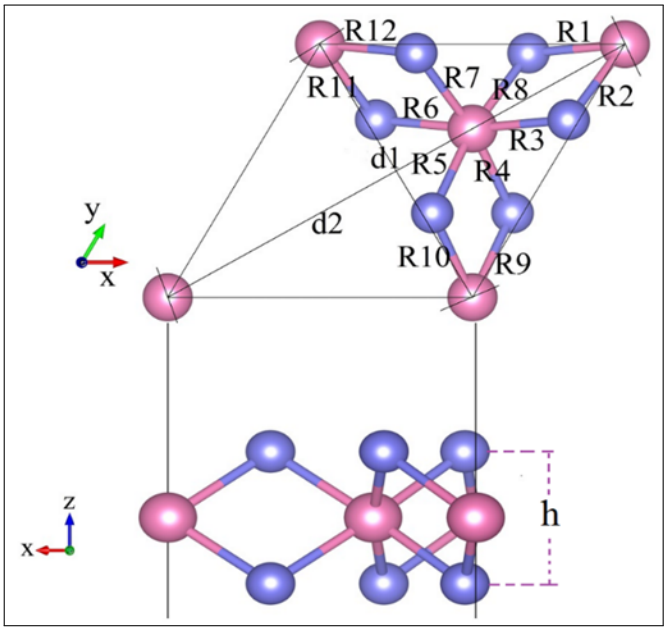

Figure 5.6: Unit cell bond lengths and thickness.

along the loading direction; R2, R7, R8, and R11 bonds belong to the second group. Interestingly, this group has the highest elongation among all bond groups due to the spatial atomic configuration. These bonds, oriented along with the transverse and loading directions with higher length variations, help the material to stretch along the loading direction. The last symmetry group R4, R5, R9, and R10 are aligned along the transverse direction and gained the lowest bond length variations. Due to their atomic spatial positioning, the bonds were extended at a strain level of ε=0.25 ε_u and subsequently decreased in length with further increasing strain values. On the other hand, we observe non-identical stretching of the bonds along the stretching direction. These may be explained by the higher tendency of the two center-two electrons (c2-2e) bonds to be stretched easier than the three center-two electrons (3c-2e) bonds, which were not studied here.
The thickness of the unit-cell gradually decreased with increasing strain levels, but the intensity of this contraction remains below 3.2%, which is consistent with the 3% thickness decrement of prior studies on 2D materials [224]. The unit-cell diagonal, d2 (large parallelogram diameter), was aligned mostly along the loading direction and gained 19.60% in length at the ultimate strain value. The other diagonal, d1 (small parallelogram diameter), did not experience considerable changes. First, it decreased 0.25% in length under compression before increasing about 1.1% when the unit-cell is stretched perfectly along the loading direction.

5.5.4 Conclusion

We conducted first-principles spin-polarized DFT calculations to predict the mechanical response and stability of defect-free single-layer $RuCl_3$ and $RuBr_3$. We first investigated the stability of the considered structure by calculating the phonon dispersions. The phonon frequencies results indicate no negative frequency inside the Brillouin zone, confirming the dynamic stability of both nanosheets. For $RuCl_3$ and $RuBr_3$ the elastic properties were found to be isotropic and the elastic modulus were computed $\sim$ 25 and $\sim$ 17 GPa.nm, respectively. Our DFT results reveal further that the tensile strain responses of these 2D systems are not isotropic, and along the zigzag direction, they are slightly stronger than the armchair direction. The maximum strain at tensile strength along with the armchair and zigzag directions were 0.75 and 0.68 for the bromide, and 0.48 and 0.44 for the chloride compounds, confirming their super-stretchability. Our results may be useful for the design of highly stretchable and flexible nanodevices using $RuCl_3$ and $RuBr_3$ as 2D components.

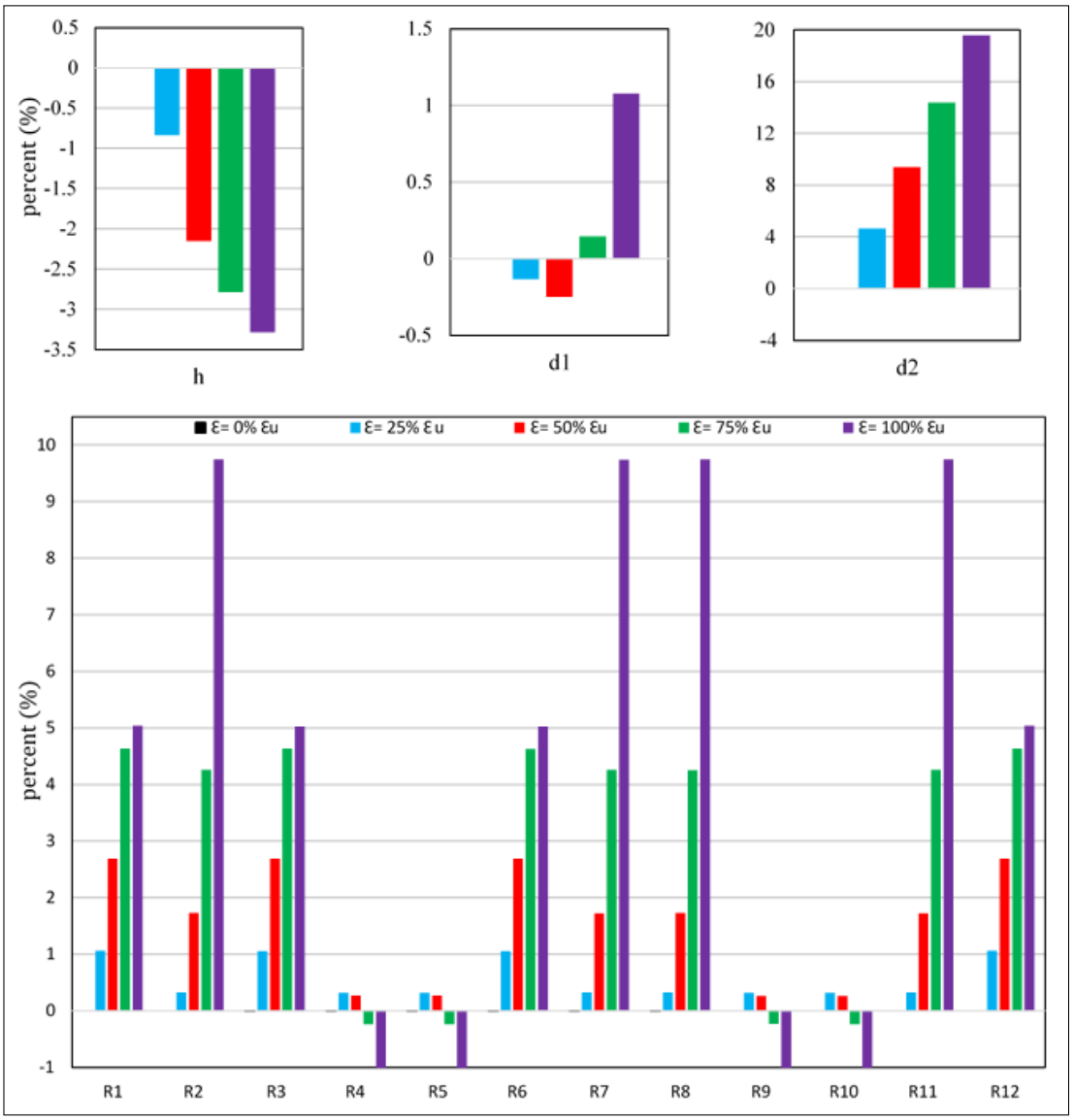

Figure 5.7: Evolution of unit-cell bond lengths and thickness variations in $RuBr_3$ with increasing strain in the uniaxial armchair direction. The variations are normalized by unstrained form length and are shown in percent.

5.6 Ab-initio mechanical and electrochemical responses of 2D nanomaterials

5.6.1 Introduction

The great success of graphene [103, 168], emerged the two-dimensional (2D) materials as a new class of materials suitable for numerous and diverse applications ranging from nanoelectronics to aerospace structures. For the applications in nanoelectronics, presenting a semiconducting electronic character with moderate and tuneable band-gap is highly desirable. Nevertheless, graphene in its natural form presents zero-band-gap semiconducting property and such that opening a band-gap in graphene requires complex physical or chemical modifications such as chemical doping or defect engineering [225, 226, 227, 228]. As an alternative, synthesize of other 2D material with an inherent semiconducting character such as transition metal dichalcogenides [106, 229, 230] has been considered as a more reliable approach to exploit in post-silicon electronics. The success of silicon in electronics is not only due to its moderate bandgap of 1.1 eV, but also because of the existence of SiO_2 as a high-quality native insulator. In this case, other competitors of silicon lack stable oxides and must rely on deposited insulators [231], which imposes compatibility challenges. A recent experimental study confirmed that 2D $ZrSe_2$ and $HfSe_2$ semiconductors with band-gaps ranging from 0.9 to 1.1 eV can serve as up-and-coming candidates to replace the silicon in electronic devices. These 2D materials are highly technologically desirable because of the existence of high-κ native dielectrics of HfO_2 and ZrO_2 [231].
For the engineering design of novel nanodevices using the 2D materials, comprehensive understanding of electronic, mechanical, and thermal properties of 2D components play crucial roles. It should be noted that for the materials at nanoscale such as the 2D materials, experimental techniques for the evaluation of properties are complicated, time-consuming, and expensive as well. In these cases, classical and first-principles theoretical approaches can be considered as fast viable alternatives to explore various material properties such as thermal conductivity, mechanical response, electrochemical performance and electronic properties in low cost and trustable level of precision [59, 110, 163, 232, 233, 234, 235]. The material properties predicted by the first-principles simulations can be later employed in the hierarchical, semi-concurrent, and concurrent multi-scale approaches [236] in order to design real nanodevices. Advanced multi-scale techniques can play critical roles in engineering and performance improvement of the future nanodevices.
Motivated by the high technological prospects for the 2D HfS_2, $HfSe_2$, ZrS_2 and $ZrSe_2$, in the present investigation we accordingly intend to investigate their properties in single-layer and free-standing form by conducting extensive first-principles density functional theory (DFT) simulations. In this case, we analyzed the structural and elec-

tronic properties of these 2D materials at minimum energy conditions. We applied uniaxial tensile loading conditions to elaborate on the mechanical properties and deformation process as well. Because of the highly attractive electronic properties of these 2D materials, we particularly explored the possibility of tuning bandgap using the uniaxial or biaxial loading conditions. This study addresses some critical properties of 2D HfS_2, $HfSe_2$, ZrS_2 and $ZrSe_2$ and therefore may act as a useful guide for their practical applications in nanodevices.

5.6.2 Computational methods

DFT calculations in this study were performed using the Vienna ab-initio simulation package (VASP) [209, 210, 211]. The plane wave basis set with an energy cut-off of 500 eV and the gradient approximation exchange-correlation functional proposed by Perdew-Burke-Ernzerhof [197] were employed. VMD [237] and VESTA [213] packages were also used for the visualization of atomic structures. Fig.(5.8), illustrates the hexagonal lattice of HfS_2, $HfSe_2$, ZrS_2 and $ZrSe_2$ atomic structure which shows ABA atomic stacking sequence.

In this work we analysed the anisotropy in the mechanical response by uniaxial

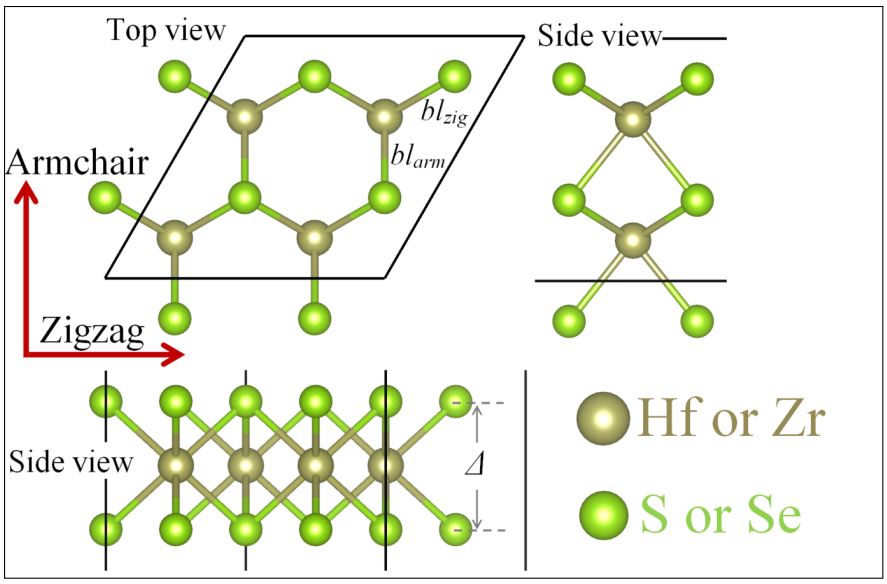

Figure 5.8: Top and side views of atomic configuration in single-layer HfS_2, $HfSe_2$, ZrS_2 and $ZrSe_2$. We studied the properties along the armchair and zigzag directions as shown.

stretching the structures along the armchair and zigzag directions. We applied periodic boundary conditions along all three Cartesian directions and such that the obtained results represent the properties of large-area single-layer films and not the nanoribbons.

Since the dynamical effects such as the temperature are not taken into consideration and periodic boundary conditions were also applied along the planar directions, only a unit-cell modelling is accurate enough for the evaluation of mechanical properties, and such that we only used a unit-cell consisting of 3 atoms. We considered a vacuum layer of 20 Å to avoid image-image interactions along the sheets normal direction. After obtaining the minimized structure, we applied loading conditions to evaluate the mechanical properties. For this purpose, we increased the periodic simulation box size along the loading direction in a multistep procedure, every step with a small engineering strain of 0.001. For the uniaxial loading conditions, upon the stretching along the loading direction the stress along the transverse direction should be negligible. To satisfy this condition, after applying the loading strain, the simulation box size along the transverse direction of the loading was changed accordingly in a way that the transverse stress remained negligible in comparison with the stress along the loading direction. For the biaxial loading condition, the equal loading strain was applied simultaneously along the both planar directions. After applying the changes in the simulation box size, the atomic positions were rescaled to avoid any sudden void formation or bond stretching as well. We then used the conjugate gradient method for the geometry optimizations, with strict termination criteria of 10^{-5} eV and 0.005 eV/Å for the energy and the forces, respectively, using a $19\times$ $19\times$ 1 Monkhorst-Pack [214] k-point mesh size. The final stress values after the termination of energy minimization process were calculated to obtain the stress-strain curves. The ground state electronic properties were first calculated using the PBE functional. Due to underestimation of experimental band-gap values using the PBE functional, we also used the screened hybrid functional HSE06 [238] and quasi-particle many-body perturbation theory (MBPT) via G_0W_0 approximation [239, 240] to evaluate the electronic properties of these materials. A $14 \times 14\times$ 1 Γ centered Monkhorst-Pack k-point mesh is used was used for PBE and HSE06 calculations.

5.6.3 Results and discussions

We first study the atomic structure of HfS_2, $HfSe_2$, ZrS_2 and $ZrSe_2$, which can be well defined by the hexagonal lattice constant (α) and transition metal-chalcogen atom bond length (*bl*). In Table (5.2) the lattice constants and the bond lengths for the considered 2D structures at their minimum energy condition are mentioned. We next study the mechanical responses of these 2D structures by conducting the uniaxial tensile simulations. In Fig. (5.9), the DFT predictions for the uniaxial stress-strain responses of HfS_2, $HfSe_2$, ZrS_2 and $ZrSe_2$, elongated along the armchair and zigzag directions are plotted. In all cases, the stress-strain responses present an initial linear relation which is followed by a nonlinear trend up to the ultimate tensile strength point, a point at which the material illustrates its maximum load bearing. The slope of the first initial linear section of the stress-strain response is equal to the elastic modulus.

In this work we therefore fitted a line to the stress-strain values for the strain levels below 0.02 to report the elastic modulus. For these initial strain levels within the elastic limit, the strain along the traverse direction (s_t) with respect to the loading strain (s_l) is acceptably constant and can be used to obtain the Poisson's ratio using the $-s_t/s_l$. Our results shown in Fig. (5.9) reveal that the initial linear response of the considered 2D structures match closely which means that their elastic properties are close. In another side, the non-linear part of the stress-strain curves are different depending on the atomic structure and loading direction as well. Our DFT results reveal that the tensile response is not isotropic and along the armchair direction the single-layer HfS_2, $HfSe_2$, ZrS_2 and $ZrSe_2$, are considerably stronger as compared with the zigzag. Such an observation is in agreement with earlier studies for the mechanical properties of transition metal dichalcogenides [241] and group IV 2D materials [242]. The obtained mechanical properties of considered 2D structures are summarized in Table (5.2). In general, the elastic modulus is around 6% higher when the structure is elongated along the armchair in comparison with zigzag. For the both tensile strength and elastic modulus we found the anisotropy in the mechanical response is almost inversely correlated with the stiffness: such that the lower the elastic modulus or tensile strength, the higher is the anisotropy in the mechanical response. However, such a correlation for $HfSe_2$ and ZrS_2 is not consistent since they show very close mechanical properties and their anisotropy in mechanical properties are also very close. Interestingly, the calculated Poisson's ratios were found to be almost independent of the structure and slightly higher Poisson's ratios were acquired along the armchair. For ultimate tensile strength point we predict that along the zigzag direction studied 2D films yield slightly higher strain values.

We next conduct the electronic structure analysis to investigate the origin of differ-

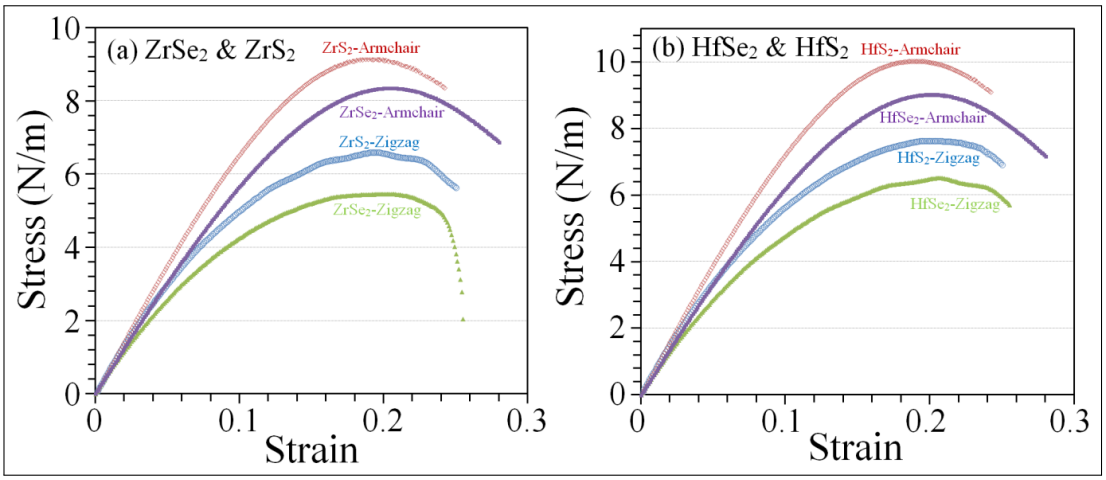

Figure 5.9: Uniaxial stress-strain responses of single-layer and free-standing HfS_2, $HfSe_2$, ZrS_2 and $ZrSe_2$ stretched along the armchair and zigzag directions.

Structure	α	*bl*	Y $_{Arm}$	Y $_{Zig}$	P$_{Arm}$	P$_{Zig}$	UTS$_{Arm}$	UTS$_{Zig}$	STS$_{Arm}$	STS$_{Zig}$	CT
HfS_2	3.535	2.572	80	76	0.40	0.34	10	7.6	0.21	0.22	1.05
$HfSe_2$	3.672	2.706	69	65	0.40	0.35	9.0	6.5	0.20	0.21	0.98
ZrS_2	3.574	2.594	72	68	0.41	0.36	9.2	6.6	0.19	0.20	0.97
$ZrSe_2$	3.705	2.726	62	58	0.40	0.34	8.3	5.5	0.21	0.22	0.90

Table 5.2: Summary of structural and mechanical properties of single-layer HfS_2, $HfSe_2$, ZrS_2 and $ZrSe_2$. α , *bl*, Y, P, CT, STS and UTS depict lattice constant, transition metal-chalcogen atom bond length, elastic modulus, Poisson's ratio, charge transfer from transition metal to a single chalcogen atom, strain at ultimate tensile strength point and ultimate tensile strength, respectively. Stress and the length units are in N/m and Å, respectively, and subscripts zig. and arm. are for the properties along the zigzag and armchair directions, respectively.

ences in the mechanical properties of studied structures. To this aim we first calculated the electron localization function (ELF) [243]. In Fig. (5.10a) a sample of obtained ELF for HfSe is illustrated which reveals that the electron localization is more concentrated around the Se atoms. This result suggests the charge transfer from the transition metal to the chalcogen atoms. To characterize this charge transfer from transition metal to every chalcogen atom, we conducted the Bader charge analysis [244] and the obtained results are included in Table (5.2). As a general trend, by increasing the charge transfer both the elastic modulus and tensile strength values increase, which is in agreement with the results for transition metal dichalcogenides [241]. Nevertheless, an exception exist and for the $HfSe_2$ and ZrS_2 the values of charge transfer are very close and in this case the lighter structure with slightly lower charge transfer presents negligibly higher elastic modulus and tensile strength.
To better understand the underlying mechanism that results in anisotropic tensile response of HfS_2, $HfSe_2$, ZrS_2 and $ZrSe_2$, we analyzed the deformation process. Due to the similarities in the deformation behaviour of the studied 2D structures, in this case we only examine the $ZrSe_2$ structure. For the deformation during the uniaxial loading, two different bonds can be distinguished, the bond along the armchair (bl_{arm}) and the bond oriented along the zigzag (bl_{zig}) direction, which are depicted in Fig. (5.8). Fig. (5.10), compares the change in the bond lengths as a function of strain for the uniaxial loading along the armchair and zigzag directions. As a general observation, during the uniaxial tensile loading, the bond oriented along the loading direction elongates and the other bond oriented along the transverse direction of loading contracts. Based on our results for the both loading directions, during the stretching the structures contract slightly along the sheet thickness, however the intensity of this contraction remains almost below 3% . For the stretching along the armchair direction, one bond is exactly along the loading direction and directly involves in the load bearing and such that by increasing the strain level this bond increases substantially. In this case, the bond ori-

ented along the transverse direction remains almost unchanged and only after the strain level of ~ 0.15 starts to contract slightly. On the other side, for the uniaxial stretching along the zigzag, one bond is almost oriented along the loading direction and the other bond is exactly along the transverse direction. In this case, based on our results shown in Fig. (5.10b), since the bond involving in the load transfer is not exactly inline of the loading by increasing the strain level the bond stretching is moderate. In this case the contraction of the bond along the transverse direction is more considerable, which helps the material to flow easier along the loading direction. As it is clear, the distinctly higher tensile strength as well as the slightly higher elastic modulus along the armchair direction can be attributed to the fact that during the stretching along the armchair half of the bonds are exactly aligned to the loading direction and such that the deformation is achieved mainly by the bond elongation.

Next, we shift our attention to explore the evolution of band-gap of aforementioned

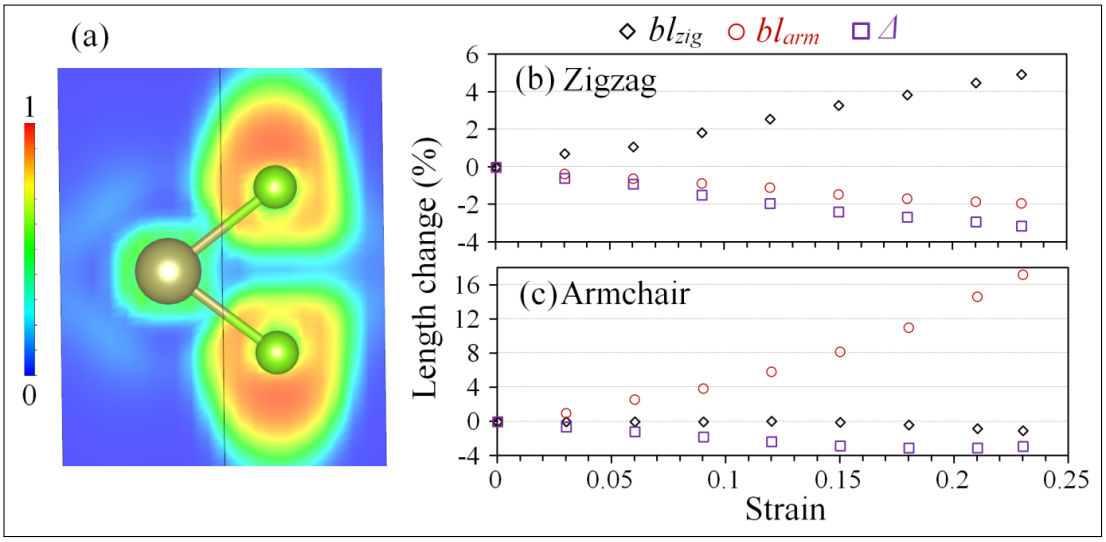

Figure 5.10: (a) Electron localization function (ELF) results of the unstrained single-layer HfSe showing the localization of electrons around the Se atoms. The change in the bond lengths and the sheet thickness for the uniaxial loading of $ZrSe_2$ structure along the (b) zigzag and (c) armchair direction.

2D materials under different loading conditions. In Fig. (5.11), the band structure and total DOS of HfS_2, $HfSe_2$, ZrS_2 and $ZrSe_2$ monolayers for different biaxial or uniaxial tensile strains by the PBE are compared. The band structure and DOS for unstrained systems and maximum magnitudes of strain are reported. It is well visible that the free strained nanostructures present indirect band-gaps in which the valence band maximum (VBM) coincides along the K-Γ direction and the conduction band minimum (CBM) locates at M-point which is in a good agreement with that reported previously for $HfSe_2$ monolayer [231]. The acquired results show that the band-gaps

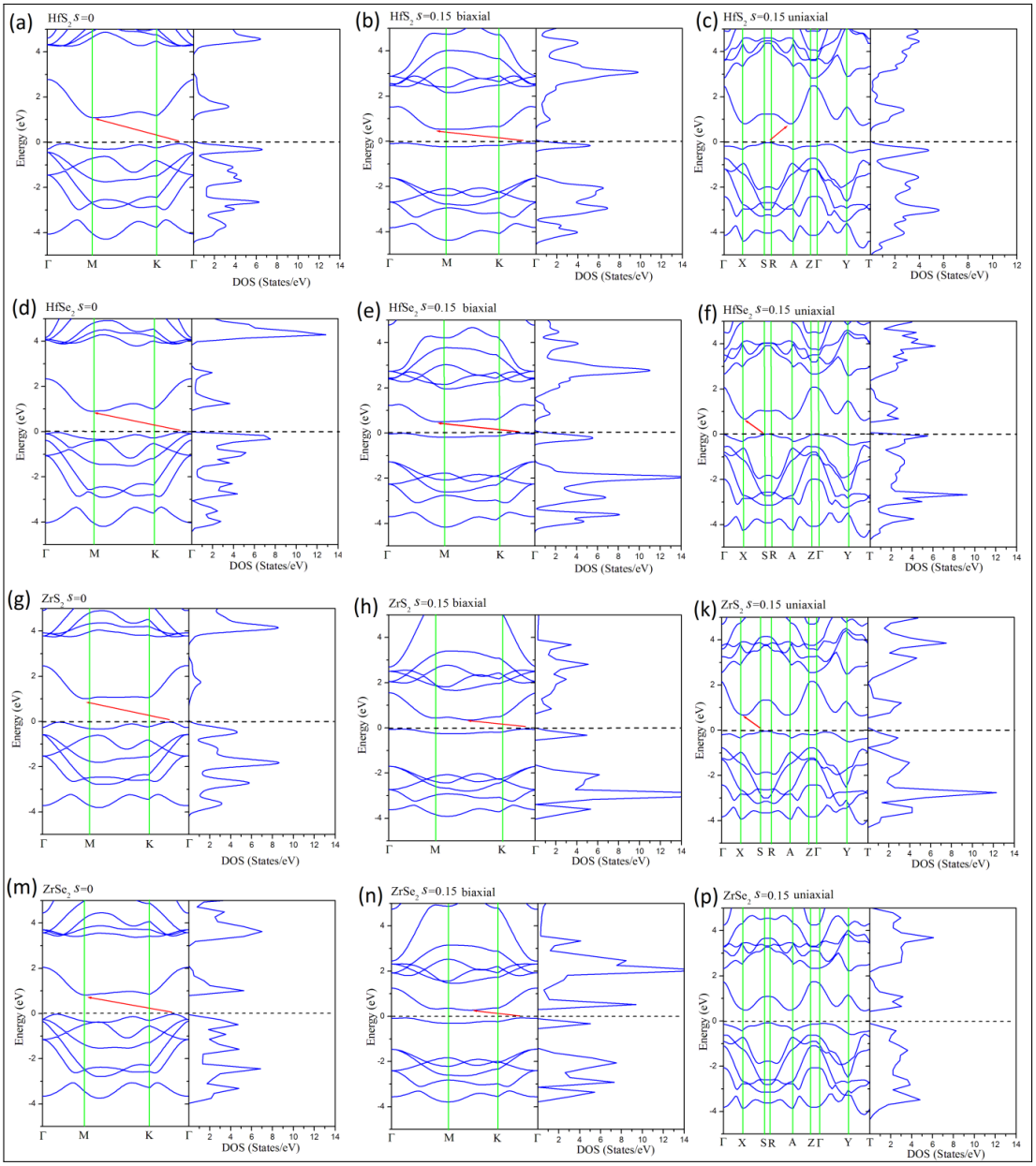

Figure 5.11: Band structure and total DOS of unstrained and strained HfS_2, $HfSe_2$, ZrS_2 and $ZrSe_2$ monolayers for different biaxial or uniaxial tensile loading predicted by the PBE functional.

of the HfS_2, $HfSe_2$, ZrS_2 and $ZrSe_2$ sheets, using PBE, are 1.15, 0.95, 1.0 and 0.85 eV, respectively, which are slightly larger than those found for transition-metal dichalcogenides monolayers in the T phase [245]. For all monolayers, their band-gap decreases when the biaxial or uniaxial tensile loading is applied. Note that the reduced band-gap for biaxial strains is lower than uniaxial ones. In order to obtain accurate results of electronic band-gap, the screened hybrid functional HSE06 and quasi-particle G_0W_0 approaches have also been used. Fig. (5.12) and Fig. (5.13) illustrate total DOS of 2D HfS_2, $HfSe_2$, ZrS_2 and $ZrSe_2$ monolayers using HSE06 and G_0W_0 approaches, respectively. The HSE06 functional and GWA approaches gave remarkably larger band-gaps than the PBE functional for the all studied structures. The corresponding values within HSE06 for 2D HfS_2, $HfSe_2$, ZrS_2 and $ZrSe_2$ monolayers are 1.72, 1.50, 1.45 and 1.22 eV. The band-gap value for $HfSe_2$ monolayer is in excellent agreement with previous calculation [231]. Taking the electron-electron interactions into account in G_0W_0 reduces screening, resulting in an increase over the PBE band-gap. The calculated indirect band-gap from G_0W_0 is 1.90, 1.70, 1.65 and 1.30 eV for the unstrained HfS_2, $HfSe_2$, ZrS_2 and $ZrSe_2$ sheets, respectively. In Table (5.3) the band-gap of the strained and unstrained systems obtained by different methods are summarized.

	$s=0$			$s=0.1$ biaxial			$s=0.15$ biaxial			$s=0.1$ uiaxial			$s=0.15$ uiaxial		
	PBE	HSE06	G_0W_0	PBE	HSE06	G_0W_0	PBE	HSE06	G_0W_0	PBE	HSE06	G_0W_0	PBE	HSE06	G_0W_0
HfS_2	1.15	1.72	1.90	0.82	1.31	1.75	0.62	1.19	1.45	0.92	1.55	1.84	0.77	1.36	1.60
$HfSe_2$	0.95	1.50	1.70	0.70	1.15	1.45	0.52	1.0	1.25	0.72	1.25	1.30	0.60	1.10	1.20
ZrS_2	1.0	1.45	1.65	0.63	1.22	1.40	0.40	0.70	0.97	0.79	1.23	1.47	0.68	0.97	1.25
$ZrSe_2$	0.85	1.25	1.30	0.56	0.97	1.01	0.38	0.67	0.76	0.63	1.05	1.12	0.52	1.0	0.84

Table 5.3: The energy band-gap (eV) values of 2D HfS_2, $HfSe_2$, ZrS_2 and $ZrSe_2$ monolayers calculated within PBE, HSE06 and G_0W_0 approaches.

5.6.4 Conclusion

We conducted extensive first-principles DFT calculations to explore the mechanical and electronic responses of pristine and single-layer HfS_2, $HfSe_2$, ZrS_2 and $ZrSe_2$ monolayers. We first investigated the mechanical responses of these 2D structures by conducting the uniaxial tensile simulations. It was found that the charge transfers from the transition metal to chalcogen atoms correlates directly to elastic modulus and tensile strength. Our DFT results reveal that the mechanical responses of these 2D systems are not isotropic and along the armchair direction the single-layer HfS_2, $HfSe_2$, ZrS_2 and $ZrSe_2$, are considerably stronger as compared with the zigzag. It was found that during the stretching along the armchair the deformation evolves more by the bond elongation which explains the higher stress values at any certain strain value as

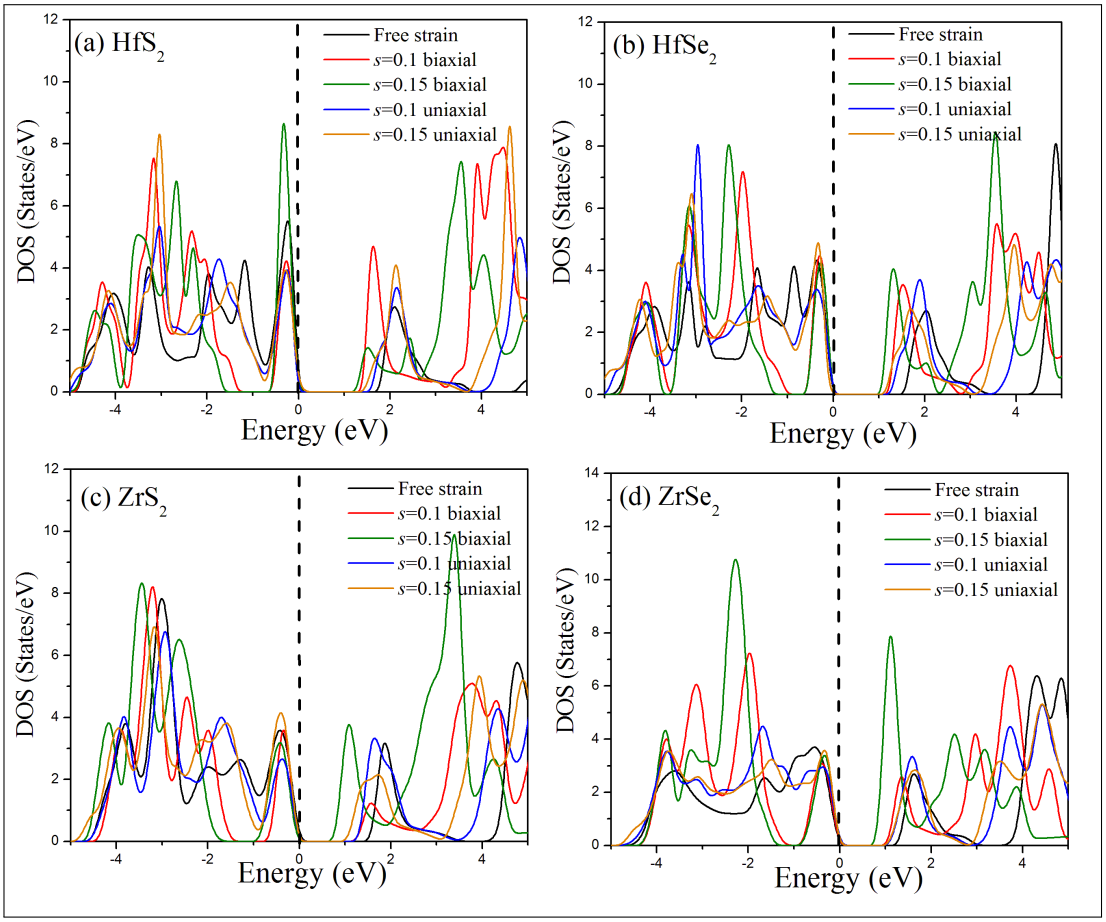

Figure 5.12: The total DOS predicted by the HSE06 functional.

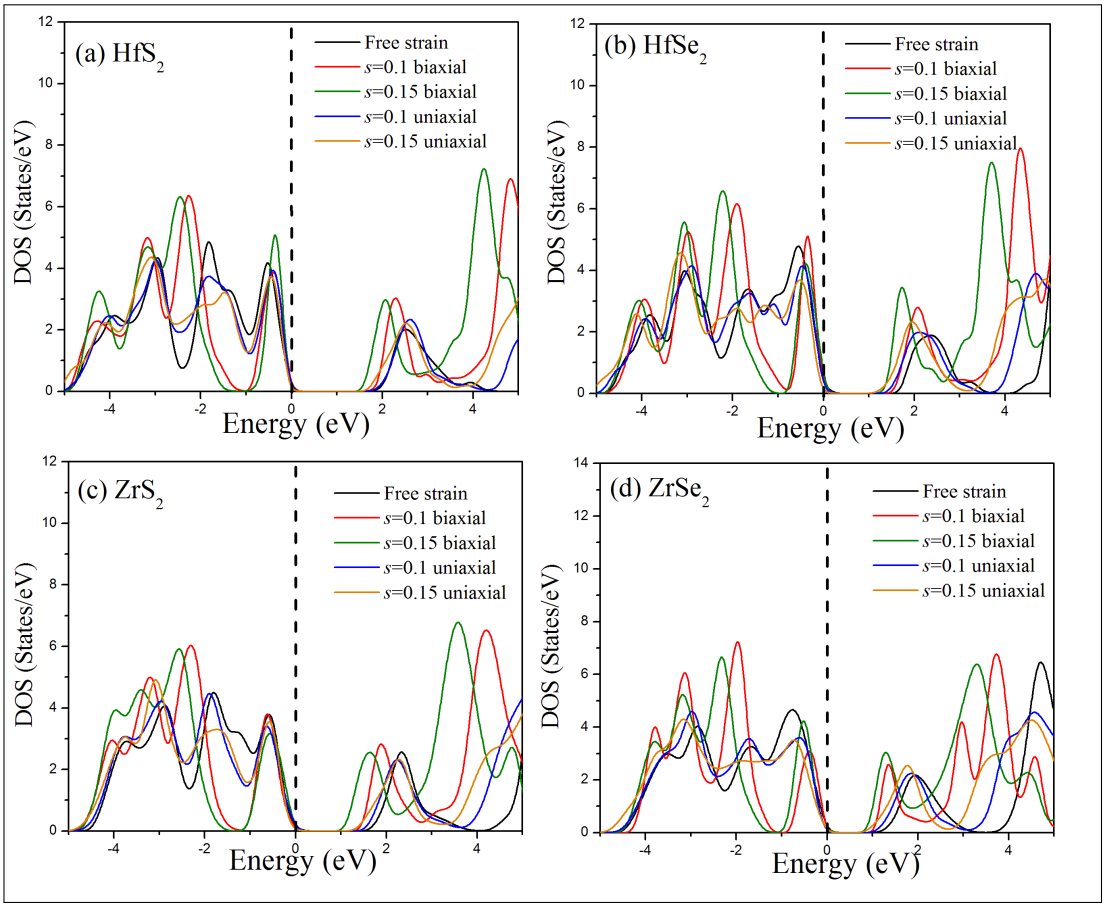

Figure 5.13: The total DOS of free-standing and single-layer HfS_2, $HfSe_2$, ZrS_2 and $ZrSe_2$ predicted by the G_0W_0 approach.

compared with the loading along the zigzag. According to the G_0W_0 method estimations, indirect band-gaps of 1.90, 1.70, 1.65 and 1.30 eV were predicted for unstrained single-layer HfS_2, $HfSe_2$, ZrS_2 and $ZrSe_2$, respectively. Based on the PBE, HSE06 and G_0W_0 methods predictions, it was found that the band-gap decreases through applying the biaxial or uniaxial tensile loading which notably confirms the tunability of electronic properties of these 2D structures. It was found that biaxial strains can be employed as a more effective approach for tuning the electronic response of HfS_2, $HfSe_2$, ZrS_2 and $ZrSe_2$.

Chapter 6

2D Anode Materials for Battery Energy Storage System

6.1 Introduction

Rechargeable metal-ion batteries play a crucial role in modern transport, communication and electronic industries [29, 30, 31]. Ordinary batteries are commonly based on Li-ion transfer and diffusion. Their superior energy density, capacity, and lifetime highlight them as the main power supply for various portable electronic devices [246, 247, 248]. A common commercial anode electrode material is graphite, which is highly stable, but it has only a moderate charge capacity of 372 mAh/g, and the ion diffusion is not fast enough. Therefore alternative anode materials have been used in order to satisfy the quickly growing market [32, 33]. During the last decade, various bulk materials like silicon have been probed as anode electrodes to improve the performance of metal-ion batteries. However, for the commercialization of these materials, there are several technical issues such as degradation [249, 250, 251, 252, 253]. Since two dimensional (2D) materials and their hetero-structures exhibit good stability, extensive adsorption energy, fast ion diffusions and high storage capacity due to their great surface to volume ratio, they have progressively attracted attention as electrodes in high performance rechargeable batteries [59, 234, 254, 255, 256, 257, 258, 259, 260, 261]. As an emerging class of 2D materials, transition metal dichalcogenides (TMD) [106, 230] exhibit unique photoelectronic, thermal and mechanical properties. They include a stoichiometric formula of MX_2 in which M is a transition metal element such as Mo, W, Sc, Cr or V; and X is a chalcogen element; such as S, Se or Te. Each monolayer contains a layer of M atoms sandwiched between two layers of X atoms. These attractive 2D nanostructures can be fabricated from bulk TMD structures by a top-down exfoliation approach [262], or they might be directly synthesized by a bottom-up technique such as molecular beam epitaxy (MBE) [263] or chemical vapour deposition

(CVD) [264]. An exciting fact about the TMD structures is their polymorphism nature. In this regard, TMDs may exist in three different structural phases including 2H, 1T and 1T' [265, 266]; 2H and 1T phases contain the hexagonal and trigonal structure, respectively and 1T' is a distorted form of 1T.
Recently 2D vanadium dichalcogenides (VX_2) including VS_2, VSe_2, and VTe_2 have gained utmost attention stemming from their outstanding optical, electrical and chemical properties [267]. In electronics and phonon dispersion calculations, Ataca *et. al* [268] predicted that all 2H and 1T VX_2 structures exhibit metallic behaviour and they are energetically stable although the 1T phase is more favourable than the 2H structure. In 2011, few-layer thick nanosheets of VS_2 were successfully synthesized from the bulk counterpart through exfoliation [262, 269, 270]. Most recently, the fabrication of the 1T VSe_2 nanosheet via a chemical vapour deposition approach has been reported [271]. Remarkably, these recently grown 2D structures show excellent metallic properties including an extensive electrical conductivity of up to 106 Sm^{-1} [271]. A theoretical study [272] suggests that VX_2 structures show fascinating magnetic properties due to their intrinsic ferromagnetism which makes them unique candidates for spintronic devices. Jing *et. al* [273] investigated the 2H VS_2 monolayer as an anode for the Li ion battery storage and they reported that this monolayer provides a larger adsorption energy, lower diffusion energy barrier, and greater ideal capacity compared to MoS_2 and common graphite anodes.
A high electrical conductivity is always among the most desirable factors for the application as anode or cathode material in rechargeable metal-ion batteries. Motivated by the recent experimental advances [262, 267, 269, 271] in the synthesis of highly conductive VX_2 nanosheets with 1T atomic structure, which is more stable than the 2H counterpart, in this study we aim to explore the application of 1T VS_2 and 1T VSe_2 as anode materials for Li-, Na-, Mg-, Ca -and Al ion-storages. For this purpose, we carried out first-principles simulations to probe the interactions of adatoms with 1T VS_2 and VSe_2 monolayers. Therefore, we computed critical factors including the adsorption energy, diffusion energy barrier, open circuit voltage profile, electronic density of states (DOS) and storage capacity.

6.2 Computational methods

We conducted first-principles density functional theory (DFT) simulations in order to explore the stretchability and application of 1T VS_2 and VSe_2 2D structures as anode materials. In this study, the spin polarized DFT method within the Vienna ab-initio simulation package (VASP) [209, 210, 211] was used. The plane wave basis set with an energy cut-off of 500 eV and generalized gradient approximation (GGA) exchange-correlation functional proposed by Perdew-Burke-Ernzerhof (PBE) [197] was also employed. A dispersion scheme, DFT-D2 [274], developed by Grimme was employed to

improve the binding energy calculations by accounting for the dispersion corrections. To illustrate the atomistic structures and charge densities, we used the VESTA [213] package.

The adsorption of Li, Na, Mg, Ca and Al adatoms were simulated over 1T VS_2 and VSe_2 super-cells under periodic boundary conditions in all directions. In order to avoid the image-image interactions, a vacuum layer of 20Å are imposed along the sheet thickness. For the studied VX_2 monolayers, 3 probable binding sites were postulated as the most favourable binding sites for Li, Na, Mg, Ca and Al adatoms; on the top of V atoms, on the top of X atoms (X= S or Se), or on the top of the V-X bonds. The optimized structure was acquired by employing the conjugate gradient method with a convergence criteria of 10^{-4} eV and 0.01 eV/Å for the energy and the forces, respectively, using a $6\times$ $6\times$ 1 Monkhorst-Pack [214] k-point mesh size. In order to simulate the gradual atoms intercalation over the VX_2 sheet as an anode material, the adatoms were randomly but uniformly positioned on the predicted stable binding sites. The DFT calculations were carried out to find energy minimized structures for different coverages of adatoms over VX_2 nano-membranes. To more precisely calculate the final energy values, charge densities and electronic density of states (DOS), we conducted single point calculations using the tetrahedron method with Blöchl corrections in which the Brillouin zone was sampled with a $15\times$ $15\times$ 1 Monkhorst k-point mesh size. Bader charge analysis [275] was then achieved using the acquired charge densities in order to estimate the charge transfer from the adatoms to the VX_2 substrate and predict the final charge capacities of VX_2 films for each studied adatom. The climbing image nudged elastic band (CNEB) [276] method was employed to simulate the diffusion of a single adatom over the single-layer VX_2. In this case, we constructed a $3\times$ 2 super-cell of the single-layer 1T VX_2.

The mechanical properties of 1T VS_2 and VSe_2 were investigated by conducting uniaxial tensile modelling for a unit-cell [145, 163]. The periodic simulation box size was increased along the loading direction with a constant engineering strain step of 0.001. Then its size along transverse loading direction was changed to comply the negligible transverse stress [131, 151, 204, 206]. Finally, the conjugate gradient method was employed to perform geometry optimization with termination criteria of 10^{-5} eV and 0.005 eV/Å for the energy and the forces, respectively, using a $25\times$ $25\times$ 1 Monkhorst-Pack [214] k-point mesh size. Once the energy minimization process was completed, the final stress values were calculated to obtain the stress-strain curves. Although the first-principles simulations provide powerful tools to investigate properties of novel materials and structures, they can only be used for systems consisting of a few-hundred atoms due to their high computational cost. Computational multiscale methods as presented in [59, 149, 277, 278, 279, 280] is a good pathway to study structures at larger length scales.

6.3 Results and discussions

The 2H phase of VS_2 or VSe_2 atomic lattice shows a hexagonal lattice with ABA atomic stacking sequence. In the 1T phase configuration the S or Se atoms on the bottom atomic plane of 2H phase is converted into the hollow center of the hexagonal lattice. Fig. (6.1),indicates the atomic lattice of 1T VS_2 or VSe_2 with ABA atomic stacking sequence. The atomic structure 1T VS_2 or VSe_2 can be represented by the hexagonal lattice constant (α) and V–S or V–Se bond length. The unit-cell energy minimization and geometry optimization, derived by the DFT method, results in the lattice constants of 1T VS_2 and VSe_2 of 3.181 Å and 3.328 Å, respectively. The V–S and V–Se bond lengths were also obtained to 2.351 Å and 2.490 Å, respectively. Moreover, our estimated lattice parameters for the 1T VS_2 phase match very closely with those of the 2H phase reported by Jing *et. al* [273], α =3.17 Å and V–S bond length of 2.36 Å. Similar to graphene, 1T MX_2 structures also show two major directions of armchair and zigzag, as shown in Fig.(6.1).

Fig. (6.2) depicts the DFT predictions for the uniaxial stress-strain responses of 1T

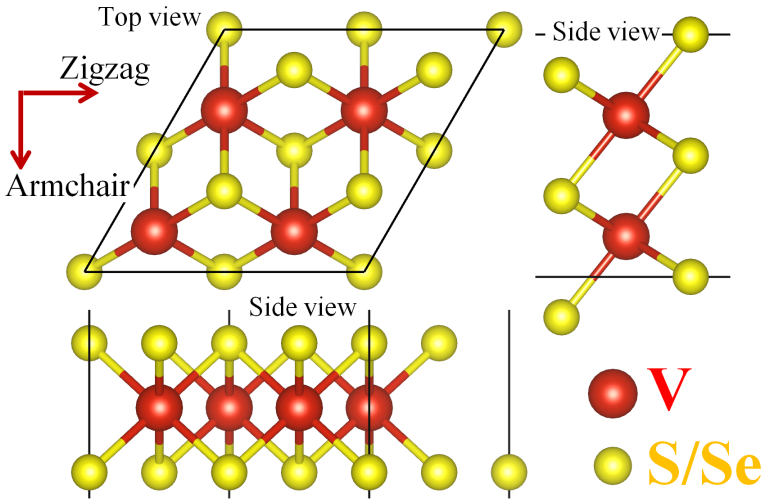

Figure 6.1: Top and side views of atomic configuration in single-layer 1T VS_2 and VSe_2.

VS_2 and VSe_2, in armchair and zigzag directions. In all cases, the stress-strain responses start with an initial linear relation followed by a nonlinear trend up to the ultimate tensile strength. The slope of the first initial linear section of the stress-strain curve is equal to the elastic modulus. As shown in the Fig. (6.2) , the initial linear responses are very close and independent from the loading direction. Therefore, in order to extract the elastic modulus, a line is fitted to the stress-strain response for the strain ratios below the 0.02. For the 1T VS_2 or VSe_2, the elastic modulus predicted as 88.5 N/m and 71 N/m, respectively. The Poisson's ratio was also estimated to be

0.16 and 0.18 for 1T VS_2 or VSe_2, respectively. On the other side, the non-linear part of the stress-strain curves are found to be distinctly different for armchair and zigzag loading in which along the zigzag direction the single-layer 1T VS_2 or VSe_2 are considerably stronger and more stretchable as compared with the armchair. Surprisingly, when the 1T VS_2 or VSe_2 are stretched along the zigzag they can yield their ultimate tensile strength at strain levels of 0.45 and 0.39, respectively. We remind that for the single-layer transition metal dichalcogenides with 2H atomic configuration their strain at tensile strength point were found to be mostly below 0.32 [241]. The strain at the ultimate tensile strength point for pristine graphene and hexagonal boron-nitride were also found to be $\sim$ 0.27 [160] and 0.3 [220], respectively. The most striking result is that, the stretchability of 1T VS_2 and VSe_2 are also considerably higher than other 2D carbon porous networks [281], and graphyne [219] structures, but are lower than Nitrogen-graphdiyne [147] and Boron-graphdiyne [150]. Overall, these results indicate that, both 1T VS_2 or VSe_2 show ultrahigh stretchability and considerable mechanical properties as well.

Let us now focus on the application of 1T VS_2 and VSe_2 as anode material for researchable batteries. The adatoms adsorption energy profiles over the anode material is the most important issue. We therefore first find the strongest binding sites and the corresponding adsorption energies of Li, Na, Mg, Ca and Al adatoms over the 1T VS_2 and VSe_2. The adsorption energy, E_{ad}, is defined by:

$$E_{ad} = E_{TM} - E_T - E_{Ma} \tag{6.1}$$

where E_T is the total energy of 1T VS_2 or VSe_2 pristine films, E_{TM} is the total energy of the system after metal atoms adsorption and E_{Ma} is the per atom lattice energy of the metal adatoms (Ma=Li, Na, Mg, or Al). For the 1T VS_2, the maximum adsorption energies for Li, Na, Mg, Ca and Al, were calculated to -1.58 eV, -1.5 eV, -0.17 eV, -1.89 eV and 0.2 eV, respectively. These preliminary results clearly indicate that 1T VS_2 cannot serve as an anode material for Al ions storage because the adsorption energy is positive. On the other hand, concerning the 1T VSe_2 structure, the maximum adsorption energies for Li, Na, Mg, Ca and Al, were calculated to be, -1.19 eV, -1.15 eV, -0.01 eV, -1.3 eV and 0.47 eV, respectively. As it is clear in the case of 1T VSe_2, this structure is not suitable for Mg and Al atoms storage since the adsorption energy is very close to zero or positive. Therefore, we subsequently consider Li, Na, Mg, Ca storage over the 1T VS_2 and neglect Mg and Al storage for the 1T VSe_2.
We found that the single adatom is the favourable adsorption place, on the top of the V atoms in which the adatoms form the strongest binding, and only in the case of Ca over the 1T VS_2 this adatom tends to adsorb on the top of the S atoms. Fig. (6.3) shows the differential charge density of the energy minimized structures of the most stable configurations of adatoms over 1T VS_2 and VSe_2 monolayers.

These results suggest that 1T VS_2 and VSe_2 surfaces strongly interact with considered alkali elements and accept electron charge densities from the adatoms. On the

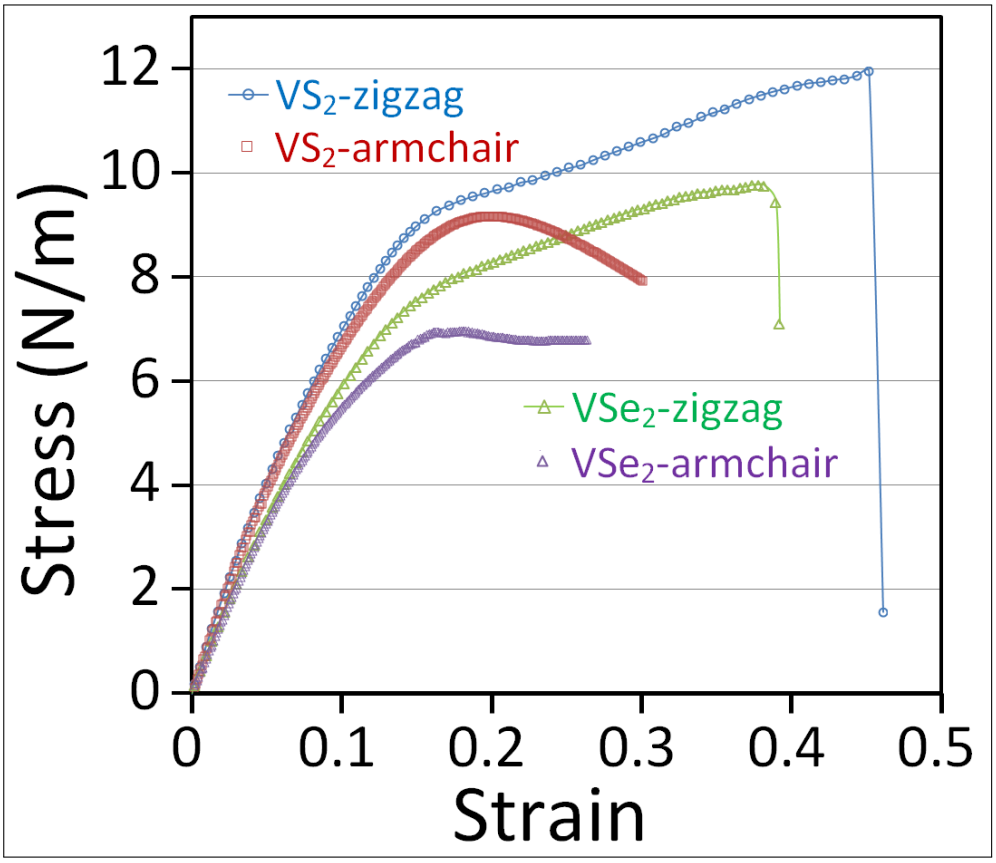

Figure 6.2: Uniaxial stress-strain responses of single-layer 1T VS_2 and VSe_2 stretched along the armchair and zigzag directions.

basis of Bader charge analysis for the single-layer 1T VS_2, from a single Li, Na, Mg and Ca adatoms, a charge transfers of 0.992 | e| , 0.992 | e| , 0.991 | e| and 1.436 | e| occurs, respectively. For the 1T VSe_2, the charge transfer values to the substrate were estimated to 0.998 | e| , 0.991 | e| and 1.398 | e| , for a single Li, Na and Ca adatom, respectively. Note that for the 2H VS_2 the charge transfer from a single Li adatom was predicted to be 0.36 | e| and 0.88 | e| by Jing *et al.* [273] and Samad *et al.* [282], respectively, which are distinctly lower than what we found for the 1T structure.
The adatoms coverage have now been increased by positioning the metal atoms uniformly on both sides of the 1T VS_2 and VSe_2 surfaces until all predicted adsorption sites were covered. Accordingly, the maximum coverage equal to 1.0 means that the system was fully covered by the adatoms (like Li_2VS_2). In order to evaluate the suitability of a material as an anode material for rechargeable batteries, the evolution of adsorption energy by increasing the adatoms coverage plays a critical role. The average

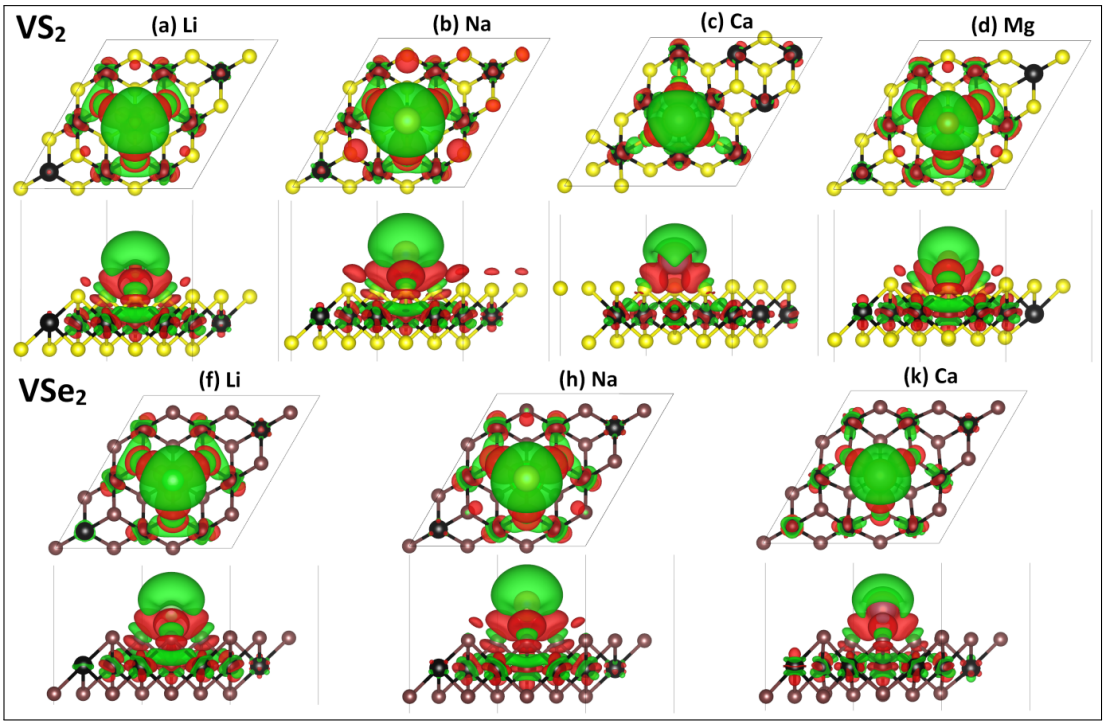

Figure 6.3: Top and side views of the most favourable adsorption sites for different adatoms over the 1T VS_2 (a-d) and VSe_2 (f-k) surfaces. Colour coding illustrate the binding charge transfer due to the adsorption of adatoms over the substrate, in which green shows the charge losses and red reveals the charge gains.

adsorption energy in this study was calculated using the following equation:

$$E_{av-ad} = \frac{(E_{TM} - n \times E_{Ma} - E_T)}{n} \tag{6.2}$$

where E_{TM} is the total energy of monolayers with *"n"* metal adatoms adsorbed on the surface. Fig. (6.4) illustrates the evolution of the average adsorption energy of adatoms over (a) 1T VS_2 and (b) VSe_2 as a function of the coverage. For the all considered cases, increasing the adatoms coverage decreases the absolute value of the adsorption energy. This observation is expected since by increasing the adatoms coverage the repulsive forces applied by the previous adsorbed atoms make the bindings of new coming metal atoms more difficult. In the case of 1T VS_2, it is obvious that due to the small content of Mg atoms the adsorption energy reaches a negligible value close to the zero, which confirms that neither the 1T VSe_2 nor the 1T VS_2 are suitable for the Mg ions storage. For the rest of studied cases, our results shown in Fig. (6.4) reveal that the average adsorption energy remains negative also for the fully covered sheets. The maximum changes in the adsorption energy occurs for Ca adatoms.

Another critical factor for the assessment of the performance of a material as an

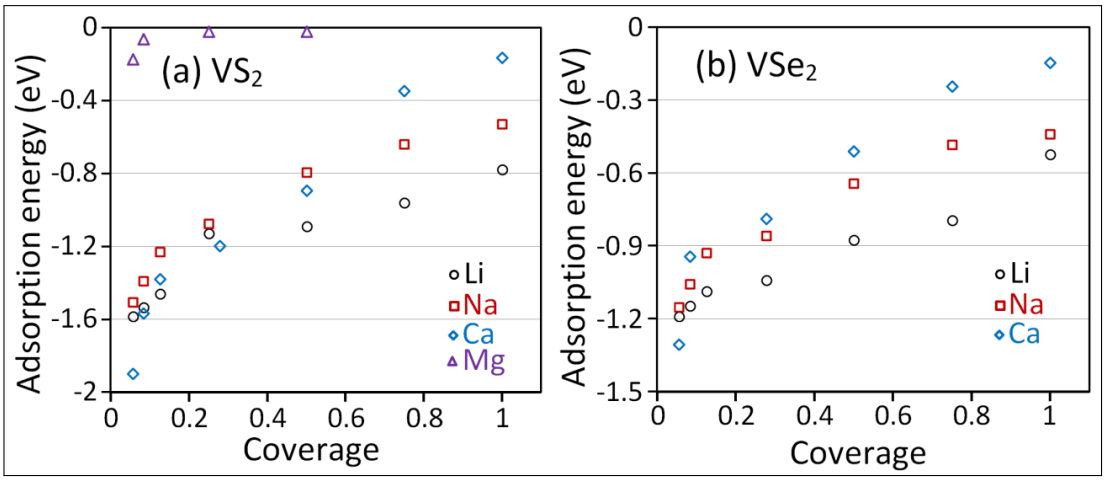

Figure 6.4: Evolution of average absorption energy as a function of adatoms coverage. Coverage equal to1 is equivalent with the system that all the most favourable adsorption sites are filled from the both sides of the 1T VS_2 and VSe_2

anode is the open-circuit voltage profile. The open-circuit voltage should be positive. However, to increase the cell output voltage, an anode material with a lower voltage range is preferable. Voltage values close to zero are also not desirable because this increases the probability of dendrite formation during the adatom intercalation in the anode, which may lead to thermal runaway and other serious damages to the battery. In this work, the average voltage in the coverage range of $x_1 \leq x \leq x_2$ can be estimated by the following equation [283, 284]:

$$V \approx \frac{\left(E_{TM_{x_1}} - E_{TM_{x_2}} + (x_2 - x_1)\, E_{Ma}\right)}{(x_2 - x_1)\,|e|} \tag{6.3}$$

where $E_{TM_{x_1}}$ and $E_{TM_{x_2}}$ are the total energies of the systems with x_1 and x_2 adsorbed metal adatoms, respectively. Fig. (6.5) shows the open circuit voltage profiles of the monolayer 1T VS_2 and VSe_2 as a function of the adatoms coverage. Note that the negative values of the voltage suggest that foreign adatoms prefer to form metallic clusters instead of adsorption to the electrode. For the Ca atoms storage using both considered nanosheets, after the coverage of 0.5 the voltage values drop below zero which means that the use of these nanosheets for the Ca atoms storage with coverage higher than 0.5 is not appropriate. On the other hand, the voltage profiles are positive and mostly below 1 V for the Li and Na adatoms which additionally confirms the suitability of 1T VS_2 or VSe_2 as an anode material for Li or Na-ion batteries. In the case of VSe_2, the voltage profiles are more desirable than VS_2 due to their lower values. At the same time, they are far enough from the zero voltage limit.

According to the obtained results for the adsorption energy and voltage profile, the

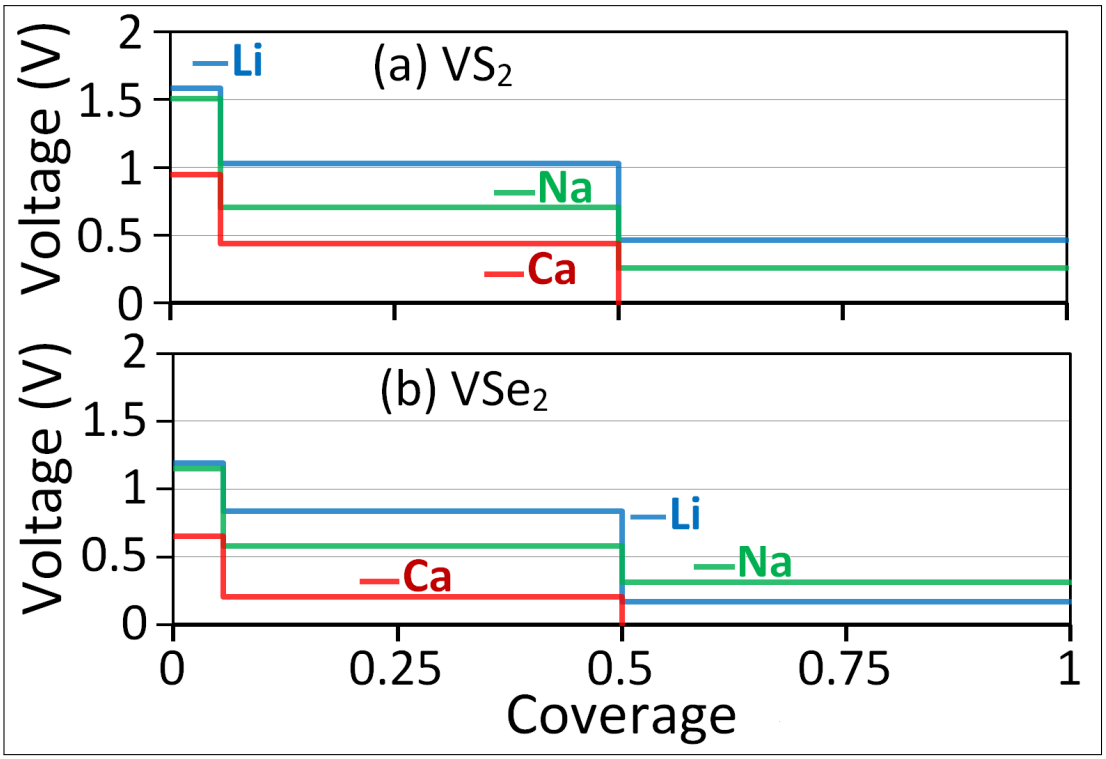

Figure 6.5: Open circuit voltage profiles as a function of adatoms coverage.

charge capacity of 1T VS_2 or VSe_2 for Li, Na and Ca ions storage can now be calculated. Bader charge analysis was employed to evaluate the charge transfer between the adatoms and the substrates. For the Li-ion storage, both 1T VS_2 and VSe_2 yield charge capacities of 466 mAh/g and 257 mAh/g, respectively. For the Na-ion storage, similar capacities of 466 mAh/g and 257 mAh/g were predicted for 1T VS_2 and VSe_2, respectively. For the Ca adatoms, charge capacities of 466 mAh/g and 257 mAh/g were predicted for 1T VS_2 and VSe_2, respectively. Note that the charge capacities of commercial graphite and TiO_2 structures for the Li ion storage were reported to be around 372 [285] and 200 mAh/g [286], respectively. Obviously, 1T VS_2 has a higher charge capacity than both graphite and TiO_2, which is appealing for future batteries.
Another important criteria for an anode material is the stability of the structure upon the adatom adsorption. In a rechargeable battery, during the service (charging/discharging) the ions coverage frequently increases or decreases. This frequent loading and unloading of the anode material may induce compositional or structural changes which might affect the efficiency and performance of the battery. Fig. (6.6) illustrates the energy minimized structures with the maximum capacity for Li, Na and Ca atoms. The studied 2D nanomembranes act very stably upon the adatoms coverage and no damages to the chemical bonds are observed. This observation is in agreement with our analysis of mechanical properties confirming a considerable stiffness of 1T VS_2 and VSe_2.

A high electronic conductivity is a desirable characteristic for both a cathode and

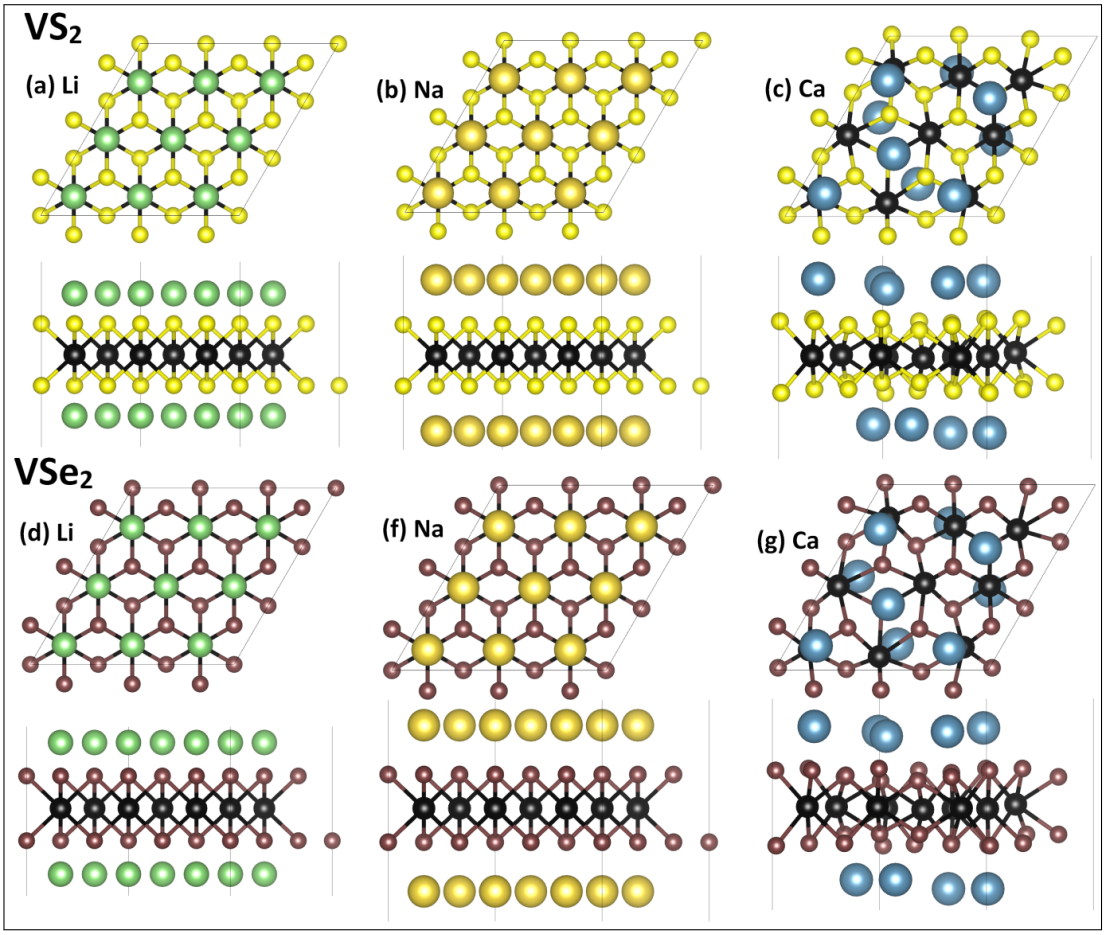

Figure 6.6: Top and side views of energy minimized 1T VS_2 and VSe_2 nanomembranes with the maximum capacity for Li, Na and Ca atoms.

anode material in batteries. To reach higher voltage outputs, the internal electronic resistances should be as low as possible which can be achieved through employing electrodes with higher electronic conductivity. Moreover, to decrease the risk of overheating and to suppress the joule heating, the electronic conductivity of electrode materials should be high. In this regard, 1T VS_2 and VSe_2 are very promising since they show an excellent electronic conductivity [271]. We analysed the electronic density of states (DOS) to probe the effects of adatom adsorption on the electronic response of 1T VS_2 and VSe_2. The DOS of all systems with various coverages of Li, Na and Ca adatoms were conducted. Fig. (6.7) confirms that in all cases, at the zero state energy (Fermi level) the DOS is not zero, which further verifies that the metallic electronic character is intact.

The usefulness of 1T VS_2 and VSe_2 with respect to the ionic conductivity was ex-

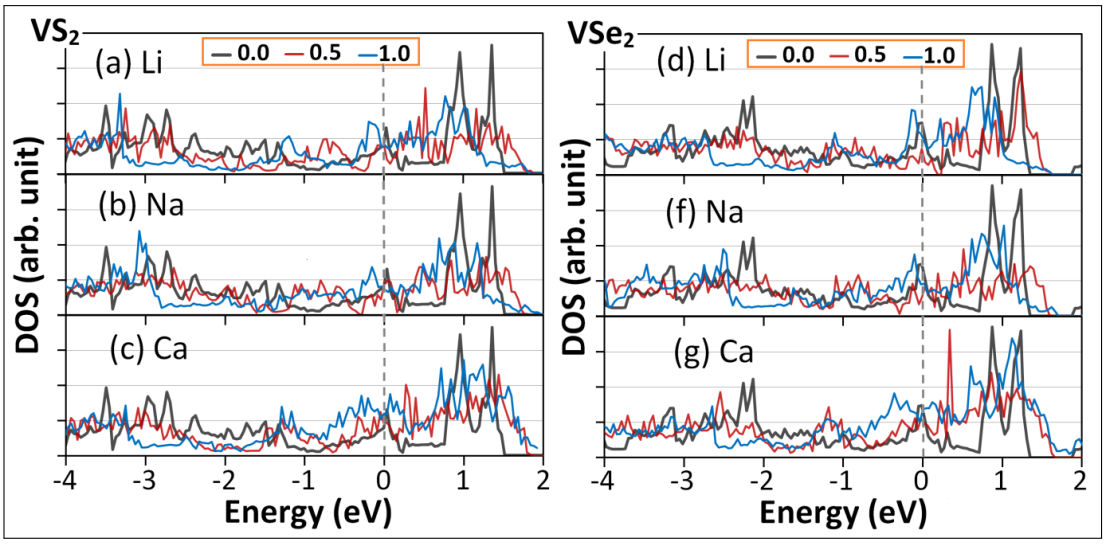

Figure 6.7: Calculated electronic density of states (DOS) for the 1T VS_2 and VSe_2 monolayers, with different coverages of adatoms (coverage of 0.0 is illustrative of the DOS for the pristine structure). The Fermi level is aligned to zero.

plored by calculating the single Li or Na adatom diffusion using the CNEB method and corresponding energy barriers. Fig. (6.8) depicts the predicted path for a single Li or Na adatom diffusion starting from the most stable adsorption site and ending on the neighbouring equivalent site predicted by the CNEB method for 1T VS_2 and VSe_2, respectively. Interestingly, for the all studied cases, the adatoms follow a zigzag path for the diffusion in which the middle point is on the top of the S or Se atoms. For the Na ion diffusion, the energy barriers over the 1T VS_2 and VSe_2 are slightly above 0.1 eV. For Li atoms, 1T VS_2 shows superior performance with a small energy barrier of 0.22 eV as compared with the barrier of 0.33 eV predicted for the 1T VSe_2. We note that the Li ion diffusion energy barrier on graphene is $\sim$ 0.37 eV [287] which is higher compared to the values we obtained for 1T VS_2 and VSe_2. For a battery system, according to the Arrhenius equation the diffusion rate of adatoms shows an exponential dependence on the energy barrier and therefore even a small difference in the energy barrier can lead to considerable changes in the diffusion rate. This clearly highlights the promising characteristics of 1T VS_2 as anode material for both Li and Na ions storage.

6.4 Conclusion

2D Vanadium dichalcogenides (VX_2) such as VS_2, VSe_2 with 1T atomic configurations have recently gained growing attention stemming from their outstanding optical,

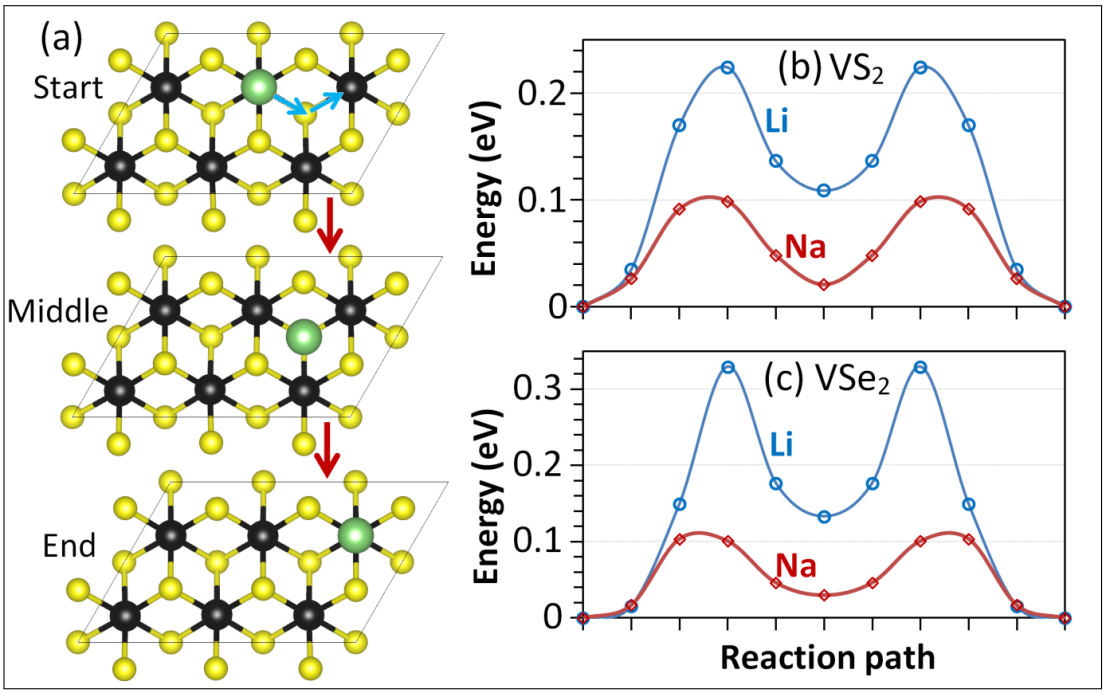

Figure 6.8: Nudged-elastic band results for the (a) diffusion path and corresponding energy barriers of Li and Na adatom hopping over single-layer1T (b) VS_2 and (c) VSe_2.

electrical and chemical properties. The main focus of the present investigation was to extensively explore the application of 1T VS_2 and VSe_2 as anode materials for Al, Mg, Ca, Na or Li-ion batteries. To this aim, we conducted first-principles density functional theory simulations.

To analyze the structural stiffness of 1T VS_2 and VSe_2, we first determined the mechanical properties by performing uniaxial tensile simulations. According to the acquired uniaxial stress-strain curves, the elastic modulus of 1T VS_2 and VSe_2 were predicted to be 88.5 N/m and 71 N/m, respectively. Despite of the isotropic elastic responses, the non-linear part of the stress-strain curves were found to be anisotropic, in which along the zigzag direction the single-layer 1T VS_2 and VSe_2 are considerably stronger and more stretchable as compared to the armchair direction. Notably, when 1T VS_2 or VSe_2 are stretched along the zigzag direction they can yield their ultimate tensile strength at strain levels of 0.45 and 0.39, respectively, which are distinctly higher compared to many other 2D materials. The ultimate tensile strength of 1T VS_2 and VSe_2 along the zigzag direction was predicted to be 12 N/m and 9.8 N/m, respectively.

We subsequently probed the potential application of 1T VS_2 and VSe_2 nanomembranes as anode materials for Li, Na, Ca, Mg and Al ion storage. We first predicted the strongest binding sites for the adatoms adsorption and then increased the coverage of metal atoms. Both 1T VS_2 and VSe_2 were found to be not suitable for Mg and Al atoms storage because of yielding very low or positive adsorption energy. The charge analysis results reveal that 1T VS_2 or VSe_2 surfaces strongly interact with single Li, Na or Ca adatoms and with high efficiency accept electron charge densities from these adatoms. Nevertheless, for Ca storage the open circuit voltage profiles become negative at coverage ratio higher than 0.5, which accordingly questions the suitability of 1T VS_2 and VSe_2 for this adatom storage.

For the 1T VS_2, the open circuit voltage profiles were predicted to be in ranges of $\sim$ 1.56 V to $\sim$ 0.46 V and $\sim$ 1.5 V to $\sim$ 0.37 V for Li and Na storages, respectively. For the 1T VSe_2, very similar open circuit voltage range of $\sim$ 1.15 V to $\sim$ 0.25 V was found for the both Li and Na atoms. According the Bader charge results, 1T VS_2 and 1T VSe_2, respectively, exhibit remarkable charge capacities of 466 mAh/g and 257 mAh/g for Li-, Ca- or Na-ion storages.

Based on the climbing image nudged elastic band results for 1T VS_2, low diffusion energy barriers of 0.22 eV and 0.1 eV were estimated for the Li and Na adatoms, respectively, promising to achieve fast charging/discharging. Our study highlights the promising prospect of highly conductive and ultrahigh stretchable 1T VS_2 for the application as an anode material for the design of advanced flexible Li or Na-ion rechargeable batteries.

Chapter 7

First-Principles Prediction of N-Triphenylene-Graphdiyne as a Remarkable Anode Material for Metal-Ions Storage

7.1 Introduction

Advanced energy storage systems are of major importance for industrial devices. Developing renewable power plants, increasing need for the electrified transport and mobile devices attract scientist to search for more efficient and reliable storage systems. Energy-storage devices must satisfy the demand for high energy density, safety, and low cost [26]. Indeed, rechargeable Lithium-ion batteries (LIB) are among the best available storage devices due to their high energy density and long life performance [27, 28]. The electrochemical reactions inside ordinary LIB lead to lithium ion insertion/extraction into/from electrodes during charging and discharging process. Batteries based on intercalation electrode materials play important roles in a wide range of portable electronic devices [29, 30, 31]. The performance of conventional metal-ion storage batteries depends on the energy/power density and transmission/diffusion rate of the ions on the electrode materials. Graphite belongs to the class of commercial anode electrodes, which is stable. Unfortunately, it has a low ion diffusion rate and charge capacity [33]. Key to success of improving the performances of metal-ion batteries are efficient alternative electrode materials, and packing them to build novel battery-cells with affordable prices.

During the last decades, extensive studies have been devoted exploring promising anode materials for rechargeable metal-ion batteries. Fabrication of two dimensional (2D) graphene (monolayer carbon allotrope) [103, 168, 169] with excellent mechani-

cal strength, high electric conductivity and heat conduction promoted the development of novel 2D materials. Such materials have gained highest interest for various applications [146]. For instance, graphene has been using in various applications, like nanoelectronics, mechanical components, thermal management systems, energy storage devices, drug, and many others. The great achievements of graphene have encouraged the search for other types of 2D structures. Despite of the high electric conductivity of the graphene, it has moderate charge capacities which is essential for applications such as energy storage devices [254, 259, 288]. To overcome this deficiency, extensive studies of novel 2D lattices with not only high electric conductivity but also high charge storage capacity have been emanated [254]. For instance, 2D carbon allotropes with covalently bonded sp and sp^2 carbon like graphdiyne [289, 290] nanosheets yield high storage capacities. Graphdiyne is a class of 2D carbon allotropes that has been experimentally synthesized through a cross-coupling reaction using hexaethynylbenzene [289]. These graphdiyne nanosheets show remarkable electrical conductivity, charge capacity, low thermal resistance, and high stretchability [147, 150, 291, 292, 293, 294]. Recent investigations confirmed graphdiyne nano-membranes as excellent materials for energy storage devices [295, 296, 297], electrochemical actuators [298], catalysts [299, 300] and water reduction [301].
A recent experimental study [302] confirmed the synthesis of a novel graphdiyne nanosheets, so called triphenylene graphdiyne (TpG), which was fabricated by the gas/liquid interfacial synthesis method. TpG exhibited polymeric nature with good thermal durability (up to 250 $^\circ$ C). Subsequently, in the recent computational studies [284, 303], the stability and properties of novel nitrogenated-TpG (N-TpG), phosphorated-TpG (P-TpG), and arsenicated-TpG (As-TpG) nanosheets were examined and confirmed. N-TpG nanosheets show the closest atomic structure as that of the pristine TpG lattice. The first-principles investigation also confirmed the high energetic stability and electric conductivity [284], which are always among the most desirable factors for the application as an anode or cathode material in batteries. In this work, we employed density functional theory (DFT) calculation to explore the application of N-TpG as an anode material for Na-, K-, Mg-, Ca-ion storages. We investigated the adsorption energy, open circuit voltage profiles, electronic density of states (DOS) and storage capacity.

7.2 Computational method

We conducted first-principles density functional theory (DFT) simulations by employing the Vienna ab-initio simulation package (VASP) [209, 210, 211]. Generalized gradient approximation (GGA) was used with exchange-correlation functional of Perdew-Burke-Ernzerhof (PBE) [197]. We used plane-wave basis set with an energy cut-off of 500 eV. The VESTA [213] package was used for the visualization of the atomic

lattice. Periodic boundary conditions in planar directions with a vacuum layer of 20 Å along the sheet thickness were imposed. Energy minimized structures were acquired by employing the conjugate gradient method with a convergence criterion of 10^{-4} eV and 0.01 eV/Å for the energy and the forces, respectively. A $3\times$ $3\times$ 1 Monkhorst-Pack [214] k-point mesh size was used for the finite number of points in the Brillouin zone (BZ). It was found that the employed $3\times$ $3\times$ 1 grid is not only computationally efficient but also yields accurate results for the adsorption energies as compared with finer k-point grids. For the simulation of gradual metal atoms intercalation, the adatoms were first added to the predicted most stable binding sites and then randomly positioned on the surface until the full capacity is reached [254, 259]. To more accuracy report the energy values, we conducted single point calculations using the tetrahedron method with Blöchl corrections and $5\times$ $5\times$ 1 Monkhorst k-point mesh size. Bader charge analysis [275] was then achieved to predict the final charge capacities.

7.3 Result and discussion

An energy-minimized N-TpG monolayer with hexagonal lattice is shown in the Fig. (7.1). Ionic/electronic relaxation and geometry optimization was derived using the DFT algorithm. The hexagonal lattice constant and average C-N bond lengths were measured to be 13.5 Å and 1.34 Å, respectively. Unit-cell optimization results indicate that the bond length variation between C-C bonds to be as $\sim$ 1.23-1.46 Å. As it shown in Fig. (7.1), to qualitatively investigate the nature of the chemical bonding in the studied structure, we also illustrated spatial-dependent electron localization function (ELF) [304] for pristine nanosheet. It takes values between 0 and 1, such that ELF equal to 0, 0.5, 1, indicates delocalized electron, electron gas-like behavior and completely localized electron regions, respectively. Electron localization intensity in the middle of the C-C bonds specify the covalent bonding features, but the electron localization of the C-N bonds is mostly around the N atoms due to the higher electronegativity of the N atoms in comparison with C atoms.

We focus on the application of N-TpG as anode material for researchable batteries. The adatoms adsorption energy profiles over the anode material is the most important issue. We first estimated the most stable adsorption sites. Our predicted strongest bonding sites, S1, S2, S3, are depicted in Fig. (7.2). These bonding sites satisfy the highest adsorption energy with minimum total energy conditions. S1 and S3 were placed inside the nanosheet plane hollow sites, while S2 was placed out-of-plane, on top of the hexagonal part. The corresponding adsorption energies of Na, K, Mg, and Ca ions over N-TpG were calculated using the following relation, in which adsorption energy (E_{Ads}) is defined by:

$$E_{Ads} = E_S - E_P - E_{At} \tag{7.1}$$

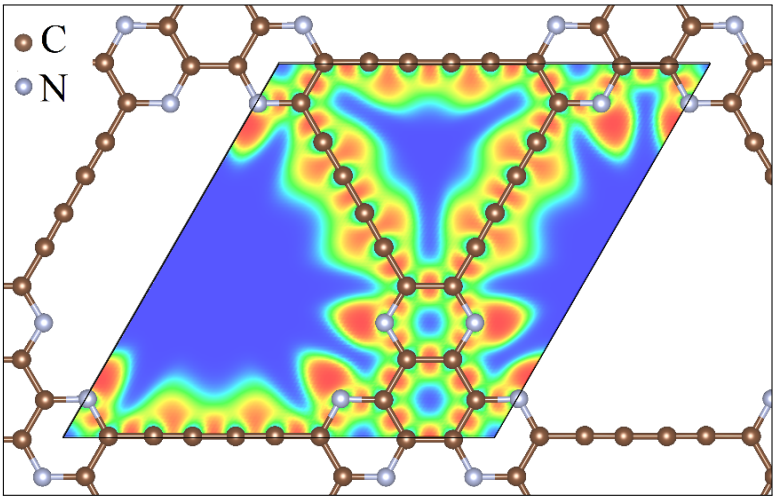

Figure 7.1: Atomic structure of N-TpG monolayer. Contours illustrate the electron localization function within the unit-cell.

where E_P is the total energy of the pristine N-TpG nanosheet, E_S is the total energy of the system after metal atoms adsorption and E_{At} is the per atom lattice energy of the metal adatoms (At =Na, K, Mg, Ca). The S1 site exhibits the maximum adsorption energies for Na, K, Mg, and Ca adatoms as -2.62 eV, -3.08 eV, -0.81 eV, and -2.48 eV, respectively. Stable binding sites are reported in detail in Table (7.1). The desired adsorption energy for the anode materials in batteries should not very close to zero or be positive value. According to the Table (7.1), except the Mg adatom in the S2 and S3 adsorption sites with the positives value of 0.92 eV and 0.73 eV respectively, the other cases have the negative adsorption energy values which indicates accpetable bonding between considered adatoms and N-TpG nanosheets. These preliminary results clearly indicate that the considered configurations for the Mg atom storage in the S2 and S3 sites, and Ca atom storage in the S2 site, are not suitable since the adsorption energies are very close to zero or positive. Generally, the highest adsorption energies were found in the S1 site. Bader charge exchange analysis for these configurations illustrates the ionization process of a single adatom over the substrate material. According to the results represented in Table (7.1), Na, K and Ca adatom were fully ionized.

Evaluation of adsorption energy by increasing adatoms coverage plays a critical role in the assessment of a material suitability as an anode. The average adsorption energy was calculated by:

$$\overline{E}_{Ads} = \frac{(E_{SM} - E_P - n \times E_{At})}{n} \tag{7.2}$$

where E_{SM} is the total energy of system with n metal adatoms adsorbed on the surface. In this study, in order to simulate the intercalation of metal ions over the N-TpG anode, we gradually and uniformly increased the coverage of metal adatoms. To this aim, metal adatoms were fist positioned at the strongest binding sites, predicted earlier.

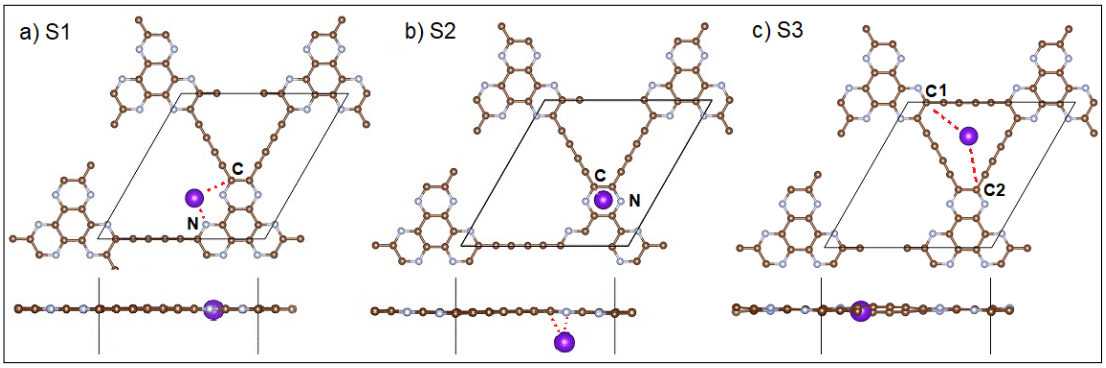

Figure 7.2: Most stable adsorption sites for Na, K, Mg and Ca atoms over N-TpG.

Table 7.1: Predicted most stable adsorption sites for the single Na, K, Mg and Ca adatoms over the single-layer N-TpG. Here, E_{Ads}, $L_{x\text{-}y}$, L_Z and ΔQ depict, respectively, the corresponding adsorption energy, distance between the x and y atoms, the out-of-plane movement of an adatom at the adsorption sites (shown in Fig.(7.2b)), and the charge transfer from a single adatom to the N-TpG monolayer according to the Bader charge analysis.

AdsSites	*Na*	*K*	*Mg*	*Ca*
	$E_{Ads} = -2.63eV$	$E_{Ads} = -3.09eV$	$E_{Ads} = -0.81eV$	$E_{Ads} = -2.48eV$
	$L_{N-Na} = 2.317Å$	$L_{N-K} = 2.735Å$	$L_{N-Mg} = 2.030Å$	$L_{N-Ca} = 2.243Å$
*S*1	$L_{C-Na} = 3.306Å$	$L_{C-K} = 3.569Å$	$L_{C-Mg} = 3.114Å$	$L_{C-Ca} = 3.225Å$
	$L_Z = 0.084Å$	$L_Z = 0Å$	$L_Z = 0Å$	$L_Z = 0Å$
	$\Delta Q = 0.99\|e\|$	$\Delta Q = 0.90\|e\|$	$\Delta Q = 1.63\|e\|$	$\Delta Q = 1.55\|e\|$
	$E_{Ads} = -1.28eV$	$E_{Ads} = -1.99eV$	$E_{Ads} = 0.92eV$	$E_{Ads} = -0.69eV$
	$L_{N-Na} = 2.629Å$	$L_{N-K} = 2.993Å$	$L_{N-Mg} = 3.920Å$	$L_{N-Ca} = 2.336Å$
*S*2	$L_{C-Na} = 2.631Å$	$L_{C-K} = 2.951Å$	$L_{C-Mg} = 3.970Å$	$L_{C-Ca} = 2.481Å$
	$L_Z = 2.180Å$	$L_Z = 2.539Å$	$L_Z = 3.541Å$	$L_Z = 2.041Å$
	$\Delta Q = 0.99\|e\|$	$\Delta Q = 0.92\|e\|$	$\Delta Q = 0.09\|e\|$	$\Delta Q = 1.42\|e\|$
	$EAds = -2.18eV$	$EAds = -2.78eV$	$EAds = 0.73eV$	$EAds = -1.94eV$
	$L_{C1-Na} = 4.349Å$	$L_{C1-K} = 4.411Å$	$L_{C1-Mg} = 6.530Å$	$L_{C1-Ca} = 4.332Å$
*S*3	$L_{C2-Na} = 4.351Å$	$L_{C2-K} = 4.338Å$	$L_{C2-Mg} = 2.888Å$	$L_{C2-Ca} = 4.284Å$
	$L_Z = 0.139Å$	$L_Z = 0.766Å$	$L_Z = 2.234Å$	$L_Z = 0.046Å$
	$\Delta Q = 1.00\|e\|$	$\Delta Q = 0.88\|e\|$	$\Delta Q = 1.24\|e\|$	$\Delta Q = 1.57\|e\|$

After filling all the strongest adsorption sites, the additional adatoms were uniformly located on the both sides of the nanosheet surface and mostly over the 4 membered carbon atom linkers. Worthy to note that there exist numerous possibilities for positioning the adatoms over the N-TpG. To count for this statistical issue, in this work for every coverage, three different structures were constructed and after the energy minimization, the results for the system with lowest energy was chosen for the average adsorption energy calculation. Fig. (7.3) illustrates the evolution of the average adsorption energy of different adatoms over N-TpG as a function of the storage capacity. According to our analysis the adsorptions of adatoms over the N-TpG do not lead to the formation of chemical bonds. Based on the results shown in Fig. (7.3), at the initial stages of the storage by increasing the adatoms content the adsorption energy decreases sharply and later declines smoothly. This observation reveals that for the high coverages of metal atoms over the N-TpG, the nature of interactions between the adatoms and N-TpG becomes weaker and approaches the very weak bonding, so called the physisorption [305]. The storage capacity is related to the number of adsorbed ions by the Faraday equation;

$$S_c = \frac{n.V_e.F}{m_a} \tag{7.3}$$

where n is the number of adatoms over nanosheet, V_e denotes the number of valance electrons of adsorbed metal atom, F is the Faraday constant and m_a designates the atomic mass of the N-TpG unit-cell. We considered n equal to 4, 7, 10,18, 22, 26, and 30 for the considered adatoms. For all those cases, an increasing adatoms coverage yields a decrease in the absolute value of the adsorption energy. This observation is expected since the high adatom coverage produces repulsive forces for the new coming atoms and makes the adsorbing more difficult. As Fig. (7.3) indicates, for the small contents of the Mg atoms, the adsorption energy reaches unsuitable positive values or values close to zero while for the fully covered sheet by Na and Ca adatoms remains negative and far enough from zero. The maximum changes in the average adsorption energy occurs for the case of K adatom, in which the adsorption energy stays negative but very close to zero after coverage of certain amount of adatoms.

Another important factor for the assessment of the performance of a material as an anode is the open-circuit voltage profile. The negative values of the voltage suggest that foreign adatoms prefer to form metallic clusters instead of adsorbing to the electrode. Thus, the open-circuit voltage should be positive. However, to increase the battery cell output voltage, a lower voltage profile for an anode is more desirable. The voltage values that are very close to zero, are also not suitable because of the risks of dendrite formation during the intercalation process, which may lead to thermal runaways and other serious damages to the battery. In this work, the average voltage in the coverage

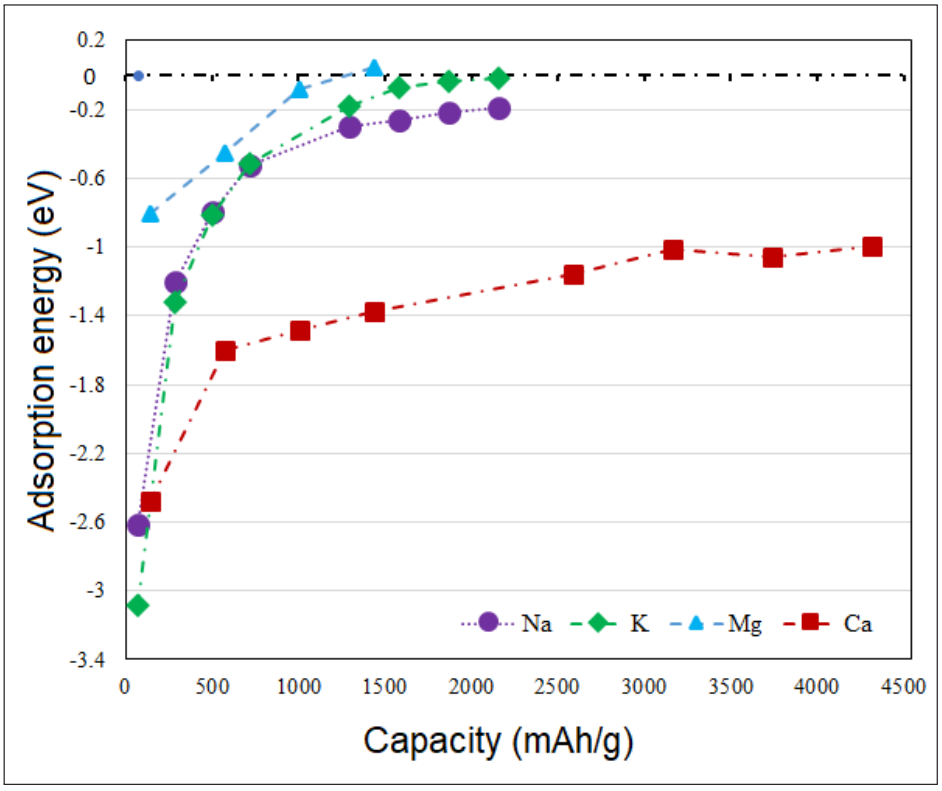

Figure 7.3: Evolution of average adsorption energy as a function of storage capacity over N-TpG.

ranging from $x_1 \leq x \leq x_2$ can be estimated by the following equation [283]:

$$V \cong \frac{\left(E_{SM_{x_1}} - E_{SM_{x_2}} + (x_2 - x_1)\, E_{At}\right)}{(x_2 - x_1)\,|e|} \tag{7.4}$$

$E_{SM_{x_1}}$ and $E_{SM_{x_2}}$ denoting the total energies of the systems with x_1 and x_2 adsorbed metal ions, respectively. Fig. (7.4) shows the open circuit voltage profiles of the monolayer N-TpG as a function of the storage capacity. The maximum coverage of 10, 26, for Mg, K, and 30 for Na, Ca atoms, respectively, can be stored over N-TpG. Hence, it can be concluded that the N-TpG can exhibit ultrahigh capacities of 1439 mAh g^{-1}, 1871 mAh g^{-1}, 2159 mAh g^{-1}, and 4319 mAh g^{-1}, respectively. Makaremi et al. [306], most recently predicted that for the Na-ion batteries, different N-graphdiyne structures, can show high storage capacities in a range of 623-934 mAh/g. According to our results N-TpG can exhibit a considerably higher storage capacity than N-graphdiyne nanosheets for the Na-ion storage. Note that the charge capacities of commercial graphite [285], TiO_2 [286], and VS_2/VSe_2 [130] structures for the Li ion storage were reported to be 372 mAh g^{-1}, 200 mAhg^{-1}, and 466 mAh g^{-1} respectively.

Obviously, the N-TpG has a higher charge capacity compared with commercial anode materials. As it is clear from the voltage profiles, after the first ion adsorption the voltage values drop immediately under the value of about 0.3 V, which indicate the desirable performance for the increase of the cell output voltage.

In charging and discharging processes of the rechargeable batteries, the ions coverage

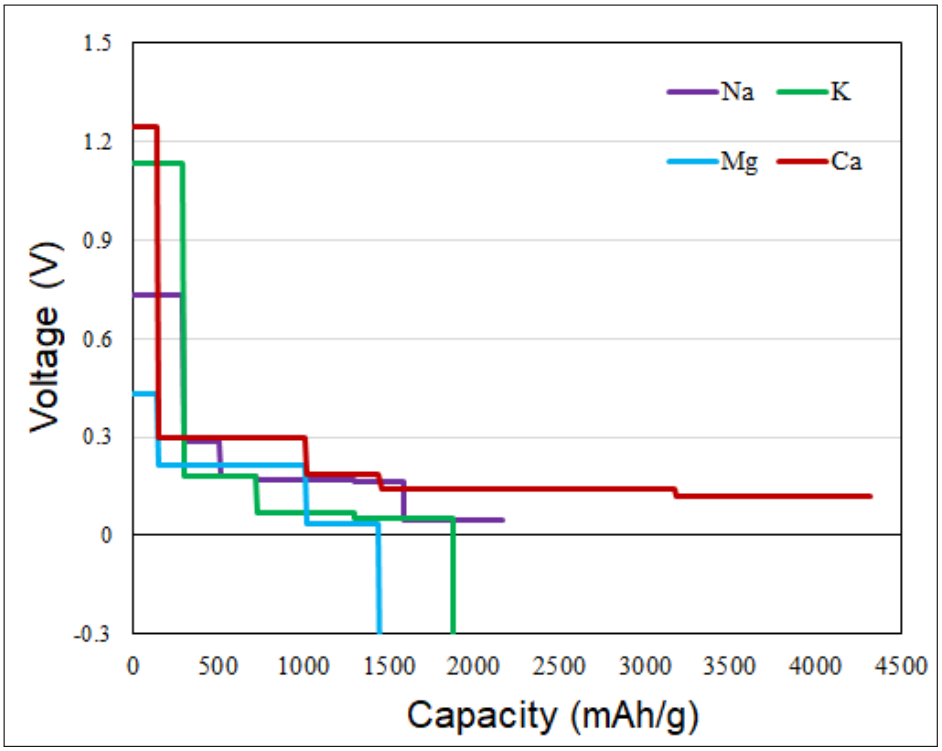

Figure 7.4: Open circuit voltage profiles as a function of adatoms coverage.

frequently increases or decreases. This frequent loading and unloading of the anode material may induce compositional or structural changes, which may accordingly affect the efficiency and performance of the battery. Another decisive criterion for the application of a material as an anode is the stability of structure after the ions adsorption. Fig. (7.5) illustrates the energy minimized structures with the maximum capacity for Na, K, Mg and Ca atoms. N-TpG acts very stably for various ions coverage and exhibits no sign of damage. It is also worthy to note that according to the ab-initio molecular dynamics calculations [284], N-TpG nanosheets can stay intact at the high temperature of 2000 K, which is certainly higher than the working temperatures of the batteries.

Metallic electronic characteristics are highly desirable for electrode materials in batteries, in order to reach internal electronic resistances. Metal atoms generally have low ionization energy and low electronegativity, so over anode material they tend to lose electrons. Therefore, we conducted total electronic density of states (DOS) calcula-

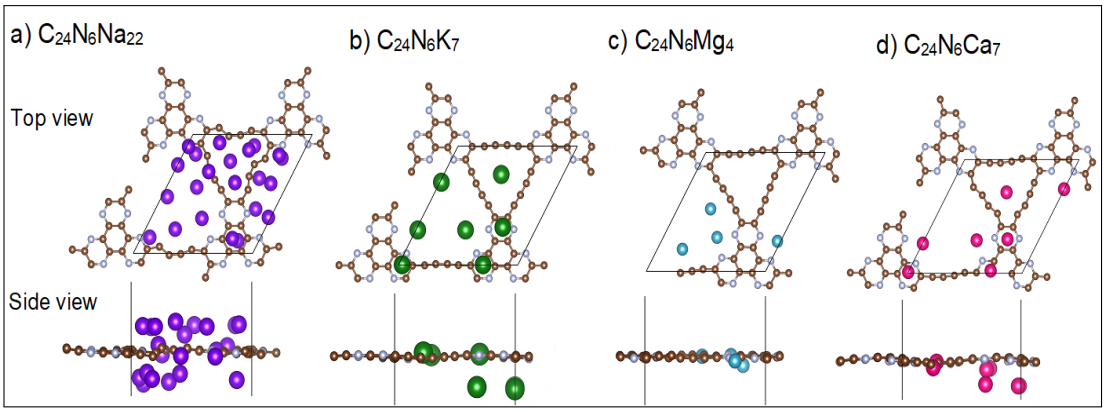

Figure 7.5: Top and side views of the most stable/energy-minimized monolayer N-TpG with content of adatoms.

tions for all the configurations with three table coverage level of 10, 22, and 30 atoms over the N-TpG for each of Na, K, Mg and Ca adatoms. In Fig. (7.6), we confirmed that at the zero-state energy (Fermi level) the DOS is not zero verifying the metallic electronic behaviour for the composite structures.

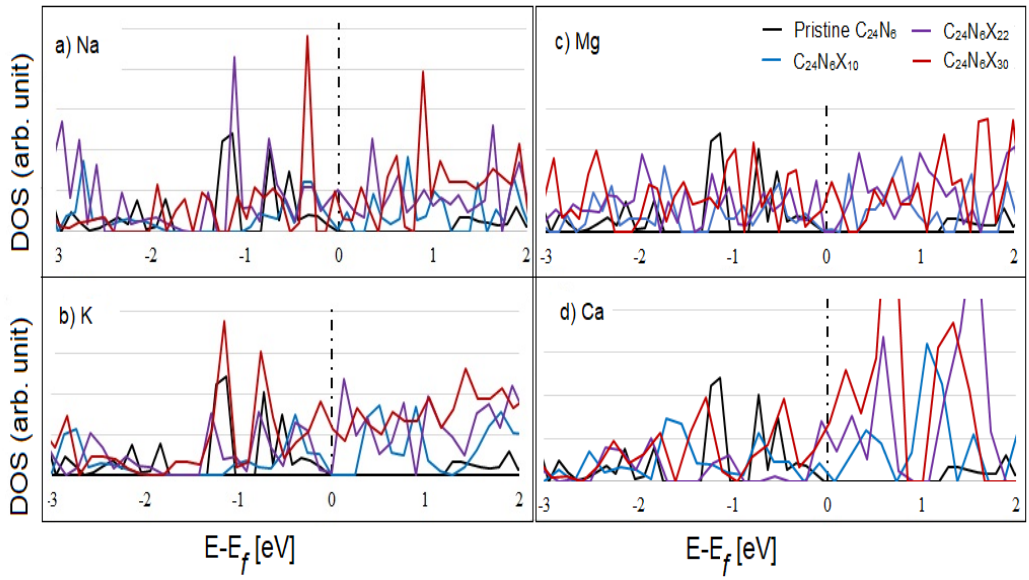

Figure 7.6: Electronic density of states (DOS) for different pristine N-TpG nanosheet and the monolayer interacting with various coverages of X = Na, K, Mg, and Ca adatoms. The dashed line represents the Fermi level and is aligned to zero.

7.4 Conclusion

We studied the potential application of N-triphenylene-graphdiyne (N-TpG) nanosheets as anode electrodes for Na, K, Mg, and Ca storages. Our results reveal that N-TpG nanosheets can yield ultrahigh capacities of 1439 mAh g^{-1}, 1871 mAh g^{-1}, 2159 mAh g^{-1}, and 4319 mAh g^{-1}, for Mg-, K-, Na-, and Ca-ion storage, respectively. Predicted open circuit voltage profiles reveal promising performance of N-TpG nanosheets, in which the voltage profiles are positive and mostly below the 0.3 V after adsorption of single adatom. The insight provided by the first-principles results highlight the outstanding prospect of the N-TpG nanosheet as an anode material to design advanced energy storage systems with superior charge capacity.

Chapter 8

Concluding Remarks and Future Prospects

8.1 Summary of achievements

This dissertation is devoted to computational multi-scale modeling of mechanical and electrochemical properties of 1D and 2D nanomaterials. The employed theories and methods are valid in specific scales from angstrom to macro scales. This work is based on the ongoing multi-scale research trend as well as the current development challenges of the novel battery energy storage systems. The results of present dissertation were verified and validated with previous simulations and experimental outcomes.
The macro-scale physics defines by the continuum field theories such as the theory of elasticity or plasticity, where the governing equations are in the field of continuum mechanics. The governing equations of the piezoelectric continuum element and discretization are represented employing FEM. A new modeling approach was presented to simulate the intrinsic discrete nature of the atomistic structure as a piezoelectric beam element.
Molecular mechanics or force field methods rely on classical mechanics and are an important part of computational material science. The molecular mechanics' methods have been used to obtain quantitative information about the chemical reaction of the large molecules. In order to capture the physical phenomena at the atomistic scale, bonded and non-bonded interactions are accounted for in the piezoelectric beam element. The accuracy of the proposed method was evaluated by performing several simulations. The elastic properties and piezoelectric coefficients of the isolated zigzag BNNT were identified with respect to the nanotube chirality, diameter, and aspect ratio. We were able to match the predicted values of other, more complex models or experiments. The model seems to be particularly useful in large scale simulations,

which will be studied in the future.
MD is a mechanics-based computer simulation method. MD plays a significant role in treating a large number of particle systems within an affordable computational framework. The extensive MD simulations were conducted to explore the mechanical properties and failure mechanism of h-BN nanosheets. The pristine h-BN at room temperature exhibits remarkable strain at failure of 0.38 and the ultimate tensile stress of 170 GPa. To provide a comprehensive vision concerning mechanical aspects of h-BN nanosheets, we modeled most critical types of defects in engineering materials, cracks, notches, and point vacancies with various sizes and concentrations under the different loading temperatures. At 300 K, ultimate tensile stresses of 95, 89 GPa, and 130 GP at corresponding strain levels of 0.18, 0.17, and 0.35 were estimated for the systems with the largest crack, notch, and Sone-Wales defects, respectively. MD simulations showed that the maximum tensile stress/strain decreased due to the increase of defect size and temperature.
Consequently, our results demonstrate that h-BN nanosheet, even with large crack and notch, could exhibit a remarkably high elastic modulus of 480 and 475 GPa at 300 K, respectively. However, Stone-Wales defects yield the most serious elastic modulus reduction in comparison to crack or notch. Our MD results reveal outstanding mechanical properties of h-BN nanosheets with and without defects, which are attractive for the designing of nanodevices with h-BN as a building block.
Solid-state systems typically have a large number of interacting particles, and their solution needs to be treated and optimized computationally. The DFT methods are based on Hohenberg-Kohn-Sham theorems providing a computationally applicable and precise approach to deal with the many-body systems. We conducted first-principles spin-polarized DFT calculations to predict the mechanical response and stability of defect-free single-layer RuCl3 and RuBr3. We first investigated the stability of the considered structure by calculating the phonon dispersions. The phonon frequencies results indicate no negative frequency inside the Brillouin zone, confirming the dynamic stability of both nanosheets. For RuCl3 and RuBr3, the elastic properties were found to be isotropic, and the elastic modulus was computed 25 and 17 GPa.nm, respectively. Our DFT results reveal further that the tensile strain responses of these 2D systems are not isotropic, and along the zigzag direction, they are slightly more durable than the armchair direction. The maximum strain at tensile strength along with the armchair and zigzag directions were 0.75 and 0.68 for bromide compounds, and 0.48 and 0.44 for chloride compounds, confirming their super-stretchability. Our results may be useful for the design of highly stretchable and flexible nanodevices using RuCl3 and RuBr3 as 2D components.
We conducted extensive first-principles DFT calculations to explore the mechanical and electronic responses of pristine and single-layer HfS2, HfSe2, ZrS2, and ZrSe2 monolayers. We first investigated the mechanical responses of these 2D structures by conducting the uniaxial tensile simulations. It was found that the charge transfers from

the transition metal to chalcogen atoms correlate directly to elastic modulus and tensile strength. Our DFT results reveal that the mechanical responses of these 2D systems are not isotropic, along the armchair direction of the single-layer HfS2, HfSe2, ZrS2, and ZrSe2, are considerably stronger as compared with the zigzag. It was found that during the stretching along with the armchair, the deformation evolves more by the bond elongation, which explains the higher stress values at any specific strain value as compared with the loading along the zigzag. According to the G0W0 method estimations, indirect band-gaps of 1.90, 1.70, 1.65, and 1.30 eV were predicted for unstrained single-layer HfS2, HfSe2, ZrS2, and ZrSe2, respectively. Based on the PBE, HSE06, and G0W0 methods predictions, it was found that the band-gap decreases through applying the biaxial or uniaxial tensile loading, which notably confirms the tunability of electronic properties of these 2D structures. It was found that biaxial strains can be employed as a more effective approach for tuning the electronic response of HfS2, HfSe2, ZrS2, and ZrSe2.

Rechargeable metal-ion batteries play a crucial role in modern transport, communication, and electronic industries. Ordinary batteries are commonly based on Li-ion transfer and diffusion. Their superior energy density, capacity, and lifetime highlight them as the main power supply for various portable electronic devices. As an emerging class of 2D materials, transition metal dichalcogenides (TMD) exhibit unique photoelectronic, thermal, and mechanical properties. The main focus of the present investigation was to extensively, explore the application of 1T VS2 and VSe2 as anode materials for Al, Mg, Ca, Na or Li-ion batteries. To this aim, we conducted first-principles density functional theory simulations.

To analyse the structural stiffness of 1T VS2 and VSe2, we first determined the mechanical properties by performing uniaxial tensile simulations. According to the acquired uniaxial stress-strain curves, the elastic modulus of 1T VS2 and VSe2 were predicted to be 88.5 N/m and 71 N/m. The ultimate tensile strength of 1T VS2 and VSe2 along the zigzag direction was predicted to be 12 N/m and 9.8 N/m. The open-circuit voltage profiles for the 1T VS2, the open circuit voltage profiles were predicted to be in ranges of 1.56 V to 0.46 V and 1.5 V to 0.37 V for Li and Na storages, respectively. For the 1T VSe2, a very similar open-circuit voltage range of 1.15 V to 0.25 V was found for both Li and Na atoms. According to the Bader charge results, 1T VS2 and 1T VSe2 exhibit remarkable charge capacities of 466 mAh/g and 257 mAh/g for Li-, Ca- or Na-ion storages. Based on the climbing image nudged elastic band results for 1T VS2, low diffusion energy barriers of 0.22 eV and 0.1 eV were estimated for the Li and Na adatoms, respectively, promising to achieve fast charging/discharging. Our study highlights the promising prospect of highly conductive and ultrahigh stretchable 1T VS2 for the application as an anode material for the design of advanced flexible Li or Na-ion rechargeable batteries.

Advanced energy storage systems are of significant importance for industrial devices. Developing renewable power plants and increasing the need for electrified transport

and mobile devices attract scientists to search for more efficient and reliable storage systems. Energy-storage devices must satisfy the demand for high energy density, safety, and low cost. A recent experimental study confirmed the synthesis of a novel graphdiyne nanosheets, so-called triphenylene graphdiyne (TpG), fabricated by the gas/liquid interfacial synthesis method. TpG exhibited polymeric nature with excellent thermal durability (up to 250 °C). Subsequently, in the recent computational studies, the stability and properties of novel nitrogenated-TpG (N-TpG), phosphorated-TpG (P-TpG), and arsenicated-TpG (As-TpG) nanosheets were examined and confirmed. We studied the potential application of N-triphenylene-graphdiyne (N-TpG) nanosheets as anode electrodes for Na, K, Mg, and Ca storages. Our results reveal that N-TpG nanosheets can yield ultra-high capacities of 1439 mAh g-1, 1871 mAh g-1, 2159 mAh g-1, and 4319 mAh g-1, for Mg-, K-, Na-, and Ca-ion storage, respectively. Predicted open-circuit voltage profiles reveal the promising performance of N-TpG nanosheets, in which the voltage profiles are positive and mostly below the 0.3 V after adsorption of single adatom. The insight provided by the first-principles results highlight the outstanding prospect of the N-TpG nanosheet as an anode material to design advanced energy storage systems with superior charge capacity.

8.2 Future research prospects

The present thesis established a methodology in various scales to investigate the mechanical and electrochemical properties of the 1D and 2D nanomaterials and evaluate the performance of novel 2D nanomaterials as electrodes for the battery energy storage systems.
A few possible extensions to the current work can be suggested as follows:

- We have presented a new approach to model the intrinsic discrete nature of the atomistic structure by using a piezoelectric beam element. We were able to match the predicted values of other, more complex models or experiments. The model seems to be particularly useful in large scale simulations, which will be studied in the future.

- The comprehensive insight provided concerning the intrinsic properties and failure mechanisms of the 2D nanomaterials those that will be used for the possible design of novel applications in future nanodevices.

- Contributing the developed methodology towards the design of micro and nanoscale battery energy storage with novel electrode materials to enhance the storage capacity and charging/discharging rates.

- Our study highlights the promising prospect of highly conductive and ultrahigh stretchable transition 2D metal-dichalcogenides for the application as an anode material for the design of advanced flexible rechargeable batteries. The metal-organic framework (MOF) will be investigated to use as electrode material for the battery energy storage system.
- Next-generation batteries will take advantage of quantum features, which will be investigated in future research.

References

[1] Jacob Fish. *Multiscale Methods: Bridging the Scales in Science and Engineering*, volume 9780199233. Oxford University Press, oct 2009. 3

[2] Bastien Chopard, Jean-Luc Falcone, Pierre Kunzli, Lourens Veen, and Alfons Hoekstra. Multiscale modeling: recent progress and open questions. *Multiscale Multidiscip. Model. Exp. Des.*, 1(1):57–68, 2018. 3

[3] Alfons Hoekstra, Bastien Chopard, and Peter Coveney. Multiscale modelling and simulation: A position paper. *Philos. Trans. R. Soc. A Math. Phys. Eng. Sci.*, 372(2021):20130377–20130377, jun 2014. 3

[4] Sergey Karabasov, Dmitry Nerukh, Alfons Hoekstra, Bastien Chopard, and Peter V. Coveney. Multiscale modelling: Approaches and challenges, aug 2014. 3

[5] Ellad B Tadmor, Ronald E Miller, and Day Monday. *Schedule for Modeling Materials : Continuum , Atomistic and Multiscale Techniques*. Number Part II. Cambridge University Press, 2014. 3

[6] Jonathan D. Halverson, Thomas Brandes, Olaf Lenz, Axel Arnold, Staš Bevc, Vitaliy Starchenko, Kurt Kremer, Torsten Stuehn, and Dirk Reith. ESPResSo++: A modern multiscale simulation package for soft matter systems. *Comput. Phys. Commun.*, 184(4):1129–1149, apr 2013. 3

[7] Robert A. Gatenby. The physical microenvironment in somatic evolution of cancer. *Multiscale Cancer Model.*, 13(1):135–152, aug 2010. 3

[8] Peter M.A. Sloot and Alfons G. Hoekstra. Multi-scale modelling in computational biomedicine. *Brief. Bioinform.*, 11(1):142–152, jan 2010. 3

[9] Hossein Talebi, Mohammad Silani, Stéphane P.A. Bordas, Pierre Kerfriden, and Timon Rabczuk. A computational library for multiscale modeling of material failure. *Comput. Mech.*, 53(5):1047–1071, may 2014. 3, 20

[10] J. Llorca, C. González, J. M. Molina-Aldareguía, J. Segurado, R. Seltzer, F. Sket, M. Rodríguez, S. Sádaba, R. Muñoz, and L. P. Canal. Multiscale modeling of composite materials: A roadmap towards virtual testing. *Adv. Mater.*, 23(44):5130–5147, nov 2011. 3

[11] F. Roters, P. Eisenlohr, L. Hantcherli, D. D. Tjahjanto, T. R. Bieler, and D. Raabe. Overview of constitutive laws, kinematics, homogenization and multiscale methods in crystal plasticity finite-element modeling: Theory, experiments, applications. *Acta Mater.*, 58(4):1152–1211, feb 2010. 3

REFERENCES

[12] Raimond L. Winslow, Natalia Trayanova, Donald Geman, and Michael I. Miller. Computational medicine: Translating models to clinical care. *Sci. Transl. Med.*, 4(158):158rv11–158rv11, oct 2012. 3

[13] Brian A. Kidd, Lauren A. Peters, Eric E. Schadt, and Joel T. Dudley. Unifying immunology with informatics and multiscale biology. *Nat. Immunol.*, 15(2):118–127, feb 2014. 3

[14] Arnulf Latz and Jochen Zausch. Multiscale modeling of lithium ion batteries: Thermal aspects. *Beilstein J. Nanotechnol.*, 6(1):987–1007, apr 2015. 3

[15] J. S. Famiglietti and E. F. Wood. Multiscale modeling of spatially variable water and energy balance processes. *Water Resour. Res.*, 30(11):3061–3078, nov 1994. 3

[16] Binghe Liu, Xu Wang, Hao-Sen Chen, Sen Chen, Hongxin Yang, Jun Xu, Hanqing Jiang, and Dai-Ning Fang. A Simultaneous Multiscale and Multiphysics Model and Numerical Implementation of a Core-Shell Model for Lithium-Ion Full-Cell Batteries. *J. Appl. Mech.*, 86(4):041005, jan 2019. 3

[17] Santiago Schnell, Ramon Grima, and Philip K Maini. Multiscale modeling in biology - New insights into cancer illustrate how mathematical tools are enhancing the understanding of life from the smallest scale to the grandest, 2007. 3

[18] Leopold Grinberg, Joseph A. Insley, Dmitry A. Fedosov, Vitali Morozov, Michael E. Papka, and George Em Karniadakis. Tightly coupled atomistic-continuum simulations of brain blood flow on Petaflop supercomputers. *Comput. Sci. Eng.*, 14(6):58–67, nov 2012. 3

[19] Joseph O. Dada and Pedro Mendes. Multi-scale modelling and simulation in systems biology. *Integr. Biol.*, 3(2):86–96, feb 2011. 3

[20] Hong Guang Sun, Yong Zhang, Dumitru Baleanu, Wen Chen, and Yang Quan Chen. A new collection of real world applications of fractional calculus in science and engineering. *Commun. Nonlinear Sci. Numer. Simul.*, 64:213–231, nov 2018. 3

[21] Martin Oliver Steinhauser. *Computational multiscale modeling of fluids and solids: Theory and applications, second edition*. Springer Berlin Heidelberg, Berlin, Heidelberg, 2016. 3

[22] Iqbal Akhund. Nuclear Energy for the Poor. *Worldview*, 21(12):12–14, sep 1978. 3

[23] Yuqian Jiang, Zhigang Shuai, and Minghua Liu. Roles of Long-Range Hopping, Quantum Nuclear Effect, and Exciton Delocalization in Exciton Transport in Organic Semiconductors: A Multiscale Study. *J. Phys. Chem. C*, 122(32):18365–18375, aug 2018. 3

[24] Chao Hu, Byeng D. Youn, and Jaesik Chung. A multiscale framework with extended Kalman filter for lithium-ion battery SOC and capacity estimation. *Appl. Energy*, 92:694–704, apr 2012. 3

[25] Jógvan Magnus Haugaard Olsen, Viacheslav Bolnykh, Simone Meloni, Emiliano Ippoliti, Martin P. Bircher, Paolo Carloni, and Ursula Rothlisberger. MiMiC: A novel framework for multiscale modeling in computational chemistry. *J. Chem. Theory Comput.*, page acs.jctc.9b00093, may 2019. 3

[26] John B. Goodenough and Youngsik Kim. Challenges for Rechargeable Li Batteries ¡sup¿†¡/sup¿. *Chem. Mater.*, 22(3):587–603, feb 2010. 3, 107

[27] Daliang Han, Jun Zhang, Zhe Weng, Debin Kong, Ying Tao, Fei Ding, Dianbo Ruan, and Quan Hong Yang. Two-dimensional materials for lithium/sodium-ion capacitors. *Mater. Today Energy*, 11:30–45, mar 2019. 3, 107

[28] Yongming Sun, Nian Liu, and Yi Cui. Promises and challenges of nanomaterials for lithium-based rechargeable batteries. *Nat. Energy*, 1(7), 2016. 3, 107

[29] Brian Huskinson, Michael P Marshak, Changwon Suh, Süleyman Er, Michael R Gerhardt, Cooper J Galvin, Xudong Chen, Alán Aspuru-Guzik, Roy G Gordon, and Michael J Aziz. A metal-free organic-inorganic aqueous flow battery. *Nature*, 505(7482):195–8, jan 2014. 3, 94, 107

[30] Steven Chu and Arun Majumdar. Opportunities and challenges for a sustainable energy future. *Nature*, 488(7411):294–303, aug 2012. 3, 94, 107

[31] A. Magasinski, P. Dixon, B. Hertzberg, A. Kvit, J. Ayala, and G. Yushin. High-performance lithium-ion anodes using a hierarchical bottom-up approach. *Nat. Mater.*, 9, 2010. 3, 94, 107

[32] Meysam Makaremi, Bohayra Mortazavi, and Chandra Veer Singh. Adsorption of Metallic, Metalloidic, and Nonmetallic Adatoms on Two-Dimensional C3N. *J. Phys. Chem. C*, 121(34):18575–18583, aug 2017. 3, 94

[33] Naoki Nitta, Feixiang Wu, Jung Tae Lee, and Gleb Yushin. Li-ion battery materials: present and future. *Mater. Today*, 18(5):252–264, jun 2015. 3, 94, 107

[34] Thomas J. R. Hughes. *The finite element method : linear static and dynamic finite element analysis*. Prentice-Hall, 1987. 7

[35] A Benjeddou. Advances in piezoelectric finite element modeling of adaptive structural elements: a survey. Technical report. 10

[36] Paolo Gaudenzi and Klaus-Jurgen Bathe. An Iterative Finite Element Procedure for the Analysis of Piezoelectric Continua. *J. Intell. Mater. Syst. Struct.*, 6(2):266–273, mar 1995. 10

[37] Kamyar Ghandi and Nesbitt W. Hagood. Nonlinear finite element modeling of phase transitions in electromechanically coupled material. volume 2715, pages 121–140. International Society for Optics and Photonics, may 1996. 10

[38] Terrell L. Hill. On Steric Effects. *J. Chem. Phys.*, 14(7):465, jul 1946. 15

[39] F. H. Westheimer and Joseph E. Mayer. The theory of the racemization of optically active derivatives of diphenyl. *J. Chem. Phys.*, 14(12):733–738, dec 1946. 15

[40] Edward M. Engler, Joseph D. Andose, and Paul R. von Schleyer. Critical Evaluation of Molecular Mechanics. *J. Am. Chem. Soc.*, 95(24):8005–8025, nov 1973. 15

[41] N. L. Allinger. Calculation of Molecular Structure and Energy by Force-Field Methods. *Adv. Phys. Org. Chem.*, 13(C):1–82, jan 1976. 15

[42] M. Born and R. Oppenheimer. Zur Quantentheorie der Molekeln. *Ann. Phys.*, 389(20):457–484, jan 1927. 15, 39

[43] A. K. Rappé, C. J. Casewit, K. S. Colwell, W. A. Goddard, and W. M. Skiff. UFF, a Full Periodic Table Force Field for Molecular Mechanics and Molecular Dynamics Simulations. *J. Am. Chem. Soc.*, 114(25):10024–10035, dec 1992. 16, 64

[44] Stephen L. Mayo, Barry D. Olafson, and William A. Goddard. DREIDING: A generic force field for molecular simulations. *J. Phys. Chem.*, 94(26):8897–8909, dec 1990. 17, 22

[45] Chunyu Li and Tsu-wei Chou. Static and dynamic properties of single- walled boron nitride nanotubes . *J. Nanosci. Nanotechnol.*, 6(February):54–60, jan 2006. 17, 22, 26

[46] Michael K. Gilson and Barry Honig. Calculation of the total electrostatic energy of a macromolecular system: Solvation energies, binding energies, and conformational analysis. *Proteins Struct. Funct. Bioinforma.*, 4(1):7–18, 1988. 17

[47] Qing Hua Qin. *Advanced mechanics of piezoelectricity*, volume 9783642297. Springer Berlin Heidelberg, Berlin, Heidelberg, 2013. 18

[48] Akbar Jafari, Akbar Afaghi Khatibi, and Mahmoud Mosavi Mashadi. Evaluation of mechanical and piezoelectric properties of boron nitride nanotube: A novel electrostructural analogy approach. *J. Comput. Theor. Nanosci.*, 9(3):461–468, mar 2012. 19, 21, 22, 25

[49] Angel Rubio, Jennifer L. Corkill, and Marvin L. Cohen. Theory of graphitic boron nitride nanotubes. *Phys. Rev. B*, 49(7):5081–5084, feb 1994. 20, 51

[50] Chunyi Zhi, Yoshio Bando, Chengchun Tang, and Dmitri Golberg. Boron nitride nanotubes. *Mater. Sci. Eng. R Reports*, 70(3-6):92–111, nov 2010. 20

[51] S. E. Lyshevski. Nano and Micromechanical Systems-Fundamentals of Nano and Microengineering. Technical Report 5, 2001. 20

[52] Jiesheng Wang, Chee Huei Lee, and Yoke Khin Yap. Recent advancements in boron nitride nanotubes. *Nanoscale*, 2(10):2028–2034, oct 2010. 20

[53] Marvin L. Cohen and Alex Zettl. The physics of boron nitride nanotubes. *Phys. Today*, 63(11):34–38, nov 2010. 20

[54] Karel Alexander N. Duerloo, Mitchell T. Ong, and Evan J. Reed. Intrinsic piezoelectricity in two-dimensional materials. *J. Phys. Chem. Lett.*, 3(19):2871–2876, oct 2012. 20

[55] Robert G. Parr. Density Functional Theory of Atoms and Molecules. In *Horizons Quantum Chem.*, pages 5–15. Springer Netherlands, Dordrecht, 1980. 20

[56] G. Kresse and J. Hafner. ¡i¿Ab initio¡/i¿ molecular dynamics for liquid metals. *Phys. Rev. B*, 47(1):558–561, jan 1993. 20

[57] Jin Ho Kang, Godfrey Sauti, Cheol Park, Vesselin I. Yamakov, Kristopher E. Wise, Sharon E. Lowther, Catharine C. Fay, Sheila A. Thibeault, and Robert G. Bryant. Multifunctional Electroactive Nanocomposites Based on Piezoelectric Boron Nitride Nanotubes. *ACS Nano*, 9(12):11942–11950, dec 2015. 20

[58] Pattabhi R. Budarapu, Robert Gracie, Shih Wei Yang, Xiaoying Zhuang, and Timon Rabczuk. Efficient coarse graining in multiscale modeling of fracture. *Theor. Appl. Fract. Mech.*, 69:126–143, feb 2014. 20

[59] Bohayra Mortazavi and Timon Rabczuk. Multiscale modeling of heat conduction in graphene laminates. *Carbon N. Y.*, 85:1–7, apr 2015. 20, 52, 83, 94, 96

[60] Mat Tolladay, Dmitry Ivanov, Neil L. Allan, and Fabrizio Scarpa. Piezoelectric effects in boron nitride nanotubes predicted by the atomistic finite element method and molecular mechanics. *Nanotechnology*, 28(35):355705, sep 2017. 20

[61] H. J. Xiang, Z. Y. Chen, and Jinlong Yang. Electronic and piezoelectric properties of BN nanotubes from hybrid density functional method. *J. Comput. Theor. Nanosci.*, 3(5):838–842, oct 2006. 20, 25, 26

[62] S. M. Nakhmanson, A. Calzolari, V. Meunier, J. Bernholc, and M. Buongiorno Nardelli. Spontaneous polarization and piezoelectricity in boron nitride nanotubes. *Phys. Rev. B - Condens. Matter Mater. Phys.*, 67(23):235406, jun 2003. 20, 25, 26

[63] Na Sai and E. J. Mele. Microscopic theory for nanotube piezoelectricity. *Phys. Rev. B - Condens. Matter Mater. Phys.*, 68(24):241405, dec 2003. 21, 22, 25, 26

[64] Jin Zhang and S. A. Meguid. Effect of number of layers upon piezoelectric behaviour of multi-walled boron nitride nanotubes. *J. Phys. D. Appl. Phys.*, 48(49):495301, dec 2015. 21

[65] Vesselin Yamakov, Cheol Park, Jin Ho Kang, Kristopher E. Wise, and Catharine Fay. Piezoelectric molecular dynamics model for boron nitride nanotubes. *Comput. Mater. Sci.*, 95:362–370, dec 2014. 21

[66] Akbar Jafari, Akbar Afaghi Khatibi, Mahmoud Mosavi Mashadi, and Akbar Ghazavizadeh. On the parameters influencing the effective properties of a piezoelectric nanocomposite film employing FEM. *J. Compos. Mater.*, 47(16):1987–2003, jul 2013. 21

[67] Abhijit P. Suryavanshi, Min-Feng Yu, Jianguo Wen, Chengchun Tang, and Yoshio Bando. Elastic modulus and resonance behavior of boron nitride nanotubes. *Appl. Phys. Lett.*, 84(14):2527–2529, apr 2004. 21, 25

[68] Nasreen G. Chopra and A. Zettl. Measurement of the elastic modulus of a multi-wall boron nitride nanotube. *Solid State Commun.*, 105(5):297–300, feb 1998. 21, 25

[69] Laetitia Vaccarini, Christophe Goze, Luc Henrard, E. Hernández, Patrick Bernier, and Angel Rubio. Mechanical and electronic properties of carbon and boron-nitride nanotubes. *Carbon N. Y.*, 38(11):1681–1690, jan 2000. 21, 25, 26

[70] V. Nirmala and P. Kolandaivel. Structure and electronic properties of armchair boron nitride nanotubes. *J. Mol. Struct. THEOCHEM*, 817(1-3):137–145, sep 2007. 22

[71] Masa Ishigami, Jay Deep Sau, Shaul Aloni, Marvin L. Cohen, and A. Zettl. Symmetry breaking in boron nitride nanotubes. *Phys. Rev. Lett.*, 97(17):176804, oct 2006. 22

[72] C. Y. Zhi, Y. Bando, C. C. Tang, Q. Huang, and D. Golberg. Boron nitride nanotubes: Functionalization and composites. *J. Mater. Chem.*, 18(33):3900–3908, aug 2008. 22

[73] R. S. Pease. An X-ray study of boron nitride. *Acta Crystallogr.*, 5(3):356–361, may 1952. 22

[74] William H Hayt and John A Buck. *Engineering Electromagnetics [M]*. McGraw-Hill Higher Education, Boston, 7th ed. edition, 1974. 22

[75] N G Chopra, R J Luyken, K Cherrey, V H Crespi, M L Cohen, S G Louie, and A Zettl. Boron nitride nanotubes. *Science (New York, N.Y.)*, 269(5226):966–7, August 1995. 25

[76] E Hernández, C Goze, P Bernier, and A Rubio. Elastic Properties of C and B x C y N z Composite Nanotubes. *Physical Review Letters*, 80(20):4502–4505, May 1998. 26

[77] Veena Verma, V. K. Jindal, and Keya Dharamvir. Elastic moduli of a boron nitride nanotube. *Nanotechnology*, 18(43):435711, oct 2007. 26

[78] N. G. Lebedev and L. A. Chernozatonskiĭ. Quantum-chemical calculations of the piezoelectric characteristics of boron nitride and carbon nanotubes. *Phys. Solid State*, 48(10):2028–2034, oct 2006. 26

[79] B. J. Alder and T. E. Wainwright. Phase Transition for a Hard Sphere System. *J. Chem. Phys.*, 27(5):1208–1209, nov 1957. 30

[80] B. J. Alder and T. E. Wainwright. Studies in molecular dynamics. I. General method. *J. Chem. Phys.*, 31(2):459–466, aug 1959. 30

[81] Hans C. Andersen. Molecular dynamics simulations at constant pressure and/or temperature. *J. Chem. Phys.*, 72(4):2384–2393, feb 1980. 31, 49

[82] Loup Verlet. Computer "experiments" on classical fluids. I. Thermodynamical properties of Lennard-Jones molecules. *Phys. Rev.*, 159(1):98–103, jul 1967. 37, 46

[83] Hockney R. W. The potential calculation and some applications. *Methods Comput. Phys.*, 8:136–211, jan 1970. 37

[84] William C. Swope, Hans C. Andersen, Peter H. Berens, and Kent R. Wilson. A computer simulation method for the calculation of equilibrium constants for the formation of physical clusters of molecules: Application to small water clusters. *J. Chem. Phys.*, 76(1):637–649, jan 1982. 37

[85] E. I. and C. William Gear. *Numerical Initial Value Problems in Ordinary Differential Equations*, volume 27. Prentice-Hall, 2006. 38

[86] F. London. Zur Theorie und Systematik der Molekularkräfte. *Zeitschrift für Phys.*, 63(3-4):245–279, mar 1930. 39

[87] P. Pradeep Kumar. Cohesion. *Encycl. Earth Sci. Ser.*, Part 3(5):157, sep 2011. 40

[88] Philip M. Morse. Diatomic molecules according to the wave mechanics. II. Vibrational levels. *Phys. Rev.*, 34(1):57–64, jul 1929. 40

[89] Julian D. Gale and Andrew L. Rohl. The General Utility Lattice Program (GULP). *Mol. Simul.*, 29(5):291–341, may 2003. 41

[90] R. A. Buckingham. The classical equation of state of gaseous helium, neon and argon. *Proc. R. Soc. London. Ser. A. Math. Phys. Sci.*, 168(933):264–283, oct 1938. 41

[91] J. Tersoff. New empirical approach for the structure and energy of covalent systems. *Phys. Rev. B*, 37(12):6991–7000, apr 1988. 42

[92] J. Tersoff. Modeling solid-state chemistry: Interatomic potentials for multicomponent systems. *Phys. Rev. B*, 39(8):5566–5568, mar 1989. 42

[93] Murray S. Daw and M. I. Baskes. Embedded-atom method: Derivation and application to impurities, surfaces, and other defects in metals. *Phys. Rev. B*, 29(12):6443–6453, jun 1984. 43

[94] M. W. Finnis and J. E. Sinclair. A simple empirical N-body potential for transition metals. *Philos. Mag. A Phys. Condens. Matter, Struct. Defects Mech. Prop.*, 50(1):45–55, jul 1984. 43

[95] Mike Finnis. *Interatomic Forces in Condensed Matter*. Oxford University Press, oct 2010. 43

[96] AM Dongare. A new Embedded Atom Method potential for atomic-scale modeling of metal-silicon systems. *Proceeding of ICCES*, (December):2522–2527, 2005. 43

[97] Frank H. Stillinger and Thomas A. Weber. Computer simulation of local order in condensed phases of silicon. *Phys. Rev. B*, 31(8):5262–5271, apr 1985. 44

[98] M. Born and T. Karman. Über Schwingungen in Raumgittern. *Phys. Z.*, 13:297–309. 45

[99] Shuichi Nosé. A unified formulation of the constant temperature molecular dynamics methods. *J. Chem. Phys.*, 81(1):511–519, jul 1984. 49, 52

[100] Ailan Cheng and Kenneth M. Merz. Application of the Nosé-Hoover chain algorithm to the study of protein dynamics. *J. Phys. Chem.*, 100(5):1927–1937, jan 1996. 49, 52

[101] H. J.C. Berendsen, J. P.M. Postma, W. F. Van Gunsteren, A. Dinola, and J. R. Haak. Molecular dynamics with coupling to an external bath. *J. Chem. Phys.*, 81(8):3684–3690, oct 1984. 49

[102] M. P. Allen, D. J. Tildesley, and Jayanth R. Banavar. Computer Simulation of Liquids . *Phys. Today*, 42(3):105–106, 2008. 49

[103] A K Geim and K S Novoselov. The rise of graphene. *Nat. Mater.*, 6(3):183–91, mar 2007. 50, 72, 83, 107

[104] K S Novoselov, D Jiang, F Schedin, T J Booth, V V Khotkevich, S V Morozov, and A K Geim. Two-dimensional atomic crystals. *Proc. Natl. Acad. Sci. U. S. A.*, 102(30):10451–3, jul 2005. 50, 72

[105] Sheneve Z. Butler, Shawna M. Hollen, Linyou Cao, Yi Cui, Jay A. Gupta, Humberto R. Gutiérrez, Tony F. Heinz, Seung Sae Hong, Jiaxing Huang, Ariel F. Ismach, Ezekiel Johnston-Halperin, Masaru Kuno, Vladimir V. Plashnitsa, Richard D. Robinson, Rodney S. Ruoff, Sayeef Salahuddin, Jie Shan, Li Shi, Michael G. Spencer, Mauricio Terrones, Wolfgang Windl, and Joshua E. Goldberger. Progress, challenges, and opportunities in two-dimensional materials beyond graphene. *ACS Nano*, 7(4):2898–2926, apr 2013. 50, 72

[106] B Radisavljevic, A Radenovic, J Brivio, V Giacometti, and A Kis. Single-layer MoS2 transistors. *Nat. Nanotechnol.*, 6(3):147–50, mar 2011. 50, 83, 94

[107] R. W. Lynch and H. G. Drickamer. Effect of high pressure on the lattice parameters of diamond, graphite, and hexagonal boron nitride. *J. Chem. Phys.*, 44(1):181–184, jan 1966. 50

[108] Kenji Watanabe, Takashi Taniguchi, and Hisao Kanda. Direct-bandgap properties and evidence for ultraviolet lasing of hexagonal boron nitride single crystal. *Nat. Mater.*, 3(6):404–409, jun 2004. 50

[109] Dmitri Golberg, Yoshio Bando, Yang Huang, Takeshi Terao, Masanori Mitome, Chengchun Tang, and Chunyi Zhi. Boron nitride nanotubes and nanosheets. *ACS Nano*, 4(6):2979–2993, jun 2010. 50

[110] Bohayra Mortazavi, Luiz Felipe C. Pereira, Jin Wu Jiang, and Timon Rabczuk. Modelling heat conduction in polycrystalline hexagonal boron-nitride films. *Sci. Rep.*, 5(1):13228, oct 2015. 50, 83

[111] Bohayra Mortazavi and Gianaurelio Cuniberti. Mechanical properties of polycrystalline boron-nitride nanosheets. *RSC Adv.*, 4(37):19137–19143, 2014. 50, 52

[112] Lu Hua Li, Jiri Cervenka, Kenji Watanabe, Takashi Taniguchi, and Ying Chen. Strong oxidation resistance of atomically thin boron nitride nanosheets. *ACS Nano*, 8(2):1457–1462, feb 2014. 50

[113] Haiqing Zhou, Jixin Zhu, Zheng Liu, Zheng Yan, Xiujun Fan, Jian Lin, Gunuk Wang, Qingyu Yan, Ting Yu, Pulickel M. Ajayan, and James M. Tour. High thermal conductivity of suspended few-layer hexagonal boron nitride sheets. *Nano Res.*, 7(8):1232–1240, aug 2014. 50

[114] Rajesh Kumar, G. Rajasekaran, and Avinash Parashar. Optimised cut-off function for Tersoff-like potentials for a BN nanosheet: A molecular dynamics study. *Nanotechnology*, 27(8):085706, feb 2016. 50

[115] Jingang Wang, Fengcai Ma, and Mengtao Sun. Graphene, hexagonal boron nitride, and their heterostructures: properties and applications. *RSC Adv.*, 7(27):16801–16822, mar 2017. 51

[116] Jun Yin, Li Jidong, Yang Hang, Yu Jin, Guoan Tai, Li Xuemei, Zhuhua Zhang, and Wanlin Guo. Boron Nitride Nanostructures: Fabrication, Functionalization and Applications. *Small*, 12(22):2942–2968, jun 2016. 51

[117] Zheng Liu, Lulu Ma, Gang Shi, Wu Zhou, Yongji Gong, Sidong Lei, Xuebei Yang, Jiangnan Zhang, Jingjiang Yu, Ken P. Hackenberg, Aydin Babakhani, Juan Carlos Idrobo, Robert Vajtai, Jun Lou, and Pulickel M. Ajayan. In-plane heterostructures of graphene and hexagonal boron nitride with controlled domain sizes. *Nat. Nanotechnol.*, 8(2):119–124, feb 2013. 51

[118] Alessandro Cresti, Norbert Nemec, Blanca Biel, Gabriel Niebler, Francois Triozon, Gianaurelio Cuniberti, and Stephan Roche. Charge Transport in Disordered Graphene-Based Low Dimensional Materials. *Nano Res.*, 1(5):361–394, 2008. 51

[119] Florian Banhart, Jani Kotakoski, and Arkady V. Krasheninnikov. Structural defects in graphene. *ACS Nano*, 5(1):26–41, jan 2011. 51

[120] Ayako Hashimoto, Kazu Suenaga, Alexandre Gloter, Koki Urita, and Sumio Iijima. Direct evidence for atomic defects in graphene layers. *Nature*, 430(7002):870–873, aug 2004. 51

[121] Jannik C. Meyer, C. Kisielowski, R. Erni, Marta D. Rossell, M. F. Crommie, and A. Zettl. Direct imaging of lattice atoms and topological defects in graphene membranes. *Nano Lett.*, 8(11):3582–3586, nov 2008. 51

[122] J. Kotakoski, A. V. Krasheninnikov, and K. Nordlund. Energetics, structure, and long-range interaction of vacancy-type defects in carbon nanotubes: Atomistic simulations. *Phys. Rev. B - Condens. Matter Mater. Phys.*, 74(24):245420, dec 2006. 51

[123] Jie Ma, Dario Alfè, Angelos Michaelides, and Enge Wang. Stone-Wales defects in graphene and other planar s p2 -bonded materials. *Phys. Rev. B - Condens. Matter Mater. Phys.*, 80(3):033407, jul 2009. 51

[124] Bohayra Mortazavi and Gianaurelio Cuniberti. Atomistic modeling of mechanical properties of polycrystalline graphene. *Nanotechnology*, 25(21), 2014. 51

[125] Bohayra Mortazavi, Markus Pötschke, and Gianaurelio Cuniberti. Multi-scale modeling of thermal conductivity of polycrystalline graphene sheets. *Nanoscale*, 6(6):3344–3352, 2014. 51

[126] Mark Kester, Yasser Heakal, Todd Fox, Arati Sharma, Gavin P. Robertson, Thomas T. Morgan, Erhan I. Altinoğlu, Amra Tabaković, Mylisa R. Parette, Sarah M. Rouse, Victor Ruiz-Velasco, and James H. Adair. Calcium phosphate nanocomposite particles for in vitro imaging and encapsulated chemotherapeutic drug delivery to cancer Cells. *Nano Lett.*, 8(12):4116–4121, dec 2008. 51

[127] Changgu Lee, Xiaoding Wei, Jeffrey W. Kysar, and James Hone. Measurement of the elastic properties and intrinsic strength of monolayer graphene. *Science (80-.).*, 321(5887):385–388, jul 2008. 51

[128] Romain Bourrellier, Sophie Meuret, Anna Tararan, Odile Stéphan, Mathieu Kociak, Luiz H.G. Tizei, and Alberto Zobelli. Bright UV single photon emission at point defects in h-BN. *Nano Lett.*, 16(7):4317–4321, jul 2016. 51

[129] Mohammad Salavati, Hamid Ghasemi, and Timon Rabczuk. Electromechanical properties of Boron Nitride Nanotube: Atomistic bond potential and equivalent mechanical energy approach. *Comput. Mater. Sci.*, 149:460–465, jun 2018. 51

[130] Mohammad Salavati and Timon Rabczuk. Application of highly stretchable and conductive two-dimensional 1T VS 2 and VSe 2 as anode materials for Li-, Na- and Ca-ion storage. *Comput. Mater. Sci.*, 160:360–367, apr 2019. 51, 113

[131] Mohammad Salavati. Electronic and mechanical responses of two-dimensional HfS 2 , HfSe 2 , ZrS 2 , and ZrSe 2 from first-principles. *Front. Struct. Civ. Eng.*, 13(2):486–494, jul 2019. 51, 73, 96

[132] A. Katzir, J. T. Suss, A. Zunger, and A. Halperin. Point defects in hexagonal boron nitride. I. EPR, thermoluminescence, and thermally-stimulated-current measurements. *Phys. Rev. B*, 11(6):2370–2377, mar 1975. 51

[133] I. Jiménez, A. Jankowski, L. Terminello, D. Sutherland, J. Carlisle, and G. Doll. Core-level photoabsorption study of defects and metastable bonding configurations in boron nitride. *Phys. Rev. B - Condens. Matter Mater. Phys.*, 55(18):12025–12037, may 1997. 51

[134] Shin-Ichi Hirano, Toshinobu Yogo, Satoshi Asada, and Shigeharu Naka. Synthesis of amorphous boron nitride by pressure pyrolysis of borazine. *Journal of the American Ceramic Society*, 72(1):66–70, jan 1989. 51

[135] Takashi Taniguchi, Koji Kimoto, Masataka Tansho, Shigeo Horiuchi, and Shinobu Yamaoka. Phase transformation of amorphous boron nitride under high pressure. *Chem. Mater.*, 15(14):2744–2751, jul 2003. 51

[136] Bohayra Mortazavi and Saïd Ahzi. Thermal conductivity and tensile response of defective graphene: A molecular dynamics study. *Carbon N. Y.*, 63:460–470, nov 2013. 51, 72

[137] Ning Ding, Xiangfeng Chen, and Chi Man Lawrence Wu. Mechanical properties and failure behaviors of the interface of hybrid graphene/hexagonal boron nitride sheets. *Sci. Rep.*, 6(1):31499, nov 2016. 51

[138] Songül Güryel, Balázs Hajgató, Yves Dauphin, Jean Marie Blairon, Hans Edouard Miltner, Frank De Proft, Paul Geerlings, and Gregory Van Lier. Effect of structural defects and chemical functionalisation on the intrinsic mechanical properties of graphene. *Phys. Chem. Chem. Phys.*, 15(2):659–665, dec 2013. 51

[139] Tongwei Han, Ying Luo, and Chengyuan Wang. Effects of temperature and strain rate on the mechanical properties of hexagonal boron nitride nanosheets. *J. Phys. D. Appl. Phys.*, 47(2):025303, jan 2014. 52

[140] Rouzbeh Abadi, Raahul Palanivel Uma, Mohammadreza Izadifar, and Timon Rabczuk. Investigation of crack propagation and existing notch on the mechanical response of polycrystalline hexagonal boron-nitride nanosheets. *Comput. Mater. Sci.*, 131:86–99, apr 2017. 52

[141] Steve Plimpton. Fast parallel algorithms for short-range molecular dynamics. *J. Comput. Phys.*, 117(1):1–19, mar 1995. 52

[142] C. Matsubara H. Matsunaga, K. Fisher. Tersoff Potential Parameters for Simulating Cubic Boron Carbonitrides. *Japanese Journal of Applied Physics*, 39(2, 1A/B):L48–L51, January 2000. 52

[143] Robert D Groot and Patrick B Warren. *The Journal of Chemical Physics simulation*, volume 97. American Institute of Physics, 2004. 52

[144] William G. Hoover. Canonical dynamics: Equilibrium phase-space distributions. *Phys. Rev. A*, 31(3):1695–1697, mar 1985. 52

[145] Bohayra Mortazavi, Gianaurelio Cuniberti, and Timon Rabczuk. Mechanical properties and thermal conductivity of graphitic carbon nitride: A molecular dynamics study. *Comput. Mater. Sci.*, 99:285–289, 2015. 52, 74, 96

[146] Bohayra Mortazavi, Meysam Makaremi, Masoud Shahrokhi, Mostafa Raeisi, Chandra Veer Singh, Timon Rabczuk, and Luiz Felipe C. Pereira. Borophene hydride: A stiff 2D material with high thermal conductivity and attractive optical and electronic properties. *Nanoscale*, 10(8):3759–3768, feb 2018. 52, 108

[147] Bohayra Mortazavi, Meysam Makaremi, Masoud Shahrokhi, Zheyong Fan, and Timon Rabczuk. N-graphdiyne two-dimensional nanomaterials: Semiconductors with low thermal conductivity and high stretchability. *Carbon N. Y.*, 137:57–67, oct 2018. 52, 74, 98, 108

[148] Bohayra Mortazavi, Mohamed E. Madjet, Masoud Shahrokhi, Said Ahzi, Xiaoying Zhuang, and Timon Rabczuk. Nanoporous graphene: A 2D semiconductor with anisotropic mechanical, optical and thermal conduction properties. *Carbon N. Y.*, 147:377–384, 2019. 52

[149] Bohayra Mortazavi, Olivier Benzerara, Hendrik Meyer, Julien Bardon, and Said Ahzi. Combined molecular dynamics-finite element multiscale modeling of thermal conduction in graphene epoxy nanocomposites. *Carbon N. Y.*, 60:356–365, aug 2013. 52, 72, 96

[150] Bohayra Mortazavi, Masoud Shahrokhi, Xiaoying Zhuang, and Timon Rabczuk. Boron-graphdiyne: A superstretchable semiconductor with low thermal conductivity and ultrahigh capacity for Li, Na and Ca ion storage. Technical Report 23, 2018. 52, 77, 98, 108

[151] Bohayra Mortazavi, Yves Rémond, Said Ahzi, and Valérie Toniazzo. Thickness and chirality effects on tensile behavior of few-layer graphene by molecular dynamics simulations. *Comput. Mater. Sci.*, 53(1):298–302, 2012. 52, 73, 96

[152] Arun K. Subramaniyan and C. T. Sun. Continuum interpretation of virial stress in molecular simulations. *Int. J. Solids Struct.*, 45(14-15):4340–4346, jul 2008. 52

[153] Alexander Stukowski. Visualization and analysis of atomistic simulation data with OVITO-the Open Visualization Tool. *Model. Simul. Mater. Sci. Eng.*, 18(1):015012, jan 2010. 52

[154] Hongwei Guo, Xiaoying Zhuang, and Timon Rabczuk. A Deep Collocation Method for the Bending Analysis of Kirchhoff Plate. *Comput. Mater. Contin.*, 58(2):433–456, 2019. 52

[155] Cosmin Anitescu, Elena Atroshchenko, Naif Alajlan, and Timon Rabczuk. Artificial neural network methods for the solution of second order boundary value problems. *Comput. Mater. Contin.*, 59(1):345–359, 2019. 52

[156] Timon Rabczuk, Huilong Ren, and Xiaoying Zhuang. A nonlocal operator method for partial differential equations with application to electromagnetic waveguide problem. *Comput. Mater. Contin.*, 59(1):31–55, 2019. 52

[157] Y. P. Varshni. Temperature dependence of the elastic constants. *Phys. Rev. B*, 2(10):3952–3958, nov 1970. 53

[158] J M Ziman. *Electrons and Phonons : The Theory of Transport Phenomena in Solids Abstract and Keywords*. Number July 2013. Clarendon Press, 2001. 53

[159] Jean Jacques Greffet. *Electrons and phonons*, volume 107. Oxford University Press, feb 2006. 53

[160] Fang Liu, Pingbing Ming, and Ju Li. Ab initio calculation of ideal strength and phonon instability of graphene under tension. *Phys. Rev. B - Condens. Matter Mater. Phys.*, 76(6):064120, aug 2007. 53, 74, 78, 98

[161] Ali Hossein Nezhad Shirazi. Molecular dynamics investigation of mechanical properties of single-layer phagraphene. *Front. Struct. Civ. Eng.*, 13(2):495–503, apr 2019. 53

[162] A. H.N. Shirazi, R. Abadi, M. Izadifar, N. Alajlan, and T. Rabczuk. Mechanical responses of pristine and defective C3N nanosheets studied by molecular dynamics simulations. *Comput. Mater. Sci.*, 147:316–321, may 2018. 53

[163] Bohayra Mortazavi. Ultra high stiffness and thermal conductivity of graphene like C3N. *Carbon N. Y.*, 118:25–34, apr 2017. 53, 74, 83, 96

[164] Bohayra Mortazavi, Zheyong Fan, Luiz Felipe C. Pereira, Ari Harju, and Timon Rabczuk. Amorphized graphene: A stiff material with low thermal conductivity. *Carbon N. Y.*, 103:318–326, jul 2016. 56

[165] W. Kohn and L. J. Sham. Self-consistent equations including exchange and correlation effects. *Phys. Rev.*, 140(4A):A1133–A1138, nov 1965. 61, 70

[166] P. Hohenberg and W. Kohn. Inhomogeneous electron gas. *Phys. Rev.*, 136(3B):B864–B871, nov 1964. 61, 69, 70

[167] Takehiko Mori and Takehiko Mori. *Quantum Chemistry of Solids*, volume 153 of *Springer Series in Solid-State Sciences*. Springer Berlin Heidelberg, Berlin, Heidelberg, 2016. 65

[168] K. S. Novoselov, A. K. Geim, S. V. Morozov, D. Jiang, Y. Zhang, S. V. Dubonos, I. V. Grigorieva, and A. A. Firsov. Electric field in atomically thin carbon films. *Science (80-.).*, 306(5696):666–669, oct 2004. 72, 83, 107

[169] A. H. Castro Neto, F. Guinea, N. M.R. Peres, K. S. Novoselov, and A. K. Geim. The electronic properties of graphene. *Rev. Mod. Phys.*, 81(1):109–162, jan 2009. 72, 107

[170] Mingsheng Xu, Tao Liang, Minmin Shi, and Hongzheng Chen. Graphene-Like Two-Dimensional Materials. *Chem. Rev.*, 113(5):3766–3798, may 2013. 72

[171] Manish Chhowalla, Hyeon Suk Shin, Goki Eda, Lain-Jong Li, Kian Ping Loh, and Hua Zhang. The chemistry of two-dimensional layered transition metal dichalcogenide nanosheets. *Nat. Chem.*, 5(4):263–75, apr 2013. 72

[172] Ganesh R. Bhimanapati, Zhong Lin, Vincent Meunier, Yeonwoong Jung, Judy Cha, Saptarshi Das, Di Xiao, Youngwoo Son, Michael S. Strano, Valentino R. Cooper, Liangbo Liang, Steven G. Louie, Emilie Ringe, Wu Zhou, Steve S. Kim, Rajesh R. Naik, Bobby G. Sumpter, Humberto Terrones, Fengnian Xia, Yeliang Wang, Jun Zhu, Deji Akinwande, Nasim Alem, Jon A. Schuller, Raymond E. Schaak, Mauricio Terrones, and Joshua A. Robinson. Recent Advances in Two-Dimensional Materials beyond Graphene. *ACS Nano*, 9(12):11509–11539, dec 2015. 72

[173] Chaoliang Tan, Xiehong Cao, Xue-Jun Wu, Qiyuan He, Jian Yang, Xiao Zhang, Junze Chen, Wei Zhao, Shikui Han, Gwang-Hyeon Nam, Melinda Sindoro, and Hua Zhang. Recent Advances in Ultrathin Two-Dimensional Nanomaterials. *Chem. Rev.*, 117(9):6225–6331, may 2017. 72

[174] H. Bengel, H. J. Cantow, S. N. Magonov, H. Hillebrecht, G. Thiele, W. Liang, and M. H. Whangbo. Tip-force induced surface corrugation in layered transition metal trichlorides MCl3 (MRu, Mo, Rh, Ir). *Surf. Sci.*, 343(1-2):95–103, dec 1995. 72

[175] H. Hillebrecht, P. J. Schmidt, H. W. Rotter, G. Thiele, P. Zönnchen, H. Bengel, H. J. Cantow, S. N. Magonov, and M. H. Whangbo. Structural and scanning microscopy studies of layered compounds MCl3 (M = Mo, Ru, Cr) and MOCl2 (M = V, Nb, Mo, Ru, Os). *J. Alloys Compd.*, 246(1-2):70–79, jan 1997. 72

[176] Pere Miró, Martha Audiffred, and Thomas Heine. An atlas of two-dimensional materials. *Chem. Soc. Rev.*, 43(18):6537–6554, aug 2014. 72

[177] Junyi Liu, Qiang Sun, Yoshiyuki Kawazoe, and Puru Jena. Exfoliating biocompatible ferromagnetic Cr-trihalide monolayers. *Phys. Chem. Chem. Phys.*, 18(13):8777–8784, mar 2016. 72

[178] Liujiang Zhou, Liangzhi Kou, Yan Sun, Claudia Felser, Feiming Hu, Guangcun Shan, Sean C. Smith, Binghai Yan, and Thomas Frauenheim. New family of quantum spin hall insulators in two-dimensional transition-metal halide with large nontrivial band gaps. *Nano Lett.*, 15(12):7867–7872, dec 2015. 72

[179] J. A. Sears, M. Songvilay, K. W. Plumb, J. P. Clancy, Y. Qiu, Y. Zhao, D. Parshall, and Young June Kim. Magnetic order in $\alpha-$RuCl3: A honeycomb-lattice quantum magnet with strong spin-orbit coupling. *Phys. Rev. B - Condens. Matter Mater. Phys.*, 91(14):144420, apr 2015. 72, 73

[180] R. D. Johnson, S. C. Williams, A. A. Haghighirad, J. Singleton, V. Zapf, P. Manuel, I. I. Mazin, Y. Li, H. O. Jeschke, R. Valentí, and R. Coldea. Monoclinic crystal structure of α-RuCl3 and the zigzag antiferromagnetic ground state. *Phys. Rev. B - Condens. Matter Mater. Phys.*, 92(23):235119, dec 2015. 72

[181] A Banerjee, C A Bridges, J-Q Yan, A A Aczel, L Li, M B Stone, G E Granroth, M D Lumsden, Y Yiu, J Knolle, S Bhattacharjee, D L Kovrizhin, R Moessner, D A Tennant, D G Mandrus, and S E Nagler. Proximate Kitaev quantum spin liquid behaviour in a honeycomb magnet. Technical Report 7, jul 2016. 72, 73

[182] Takuya Aoyama, Yoshinao Hasegawa, Shojiro Kimura, Tsuyoshi Kimura, and Kenya Ohgushi. Anisotropic magnetodielectric effect in the honeycomb-type magnet α-RuCl3. *Phys. Rev. B*, 95(24):245104, jun 2017. 72

[183] A. U.B. Wolter, L. T. Corredor, L. Janssen, K. Nenkov, S. Schönecker, S. H. Do, K. Y. Choi, R. Albrecht, J. Hunger, T. Doert, M. Vojta, and B. Büchner. Field-induced quantum criticality in the Kitaev system α-RuCl 3. *Phys. Rev. B*, 96(4), apr 2017. 72

[184] Arnab Banerjee, Jiaqiang Yan, Johannes Knolle, Craig A. Bridges, Matthew B. Stone, Mark D. Lumsden, David G. Mandrus, David A. Tennant, Roderich Moessner, and Stephen E. Nagler. Neutron scattering in the proximate quantum spin liquid α-RuCl 3. *Science (80-.).*, 356(6342):1055–1059, jun 2017. 72

[185] Daniel Weber, Leslie M. Schoop, Viola Duppel, Judith M. Lippmann, Jürgen Nuss, and Bettina V. Lotsch. Magnetic Properties of Restacked 2D Spin 1/2 honeycomb RuCl3 Nanosheets. *Nano Lett.*, 16(6):3578–3584, jun 2016. 72, 73

[186] Martin Grönke, Peer Schmidt, Martin Valldor, Steffen Oswald, Daniel Wolf, Axel Lubk, Bernd Büchner, and Silke Hampel. Chemical vapor growth and delamination of α-RuCl3 nanosheets down to the monolayer limit. *Nanoscale*, 10(40):19014–19022, oct 2018. 73

[187] N. I. KOLBIN and A. N. RYABOV. Reaction of chlorine upon ruthenium over the tempreture ranege. *Vestn. Leningr. Univ., Ser. Fiz. ikhim.No 4,*, 14(22):121–7, 1959. 73

[188] M. Ziatdinov, A. Banerjee, A. Maksov, T. Berlijn, W. Zhou, H. B. Cao, J. Q. Yan, C. A. Bridges, D. G. Mandrus, S. E. Nagler, A. P. Baddorf, and S. V. Kalinin. Atomic-scale observation of structural and electronic orders in the layered compound α-RuCl 3. *Nat. Commun.*, 7(1):13774, dec 2016. 73

[189] K. W. Plumb, J. P. Clancy, L. J. Sandilands, V. Vijay Shankar, Y. F. Hu, K. S. Burch, Hae Young Kee, and Young June Kim. α- RuCl3: A spin-orbit assisted Mott insulator on a honeycomb lattice. *Phys. Rev. B - Condens. Matter Mater. Phys.*, 90(4):041112, jul 2014. 73

[190] Heung Sik Kim, Vijay Shankar, Andrei Catuneanu, and Hae Young Kee. Kitaev magnetism in honeycomb RuCl3 with intermediate spin-orbit coupling. *Phys. Rev. B - Condens. Matter Mater. Phys.*, 91(24):241110, jun 2015. 73

[191] Heung Sik Kim and Hae Young Kee. Crystal structure and magnetism in α-RuCl3: An ab initio study. *Phys. Rev. B*, 93(15):155143, apr 2016. 73

[192] Luke J. Sandilands, Yao Tian, Anjan A. Reijnders, Heung Sik Kim, K. W. Plumb, Young June Kim, Hae Young Kee, and Kenneth S. Burch. Spin-orbit excitations and electronic structure of the putative Kitaev magnet α-RuCl3. *Phys. Rev. B*, 93(7), feb 2016. 73

[193] Yumi Kubota, Hidekazu Tanaka, Toshio Ono, Yasuo Narumi, and Koichi Kindo. Successive magnetic phase transitions in α-RuCl3: XY-like frustrated magnet on the honeycomb lattice. *Phys. Rev. B - Condens. Matter Mater. Phys.*, 91(9):094422, mar 2015. 73

[194] M. Majumder, M. Schmidt, H. Rosner, A. A. Tsirlin, H. Yasuoka, and M. Baenitz. Anisotropic Ru3+ 4d5 magnetism in the α-RuCl3 honeycomb system: Susceptibility, specific heat, and zero-field NMR anisotropic Ru3+4d5 magnetism in the ⋯ M. Majumder et al. *Phys. Rev. B - Condens. Matter Mater. Phys.*, 91(18):180401, may 2015. 73

[195] F. Iyikanat, M. Yagmurcukardes, R. T. Senger, and H. Sahin. Tuning electronic and magnetic properties of monolayer α-RuCl3 by in-plane strain. *J. Mater. Chem. C*, 6(8):2019–2025, feb 2018. 73

[196] S. Sarikurt, Y. Kadioglu, F. Ersan, E. Vatansever, O. Üzengi Aktürk, Y. Yüksel, Akinci, and E. Aktürk. Electronic and magnetic properties of monolayer α-RuCl3: A first-principles and Monte Carlo study. *Phys. Chem. Chem. Phys.*, 20(2):997–1004, jan 2018. 73

[197] John P. Perdew, Kieron Burke, and Matthias Ernzerhof. Generalized gradient approximation made simple. *Phys. Rev. Lett.*, 77(18):3865–3868, oct 1996. 73, 74, 84, 95, 108

[198] Fatih Ersan, Erol Vatansever, Sevil Sarikurt, Yusuf Yüksel, Yelda Kadioglu, H. Duygu Ozaydin, Olcay Üzengi Aktürk, Ümit Akıncı, and Ethem Aktürk. Exploring the electronic and magnetic properties of new metal halides from bulk to two-dimensional monolayer: RuX3 (X=Br, I). *Journal of Magnetism and Magnetic Materials*, 476:111 – 119, 2019. 73

[199] Tran Quang Trung and Nae-Eung Lee. Recent Progress on Stretchable Electronic Devices with Intrinsically Stretchable Components. *Advanced Materials*, 29(3):1603167, 2017. 73

[200] Yandong Ma, Ying Dai, Meng Guo, Chengwang Niu, Yingtao Zhu, and Baibiao Huang. Evidence of the existence of magnetism in pristine VX 2 monolayers (X = S, Se) and their strain-induced tunable magnetic properties. *ACS Nano*, 6(2):1695–1701, feb 2012. 73

[201] Yungang Zhou, Zhiguo Wang, Ping Yang, Xiaotao Zu, Li Yang, Xin Sun, and Fei Gao. Tensile strain switched ferromagnetism in layered NbS2 and NbSe2. *ACS Nano*, 6(11):9727–9736, nov 2012. 73

[202] Ju Li, Zhiwei Shan, and Evan Ma. Elastic strain engineering for unprecedented materials properties. *MRS Bull.*, 39(2):108–114, feb 2014. 73

[203] Shengxue Yang, Cong Wang, Hasan Sahin, Hui Chen, Yan Li, Shu Shen Li, Aslihan Suslu, Francois M. Peeters, Qian Liu, Jingbo Li, and Sefaattin Tongay. Tuning the optical, magnetic, and electrical properties of ReSe2 by nanoscale strain engineering. *Nano Lett.*, 15(3):1660–1666, mar 2015. 73

[204] Dae Hyeong Kim, Nanshu Lu, Rui Ma, Yun Soung Kim, Rak Hwan Kim, Shuodao Wang, Jian Wu, Sang Min Won, Hu Tao, Ahmad Islam, Ki Jun Yu, Tae Il Kim, Raeed Chowdhury, Ming Ying, Lizhi Xu, Ming Li, Hyun Joong Chung, Hohyun Keum, Martin McCormick, Ping Liu, Yong Wei Zhang, Fiorenzo G. Omenetto, Yonggang Huang, Todd Coleman, and John A. Rogers. Epidermal electronics. *Science (80-.).*, 333(6044):838–843, aug 2011. 73, 96

[205] Bohayra Mortazavi, Said Ahzi, Valérie Toniazzo, and Yves Rémond. Nitrogen doping and vacancy effects on the mechanical properties of graphene: A molecular dynamics study. *Phys. Lett. Sect. A Gen. At. Solid State Phys.*, 376(12-13):1146–1153, 2012. 73

[206] Bohayra Mortazavi and Said Ahzi. Molecular dynamics study on the thermal conductivity and mechanical properties of boron doped graphene. *Solid State Commun.*, 152(15):1503–1507, 2012. 73, 96

[207] Marcelo Galván, Alberto Vela, and José L. Gázquez. Chemical reactivity in spin-polarized density functional theory. *J. Phys. Chem.*, 92(22):6470–6474, nov 1988. 74

[208] Frank De Proft, Eduardo Chamorro, Patricia Pérez, Mario Duque, Freija De Vleeschouwer, and Paul Geerlings. Spin-polarized reactivity indices from density functional theory: theory and applications. In *Chem. Model.*, pages 63–111. Royal Society of Chemistry, Cambridge, sep 2009. 74

[209] G. Kresse and D. Joubert. From ultrasoft pseudopotentials to the projector augmented-wave method. *Phys. Rev. B - Condens. Matter Mater. Phys.*, 59(3):1758–1775, jan 1999. 74, 84, 95, 108

[210] G. Kresse and J. Furthmüller. Efficiency of ab-initio total energy calculations for metals and semiconductors using a plane-wave basis set. *Comput. Mater. Sci.*, 6(1):15–50, jul 1996. 74, 84, 95, 108

[211] G. Kresse and J. Furthmüller. Efficient iterative schemes for ab initio total-energy calculations using a plane-wave basis set. *Phys. Rev. B - Condens. Matter Mater. Phys.*, 54(16):11169–11186, oct 1996. 74, 84, 95, 108

[212] P. E. Blöchl. Projector augmented-wave method. *Phys. Rev. B*, 50(24):17953–17979, dec 1994. 74

[213] Koichi Momma and Fujio Izumi. VESTA 3 for three-dimensional visualization of crystal, volumetric and morphology data. *J. Appl. Crystallogr.*, 44(6):1272–1276, dec 2011. 74, 84, 96, 108

[214] Hendrik J. Monkhorst and James D. Pack. Special points for Brillouin-zone integrations. *Phys. Rev. B*, 13(12):5188–5192, jun 1976. 74, 85, 96, 109

[215] Atsushi Togo, Fumiyasu Oba, and Isao Tanaka. First-principles calculations of the ferroelastic transition between rutile-type and CaCl2-type SiO2 at high pressures. *Phys. Rev. B - Condens. Matter Mater. Phys.*, 78(13):134106, oct 2008. 74

[216] Atsushi Togo and Isao Tanaka. First principles phonon calculations in materials science. *Scr. Mater.*, 108:1–5, nov 2015. 74

[217] T.H.E. Kings. "Advanced mechanics of materials" 5th edition, A.P. Boresi, R.J. Schmidt and O.M. Sidebottom . *Strain*, 29(4):141–142, nov 2008. 76

[218] Bohayra Mortazavi, Masoud Shahrokhi, Meysam Makaremi, Gianaurelio Cuniberti, and Timon Rabczuk. First-principles investigation of Ag-, Co-, Cr-, Cu-, Fe-, Mn-, Ni-, Pd- and Rh-hexaaminobenzene 2D metal-organic frameworks. *Mater. Today Energy*, 10:336–342, dec 2018. 77

[219] Qing Peng, Wei Ji, and Suvranu De. Mechanical properties of graphyne monolayers: A first-principles study. *Phys. Chem. Chem. Phys.*, 14(38):13385–13391, 2012. 77, 98

[220] Qing Peng, Wei Ji, and Suvranu De. Mechanical properties of the hexagonal boron nitride monolayer: Ab initio study. *Comput. Mater. Sci.*, 56:11–17, 2012. 78, 98

[221] Bohayra Mortazavi and Yves Rémond. Investigation of tensile response and thermal conductivity of boron-nitride nanosheets using molecular dynamics simulations. *Phys. E Low-Dimensional Syst. Nanostructures*, 44(9):1846–1852, jun 2012. 78

[222] Zenan Qi, David K. Campbell, and Harold S. Park. Atomistic simulations of tension-induced large deformation and stretchability in graphene kirigami. *Phys. Rev. B - Condens. Matter Mater. Phys.*, 90(24):245437, dec 2014. 78

[223] Tongwei Han, Fabrizio Scarpa, and Neil L. Allan. Super stretchable hexagonal boron nitride Kirigami. *Thin Solid Films*, 632:35–43, 2017. 78

[224] Yugang Sun and John A. Rogers. Inorganic semiconductors for flexible electronics. *Adv. Mater.*, 19(15):1897–1916, aug 2007. 81

[225] F. Guinea, M. I. Katsnelson, and a. K. Geim. Energy gaps, topological insulator state and zero-field quantum Hall effect in graphene by strain engineering. *Nature Physics*, 6(1):30–33, 2009. 83

[226] Lherbier, Aurélien Botello-MMéndez, Andrés Rafael Charlier, and Jean-Christophe. Electronic and optical properties of pristine and oxidized borophene. *2D Materials*, 3(4):045006, October 2016. 83

[227] Aurélien Lherbier, X. Blase, Yann Michel Triozon Niquet, and Stephan François Roche. Charge transport in chemically doped 2D graphene. *Physical Review Letters*, 101(3), 2008. 83

[228] T. B. Martins, R. H. Miwa, AJ. Da Silva, and A. Fazzio. Electronic and transport properties of boron-doped graphene nanoribbons. *Physical Review Letters*, 98(19):196803, May 2007. 83

[229] a K Geim and I V. Grigorieva. Van der Waals heterostructures. *Nature*, 499(7459):419–25, 2013. 83

[230] Qing Hua Wang, Kourosh Kalantar-Zadeh, Andras Kis, Jonathan N. Coleman, and Michael S. Strano. Electronics and optoelectronics of two-dimensional transition metal dichalcogenides. *Nat. Nanotechnol.*, 7(11):699–712, 2012. 83, 94

[231] Michal J. Mleczko, Chaofan Zhang, Hye Ryoung Lee, Hsueh-Hui Kuo, Blanka Magyari-Köpe, Robert G. Moore, Zhi-Xun Shen, Ian R. Fisher, Yoshio Nishi, and Eric Pop. HfSe2 and ZrSe2: Two-dimensional semiconductors with native high-k oxides. *Science Advances*, 3(8):e1700481, August 2017. 83, 88, 90

[232] M. Shahrokhi and C. Leonard. Quasi-particle energies and optical excitations of wurtzite BeO and its nanosheet. *Journal of Alloys and Compounds*, 682:254–262, October 2016. 83

[233] M. Shahrokhi and C. Leonard. Tuning the band gap and optical spectra of silicon-doped graphene: Many-body effects and excitonic states. *Journal of Alloys and Compounds*, 693:1185–1196, February 2017. 83

[234] Bohayra Mortazavi, Masoud Shahrokhi, Meysam Makaremi, and Timon Rabczuk. Theoretical realization of Mo2P; a novel stable 2D material with superionic conductivity and attractive optical properties. *Appl. Mater. Today*, 9:292–299, dec 2017. 83, 94

[235] Bohayra Mortazavi, Obaidur Rahaman, Arezoo Dianat, and Timon Rabczuk. Mechanical responses of borophene sheets: A first-principles study. *Phys. Chem. Chem. Phys.*, 18(39):27405–27413, oct 2016. 83

[236] Hossein Talebi, Mohammad Silani, and Timon Rabczuk. Concurrent multiscale modeling of three dimensional crack and dislocation propagation. *Adv. Eng. Softw.*, 80(C):82–92, feb 2015. 83

[237] William Humphrey, Andrew Dalke, and Klaus Schulten. VMD: Visual molecular dynamics. *J. Mol. Graph.*, 14(1):33–38, feb 1996. 84

[238] Aliaksandr V. Krukau, Oleg A. Vydrov, Artur F. Izmaylov, and Gustavo E. Scuseria. Influence of the exchange screening parameter on the performance of screened hybrid functionals. *The Journal of Chemical Physics*, 125(22):224106, December 2006. 85

[239] M. Shishkin and G. Kresse. Self-consistent GW calculations for semiconductors and insulators. *Phys. Rev. B - Condens. Matter Mater. Phys.*, 75(23), 2007. 85

[240] M. Shishkin, M. Marsman, and G. Kresse. Accurate quasiparticle spectra from self-consistent GW calculations with vertex corrections. *Phys. Rev. Lett.*, 99(24), 2007. 85

[241] Junwen Li, Nikhil V. Medhekar, and Vivek B. Shenoy. Bonding charge density and ultimate strength of monolayer transition metal dichalcogenides. *J. Phys. Chem. C*, 117(30):15842–15848, 2013. 86, 87, 98

[242] Bohayra Mortazavi, Obaidur Rahaman, Meysam Makaremi, Arezoo Dianat, Gianaurelio Cuniberti, and Timon Rabczuk. First-principles investigation of mechanical properties of silicene, germanene and stanene. *Phys. E Low-Dimensional Syst. Nanostructures*, 87:228–232, 2017. 86

[243] B Silvi and A Savin. Classification of Chemical-Bonds Based on Topological Analysis of Electron Localization Functions. *Nature*, 371(6499):683–686, 1994. 87

[244] Graeme Henkelman, Andri Arnaldsson, and Hannes Jónsson. A fast and robust algorithm for Bader decomposition of charge density. *Comput. Mater. Sci.*, 36(3):354–360, 2006. 87

[245] Hongyan Guo, Ning Lu, Lu Wang, Xiaojun Wu, and Xiao Cheng Zeng. Tuning electronic and magnetic properties of early transition-metal dichalcogenides via tensile strain. *J. Phys. Chem. C*, 118(13):7242–7249, 2014. 90

[246] Hongzhen Tian, Zhi Wei Seh, Kai Yan, Zhongheng Fu, Peng Tang, Yingying Lu, Ruifeng Zhang, Dominik Legut, Yi Cui, and Qianfan Zhang. Theoretical Investigation of 2D Layered Materials as Protective Films for Lithium and Sodium Metal Anodes. *Adv. Energy Mater.*, 7(13), 2017. 94

[247] Vinodkumar Etacheri, Rotem Marom, Ran Elazari, Gregory Salitra, and Doron Aurbach. Challenges in the development of advanced Li-ion batteries: A review. *Energy Environ. Sci.*, 4(9):3243–3262, 2011. 94

[248] Le Shi and Tianshou Zhao. Recent advances in inorganic 2D materials and their applications in lithium and sodium batteries. *J. Mater. Chem. A*, 5(8):3735–3758, 2017. 94

[249] Junyi Liu, Shuo Wang, and Qiang Sun. All-carbon-based porous topological semimetal for Li-ion battery anode material. *Proc. Natl. Acad. Sci.*, 114(4):651–656, 2017. 94

[250] Evan M Erickson, Chandan Ghanty, and Doron Aurbach. New Horizons for Conventional Lithium Ion Battery Technology. *J. Phys. Chem. Lett.*, pages 3313–3324, 2014. 94

[251] Mi Hee Park, Min Gyu Kim, Jaebum Joo, Kitae Kim, Jeyoung Kim, Soonho Ahn, Yi Cui, and Jaephil Cho. Silicon nanotube battery anodes. *Nano Lett.*, 9(11):3844–3847, 2009. 94

[252] Tzu Liang Chan and James R. Chelikowsky. Controlling diffusion of lithium in silicon nanostructures. *Nano Lett.*, 10(3):821–825, 2010. 94

[253] Martin Ebner, Federica Marone, Marco Stampanoni, and Vanessa Wood. Visualization and quantification of Electrochemical and Mechanical. *Science (80-.).*, 342(November):716–721, nov 2013. 94

[254] Bohayra Mortazavi, Arezoo Dianat, Obaidur Rahaman, Gianaurelio Cuniberti, and Timon Rabczuk. Borophene as an anode material for Ca, Mg, Na or Li ion storage: A first-principle study. *J. Power Sources*, 329:456–461, mar 2016. 94, 108, 109

[255] Oriol Lopez-Sanchez, Dominik Lembke, Metin Kayci, Aleksandra Radenovic, and Andras Kis. Ultrasensitive photodetectors based on monolayer MoS 2. *Nat. Nanotechnol.*, 8(7):497–501, 2013. 94

[256] Ekaterina Pomerantseva and Yury Gogotsi. Two-dimensional heterostructures for energy storage. *Nat. Energy*, 2(7):17089, jun 2017. 94

[257] Tomoki Yamashita, Hiroyoshi Momida, and Tamio Oguchi. Crystal structure predictions of NaxC6O6 for sodium-ion batteries: First-principles calculations with an evolutionary algorithm. *Electrochim. Acta*, 195:1–8, 2016. 94

[258] Kristen S. Williams, Victor Rodriguez-Santiago, and Jan W. Andzelm. Modeling reaction pathways for hydrogen evolution and water dissociation on magnesium. *Electrochim. Acta*, 210:261–270, 2016. 94

[259] Bohayra Mortazavi, Arezoo Dianat, Gianaurelio Cuniberti, and Timon Rabczuk. Application of silicene, germanene and stanene for Na or Li ion storage: A theoretical investigation. *Electrochim. Acta*, 213:865–870, mar 2016. 94, 108, 109

[260] Meysam Makaremi, Bohayra Mortazavi, and Chandra Veer Singh. Carbon ene-yne graphyne monolayer as an outstanding anode material for Li/Na ion batteries. *Appl. Mater. Today*, 10:115–121, mar 2018. 94

[261] Meysam Makaremi, Bohayra Mortazavi, and Chandra Veer Singh. 2D Hydrogenated graphene-like borophene as a high capacity anode material for improved Li/Na ion batteries: A first principles study. *Mater. Today Energy*, 8:22–28, 2018. 94

[262] Jonathan N. Coleman, Mustafa Lotya, Arlene O'Neill, Shane D. Bergin, Paul J. King, Umar Khan, Karen Young, Alexandre Gaucher, Sukanta De, Ronan J. Smith, Igor V. Shvets, Sunil K. Arora, George Stanton, Hye Young Kim, Kangho Lee, Gyu Tae Kim, Georg S. Duesberg, Toby Hallam, John J. Boland,

Jing Jing Wang, John F. Donegan, Jaime C. Grunlan, Gregory Moriarty, Aleksey Shmeliov, Rebecca J. Nicholls, James M. Perkins, Eleanor M. Grieveson, Koenraad Theuwissen, David W. McComb, Peter D. Nellist, and Valeria Nicolosi. Two-dimensional nanosheets produced by liquid exfoliation of layered materials. *Science (80-.).*, 331(6017):568–571, 2011. 94, 95

[263] E. Xenogiannopoulou, P. Tsipas, K. E. Aretouli, D. Tsoutsou, S. A. Giamini, C. Bazioti, G. P. Dimitrakopulos, Ph Komninou, S. Brems, C. Huyghebaert, I. P. Radu, and A. Dimoulas. High-quality, large-area MoSe2 and MoSe2/Bi2Se3 heterostructures on AlN(0001)/Si(111) substrates by molecular beam epitaxy. *Nanoscale*, 7(17):7896–7905, 2015. 94

[264] Y H Lee, X Q Zhang, W Zhang, M T Chang, C T Lin, K D Chang, Y C Yu, J T Wang, C S Chang, L J Li, and T W Lin. Synthesis of large-area MoS2 atomic layers with chemical vapor deposition. *Adv Mater*, 24(17):2320–2325, 2012. 95

[265] Manish Chhowalla, Damien Voiry, Jieun Yang, Hyeon Suk Shin, and Kian Ping Loh. Phase-engineered transition-metal dichalcogenides for energy and electronics. *MRS Bull.*, 40(7):585–591, 2015. 95

[266] Matteo Calandra. Chemically exfoliated single-layer MoS 2: Stability, lattice dynamics, and catalytic adsorption from first principles. *Phys. Rev. B - Condens. Matter Mater. Phys.*, 88(24), 2013. 95

[267] Yong Wang, Zdenek Sofer, Jan Luxa, and Martin Pumera. Lithium Exfoliated Vanadium Dichalcogenides (VS2, VSe2, VTe2) Exhibit Dramatically Different Properties from Their Bulk Counterparts. *Adv. Mater. Interfaces*, 3(23), 2016. 95

[268] C. Ataca, H. Şahin, and S. Ciraci. Stable, single-layer MX 2 transition-metal oxides and dichalcogenides in a honeycomb-like structure. *J. Phys. Chem. C*, 116(16):8983–8999, 2012. 95

[269] Jun Feng, Xu Sun, Changzheng Wu, Lele Peng, Chenwen Lin, Shuanglin Hu, Jinlong Yang, and Yi Xie. Metallic few-layered VS2 ultrathin nanosheets: High two-dimensional conductivity for in-plane supercapacitors. *J. Am. Chem. Soc.*, 133(44):17832–17838, 2011. 95

[270] Meysam Makaremi, Sean Grixti, Keith T. Butler, Geoffrey A. Ozin, and Chandra Veer Singh. Band Engineering of Carbon Nitride Monolayers by N-Type, P-Type, and Isoelectronic Doping for Photocatalytic Applications. *ACS Appl. Mater. Interfaces*, 10(13):11143–11151, apr 2018. 95

[271] Zhepeng Zhang, Jingjing Niu, Pengfei Yang, Yue Gong, Qingqing Ji, Jianping Shi, Qiyi Fang, Shaolong Jiang, He Li, Xiebo Zhou, Lin Gu, Xiaosong Wu, and Yanfeng Zhang. Van der Waals Epitaxial Growth of 2D Metallic Vanadium Diselenide Single Crystals and their Extra-High Electrical Conductivity. *Adv. Mater.*, 29(37), 2017. 95, 103

[272] Huei Ru Fuh, Kai Wei Chang, Sheng Hsiung Hung, and Horng Tay Jeng. Two-Dimensional Magnetic Semiconductors Based on Transition-Metal Dichalcogenides VX2 (X = S, Se, Te) and Similar Layered Compounds VI2 and Co(OH)2. *IEEE Magn. Lett.*, 8, 2017. 95

[273] Yu Jing, Zhen Zhou, Carlos R. Cabrera, and Zhongfang Chen. Metallic VS2 monolayer: A promising 2D anode material for lithium ion batteries. *J. Phys. Chem. C*, 117(48):25409–25413, 2013. 95, 97, 99

[274] Stefan Grimme. Semiempirical GGA-type density functional constructed with a long-range dispersion correction. *J. Comput. Chem.*, 27(15):1787–1799, nov 2006. 95

[275] W. Tang, E. Sanville, and G. Henkelman. A grid-based Bader analysis algorithm without lattice bias. *J. Phys. Condens. Matter*, 21(8):084204, feb 2009. 96, 109

[276] Graeme Henkelman, Blas P. Uberuaga, and Hannes Jónsson. Climbing image nudged elastic band method for finding saddle points and minimum energy paths. Technical Report 22, 2000. 96

[277] Alireza Tabarraei, Shohreh Shadalou, and Jeong Hoon Song. Mechanical properties of graphene nanoribbons with disordered edges. *Comput. Mater. Sci.*, 96(PA):10–19, jan 2015. 96

[278] Eliezer Fernando Oliveira, Ricardo Paupitz Barbosa Dos Santos, Pedro Alves Da Silva Autreto, Stanislav Moshkalev, and Douglas Soares Galvão. Improving Graphene-metal Contacts: Thermal Induced Polishing. *MRS Adv.*, 3(1-2):73–78, jan 2018. 96

[279] R. A. Bizao, T. Botari, E. Perim, Nicola M. Pugno, and D. S. Galvao. Mechanical properties and fracture patterns of graphene (graphitic) nanowiggles. *Carbon N. Y.*, 119:431–437, 2017. 96

[280] Yao Fu and Jeong Hoon Song. Heat flux expressions that satisfy the conservation laws in atomistic system involving multibody potentials. *J. Comput. Phys.*, 294:191–207, 2015. 96

[281] Hao Sun, Sankha Mukherjee, Matthew Daly, Ajay Krishnan, Manohar Harsha Karigerasi, and Chandra Veer Singh. New insights into the structure-nonlinear mechanical property relations for graphene allotropes. *Carbon N. Y.*, 110:443–457, 2016. 98

[282] Abdus Samad and Young Han Shin. MoS 2 @VS 2 Nanocomposite as a Superior Hybrid Anode Material. *ACS Appl. Mater. Interfaces*, 9(35):29942–29949, aug 2017. 99

[283] M. Aydinol, A. Kohan, G. Ceder, K. Cho, and J. Joannopoulos. Ab initio study of lithium intercalation in metal oxides and metal dichalcogenides. *Phys. Rev. B - Condens. Matter Mater. Phys.*, 56(3):1354–1365, jul 1997. 101, 113

[284] Bohayra Mortazavi, Masoud Shahrokhi, Mohamed E. Madjet, Meysam Makaremi, Said Ahzi, and Timon Rabczuk. N-, P-, As-triphenylene-graphdiyne: Strong and stable 2D semiconductors with outstanding capacities as anodes for Li-ion batteries, jan 2019. 101, 108, 114

[285] J M Tarascon and M Armand. Issues and challenges facing rechargeable lithium batteries. *Nature*, 414(6861):359–67, nov 2001. 102, 113

[286] Zhenguo Yang, Daiwon Choi, Sebastien Kerisit, Kevin M. Rosso, Donghai Wang, Jason Zhang, Gordon Graff, and Jun Liu. Nanostructures and lithium electrochemical reactivity of lithium titanites and titanium oxides: A review, jul 2009. 102, 113

[287] Elad Pollak, Baisong Geng, Ki Joon Jeon, Ivan T. Lucas, Thomas J. Richardson, Feng Wang, and Robert Kostecki. The interaction of Li+ with single-layer and few-layer graphene. *Nano Lett.*, 10(9):3386–3388, 2010. 104

[288] Bohayra Mortazavi, Obaidur Rahaman, Said Ahzi, and Timon Rabczuk. Flat borophene films as anode materials for Mg, Na or Li-ion batteries with ultra high capacities: A first-principles study. *Appl. Mater. Today*, 8:60–67, sep 2017. 108

[289] Guoxing Li, Yuliang Li, Huibiao Liu, Yanbing Guo, Yongjun Li, and Daoben Zhu. Architecture of graphdiyne nanoscale films. *Chem. Commun.*, 46(19):3256–3258, may 2010. 108

[290] R. H. Baughman, H. Eckhardt, and M. Kertesz. Structure-property predictions for new planar forms of carbon: Layered phases containing sp 2 and sp atoms. *J. Chem. Phys.*, 87(11):6687–6699, dec 1987. 108

[291] Yongjun Li, Liang Xu, Huibiao Liu, and Yuliang Li. ChemInform Abstract: Graphdiyne and Graphyne: From Theoretical Predictions to Practical Construction. *ChemInform*, 45(23):no–no, mar 2014. 108

[292] Mengqiu Long, Ling Tang, Dong Wang, Yuliang Li, and Zhigang Shuai. Electronic structure and carrier mobility in graphdiyne sheet and nanoribbons: Theoretical predictions. *ACS Nano*, 5(4):2593–2600, apr 2011. 108

[293] L. D. Pan, L. Z. Zhang, B. Q. Song, S. X. Du, and H. J. Gao. Graphyne- and graphdiyne-based nanoribbons: Density functional theory calculations of electronic structures. *Appl. Phys. Lett.*, 98(17):173102, apr 2011. 108

[294] Ning Wang, Xiaodong Li, Zeyi Tu, Fuhua Zhao, Jianjiang He, Zhaoyong Guan, Changshui Huang, Yuanping Yi, and Yuliang Li. Synthesis and Electronic Structure of Boron-Graphdiyne with an sp-Hybridized Carbon Skeleton and Its Application in Sodium Storage. *Angew. Chemie - Int. Ed.*, 57(15):3968–3973, 2018. 108

[295] Changshui Huang, Shengliang Zhang, Huibiao Liu, Yongjun Li, Guanglei Cui, and Yuliang Li. Graphdiyne for high capacity and long-life lithium storage. *Nano Energy*, 11:481–489, jan 2015. 108

[296] Hong Shang, Zicheng Zuo, Le Yu, Fan Wang, Feng He, and Yuliang Li. Low-Temperature Growth of All-Carbon Graphdiyne on a Silicon Anode for High-Performance Lithium-Ion Batteries. *Adv. Mater.*, 30(27):1801459, jul 2018. 108

[297] Hong Shang, Zicheng Zuo, Liang Li, Fan Wang, Huibiao Liu, Yongjun Li, and Yuliang Li. Ultrathin Graphdiyne Nanosheets Grown In Situ on Copper Nanowires and Their Performance as Lithium-Ion Battery Anodes. *Angew. Chemie - Int. Ed.*, 57(3):774–778, 2018. 108

[298] Chao Lu, Ying Yang, Jian Wang, Ruoping Fu, Xinxin Zhao, Lei Zhao, Yue Ming, Ying Hu, Hongzhen Lin, Xiaoming Tao, Yuliang Li, and Wei Chen. High-performance graphdiyne-based electrochemical actuators. *Nat. Commun.*, 9(1):752, dec 2018. 108

[299] Panyong Kuang, Bicheng Zhu, Yuliang Li, Huibiao Liu, Jiaguo Yu, and Ke Fan. Graphdiyne: A superior carbon additive to boost the activity of water oxidation catalysts. *Nanoscale Horizons*, 3(3):317–326, may 2018. 108

[300] Yasong Zhao, Jiawei Wan, Huiying Yao, Lijuan Zhang, Kaifeng Lin, Lei Wang, Nailiang Yang, Daobin Liu, Li Song, Jia Zhu, Lin Gu, Lei Liu, Huijun Zhao, Yuliang Li, and Dan Wang. Few-layer graphdiyne doped with sp-hybridized nitrogen atoms at acetylenic sites for oxygen reduction electrocatalysis. *Nat. Chem.*, 10(9):924–931, sep 2018. 108

[301] Huidi Yu, Yurui Xue, Lan Hui, Chao Zhang, Yingjie Zhao, Zhibo Li, and Yuliang Li. Controlled Growth of MoS 2 Nanosheets on 2D N-Doped Graphdiyne Nanolayers for Highly Associated Effects on Water Reduction. *Adv. Funct. Mater.*, 28(19):1707564, 2018. 108

[302] Ryota Matsuoka, Ryojun Toyoda, Ryo Shiotsuki, Naoya Fukui, Keisuke Wada, Hiroaki Maeda, Ryota Sakamoto, Sono Sasaki, Hiroyasu Masunaga, Kosuke Nagashio, and Hiroshi Nishihara. Expansion of the Graphdiyne Family: A Triphenylene-Cored Analogue. *ACS Appl. Mater. Interfaces*, 11(3):2730–2733, 2019. 108

[303] Bohayra Mortazavi, Masoud Shahrokhi, Mohamed E. Madjet, Tanveer Hussain, Xiaoying Zhuang, and Timon Rabczuk. N-, B-, P-, Al-, As-, and Ga-graphdiyne/graphyne lattices: First-principles investigation of mechanical, optical and electronic properties. *J. Mater. Chem. C*, 7(10):3025–3036, mar 2019. 108

[304] B. Silvi and A. Savin. Classification of chemical bonds based on topological analysis of electron localization functions. *Nature*, 371(6499):683–686, oct 1994. 109

[305] M. Scheffler and C. Stampfl. Chapter 5 Theory of adsorption on metal substrates. *Handb. Surf. Sci.*, 2:285–356, nov 2000. 112

[306] Meysam Makaremi, Bohayra Mortazavi, Timon Rabczuk, Geoffrey A. Ozin, and Chandra Veer Singh. Theoretical Investigation: 2D N-Graphdiyne Nanosheets as Promising Anode Materials for Li/Na Rechargeable Storage Devices. *ACS Appl. Nano Mater.*, 2(1):127–135, jan 2019. 113

[307] Wenzhuo Cao, Jienan Zhang, and Hong Li. Batteries with high theoretical energy densities. *Energy Storage Materials*, 26:46–55, apr 2020.

[308] Kunlei Zhu, Qian Li, Zhongmeng Xue, Qi Yu, Xicheng Liu, Zhongqiang Shan, and Kai Liu. Mesoporous TiO2 Spheres as Advanced Anodes for Low-Cost, Safe, and High-Areal-Capacity Lithium-Ion Full Batteries, feb 2020.

[309] Lei Zhang, Hao Bin Wu, Srinivasan Madhavi, Huey Hoon Hng, and Xiong Wen Lou. Formation of Fe 2O 3 microboxes with hierarchical shell structures from metal-organic frameworks and their lithium storage properties. *Journal of the American Chemical Society*, 134(42):17388–17391, oct 2012.

[310] James C. Pramudita, Divya Sehrawat, Damian Goonetilleke, and Neeraj Sharma. An Initial Review of the Status of Electrode Materials for Potassium-Ion Batteries, dec 2017.

[311] Richard Schmuch, Ralf Wagner, Gerhard Hörpel, Tobias Placke, and Martin Winter. Performance and cost of materials for lithium-based rechargeable automotive batteries, apr 2018.

[312] Mohammad Salavati, Naif Alajlan, and Timon Rabczuk. Super-stretchability in two-dimensional RuCl 3 and RuBr 3 confirmed by first-principles simulations. *Phys. E Low-Dimensional Syst. Nanostructures*, 113:79–85, may 2019.

[313] Mohammad Salavati and Timon Rabczuk. First-principles investigation of N-triphenylene-graphdiyne nanosheets as an anode material for Na, K, Mg and Ca storage. *Comput. Mater. Sci.*, 169:109093, nov 2019.

Academic Curriculum Vitae

Mohammad Salavati

Institute of Structural Mechanics
Bauhaus-University Weimar
Marienstrasse 15, 99423 Weimar, Germany
Email: mohammad.salavati@uni-weimar.de

Education

- Ph.D : Computational Mechanics, Institute of Structural Mechanics, Bauhaus-University Weimar, Germany, July 2014 - June 2019 (Submission process)$\sim$June 2020 (Defended).
- M.Sc: Structural Engineering, Dokuz Eylul University, Turkey.
- B.Sc: Civil Engineering, University of Applied Sciences and Technology, Iran.

Publications

1. M. Salavati, T. Rabczuk, *First-principles investigation of N-triphenylene-graphdiyne nanosheets as an anode material for Na, K, Mg and Ca storage,*. Comput. Mater. Sci. 169 (2019). doi:10.1016/j.commatsci.2019.109093
2. M. Salavati, N. Alajlan, T. Rabczuk, *Super-stretchability in two-dimensional RuCl 3 and RuBr 3 confirmed by first-principles simulations,* . Phys. E Low-Dimensional Syst. Nanostructures. 113 (2019) 79–85. doi:10.1016/j.physe.2019.05.011.
3. M. Salavati , *Mechanical responses of pristine and defective hexagonal-BN nanosheets; molecular dynamics simulations,* In Front. Struct. Civ. Eng. Springer (2020) doi: https://doi.org/10.1007/s11709-020-0616-5
4. M. Salavati, T. Rabczuk, *2D VS2 and VSe2 and 2D N-TpG nanosheets interacted with Li, Na, K, Mg, Ca, and Al- ions,* Biomolecular mechanisms at functionalized solid surfaces, Poster representation, CECAM workshop 2019, Sorbonne University, Paris.

5. M. Salavati, T. Rabczuk,*Application of highly stretchable and conductive two-dimensional 1T VS2 and VSe2 as anode materials for Li-, Na- and Ca-ion storage,* Comput. Mater. Sci. 160 (2019) 360–367. doi:https://doi.org/10.1016/j.commatsci.2019.01.018.

6. M. Salavati, *Electronic and mechanical responses of two-dimensional HfS2, HfSe2, ZrS2, and ZrSe2 from first-principles,* Front. Struct. Civ. Eng. (2018) 1–9. doi:10.1007/s11709-018-0491-5.

7. M. Salavati, H. Ghasemi, T. Rabczuk, *Electromechanical properties of Boron Nitride Nanotube: Atomistic bond potential and equivalent mechanical energy approach,* Comput. Mater. Sci. 149 (2018) 460–465. doi: 10.1016/J.COMMATSCI.2018.03.037.